Karlsruhe Institute of Technology

# Design Study of the Large Hadron Electron Collider and a Rapid Cycling Synchrotron as Alternative to the PS Booster Upgrade at CERN

Zur Erlangung des akademischen Grades eines
DOKTORS DER NATURWISSENSCHAFTEN

von der Fakultät für Physik
des Karlsruher Institutes für Technologie (KIT)

genehmigte
DISSERTATION
von

Dipl.-Phys.
**Miriam Fitterer**
aus Mannheim

Tag der mündlichen Prüfung: 22. Februar 2013
Hauptreferent: **Prof. Dr. Tilo Baumbach**
Korreferent: **Prof. Dr. Günter Quast**

# Zusammenfassung

Mit dem Large Hadron Collider (LHC) ist es zum ersten Mal möglich, die Teilchenphysik im TeV Bereich zu erforschen. Ein essentieller Parameter ist hierbei die Luminosität. Um die Luminosität - und damit die Wahrscheinlichkeit am LHC neue Physik jenseits des Standardmodells der Teilchenphysik zu entdecken - weiter zu erhöhen, ist es vorgesehen den LHC selbst und die LHC Injektoren - die Beschleunigerkette, die den Strahl für den LHC vorbereitet - in 2020 teilweise zu erneuern und weiter auszubauen.
Einer der LHC Injektoren, der zweite in der Kette, ist der Proton Synchrotron (PS) Booster. Eine der Hauptlimitationen des PS Booster sind Raumladungseffekte - die Wirkung des elektromagnetischen Feldes des Strahls auf sich selbst, welche im Allgemeinen mit steigender Strahlenergie abnehmen. Um im Fall des PS-Booster die Strahlparameter weiter zu verbessern, ist daher eine Erhöhung der Strahlenergie von 1.4 GeV auf 2 GeV geplant. Anstatt jedoch den mittlerweile schon recht alten (Baujahr 1972) PS Booster teilweise zu erneuern und auszubauen, wurde vorgeschlagen einen komplett neuen Beschleuniger, ein Rapid Cycling Synchrotron (RCS), zu bauen, welches dann in Zukunft den PS Booster ersetzen würde. In dieser Arbeit werden mehrere Optionen für die Strahlführung im RCS - die sogenannte Magnetstruktur und Optik - untersucht und verschiedene Magnetstrukturen und Optiken in Hinblick auf Raumladungseffekte verglichen. Die Studien ergaben, dass ein dem PS Booster ähnliche Magnetstruktur und Optik einer dem RCS ähnlichen in Hinblick auf die Unterdrückung von Raumladungseffekten überlegen ist.
Des Weiteren wurde vorgeschlagen das LHC Physikprogramm durch tiefinelastische Lepton-Nukleon Kollisionen, dem Large Hadron Electron Collider (LHeC), zu ergänzen. In diesem Fall würde der LHC Protonstrahl mit einem Elektron- bzw. Positronstrahl kollidieren, welcher in einer separaten neuen Maschine beschleunigt werden würde. Als Elektronbeschleuniger werden zwei Optionen in Betracht gezogen: ein neuer “Energy Recovery” Linac - die Linac-Ring Option - oder die Installation eines Elektronenringes im schon existierenden LHC Tunnel - die Ring-Ring Option. Eine der Hauptherausforderungen der Ring-Ring Option ist die Integration des Elektronringes in den existierenden LHC Tunnel. Im Rahmen dieser Arbeit wurde ein Elektronringlayout, -magnetstruktur und -optik entwickelt, welche mit den Hauptintegrationsbedingungen kompatibel ist und die die von seiten der Teilchenphysikexperimente festgesetzten Designparameter erreicht. Ausserdem wurden verschiedene strahldynamische Aspekte des Elektronenbeschleunigers untersucht, darunter Korrekturen der chromatischen Aberration, Kopplungsschemata unter Berücksichtigung der Kollision des Elektronenstrahls mit dem LHC Protonstrahl und der Einfluss von Umfangsfehlern auf die Elektronenstrahldynamik, und Lösungen für den LHeC erarbeitet.

# Abstract

With the Large Hadron Collider (LHC) the exploration of particle physics at center of mass energies at the TeV scale has begun. To extend the discovery potential of the LHC, a major upgrade is foreseen around 2020 of the LHC itself and the LHC injectors - the chain of accelerators preparing the beam for the LHC.
One of the injectors - the second one in the chain - is the Proton Synchrotron (PS) Booster. Its performance is currently limited by the space-charge effect, which is the effect of the electromagnetic field of the particle beam on itself. This effect becomes weaker with higher energy, and therefore an energy upgrade of the PS Booster to 2 GeV maximum beam energy is foreseen. As the PS Booster is with its 40 years already an old machine, the construction of a new accelerator, a Rapid Cycling Synchrotron (RCS), to replace the PS Booster has been proposed. In this thesis different options for the beam guidance in the RCS - referred to as lattice and optics - are studied, followed by a more general comparison of different lattices and optics and their performance under consideration of the space-charge effect.
To further complement the LHC physics program, also the possibility of deep inelastic lepton-nucleon scattering at the LHC has been suggested, referred to as Large Hadron Electron Collider (LHeC). In this case the proton beam of the LHC collides with the electron beam, which is accelerated in a separate newly built machine. Two options are considered as electron accelerator: a new energy recovery linac - the Linac-Ring option - and the installation of an electron ring in the existing LHC tunnel - the Ring-Ring option. One of the main challenges of the Ring-Ring option is the integration of the electron ring in the current LHC tunnel. A layout, lattice and optics of the electron accelerator is developed in this thesis, which meets the requirements with regard to integration and reaches the beam parameters demanded by the particle physics experiments.

# Contents

# Introduction

In 2008 the Large Hadron Collider (LHC) built at the European Organization for Nuclear Research (CERN) in Geneva and its experiments started operation with the main aim of finding or excluding the existence of a Higg's particle. Only four years later, on the 4th July 2012, the two main experiments ATLAS and CMS announced the discovery of a Higg's like Boson with a mass of around 125 GeV which was then first published in [1] and [2].

Even though the existence of a Higg's like particle has been demonstrated, its nature is still unknown and the studies of its properties are therefore one of the main objectives of the following operational years of the LHC, in addition to the search for new physics beside the standard model. As the cross section for the production of the Higg's particle,

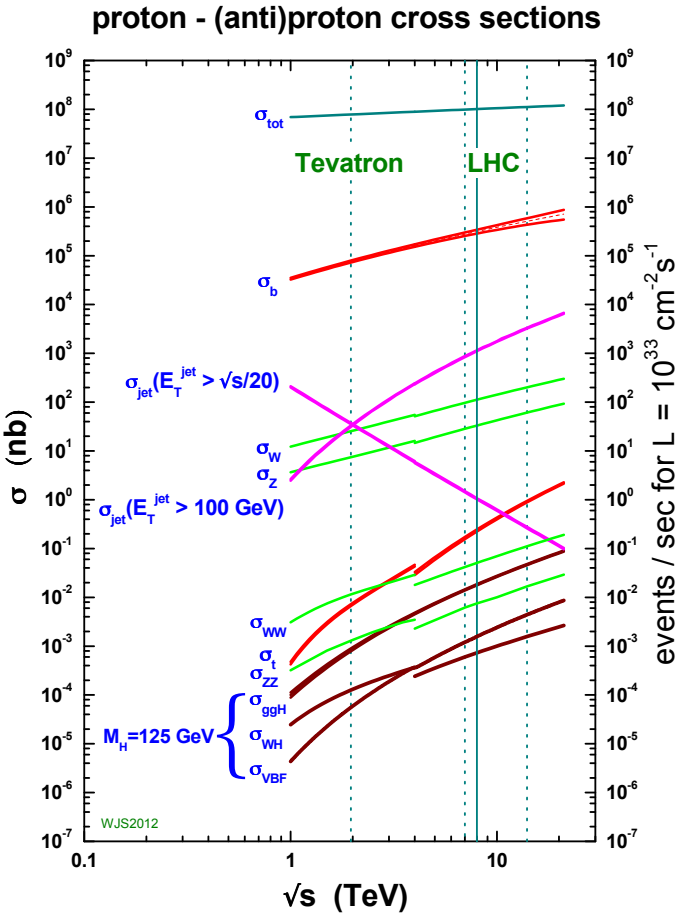


**Figure 1:** Higg's cross sections. Plot is taken from [3].

illustrated in Fig. 1, as well as the cross section for the production of non-standard model particles are in general very small at energies reachable with the LHC, an as high as possible luminosity (rate of collisions) is desired in order to obtain enough statistics in a still reasonable time frame. For this reason an increase in luminosity is foreseen around 2020 with the aim of producing a total luminosity of 3000 $\text{fb}^{-1}$ in 10-12 years in comparison to $200 - 300$ $\text{fb}^{-1}$ expected with the present LHC in 10-12 years of operation. In order to achieve this goal not only the LHC needs to be upgraded - referred to as High Luminosity LHC upgrade (HL-LHC upgrade) [4] - but also the LHC injectors - summarized in the LHC Injectors Upgrade (LIU) [5] - which are providing the beam for the LHC and also for various other experiments at CERN. A schematic view of the CERN accelerator complex is shown in Fig. 2.

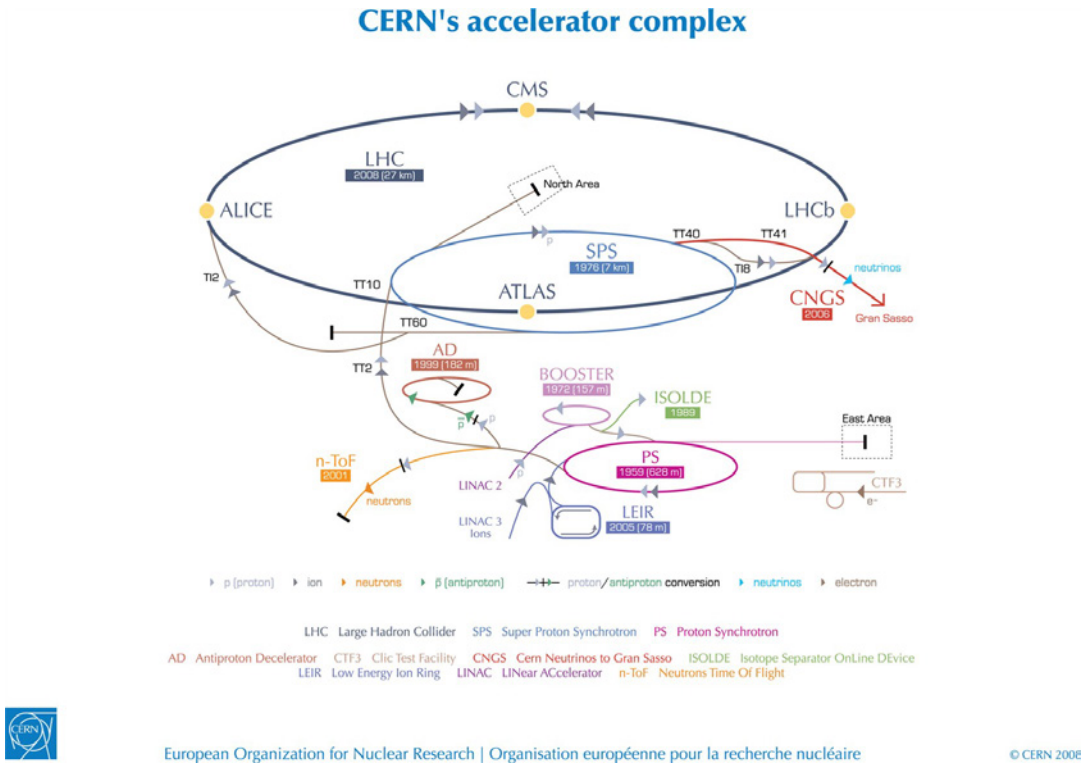


**Figure 2:** CERN accelerator complex. The protons for the LHC are obtained by generating them in a proton source. The protons are then injected from the source into the linear accelerator (LINAC2), then the Proton Synchrotron (PS) Booster, followed by the Proton Synchrotron (PS) and the Super Proton Synchrotron (SPS), before finally reaching the Large Hadron Collider (LHC), where after a consolidation program in 2013/2014 they will be accelerated to their final energy of nominal 7 TeV. Plot is taken from [6].

One of the main limitations of the LHC injectors is currently the maximum achievable beam brightness due to space-charge effects. The space-charge effect is in general weaker for higher beam energies. The injector upgrade therefore foresees to replace the first accelerator in the injector chain - LINAC2 - by a new linac - LINAC4 - which then accelerates $\text{H}^-$-ions[1] to an energy of 160 MeV instead of previously 50 MeV. This increases

[1] Many bunches from LINAC4 will be injected into the PS Booster and form one PS Booster bunch per ring. In this injection process the $\text{H}^-$-ions pass a stripping foil converting them to protons. With this

the injection energy, and thus mitigates space-charge effects in the following machine, the PS Booster. To further mitigate space-charge effects in the LHC injector chain, the protons will be accelerated in the PS Booster to 2 GeV, instead of 1.4 GeV, and then transferred to the next accelerator, the PS. The increase of the injection and extraction energy and the change from a proton injection to $H^-$ injection involves a major upgrade of the existing PS Booster [7]. The PS Booster is, with its 40 years, already quite an old machine and it was therefore considered to build a new machine instead of upgrading the old one. As an alternative, a Rapid Cycling Synchrotron (RCS) was proposed. The following study of both options though revealed that considering cost, performance and reliability, the upgrade of the current PS Booster still represented the better option (see [8] and [9] for further details). In the SPS, the beam energy is already high enough that other effects become more relevant than space-charge. The performance limitations, expressed as reachable emittance and bunch intensity at transfer to the LHC, of all three synchrotrons after the injector upgrade are illustrated in Fig. 3 and reveal the challenge of providing the high brightness beams requested by the HL-LHC.

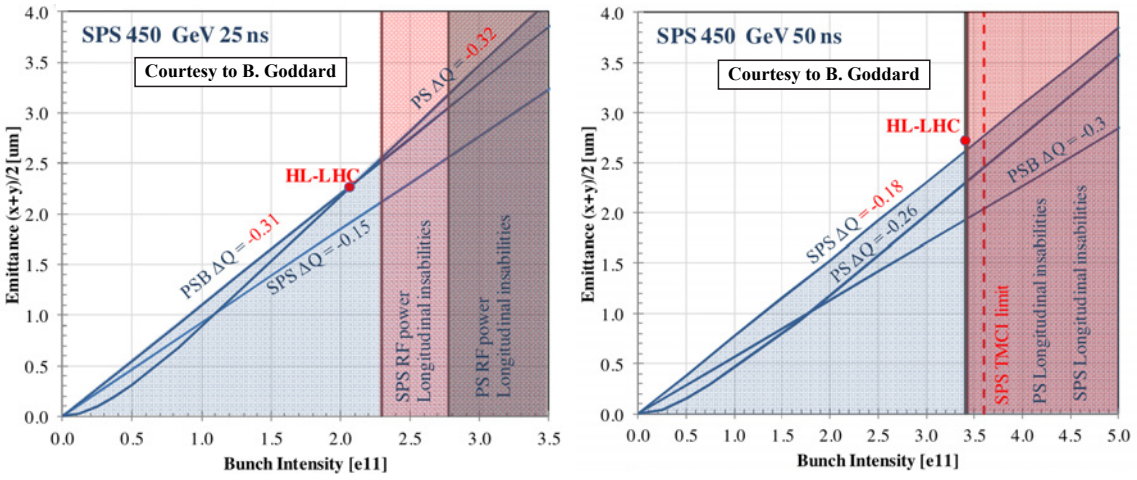


**Figure 3:** Emittance versus bunch intensity at SPS extraction for 25 ns bunches (left) and 50 ns bunches (right). The performance limitations due to space-charge effects are indicated in blue and those performance limitations which are due to other collective effects as well as hardware limitations in red, where the individual curves represent the limits from the different injectors. Plots are taken from [5].

To further extend and complement the LHC physics program, a lepton-nucleon collider, the Large Hadron Electron Collider (LHeC), has been proposed with the main motivation to explore the world of lepton-nucleon scattering at the TeV scale. The diversity of physics at the TeV scale which could be covered by a hadron-hadron, a future lepton-lepton and in addition a lepton-hadron collider is illustrated schematically in Fig. 4.
In the case of the LHeC the 7 TeV proton or heavy ion beam is provided by the already existing LHC. As electron accelerator with a beam energy of 60 GeV two options have been studied: a new electron synchrotron installed on top of the LHC in the existing tunnel (the "Ring-Ring" option) and a new energy recovery linac (the "Linac-Ring" option).

method it is possible to inject into the same phase space area several times and thus increase the maximum number of particles to be injected into the PS Booster.

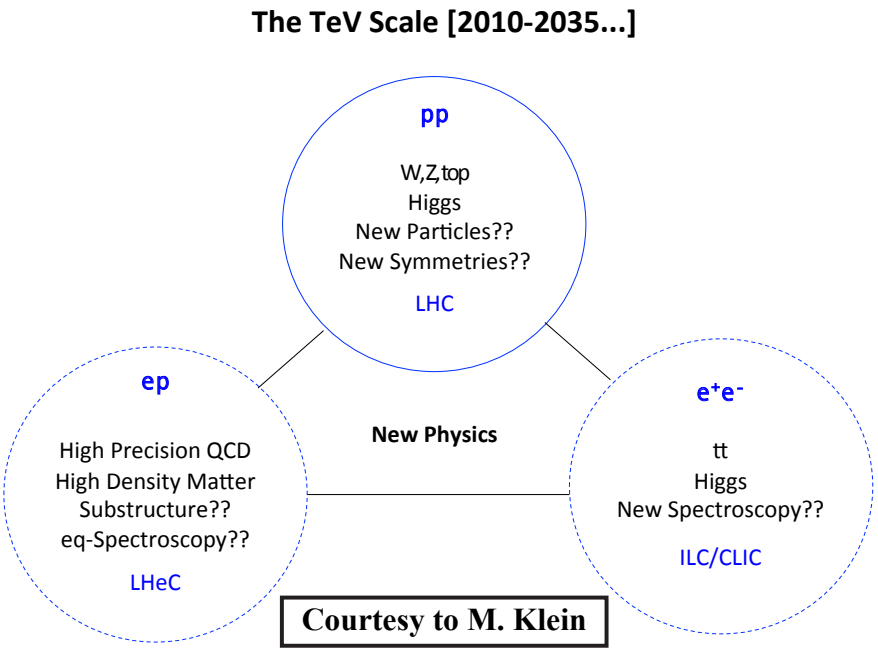


**Figure 4:** Physics at the TeV scale. The LHeC would extend and complement the physics program covered by a hardron collider, the LHC, and a future lepton collider like the ILC or CLIC. Plot is taken from [10].

Both options provide the possibility to operate in parallel with standard LHC proton-proton, proton-ion or ion-ion operation. The luminosity and beam energy are in both cases mainly constrained by the assumed wall-plug power limit of 100 MW, leading to a maximum luminosity of more than $10^{33}\,\mathrm{cm}^{-2}\mathrm{s}^{-1}$. The Ring-Ring option provides this maximum luminosity in the case of electron-proton and positron-proton collisions whereas the Linac-Ring option realistically has a significantly reduced luminosity in the case of positron-proton collisions. On the other hand the Linac-Ring option may have a high beam polarization in contrast to the Ring-Ring option where the polarization of the electron beam is very difficult due to the high beam energy. Further details on the physics program and both accelerator options are documented in the Conceptional Design Report (CDR) [10]. Following the publication of the CDR it has been decided in a recent workshop to pursue the Linac-Ring option further [11], keeping the Ring-Ring option as backup.

Within this thesis the lattice and optics design of the LHeC Ring-Ring option with exception of the interaction region, and the lattice and optics design of the RCS, considered as alternative to the LIU PS Booster energy upgrade in view of the HL-LHC, have been studied. The thesis is divided according to the two different accelerators in two parts, where the LHeC Ring-Ring option studies are presented in chapter 2 and the RCS studies in chapter 3. Both chapters are preceded by a short introduction to accelerator physics (chapter 1) addressing topics relevant for the studies presented in this thesis.

The LHeC Ring-Ring option, chapter 2, addresses the following topics:

Section 2.1 discusses and reviews the design parameters chosen for the CDR [10] and gives possible options to further increase the performance of the LHeC.

Section 2.2 presents the general layout and geometry of the electron ring and in particular the layout of the bypasses around the LHC proton physics experiments.

Section 2.3 shows the linear optics of the electron ring, explicitly the arc cell, insertion and bypass optics.

Section 2.3 addresses different aspects of beam dynamics considered to be particularly relevant for the LHeC: the correction of chromatic aberrations and off-momentum beta-beating (Sec. 2.4.2), linear coupling and the matching of the electron beam size to the proton beam size at the interaction point (Sec. 2.4.3) and the effect of circumference errors on the damping partition (Sec. 2.4.4).

All studies of the LHeC Ring-Ring option performed in the framework of this thesis are then summarized in Sec. 2.5.

The chapter about the RCS studies, chapter 3, is divided in two parts:

Sec. 3.1 and Sec. 3.2 give a short overview of the PS Booster upgrade and the proposal of a RCS and summarize the studies performed in view of the technical report of a RCS [9].

Sec. 3.3 to 3.6 focus on more general studies of space-charge dominated lattices motivated by the design study of the RCS.

Sec. 3.3 to 3.5 present the preparatory work for the space-charge simulations, starting with a summary of the general beam and lattice parameters assumed for the simulations (Sec. 3.3) and a description of the space-charge simulation methods and settings used in this thesis (Sec. 3.4), i.e. the lattice description in PTC (Sec. 3.4.1) and a convergence study (Sec. 3.4.2).

Sec. 3.6 summarizes the space-charge simulation results for different lattice types. In particular the impact of variations of the beam size, the lattice symmetry and periodicity and the dispersion suppressor scheme on the emittance blow-up have been studied.

The RCS studies are then concluded by Sec. 3.7, which tries to answer the initial question, based on the results obtained in this thesis, whether or not a better performance is to be expected of the RCS or PS Booster.

# 1. Concepts of Accelerator Physics

In this chapter a short introduction to the basics of accelerator physics and topics relevant for this thesis is given. For further details it is referred to e.g. [12] and [13].

## 1.1 Layout and Components of Accelerators

In general, magnetic fields are used for the guidance and focusing of high energy charged particle beams[1]. The beam guidance is provided by dipole magnets, where the radius of curvature $\rho$ for a particle of charge $e$ and momentum $p$ in a dipole of magnetic field $B$ is given by

$$\frac{1}{\rho} = \left| \frac{e}{p} B \right| . \tag{1.1}$$

The parameter

$$B\rho = \frac{p}{e} \tag{1.2}$$

is also referred to as beam rigidity and often used for the normalization of magnetic fields in beam dynamics.

For the focusing of the beam quadrupole magnets are used. The transverse field components of a quadrupole increase linearly with the distance from the center and vanish in the center of the magnet

$$B_x(y) = gy, \quad B_y(x) = gx\,. \tag{1.3}$$

This linear dependence and the same sign of the magnetic field in both planes leads to a focusing effect in one plane and a defocusing effect in the other plane. To focus the beam in both transverse planes, horizontally and vertically focusing elements have to be alternated. One of the most basic structures often used in the arcs of circular accelerators is the FODO cell shown in Fig. 1.1, where F stands for focusing quadrupole, D for defocusing quadrupole and O for drift space. More information about the optical properties of this cell type can be found in Appendix A.

[1] For low energy particle beams electrostatic elements are also used. As it is much easier to generate high magnetic fields than electric fields, electric beam guidance elements are not feasible anymore for higher energies.

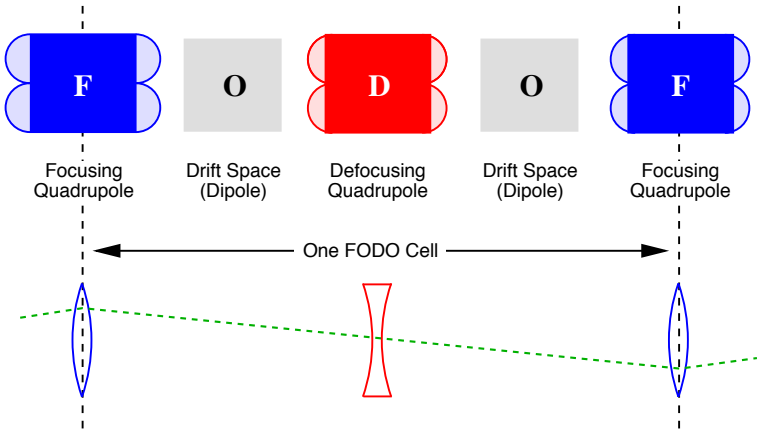


**Figure 1.1:** FODO cell: Focusing structure often used in circular accelerator arcs.

## 1.2 Frenet-Serret Coordinate System

In a circular accelerator the path taken by a particle of central design momentum $p_0$ through the arrangement of dipoles is referred to as reference orbit. It has proven to be beneficial to use a coordinate system with the reference orbit as reference called the Frenet-Serret coordinate system which is illustrated in Fig. 1.2.

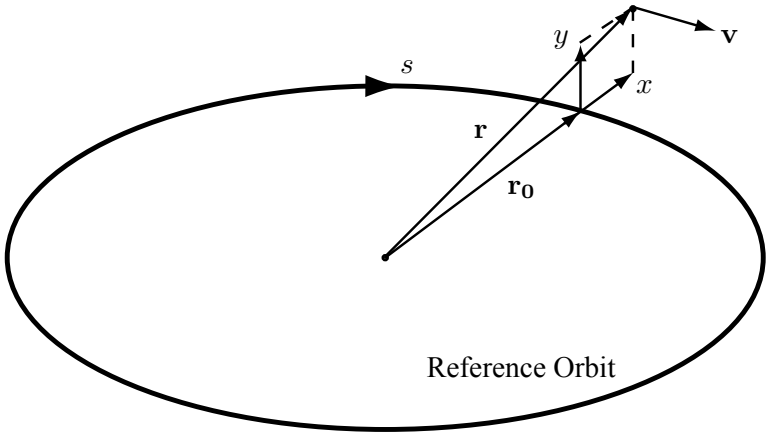


**Figure 1.2:** The Frenet-Serret coordinate system used for circular accelerators. $\mathbf{r_0}(s)$ is the reference orbit. $\hat{x}$, $\hat{y}$ and $\hat{s}$ form the basis of the coordinate system. Any transverse position of the beam particles can then be expressed by $\mathbf{r} = \mathbf{r_0} + x\hat{x} + y\hat{y}$, where $x$ and $y$ are the betatron coordinates.

As the transverse coordinates $x$ and $y$ are usually small compared to the bending radius $\rho$, one can expand the magnetic field along the reference orbit

$$B_z(x,y) = \frac{B_{z0}}{B\rho} + \frac{1}{B\rho}\left(\left(\frac{\partial B_z}{\partial x}\right)\Big|_{x=0} x + \left(\frac{\partial B_z}{\partial y}\right)\Big|_{y=0} y\right) + \cdots, \quad z = x,\, y\,. \tag{1.4}$$

In optics the magnetic fields are usually normalized in respect to the beam rigidity $B\rho$ defined in Eqn. 1.2. The Taylor expansion of Eqn. 1.4 can then be expressed as

$$\begin{array}{rcccccccc} \frac{1}{B\rho}B_x(x,y) & = & & & ky & + & sxy & + \cdots & \\ \frac{1}{B\rho}B_y(x,y) & = & \frac{1}{\rho_x} & + & kx & + & \frac{1}{2}m(x^2-y^2) & + \cdots & \\ & = & \text{dipole} & + & \text{quadrupole} & + & \text{sextupole} & + \cdots & \end{array} \tag{1.5}$$

where only horizontal bending magnets have been included. As mentioned before, dipoles are used for the bending of the beam, quadrupoles for the focusing and sextupole magnets for the chromaticity correction which is discussed in further detail in Sec. 1.4.3 and Appendix C.

## 1.3 Linear Transverse Motion

In this section the transverse motion including the effect of dipoles and quadrupoles is discussed.

### 1.3.1 Equation of motion

Under the assumption of the existence of a closed-orbit and periodic magnet strengths $k(s) = k(s+L)$ with $L$ being the length of one period, the transverse particle motion can be described by the Hill's equation

$$z'' + K_z(s)z = 0,\ z = x,\, y \tag{1.6}$$

with

$$\begin{aligned} K_x(s) &= -k(s) + \tfrac{1}{\rho^2}\,, \\ K_y(s) &= k(s)\,, \end{aligned} \tag{1.7}$$

where $k(s)$ is the normalized quadrupole strength and $\rho$ the bending radius of the dipoles. As most accelerators include mainly horizontal dipoles, the effect of the vertical dipoles has been neglected. The linear independent periodic solutions of the Hill's equation are given according to the Floquet theorem as

$$z(s) = aw(s)e^{i(\psi(s)+\psi_0)}, \quad z^*(s) = aw(s)e^{-i(\psi(s)+\psi_0)} \tag{1.8}$$

with $a$ constant and $w$ and $\psi$ the amplitude and phase function, respectively. The index $z$, indicating either the horizontal or vertical plane, has been and will be omitted in the following if the distinction is obvious.

### 1.3.2 Matrix formalism, Courant-Snyder invariant, emittance and phase space

Like the solution of any linear differential equation the solution of Hill's equation can be expressed in matrix form

$$\mathbf{z}(s) = M(s|s_0)\mathbf{z}(s_0), \quad \mathbf{z}(s) := \big(z(s),\, z'(s)\big)^T\,, \tag{1.9}$$

where $M(s|s_0)$ is the transfer matrix form $s_0$ to $s$. Explicit expressions for the transfer matrices of different elements can be found in e.g. [12]. The transfer matrix of a section reaching from $s_0$ to $s$ and consisting of different subsections is given by the product of the transfer matrices of the subsections

$$M(s|s_0) = M(s|s_{n-1}) \dots M(s_1|s_0)\,. \tag{1.10}$$

Thus, the transfer matrix of a section or the complete accelerator can be obtained by concatenating the transfer matrices of the individual elements.
Moreover, an accelerator is usually constructed of different periodic sections. E.g. the PS Booster consists of 16 equivalent sections. Let $L$ be the length of one such section, then one can define

$$\mathbf{M}(s) = M(s+L|s)\,. \tag{1.11}$$

It can be shown that $\det(\mathbf{M}) = 1$ and under this condition $\mathbf{M}$ can be parametrized as

$$\mathbf{M} = \begin{pmatrix} \cos\phi + \alpha\sin\phi & \beta\sin\phi \\ -\gamma\sin\phi & \cos\phi - \alpha\sin\phi \end{pmatrix}, \tag{1.12}$$

where $\alpha$, $\beta$ and $\gamma = (1+\alpha^2)/\beta$ are the Courant-Snyder parameters or Twiss parameters and $\phi$ the phase advance[2]. The amplitude function $w(s)$ of the solution of Hill's equation (Eqn. 1.8) is related to this parametrization of $\mathbf{M}$ in the following way

$$w^2 = \beta, \quad \alpha = -ww' = -\frac{\beta'}{2}\,. \tag{1.13}$$

Thus, the amplitude is proportional to the square of the Courant-Snyder parameter $\beta$, referred to as beta-function and the parameter $\alpha$ is proportional to the slope of the beta-function. Furthermore, one defines the phase-advance $\phi$ as

$$\phi := \int_0^L \frac{ds}{\beta(s)}\,. \tag{1.14}$$

With this definition the phase function $\psi$ of the solution of Hill's equation is equal to the phase advance $\phi$ in the sense that $\phi = \psi(s=L) - \psi(s=0)$. The phase advance over the complete accelerator with a circumference $C$ divided by $2\pi$ is referred to as tune $Q$

$$Q_z := \frac{1}{2\pi}\int_s^{s+C} \frac{ds}{\beta_z(s)} \tag{1.15}$$

which is in other words just the number of betatron oscillations per turn.
Using the relation between the amplitude and phase of the solution of Hill's equation and the Courant-Snyder parameterization, the cosine like solution of Hill's equation is given by

$$\begin{aligned} z(s) &= a\sqrt{\beta_z(s)}\cos\left(\phi_z+\phi_0\right), \\ z'(s) &= -a\tfrac{1}{\sqrt{\beta_z(s)}}\left(\sin\left(\phi_z+\phi_0\right)+\alpha_z\cos\left(\phi_z+\phi_0\right)\right), \end{aligned} \tag{1.16}$$

and defines an ellipse in the $(z,z')$-phase-space illustrated in Fig. 1.3. The area enclosed by this ellipse is equal to $\pi a^2$ and a constant of the motion in the absence of non-conservative forces like e.g. synchrotron radiation. The ellipse equation can be written as

$$\gamma z^2 + 2\alpha z z' + \beta z'^2 =: C(z,z') = 2J = \text{const}\,. \tag{1.17}$$

The constant $C(z,z')$ is also referred to as the Courant-Snyder invariant. The Courant-Snyder invariant is equal to twice the action $J$, where $J$ is the action variable of the

[2]The convention for the sign of $\phi$ is that $\beta$ is positive for $|\text{trace}(\mathbf{M})| \leq 2$ and $\text{Im}(\sin\phi) > 0$ if $|\text{trace}(\mathbf{M})| > 2$.

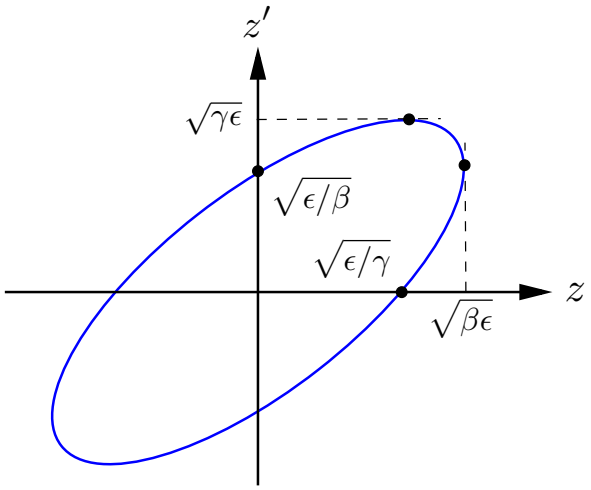


**Figure 1.3:** Phase-space ellipse.

Hamiltonian leading to the Hill's equation. Correctly, the term action should be used for the amplitude of a single particle. For an ensemble of particles one defines the rms-emittance of the ensemble

$$\epsilon_{\mathrm{rms},z} = \sqrt{\sigma_z^2\sigma_{z'}^2 - \sigma_{zz'}^2}\,, \tag{1.18}$$

where $\sigma_i$ are the beam moments. The first moments $\sigma_z$ and $\sigma_{z'}$ are the beam size and beam divergence given by

$$\sigma_z = \sqrt{\beta_z\epsilon_{z,\mathrm{rms}}}, \quad \sigma_{z'} = \sqrt{\gamma_z\epsilon_{z,\mathrm{rms}}}\,. \tag{1.19}$$

However, the term "emittance" is often loosely used for the single particle emittance defined as twice the action $\epsilon := 2J$. The betatron oscillation of a particle with single particle emittance $\epsilon$ can then be expressed by

$$z = \sqrt{\beta_z\epsilon_z}\cos(\phi_z), \quad z'(s) = -\sqrt{\gamma_z\epsilon_z}\cos(\tilde{\phi_z})\,, \tag{1.20}$$

where $\tilde{\phi_z} = \phi_z - \arctan(\alpha_z^{-1})$. The phase $\phi_0$ present in Eqn. 1.16 has been set to zero. An important beam characteristic is also the brightness of the beam defined as [14]

$$\mathcal{B}_0 = \frac{F}{4\pi^2\epsilon_{x,\mathrm{rms}}\epsilon_{y,\mathrm{rms}}}\,, \tag{1.21}$$

where $F$ is the particle flux or longitudinal particle density and $\epsilon_{i,\mathrm{rms}}$ the transverse emittances.

### 1.3.3 Linear coupling

Linear coupling can be generated by either skew quadrupoles, which are quadrupoles rotated by 45° (see Fig. 1.4), or solenoids, which are part of most high energy physics detectors installed at the low-beta insertions. In addition, a deviation of the closed-orbit in magnets with higher order magnetic fields gives rise to skew components and thus coupling. In general, coupling is an unwanted effect as the behavior of the beam is more difficult to understand and the machine operation becomes more complicated. The LHeC

presents a special case in this respect, as linear coupling is desired in order to match the flat electron beam to the round proton beam at the interaction point (IP) and thus avoid harmful beam-beam effects.
The magnetic field of a skew quadrupole is given by

$$\begin{aligned} B_x(x) &= -\tfrac{1}{2}gx\,, \\ B_y(y) &= \tfrac{1}{2}gy \end{aligned} \tag{1.22}$$

with $g = \left(\frac{\partial B_y}{\partial y} - \frac{\partial B_x}{\partial x}\right)\Big|_{x=y=0}$. The field and the effect of a skew quadrupole compared to a "normal" quadrupole on the beam is shown schematically in Fig. 1.4. The particles in the center of the beam are moving away from the center without experiencing any kick. The particles at the left and right exterior of the beam get kicked down or upward and particles at intermediate positions receive a kick in the horizontal and vertical direction resulting in a coupling of the transverse planes.

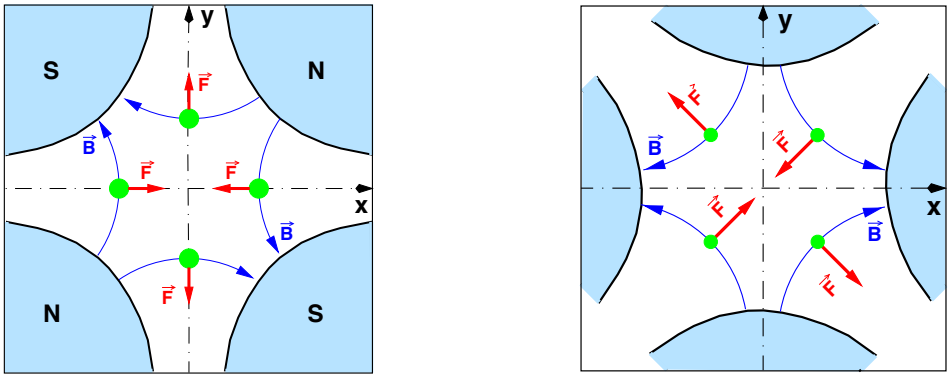


**Figure 1.4:** Cross section of a "normal" quadrupole (left) and a skew quadrupole (right) with magnetic field lines and forces.

In order to describe the optics of a lattice with skew elements or solenoids, the Twiss parameters and emittances introduced in Sec. 1.3.2 have to be generalized. In analogy to Eqn. 1.8 and following the approach taken in [15] the two independent solutions of the equation of motion can be expressed by:

$$\mathbf{z}_I(s) = \sqrt{\epsilon_I}\mathbf{v}_I(s)e^{i(\psi_I(s)+\psi_{0I})}, \quad \mathbf{z}_{II}(s) = \sqrt{\epsilon_{II}}\mathbf{v}_{II}e^{-i(\psi_{II}(s)+\psi_{0II})}\,. \tag{1.23}$$

The parameters $\epsilon_I$ and $\epsilon_{II}$ replace the horizontal and vertical emittance in the uncoupled case and are the new constants of the motion. The vectors $\mathbf{v}_{I,II}$ are the eigenvectors of the one-turn transfer matrix taken at the position $s$ in the lattice and are equivalent to the amplitude function $w(s)$ in Eqn. 1.8. The trajectory $\mathbf{z}(s)$ of a particle with single particle emittance $\epsilon_I$ and $\epsilon_{II}$ is then given by in Frenet-Serret coordinates:

$$\mathbf{z} = \begin{pmatrix} \sqrt{\beta_{xI}\epsilon_I}\cos\phi_{xI} + \sqrt{\beta_{xII}\epsilon_{II}}\cos\phi_{xII} \\ \sqrt{\gamma_{xI}\epsilon_I}\cos\tilde{\phi}_{xI} + \sqrt{\gamma_{xII}\epsilon_{II}}\cos\tilde{\phi}_{xII} \\ \sqrt{\beta_{yI}\epsilon_I}\cos\phi_{yI} + \sqrt{\beta_{yII}\epsilon_{II}}\cos\phi_{yII} \\ \sqrt{\gamma_{yI}\epsilon_I}\cos\tilde{\phi}_{yI} + \sqrt{\gamma_{yII}\epsilon_{II}}\cos\tilde{\phi}_{yII} \end{pmatrix}, \tag{1.24}$$

where $\alpha_{xI,II}$, $\beta_{xI,II}$, $\gamma_{xI,II}$ and $\alpha_{yI,II}$, $\beta_{yI,II}$, $\gamma_{yI,II}$ are the projections of the Twiss parameters of the two modes onto the horizontal and vertical plane. The phases $\phi_{iz}$ and $\tilde{\phi}_{iz}$ are equivalent to the horizontal and vertical tunes in the uncoupled case with

$$\begin{aligned} \phi_{xI}(s+C) - \phi_{xI}(s) = \phi_{yI}(s+C) - \phi_{yI}(s) = Q_I \,, \\ \phi_{xII}(s+C) - \phi_{xII}(s) = \phi_{yII}(s+C) - \phi_{yII}(s) = Q_{II} \,, \end{aligned} \tag{1.25}$$

where $Q_{I,II}$ are the tunes of the two modes.

## 1.4 Off-Momentum Motion

Until now only the motion of particles with nominal beam momentum $p_0$ has been studied. In this section the effect of the different deflection of particles with a momentum deviation $\delta = \Delta p/p = (p - p_0)/p_0$ in a magnetic field is summarized.

### 1.4.1 Dispersion function

Including terms until first order in $\delta$ the transverse motion of a particle with momentum deviation $\delta$ is given by an inhomogenous differential equation whose solution can be expressed as a linear superposition of the particular solution and the solution of the (homogeneous) Hill's equation:

$$x = x_\beta(s) + D(s)\delta \,, \tag{1.26}$$

where $x_\beta(s)$ and $D(s)$ satisfy the differential equations

$$x''_\beta + (K_x(s) + \Delta K_x)\, x_\beta = 0 \,, \tag{1.27}$$

$$D'' + (K_x(s) + \Delta K_x)\, D = \frac{1}{\rho} + O(\delta) \tag{1.28}$$

with

$$K_x(s) = -k_x(s) + \frac{1}{\rho^2}, \quad \Delta K_x = \left(-\frac{2}{\rho^2} + k_x(s)\right)\delta + O(\delta^2) \,. \tag{1.29}$$

To first order the dispersion function $D(s)$ satisfies the inhomogenous equation

$$D'' + K_x(s)D = \frac{1}{\rho} \,, \tag{1.30}$$

and as $K_x(s)$ and $\rho(s)$ are periodic functions of $s$, the dispersion function must satisfy the closed-orbit condition:

$$D(s+C) = D(s) \,. \tag{1.31}$$

Thus, a momentum deviation results in first order in a displacement of the closed-orbit and the parameter $x_\beta(s)$ then describes the betatron motion along the new closed-orbit $D(s)\delta$.

### 1.4.2 Momentum compaction factor and transition energy

A particle with a momentum deviation $\delta$ travels on a different closed-orbit than the reference particle given by $D(s)\delta$ in linear approximation. The deviation of the total path length of an off-momentum particle from that of the on-momentum one is then

$$\Delta C = \oint \frac{D(s)\delta}{\rho} ds \,, \tag{1.32}$$

and is usually expressed by the momentum compaction factor $\alpha_c$ defined by:

$$\alpha_c := \frac{1}{C} \oint \frac{D(s)}{\rho} ds \,, \tag{1.33}$$

where $C$ is the ring circumference.
The difference in path length between particles of different momenta in turn results in a difference in revolution time $T = C/v$ with $v$ being the particle velocity

$$\frac{\Delta T}{T_0} = \frac{\Delta C}{C} - \frac{\Delta v}{v} = \left(\alpha_c - \frac{1}{\gamma^2}\right)\delta = \left(\frac{1}{\gamma_\mathrm{T}^2} - \frac{1}{\gamma^2}\right) = \eta\delta \,. \tag{1.34}$$

The parameter $\gamma_\mathrm{T} := \sqrt{1/\alpha_c}$ is called the transition-$\gamma$ with $\gamma_\mathrm{T} mc^2$ being the transition energy and the parameter $\eta$ is the phase-slip factor defined by $\eta := \left(\alpha_c - \frac{1}{\gamma^2}\right)$.

### 1.4.3 Chromatic aberrations

The effective focusing strength seen by a particle depends on its momentum rigidity, where a higher energy particle with a momentum deviation $\delta = (p - p_0)/p_0 > 0$ from the reference momentum $p_0$ experiences a smaller deflection than a lower energy particle with $\delta < 0$. This dependence of the effective focusing strength on the particle momentum is called chromatic aberration.

#### 1.4.3.1 Linear chromaticity

Neglecting higher orders and dispersive effects the gradient error $\Delta k_{x/y}$ of a quadrupole or quadrupolar component of normalized strength $k_z$ seen by an off-momentum particle is given by Eqn. 1.29

$$\Delta k_z = -k_z\delta, \quad z = x, y \,. \tag{1.35}$$

This results in a tune-shift according to Eqn. 1.80

$$\Delta Q_z = -\left(\frac{1}{4\pi} \oint \beta_z k_z ds\right)\delta, \quad z = x, y \,. \tag{1.36}$$

The (linear) chromaticity is now defined as the derivative of the betatron tune versus the momentum deviation

$$\xi_z := \frac{d(\Delta Q_z)}{d\delta} \,. \tag{1.37}$$

The chromaticity arising only from quadrupoles is called the natural chromaticity with

$$\xi_{z,\mathrm{nat}} = -\frac{1}{4\pi} \oint \beta_z k_z ds \,. \tag{1.38}$$

#### 1.4.3.2 Linear chromaticity correction with sextupoles

As a particle beam has usually a certain momentum spread, a non-vanishing chromaticity leads to a tune-spread in the beam. If the tune-spread becomes too large, the beam crosses dangerous resonance lines leading to an instability or even total loss of the beam. In the case of a FODO lattice the natural chromaticity is approximately equal to minus the tune of the machine (Eqn. A.7) and can thus become quite large for big machines like LEP, LHC and LHeC with tunes in the range of 100 or even larger. Also for machines with a large momentum spread like the RCS presented in this thesis, even a relatively small chromaticity can lead to a large tune-spread. Furthermore, a negative chromaticity can lead to the head-tail instability and eventual beam loss [16].
A correction of the linear chromaticity can be achieved with sextupole magnets. The equation of motion including quadrupole and sextupole magnets reads

$$\begin{aligned} x'' + k(1-\delta)x + \tfrac{1}{2}m(x^2 - y^2) &= 0\,, \\ y'' - k(1-\delta)y - mxy &= 0\,, \end{aligned} \tag{1.39}$$

where $k$ and $m$ are the normalized quadrupole and sextupole strength. Substituting the transverse displacement $x$ and $y$ by the position of an off-momentum particle with momentum deviation $\delta$ under the assumption of zero vertical dispersion

$$x = x_\beta + D_x\delta, \quad y = y_\beta\,, \tag{1.40}$$

and keeping only terms linear in $\delta$, $x_\beta$ and $y_\beta$ and ignoring higher order derivatives of the dispersion, one obtains:

$$\begin{aligned} x''_\beta + kx_\beta &= (k - mD_x)x_\beta\delta\,, \\ y''_\beta - ky_\beta &= -(k - mD_x)y_\beta\delta\,. \end{aligned} \tag{1.41}$$

The perturbation terms are now linear in $x_\beta$ and $y_\beta$ and can be seen as a quadrupole error $\Delta k = (k - mD_x)\delta$ leading to the following expression for the chromaticity

$$\begin{aligned} \xi_x &= -\tfrac{1}{4\pi}\oint \beta_x(k - mD_x)ds\,, \\ \xi_y &= \tfrac{1}{4\pi}\oint \beta_y(k - mD_x)ds\,. \end{aligned} \tag{1.42}$$

Hence, sextupole magnets located at positions with nonzero dispersion can be used to correct the chromaticity. Further details concerning the placement and number of sextupole families are given in Appendix C.

## 1.5 Longitudinal Motion

The longitudinal motion is dominated by the effect of energy gain and loss of the beam particles, where the energy gain is obtained in the RF cavities while the energy loss can be caused by collective effects like e.g. synchrotron radiation or decelerating RF cavities. In this chapter only the most common case, which applies for the studies performed in this thesis, of an accelerating RF cavity and energy loss due to synchrotron radiation is described.

### 1.5.1 Longitudinal equation of motion and phase stability

In the following treatment the simplification of only one RF cavity in the ring is made, which stands representatively for a sequence of RF cavities installed at one or several locations in the ring. For the beam to be accelerated in the RF cavity, a reference particle with $\Delta E = 0$ must experience the same voltage at each passage of the RF cavity either to obtain the wanted acceleration or to compensate for the energy loss experienced during one turn. Consequently, the RF frequency $f_{\mathrm{RF}}$ must be a multiple of the revolution frequency $f_{\mathrm{rev}}$

$$f_{\mathrm{RF}} = h f_{\mathrm{rev}}\,, \tag{1.43}$$

where the parameter $h$ is called the harmonic number of the RF system. In general the RF voltage $V$ is approximately sinusoidal

$$V(\phi) = \hat{V}_0 \sin\phi\,, \tag{1.44}$$

where $\hat{V}_0$ is the peak voltage and $\phi$ the RF phase. Particles with energies differing from the beam energy thus see a different RF voltage due to their different revolution frequencies (Eqn. 1.34) and, consequently, arrive later or earlier at the RF cavity. The longitudinal motion can then only be stable, if particles with a smaller energy will experience a larger energy gain and vice versa. This is illustrated in Fig. 1.5 and expressed by the simple condition

$$\eta \cos\phi_s < 0 \text{ and } \sin\phi_s > 0\,. \tag{1.45}$$

The parameter $\phi_s$ is the synchronous phase at which the reference particle with $\Delta E = 0$ arrives and $\eta$ the phase slip factor defined in Eqn. 1.34. For storage rings with non-

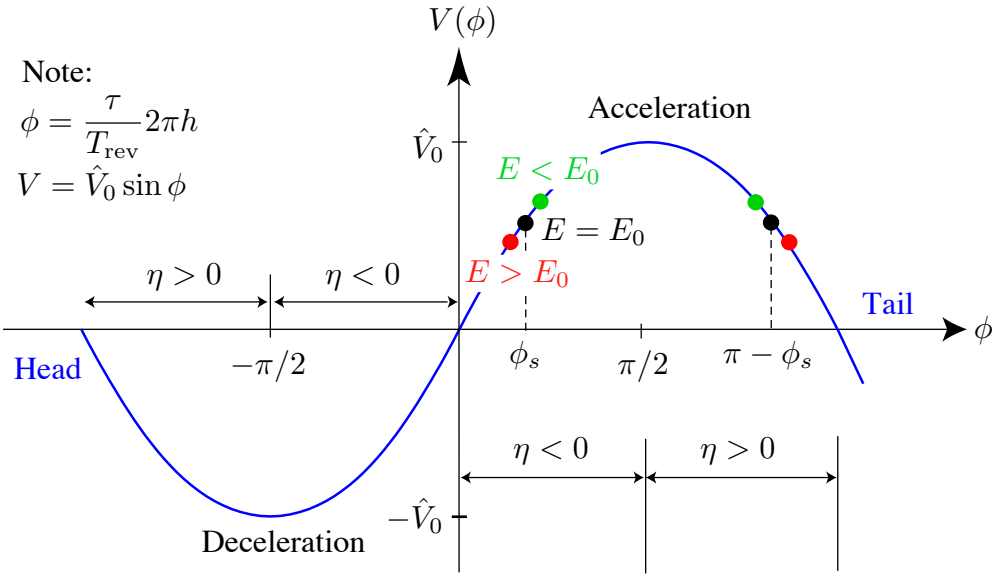


**Figure 1.5:** RF phase stability.

negligible synchrotron radiation losses, like the LHeC electron ring, the synchronous phase $\phi_s$ is such that the RF cavity exactly restores the energy loss per turn $U_0$ of the reference particle

$$U_0 = \hat{V}_0 \sin\phi_s\,. \tag{1.46}$$

In the case of negligible synchrotron radiation losses and acceleration, which is the case for the CERN RCS, the synchronous phase $\phi_s$ depends on the maximum RF voltage, the ramping time and the bunch length. All three parameters are connected by the maximum energy-phase acceptance which is referred to as RF-bucket illustrated in Fig. 1.6.

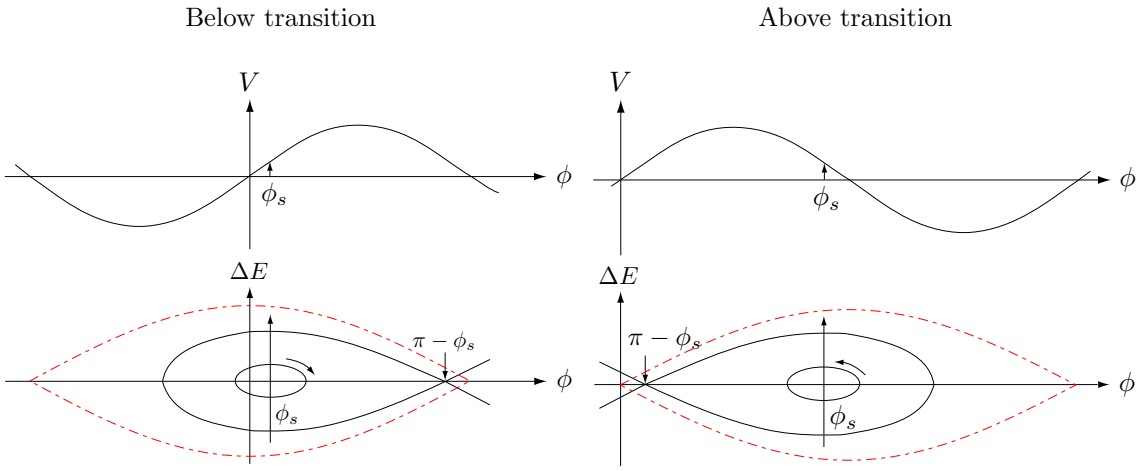


**Figure 1.6:** RF-voltage and bucket in the case of acceleration with a synchronous phase $\phi_s$. The bucket with $\phi_s = 0$ is shown in dot-dashed red. For $\phi_s \neq 0$ the energy and phase acceptance is reduced. For small phase and energy deviations the RF-voltage is approximately linear and the synchrotron motion can be described by an ellipse in the $\Delta E$-$\phi$-space, where the motion is clockwise below transition (left) and anticlockwise above transition (right).

The synchronous phase $\phi_s$ usually lies in the almost linear part of the sinusoidal RF-voltage. With this approximation and for small deviations $\psi := \phi - \phi_s$ the synchrotron motion is described by the equation of motion of a damped harmonic oscillator

$$\ddot{\psi} + 2\alpha_s \dot{\psi} + \omega_s^2 \psi = 0 \tag{1.47}$$

with an oscillation frequency $\omega_s$ referred to as synchrotron frequency and a damping constant $\alpha_s$. The parameter $\alpha_s$ is the damping decrement accounting for the damping effect of the synchrotron radiation and is given by:

$$\alpha_s = -\frac{1}{2T_0} \left.\frac{dU}{dE}\right|_{E_0} , \tag{1.48}$$

where $T_0$ is the revolution time, $U$ the energy loss per turn and $E_0$ the energy of the reference particle. For a sinusoidal RF voltage the synchrotron frequency is given by

$$\omega_s^2 = -\omega_{\mathrm{rev}}^2 \frac{h\eta e\hat{V}_0 \cos\phi_s}{2\pi\beta^2 E_0} , \tag{1.49}$$

where $\omega_{\mathrm{rev}}$ is the revolution frequency, $\beta$ the relativistic beta and $E_0$ the energy of the reference particle.

### 1.5.2 Synchrotron radiation and radiation damping

Accelerated charged particles emit synchrotron radiation, where the energy loss rate depends quadratically on the accelerating force and the angle between the particles velocity

and force. The loss rate is larger by a factor of $\gamma^2$, if the particle's velocity is perpendicular to the force, so that in typical circular accelerators the longitudinal forces can be neglected and the force is given by $ecB$, where $c$ is the speed of light and $B$ is the local magnetic field strength. The energy loss due to synchrotron radiation for a particle with charge $e$ and energy $E_0$ is then given by using the notation introduced by Sands [17]

$$P_\gamma = \frac{cC_\gamma}{2\pi}\frac{E_0^4}{\rho^2}\,. \tag{1.50}$$

Here the magnetic field strength is expressed in terms of the bending radius $\frac{1}{\rho} = \frac{e}{p}B$ and $C_\gamma$ is a constant defined by

$$C_\gamma = \frac{4\pi}{3}\frac{r_e}{(mc^2)^3} = 8.85 \times 10^{-5}\ \mathrm{mGeV}^{-3}\,, \tag{1.51}$$

where $r_e$ the classical electron radius. Integrating Eqn. 1.50 once around the ring yields the energy loss per turn of a particle of energy $E_0$ on the ideal orbit:

$$U_0 = \oint P_\gamma = \frac{C_\gamma}{2\pi}E_0^4 I_2\,, \tag{1.52}$$

where $I_2$ defines the so-called second synchrotron radiation integral[3]

$$I_2 = \oint \frac{1}{\rho(s)^2}ds\,. \tag{1.53}$$

The total power loss due to synchrotron radiation is then simply the product of the beam intensity with energy loss per turn

$$P_{\mathrm{Beam}} = \frac{U_0 N_b I_b}{e} \tag{1.54}$$

with $N_b$ the number of bunches and $I_b$ the bunch current.

#### 1.5.2.1 Radiation damping and Robinson criterion

According to Eqn. 1.52 the rate of energy loss due to synchrotron radiation increases with the particle energy. As a consequence, a particle with a higher than ideal energy will lose more energy than the ideal particle and a particle with lower energy will lose less, resulting in a reduction of the energy difference between three such particles. The resulting reduction in energy spread is referred to as longitudinal radiation damping.
In the transverse plane the emission of a photon leads to a loss of longitudinal as well as transverse momentum. In the cavities only the longitudinal momentum loss is replaced, yielding a net loss of transverse momentum or transverse damping.
Although the damping mechanisms are different for the transverse and longitudinal plane, the total amount of damping is limited and determined by the total synchrotron radiation loss. This correlation of damping decrements in all degrees of freedom was first derived by Robinson [19] and is known as the "Robinson criterion". Furthermore betatron and synchrotron oscillation amplitudes are damped exponentially:

$$A_i = A_{i,0}e^{-\alpha_i t},\ i = x, y, s \text{ and } \alpha_i = \frac{cC_\gamma}{4\pi C}E_0^3 I_2 J_i\,. \tag{1.55}$$

[3]The synchrotron radiation integrals are a class of integrals describing the effect of synchrotron radiation in a synchrotron. A derivation of the most common synchrotron radiation integrals can be found in [18].

The parameters $\alpha_i$ are the damping decrements - the reciprocal of the damping time $\tau_i$ - where $\alpha_s$ has been already introduced in Eqn. 1.48, and $J_i$ are the damping partition numbers given by:

$$J_x = 1 - \frac{I_{4x}}{I_2}\,, \tag{1.56}$$

$$J_y = 1 - \frac{I_{4y}}{I_2}\,, \tag{1.57}$$

$$J_s = 2 + \frac{I_{4x} + I_{4y}}{I_2}\,. \tag{1.58}$$

For a planar ring the fourth synchrotron radiation integral $I_4$ can be expressed by

$$I_{4i} = \oint \frac{D_i}{\rho^3}(1 + 2\rho^2 k)ds,\ i = x, y\,, \tag{1.59}$$

where $k$ is the normalized quadrupole strength, $\rho$ the bending radius and $D$ the dispersion. In this notation Robinson's criterion reads

$$\sum_i J_i = 4\,. \tag{1.60}$$

The equilibrium energy spread and emittance of a synchrotron radiation dominated storage ring is reached if the damping effect is equal to the quantum excitation rate. In the longitudinal plane the statistical emission of photons leads to an energy spread. The equilibrium energy spread can be expressed with the third synchrotron radiation integral $I_3$

$$\left(\frac{\sigma_E}{E}\right)^2 = C_q \gamma^2 \frac{I_3}{J_s I_2} \tag{1.61}$$

with $C_q = \frac{55}{32\sqrt{3}} \frac{\hbar c}{m_0 c^2}$ for electrons and

$$I_3 = \oint \left( \frac{1}{|\rho_x^3|} + \frac{1}{|\rho_y^3|} \right) ds\,. \tag{1.62}$$

In the transverse plane the emission of a photon with energy $\varepsilon$ does not change its actual position and direction. However, the position $u$ with respect to the reference orbit, which is a combination of its betatron oscillation amplitude and a chromatic distribution due to a finite energy deviation and dispersion $D$, is changed. This perturbation will modify the phase ellipse $\gamma u^2 + 2\alpha u u' + \beta u'^2 = a^2$ the particle moves on. The average variation of the phase ellipse or oscillation amplitude $a$ due to the emission of photons with energy $\varepsilon$ is usually expressed by the curly H-function $\mathscr{H}(s)$

$$\langle \delta a^2 \rangle = \frac{\varepsilon^2}{E_0^2} \mathscr{H}(s) \tag{1.63}$$

with

$$\mathscr{H}(s) = \gamma D^2 + 2\alpha D D' + \beta D'^2\,. \tag{1.64}$$

Equilibrium is again reached when the increase in oscillation amplitude due to quantum excitation and the damping of the same are of equal strength yielding the following expression for the emittance:

$$\epsilon_i = C_q \frac{\gamma^2}{J_i} \frac{I_{5i}}{I_2},\ i = x, y\,, \tag{1.65}$$

where $I_5$ is the fifth synchrotron radiation integral defined by:

$$I_{5i} = \oint \frac{\mathscr{H}_i}{\rho^3} ds \,. \tag{1.66}$$

In most storage rings the vertical dispersion is zero for the ideal lattice, which would imply $\epsilon_y = 0$. In reality, the vertical dispersion does not vanish due to field and alignment errors of the magnets and thus $\epsilon_y$ is determined by the magnitude and influence of these errors.

#### 1.5.2.2 Variation of damping partition

Robinson's criterion states that the sum of the damping partition numbers is a constant. However the distribution between them can be changed by displacing the particle orbit transversely, which is done in practice by changing the RF frequency $f_{\mathrm{RF}}$ of the storage ring. In case of an off-momentum orbit the quadrupoles of the ring now also act as dipoles resulting in a non-vanishing term $2D_i\rho^2 k$ of $I_4$ and a change of the damping partition. The change in $I_4$ is given by the eighth synchrotron radiation integral

$$\Delta I_{4i} = 2 I_{8i} \delta \tag{1.67}$$

with $\delta = \frac{\Delta p}{p_0} = -\frac{1}{\alpha_c}\frac{\Delta f_{\mathrm{RF}}}{f_{\mathrm{RF}}}$ and

$$I_{8i} = \oint k^2 D_i^2 ds \,. \tag{1.68}$$

#### 1.5.2.3 Synchrotron radiation including coupling

As the vertical dispersion in storage rings is usually zero or very small, the main effect of coupling is the generation of vertical emittance due to:

- coupling between the vertical and longitudinal plane in regions where radiation is emitted, i.e. vertical dispersion in dipoles
- coupling between the vertical and horizontal plane in regions where radiation is emitted, i.e. betatron coupling in dipoles

It is important to note that coupling does not necessarily lead to an increase of the vertical emittance.
As derived in Appendix D, the emittances $\epsilon_i$ in the coupled and $\epsilon_{0i}$ in the uncoupled case, are related by:

$$\epsilon_x = \frac{\epsilon_{0x} J_x}{J_x + \kappa}, \qquad \epsilon_y = \frac{\epsilon_{0x} J_x \kappa}{J_x + \kappa}, \text{ with } \kappa = \frac{\epsilon_y}{\epsilon_x} \,. \tag{1.69}$$

These equations are only valid under the assumption of a vanishing vertical emittance in the uncoupled case ($\epsilon_{0y} = 0$), no vertical dispersion in both cases ($D_y = D_{y0} = 0$) and no change of the horizontal damping partition ($J_x = J_{0x}$).
Explicit expressions for the synchrotron radiation integrals can be found in [20]. In Appendix E a short summary of the method by Chao [21] to calculate the damping decrements and the equilibrium emittances is given.

## 1.6 Perturbations

The first step in every design of an accelerator is the study of the beam dynamics under ideal conditions described by the linear Hill's equation (Eqn. 1.6) and the beam dynamics including small momentum deviations expressed by the dispersion function, which as well satisfies a linear differential equation (Eqn. 1.30). The next step is then in most cases the correction of chromatic aberrations with non-linear sextupole fields. The sextupoles usually present the first non-linear element to be incorporated in the design, octupoles are in some cases like e.g. the LHC still included and very rarely decapoles. All three non-linear magnet types serve the correction of the deviation of the magnetic field from the desired one. This deviation can for example be caused by misalignment or rotation of the magnets, unwanted but unavoidable higher order multipole fields of the magnets, insertions like e.g. detectors in colliders or wigglers in lightsources or collective effects like beam-beam and space-charge. In addition, an offset of the beam with respect to the magnet center in higher order multipoles leads to a so called feed-down effect meaning that a quadrupole leads to a dipole component, a sextupole to a quadrupolar and dipolar component etc. In general, a displacement in any higher order multipole introduces field errors on the beam axis in all lower orders.

### 1.6.1 Linear perturbations

The lowest order perturbation is the one of a dipolar field error, here expressed as an error in the bending radius $\Delta\rho_z(s)$, in an otherwise ideal accelerator leading to the modified Hill's equation

$$z'' + K_z(s)z = \Delta\rho_z(s),\ z = x, y\,, \tag{1.70}$$

where $K_z(s)$ is given by Eqn. 1.7 and $z$ stands in the following for either the horizontal or vertical plane. As the bending field of the dipoles defines the closed-orbit of the beam particles, a dipole field error consequently results in a change of the same with the new closed-orbit being the solution of Eqn. 1.70. One way to solve Eqn. 1.70 is to first make a transformation to normalized coordinates $w_z = z/\sqrt{\beta_z}$ and $\varphi_z = \frac{1}{\nu_z}\int_0^s d\tilde{s}/\beta_z(\tilde{s})$ with $\nu_z$ being the betatron tune, yielding

$$\frac{d^2 w_z}{d\varphi^2} + \nu_z^2 w_z = \nu_z^2 \beta^{3/2}\Delta\rho_z = \nu_z^2 f(\varphi)\,. \tag{1.71}$$

The right hand side is a periodic function of $\varphi$ with period $2\pi$, as is $w_z(\varphi)$ and both can be expanded into a Fourier series leading after some arithmetics to the solution

$$w_z(\varphi_z) = \frac{z_{\mathrm{co}}(\varphi_z)}{\sqrt{\beta_z(\varphi_z)}} = \sum_{k_z=-\infty}^{\infty} \frac{\nu_z^2 f_{k_z}}{\nu_z^2 - k_z^2} e^{ik_z\varphi_z} \tag{1.72}$$

with $f_{kz}$ being the Fourier components of $f(\varphi_z)$ given by

$$f_{k_z} = \frac{1}{2\pi}\oint \beta_z^{3/2}\Delta\rho_z\, e^{-ik_z\varphi_z} d\varphi_z\,, \tag{1.73}$$

and $z_{\mathrm{co}}$ the closed-orbit displacement. It is obvious that due to the term $\nu_z^2 - k^2$ the closed-orbit may not even exist if the betatron tune takes on integer values

$$\nu_z = k_z, \quad k_z \in \mathbb{N}\,. \tag{1.74}$$

The Fourier components $f_k$ are also referred to as stopband integrals and in the case of a dipole field error more specifically as integer stopband integrals based on the resonant behaviour for integer values of the betatron tune.
The next higher order perturbations are quadrupolar field errors $\Delta k_z(s)$ in an otherwise ideal accelerator leading to the modified Hill's equation

$$z'' + K_z(s)z = -\Delta k_z(s)z\,, \tag{1.75}$$

where $K_z(s)$ is again given by Eqn. 1.7. As the beta-function depends on the distribution of the quadrupoles, quadrupole errors induce a distortion of the same. The distortion of the beta-function, also called beta-beating, can be derived in a similar way as the closed-orbit distortion in the case of dipole field errors, yielding

$$\frac{\Delta\beta_z(s)}{\beta_z(s)} = -\frac{\nu_{0z}}{2}\sum_{p_z=-\infty}^{\infty}\frac{f_{p_z}e^{ip_z\varphi_z}}{\nu_{0z}^2-(p_z/2)^2}\,. \tag{1.76}$$

The resonance condition is now satisfied for half integer values of the unperturbed betatron tune

$$\nu_{0z} = \frac{p_z}{2}, \quad p_z \in \mathbb{N}\,. \tag{1.77}$$

The Fourier components $f_{p_z}$ are thus accordingly referred to as half-integer stopband integrals with $f_{p_z}$ given by

$$f_{p_z} = \frac{1}{2\pi}\oint \beta_z(\tilde{s})\Delta k_z(s)e^{-ip_z\varphi}d\tilde{s} \tag{1.78}$$

Using that $f_{-p_z} = f_{p_z}^*$ Eqn. 1.76 can also be written in the following form used later in this thesis:

$$\frac{\Delta\beta_z(s)}{\beta_z(s)} = -\frac{1}{2\sin(2\pi\nu_{0z})}\int_s^{s+C}\Delta k_z(\tilde{s})\beta_z(\tilde{s})\cos\left(2\nu_0(\pi+\phi_z(s)-\phi_z(\tilde{s}))\right)d\tilde{s}\,, \tag{1.79}$$

where $C$ is the ring circumference.
As a consequence of the change of the beta-function and thus number of betatron oscillations per turn, quadrupole errors induce a tune-shift which is given by

$$\Delta\nu_z = \nu_z - \nu_{0z} = \frac{1}{4\pi}\oint \beta_z(\tilde{s})\Delta k_z(\tilde{s})d\tilde{s}\,. \tag{1.80}$$

### 1.6.2 Non-linear perturbations

The general equation of motion for a single perturbation $p_{nz}$ of order $n$ is

$$\frac{d^2w_z}{d\varphi^2} + \nu_{0z}^2 w_z = \kappa_{nz}(\varphi)w_z^{n-1}\,. \tag{1.81}$$

For small perturbations the equation of motion can be solved in a similar way as the equation for linear perturbations, leading to the resonance condition

$$l\,\nu_{0z} = p, \quad l,p \in \mathbb{Z} \text{ and } |l| \le n\,. \tag{1.82}$$

### 1.6.3 Coupling resonances

In the case of a dependence of the perturbation on the betatron oscillation amplitudes in both transverse planes, the general equation of motion is given by

$$\frac{d^2 w_x}{d\varphi_x^2} + \nu_{0x}^2 w_x = \kappa_{nm}(\varphi_x) w_x^{m-1} w_y^{n-1} \,. \tag{1.83}$$

where representatively for both planes the equation for the horizontal plane is stated here. This leads to a coupling between both planes and consequently a resonance condition including the horizontal and vertical tune

$$l\nu_{0x} + q\nu_{0y} = p, \quad l, p, q \in \mathbb{Z},\ |l| \leq m \text{ and } |q| \leq n \,. \tag{1.84}$$

A similar equation as Eqn. 1.84 can also be derived for the vertical plane leading to the general resonance condition

$$m\nu_{0x} + n\nu_{0y} = p, \quad m,\, n,\, p \in \mathbb{Z} \tag{1.85}$$

with $|m| + |n|$ being the order of the resonance. The case of the linear coupling resonance $\nu_{0x} \pm \nu_{0y} = p$, relevant for the LHeC, for which linear coupling between the two planes is desired (see Sec. 2.4.3), is discussed in more detail in Appendix F.

### 1.6.4 Systematic and non-systematic resonances

In a very simplified picture a lattice consisting of $N$ superperiods and a tune of $\nu_{0x,0y}$ is equivalent to a lattice consisting of only one superperiod and a tune of $\nu_{0x,0y}/N$. Substituting $\nu_{0x,0y}$ by $\tilde{\nu}_{0x,0y} = \nu_{0x,0y}/N$ in Eqn. 1.85 then leads to the resonance condition

$$m\nu_{0x} + n\nu_{0y} = pN, \quad m,\, n,\, p \in \mathbb{Z} \,. \tag{1.86}$$

Thus, a high superperiodicity actually eliminates many resonances or rather reduces their stopband integrals and they are referred to as non-systematic resonances. Resonances satisfying Eqn. 1.86 are called systematic resonances. All resonances can be visualized in a resonance diagram for which an example is presented in Fig. 1.7.

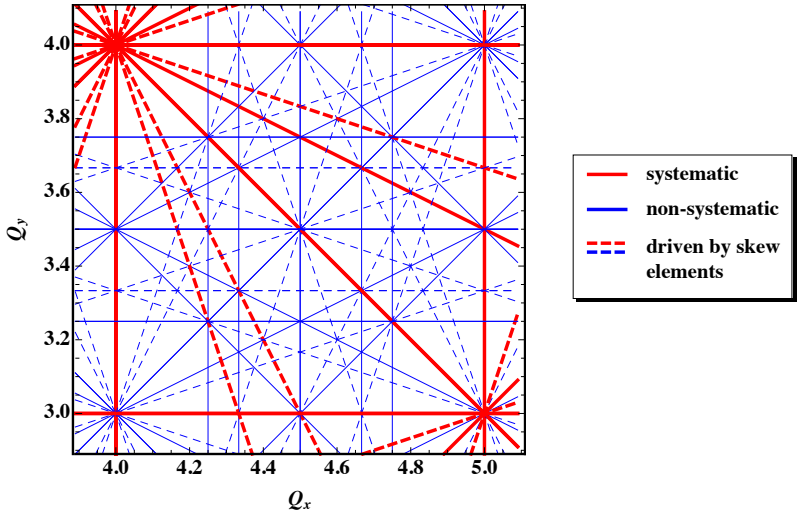


**Figure 1.7:** Resonance diagram until 4th order for a lattice with superperiodicity 4.

### 1.6.5 Detuning with amplitude and momentum

It has been derived in Sec. 1.6.1 that quadrupolar errors lead to an amplitude independent tune-shift. For sextupolar or higher order multipoles this tune-shift becomes amplitude dependent and is referred to as detuning with amplitude. As the perturbation and thus tune-shift is usually small, the detuning can be expressed by Taylor expansion in the horizontal and vertical action $J_{x/y}$:

$$Q_z(J_x, J_y) \approx Q_z + \alpha_{z,10}J_x + \alpha_{z,01}J_y + \frac{1}{2}\left(\alpha_{z,20}J_x^2 + 2\alpha_{z,11}J_xJ_y + \alpha_{z,02}J_y^2\right) + \ldots, \quad z = x, y\,. \tag{1.87}$$

The coefficients $\alpha_{z,ij}$ are called the anharmonicities.

The same is valid for momentum deviations $\delta = \Delta p/p_0$ referred to as detuning with momentum and expressed by a Taylor expansion in $\delta$

$$Q_z(\delta) = Q_{0,z} + Q'_z\delta + \frac{1}{2!}Q''_z\delta^2 + \frac{1}{3!}Q'''_z\delta^3 + \ldots \tag{1.88}$$

The terms $Q_z^{(n)}$ with $n \geq 2$ are the higher order chromaticities. In the case of the detuning with momentum also higher order dispersive effects have to be considered as well. A method to correct the first and second order chromaticity using sextupole families is described in Appendix C and applied to the LHeC in Sec. 2.4.2.

## 1.7 Space-Charge and Beam-Beam Effects

The Coulomb forces arising from a charged particle beam can contribute considerably to the forces encountered by individual particles in a beam transport line or a circular collider. These forces may act directly on the particles of the beam referred to as direct space-charge force or on the particles of the counter-rotating beam in the case of a collider known as beam-beam force (Fig. 1.8). Both forces scale with the number of particles and roughly inversely with the beam size and can present severe stability problems for high brightness beams.

As will be shown later, the direct space-charge force scales with $1 - \beta^2 = \frac{1}{\gamma^2}$ and becomes completely negligible as the beam velocity approaches the speed of light in which case the electric and magnetic force cancel each other completely. It is therefore only relevant for low energy beams, especially for particle species with a high mass like protons or ions with $\gamma = E/(m_0c^2)$ being then considerably smaller compared to e.g. electrons of the same energy. In addition to the direct space-charge effect, the beam is influenced by its environment like the beam pipe, magnets, collimators etc. referred to as indirect space-charge effects. For a smooth, perfectly conducting wall they can be calculated by introducing image charges and currents and are often referred to as image effects. Those indirect space-charge effects do not become negligible as the beam velocity approaches the speed of light and are thus more relevant for high energy beams. In the case of the beam-beam effect the force scales with $1 + \beta^2 = 2 - \frac{1}{\gamma^2}$. This scaling with energy is usually not relevant as colliders are usually built for high energy beams with $\beta \approx 1$. Furthermore, due to the high energy the space-charge force of the beams is usually neglected.

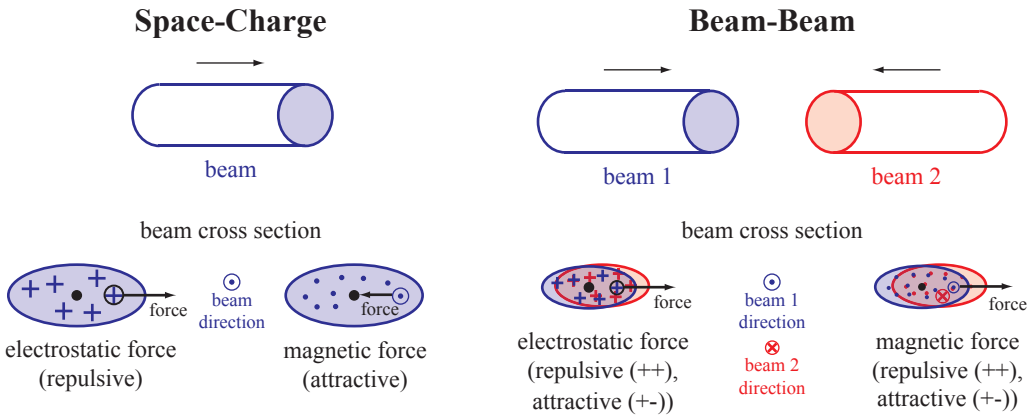


**Figure 1.8:** Space-charge (left) and beam-beam effects (right). The beam particles experience the effect of the electric and magnetic force. In the case of the space-charge effect (left) the repulsive Coulomb force is canceled by the attractive magnetic force as the velocity approaches the speed of light ($\beta \to 1$), while for the beam-beam effect (right) both forces are either attractive for oppositely charged beams or repulsive for equally charged beams.

In the case of the direct space-charge effect, the self-field of the beam acts on the beam particles of the same beam which have self-evidently the same charge. The direct space-charge force is therefore always repellent. In the case of the beam-beam effect the colliding beams can either have the same charge, in which case the force is repellent, or opposite charge in which case it is attractive. For small amplitude particles the space-charge and beam-beam force is quasi linear and can be described as a defocusing or focusing quadrupole respectively. A good measure for the strength of this quadrupole is the tune-shift or spread caused by it referred to as direct space-charge and beam-beam tune-shift.
Another difference between the space-charge and beam-beam effect is the spacial distribution of the force. The space-charge effect can in general be seen as a rather equally distributed defocusing non-linear force, while the beam-beam force is localized to the beam crossings at the interaction points where the beam then experiences a strong focusing or defocusing non-linear kick. In colliders the beams are also often stored over a long time period while low energy machines have shorter cycles requiring less beam stability. Due to the strong localization of the beam-beam force and in addition the longer cycle time the beam-beam tune-shifts observed are much smaller than the possible space-charge tune-shifts. For electron colliders the maximum reachable beam-beam tune-shifts lie in the range of 0.1 reached at KEKB [22] and for proton machines around 0.017 reached at the LHC [23]. The observed tune-shifts for electron or more general lepton beams are higher because the oscillations caused by the beam-beam interaction are damped by synchrotron radiation which scales with $1/m_0^3$ and is in general negligible for hadron beams[4]. Space-charge tune-shifts can be as high as 0.5. The value of 0.5 is kind of a hard upper limit for the space-charge tune-shift, as for larger tune-shifts the beam crosses either the

[4] An exception is the LHC, where the synchrotron radiation is visible on synchrotron radiation light monitors and damping effects can be observed due to the high beam energy of 7 TeV

integer or half integer resonance which usually leads to immediate beam instability or even instantaneous loss of the beam. Another difference arising from the different spacial distribution is that in the case of a beam instability caused by the space-charge effect, the beam emittance in general blows up where the blow-up eventually saturates as the space-charge force decreases with increasing beam size. In the case of the beam-beam effect the beams are usually lost right after becoming unstable.

### 1.7.1 Transverse self-field

For the majority of beams for which space-charge or beam-beam effects play a role the longitudinal dimension of the beam is considerably larger than the transverse one and can be added after the calculation of the transverse field as a charge density $\lambda(s)$, where $s$ is the longitudinal coordinate in the Frenet-Serret coordinates. One way to determine the self-field of the beam is using the Poisson equation

$$\Delta U = -\frac{1}{\epsilon_0}\rho\left(x,y\right) , \tag{1.89}$$

where $\rho$ is the charge density of the beam and $U$ the electric potential. The electric field is then given by:

$$\mathbf{E} = -\nabla U\left(x,y\right) . \tag{1.90}$$

The magnetic field $\mathbf{B}$ of a bunch moving with speed $\boldsymbol{\beta}c$ follows from the electric field $\mathbf{E}$ with

$$\mathbf{B} = \boldsymbol{\beta} \times \mathbf{E}/c \tag{1.91}$$

The distribution of particle beams is often shaped by statistical processes like e.g. synchrotron radiation and thus most beam distributions are Gaussian or can be approximated well enough by a Gaussian distribution. The Gaussian distribution and most other beam distribution lead to a non-linear electric field and not always solvable equations of motions. In this respect the idealistic Kapchinskij-Vladimirskij (KV) distribution represents a special distribution as it yields a perfectly linear space-charge force and solvable equation of motions and is often used for space-charge studies[5].

#### 1.7.1.1 Kapchinskij-Vladimirskij (KV) distribution

In the case of the Kapchinskij-Vladimirskij (KV) distribution the particles are uniformly distributed on a constant emittance surface of the 4-dimensional phase space. In action-angle variables the distribution can be written as

$$\rho(J_x, J_y) = \frac{4Nq}{\epsilon_x\epsilon_y}\delta\left(\frac{2J_x}{\epsilon_x} + \frac{2J_y}{\epsilon_y} - 1\right) , \tag{1.92}$$

where $N$ is the number of particles per unit length, $q$ the particle charge, $J_i$ the action, $\epsilon_i$ the emittance, $\delta$ the Dirac delta function and $a$ and $b$ the envelope radii of the beam with

$$a = \sqrt{\beta_x\epsilon_x}, \quad b = \sqrt{\beta_y\epsilon_y} . \tag{1.93}$$

[5] In the case of the KV-distribution the space-charge field can be simply added as a defocusing quadrupole to the Hill's equation.

The distribution function of the KV-distribution is then given by

$$\rho(x,y) = \frac{Nq}{\pi ab}\Theta\left(1 - \frac{x^2}{a^2} + \frac{y^2}{b^2}\right), \tag{1.94}$$

where $\Theta(z)$ is equal to 1 if $z \geq 0$ and 0 if $z < 0$ with an rms emittances of

$$\epsilon_{x,\mathrm{rms}} = \frac{\langle x^2\rangle}{\beta_x} = \frac{\epsilon_x}{4}, \quad \epsilon_{y,\mathrm{rms}} = \frac{\langle y^2\rangle}{\beta_y} = \frac{\epsilon_y}{4}. \tag{1.95}$$

Neglecting the transverse velocity, hence $\boldsymbol{\beta} = (0,\, 0,\, \beta)$, Eqns. 1.89 - 1.91 yields for the components of the electric and magnetic self-field

$$E_x = \frac{1}{\pi\epsilon_0}\frac{Nq}{a(a+b)}x, \qquad E_y = \frac{1}{\pi\epsilon_0}\frac{Nq}{b(a+b)}y, \tag{1.96}$$

$$B_x = -\frac{\mu_0}{\pi}\frac{Nq\beta c}{b(a+b)}y, \qquad B_y = \frac{\mu_o}{\pi}\frac{Nq\beta c}{a(a+b)}x. \tag{1.97}$$

Both the electric and magnetic field depend linearly on the transverse position $x$ and $y$.

#### 1.7.1.2 Gaussian distribution

The Gaussian distribution function in the 4-dimensional phase space in action-angle variables is defined by

$$\rho(J_x, J_y) = \frac{Nq}{\epsilon_{x,\mathrm{rms}}\epsilon_{y,\mathrm{rms}}} e^{-\left(\frac{J_x}{\epsilon_{x,\mathrm{rms}}} + \frac{J_y}{\epsilon_{y,\mathrm{rms}}}\right)}, \tag{1.98}$$

leading to the beam distribution function

$$\rho(x,y) = \frac{Nq}{2\pi\sigma_x\sigma_y} e^{-\frac{x^2}{2\sigma_x^2} - \frac{y^2}{2\sigma_y^2}}, \tag{1.99}$$

where $\sigma_i = \sqrt{\beta_i\epsilon_{i,\mathrm{rms}}}$ is the rms beam size.
In the case of elliptical beams ($\sigma_x \neq \sigma_y$ and $\sigma_x > \sigma_y$) the components of the electric field are given by the Basetti-Erskin formula [24]:

$$\begin{aligned} E_x &= \frac{Nq}{2\epsilon_0\sqrt{2\pi\left(\sigma_x^2 - \sigma_y^2\right)}}\mathrm{Im}\left[w\left(\frac{x+iy}{\sqrt{2\left(\sigma_x^2-\sigma_y^2\right)}}\right) - e^{-\frac{x^2}{2\sigma_x^2}+\frac{y^2}{2\sigma_y^2}} w\left(\frac{x\frac{\sigma_y}{\sigma_x}+iy\frac{\sigma_x}{\sigma_y}}{\sqrt{2\left(\sigma_x^2-\sigma_y^2\right)}}\right)\right], \\ E_y &= \frac{Nq}{2\epsilon_0\sqrt{2\pi\left(\sigma_x^2 - \sigma_y^2\right)}}\mathrm{Re}\left[w\left(\frac{x+iy}{\sqrt{2\left(\sigma_x^2-\sigma_y^2\right)}}\right) - e^{-\frac{x^2}{2\sigma_x^2}+\frac{y^2}{2\sigma_y^2}} w\left(\frac{x\frac{\sigma_y}{\sigma_x}+iy\frac{\sigma_x}{\sigma_y}}{\sqrt{2\left(\sigma_x^2-\sigma_y^2\right)}}\right)\right], \end{aligned} \tag{1.100}$$

where the function $w(z)$ is the complex error function defined by [25]:

$$w(z) = e^{-z^2}\left(1 + \frac{2i}{\sqrt{\pi}}\int_0^z e^{t^2} dt\right). \tag{1.101}$$

The magnetic field can be obtained by Eqn. 1.91 with $\boldsymbol{\beta} = (0,\, 0,\, \beta)$.
For round beams ($\sigma_x = \sigma_y = \sigma$) the electric and magnetic field can be expressed with more elementary functions and read in cylindrical coordinates:

$$\begin{aligned} E_r &= \frac{1}{2\pi\epsilon_0}\frac{Nq}{r}\left(1 - e^{-\frac{r^2}{2\sigma^2}}\right), \\ B_\phi &= \frac{\mu_0\beta}{2\pi c}\frac{Nq}{r}\left(1 - e^{-\frac{r^2}{2\sigma^2}}\right). \end{aligned} \tag{1.102}$$

All other components of the electric and magnetic field are 0.

### 1.7.2 Lorentz force from space-charge self-field

The forces exerted on individual particles of charge $q$ by the space-charge self-field of the same or another beam are given by the Lorentz force:

$$\mathbf{F} = qf_q\mathbf{E} + qf_qf_v(\mathbf{v} \times \mathbf{B})\,, \tag{1.103}$$

where the nomenclature as in [12] is used with $f_q = 1$ if the individual particle and the beam particles have the same charge and $f_q = -1$ if they have opposite charge. Similarly $f_v = 1$ if the individual particle and the beam move in the same direction or $f_v = -1$ if they move into opposite directions. In general the transverse velocities are small compared to the longitudinal ones and $\boldsymbol{\beta}$ can be approximated by $\boldsymbol{\beta} = (0,\, 0,\, \beta)$. Under this approximation and using Eqn. 1.91 the transverse components of the Lorentz force can be expressed as

$$F_z = qf_q(1 + \beta^2 f_v)E_z, \quad z = x, y\,. \tag{1.104}$$

The self-field force factors are summarized in Table 1.1 for a better overview. In the case

| **space-charge** | | **beam-beam** | |
|---|---|---|---|
| $++ \uparrow\uparrow$ | $+- \uparrow\uparrow$ | $++ \uparrow\downarrow$ | $+- \uparrow\downarrow$ |
| $-- \uparrow\uparrow$ | $-+ \uparrow\uparrow$ | $-- \uparrow\downarrow$ | $-+ \uparrow\downarrow$ |
| $+(1-\beta^2)$ | $-(1-\beta^2)$ | $+(1+\beta^2)$ | $-(1+\beta^2)$ |

**Table 1.1:** Self-field force factors introduced in Eqn. 1.103. The $+/-$ signs stand for the sign of the individual particle and beam particles and the arrows $\uparrow\downarrow$ for the direction of the same.

of the space-charge force the magnetic field compensates the electric field for relativistic beams ($\beta \to 1 \Rightarrow (1-\beta^2) = \frac{1}{\gamma^2} \to 0$) which is not the case for beam-beam effects.
Applying Eqn. 1.104 to the KV-distribution yields in Cartesian coordinates

$$F_x = \frac{1}{4\pi\epsilon_0} qf_q(1 + \beta^2 f_v)\frac{4\lambda}{a(a+b)}x, \quad F_y = \frac{1}{4\pi\epsilon_0} qf_q(1 + \beta^2 f_v)\frac{4\lambda}{b(a+b)}y\,. \tag{1.105}$$

Doing the same for the Gaussian distribution in cylindrical coordinates yields

$$F_r = \frac{2\lambda}{4\pi\epsilon_0} qf_q(1 + \beta^2 f_v)\frac{1}{r}(1 - e^{-\frac{r^2}{2\sigma^2}})\,. \tag{1.106}$$

For small $r$, so near the beam center, the Lorentz force can be linearised by Taylor-expanding the exponential function leading to

$$F_r = \frac{2\lambda}{4\pi\epsilon_0} qf_q(1 + \beta^2 f_v)\frac{r}{2\sigma^2}, \quad \text{for } r \ll \sigma\,. \tag{1.107}$$

### 1.7.3 Space-charge effects

In the preceding sections, only the Lorentz force generated by the beam itself and acting on a single beam particle has been considered, referred to as incoherent direct space-charge effect (Sec. 1.7.3.1). In addition, electromagnetic fields induced in the surroundings of the beam can effect the beam itself, known as incoherent indirect space-charge

effects (Sec. 1.7.3.2). Last but not least, oscillations of the beam centroid can induce oscillating electromagnetic fields in the surroundings of the beam, which are called coherent indirect space-charge effects. In all three cases the Lorentz force is linear or approximately linear in the transverse coordinates $x$ and $y$ and thus the space-charge force can be seen as a continuous quadrupolar perturbation, which can be added as an additional term $K_{\mathrm{SC}}$ in the linear Hill's equation (Eqn. 1.6):

$$z'' + (K(s) + K_{\mathrm{SC,z}}(s))z = 0, \quad z = x, y\,. \tag{1.108}$$

In a synchrotron, a good measure for the "strength" of the space-charge effect is the tune-shift $\Delta Q_z$ caused by the additional quadrupolar perturbation given by:

$$\Delta Q_z = \frac{1}{4\pi} \int_0^{2\pi R} K_{\mathrm{SC,z}}(s)\beta_z(s)ds, \quad z = x, y\,, \tag{1.109}$$

where $2\pi R$ is the circumference of the synchrotron and $\beta_z$ the beta-function.
The incoherent and coherent tune-shift for different shapes of the vacuum chamber and magnetic pole distances can be expressed by the Laslett coefficients where an elliptical uniform beam distribution (KV distribution) is assumed in all cases. For the explicit formula see the original paper [26]. In the following, the different space-charge effects are described using simple examples.

#### 1.7.3.1 Direct incoherent space-charge effect

In the case of the direct incoherent space-charge effect the Lorentz force is given by Eqn. 1.104

$$F_z = q(1 - \beta^2)E_z, \quad z = x, y\,, \tag{1.110}$$

and is always repellent leading to a negative tune-shift $\Delta Q_z < 0$. In the case of the KV-distribution the Lorentz force is linear in $x$ and $y$ and the equations of motion (Eqn. 1.108) are exactly solvable [27]. In this case the tune-shift is given by

$$\Delta Q_x = -\frac{2r_0}{\beta^2\gamma^3\epsilon_x}\left\langle \frac{a}{a+b} \right\rangle, \quad \Delta Q_y = -\frac{2r_0}{\beta^2\gamma^3\epsilon_y}\left\langle \frac{b}{a+b} \right\rangle. \tag{1.111}$$

By introducing form factors and expressing the semiaxis of the ellipse as rms-beamsizes Eqn. 1.111 can be extended to other more realistic distributions [28]

$$\Delta Q_{x,y} = -\frac{r_0}{\pi}\left(\frac{q^2}{A}\right)\frac{N}{\beta^2\gamma^3}\frac{F_{x,y}G_{x,y}}{B_f}\left\langle \frac{\beta_{x,y}}{\sigma_{x,y}\left(\sigma_x + \sigma_y\right)} \right\rangle, \tag{1.112}$$

where $F_{x,y}$ is a form factor derived from the Laslett coefficients [26] for incoherent tune-shifts, $G_{x,y}$ a form factor depending on the transverse distribution with $G_{x,y} = 1$ for the KV-distribution and $G_{x,y} = 2$ for Gaussian and $1 < G_{x,y} < 2$ in the case of all other distributions. The parameter $B_f$ is the bunching factor defined as the mean current divided by the peak current of the bunch with $B_f < 1$ for bunched beams and $B_f = 1$ for unbunched beams and accounts for the increase in the space-charge tune-shift for bunched beams. The term $\left(\frac{q^2}{A}\right)$ includes the strong space-charge force experienced in the case of ion beams where $q$ is the charge state and $A$ the mass of the ions.

A comparison of the expressions for the direct incoherent space-charge tune-shift and the beam-beam tune-shift (Eqn. 1.124) shows that both depend on the beam size and on the beam intensity. As in the case of the space-charge effect, the beam experiences its self-field continuously and the beam size dependent term $\frac{\beta_{x,y}}{\sigma_{x,y}(\sigma_x+\sigma_y)}$ is averaged over the complete ring. For the beam-beam effect the interaction is localized and the beam sizes are assumed to be constant[6]. Furthermore, the direct incoherent space-charge tune-shift scales strongly with the beam energy, explicitly with $\frac{1}{\gamma^2}$ (Eqn. 1.112), while the beam-beam tune-shift only depends on the normalized emittance of the beam (Eqn. 1.124), which is energy independent[7].

### 1.7.3.2 Indirect incoherent space-charge effect

In a real machine the beam also induces surface charges or currents in its environment that act back on the beam known as indirect space-charge effects. The simplest example which illustrates the principle of this effect is a continuous round beam represented by a line charge $\lambda$ of infinite length between two parallel perfectly conducting plates.

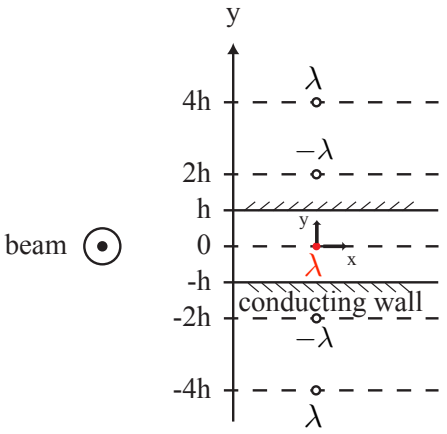


**Figure 1.9:** A particle beam represented by a line charge $\lambda$ between two parallel perfectly conducting plates of distance $2h$.

The boundary condition that the electric field parallel to the plate must vanish ($E_{||} = 0$) is satisfied by introducing an infinite number of image line charges of alternating sign at positions $\ldots -4h$, $-2h$, $2h$, $4h$ $\ldots$ (Fig. 1.9). The electric field at position $y$ between the conducting plates is then given by the sum over the electric field generated by all image line charges. As there are no image charges between parallel plates, the divergence of the electric field is zero ($\nabla \cdot \mathbf{E} = 0$). From this condition the horizontal component $E_x$ can be derived, yielding [28]

$$E_x = -\frac{\lambda}{4\pi\epsilon_0 h^2}\frac{\pi^2}{12}x, \quad E_y = \frac{\lambda}{4\pi\epsilon_0 h^2}\frac{\pi^2}{12}y\,, \tag{1.113}$$

and for the Lorentz force acting on a particle of charge $q$

$$F_x = -\frac{q\lambda}{4\pi\epsilon_0 h^2}\frac{\pi^2}{12}x, \quad E_y = \frac{q\lambda}{4\pi\epsilon_0 h^2}\frac{\pi^2}{12}y\,. \tag{1.114}$$

[6] For small beta-functions at the IP and short bunches, the dependence of the beam size on the longitudinal position $s$ can not be neglected any more. This effect is known as hourglass effect.

[7] Here synchrotron radiation effects are not taken into account

For the geometry considered in this section, the electric image field is vertically defocusing and horizontally focusing and increases for small chamber heights $h$. This is the case for most synchrotrons as the horizontal aperture is often larger than the vertical, due to the non-vanishing dispersion and thus larger beam size in the horizontal plane. Furthermore, the Lorentz force from indirect space-charge effects (Eqn. 1.113) is independent of the relativistic $\gamma$-factor leading to a $\frac{1}{\gamma}$ dependence of the tune-shift compared to a $\frac{1}{\gamma^2}$ dependence for the direct space-charge effect. Thus, the indirect space-charge effect becomes much more relevant for high beam energies as it decreases much slower than the direct space-charge effect.
Similarly, as the electric field of the beam leads to image charges, its magnetic field induces mirror currents resulting in a tune-shift scaling as well with $\frac{1}{\gamma}$. For further details it is referred to [26].

#### 1.7.3.3 Indirect coherent space-charge effect

A coherently oscillating beam where the oscillation can be for example caused by an injection kicker, induces image charges and currents in its environment, which are oscillating as well. For a round beam with line charge $\lambda$ and radius $a$ performing a coherent oscillation inside a round beam pipe of radius $\rho$ with $a \ll \rho$, the electric field and Lorentz force generated by the induced image charges are given by [28]

$$E_z(\bar{z}) = \frac{\lambda}{2\pi\epsilon_0}\frac{1}{\rho^2}\bar{z}, \quad z = x, y\,, \tag{1.115}$$

$$F_z(\bar{z}) = \frac{q\lambda}{2\pi\epsilon_0}\frac{1}{\rho^2}\bar{z}, \quad z = x, y\,, \tag{1.116}$$

where $(\bar{x}, \bar{y})$ denotes the position of the beam centroid. According to Eqn. 1.116, the Lorentz force is repelling in both planes, thus is having a "defocusing" effect on the beam, and it is linear in $\bar{x}$ and $\bar{y}$, inducing a coherent negative tune-shift. Furthermore, it is independent of $\lambda$, resulting in a $\frac{1}{\gamma}$ dependence of the tune-shift.

### 1.7.4 Beam-beam

In the case of beam-beam effects, the beams are moving in opposite directions and the Lorentz force is given by Eqn. 1.103 with $f_v = -1$:

$$F_z = q f_q (1 + \beta^2) E_z, \quad z = x, y\,. \tag{1.117}$$

It is repellent, and thus defocusing, in the case of equal, and attractive, and thus focusing, in the case of opposite charged particles. In most colliders where beam-beam effects are relevant, the bunches are usually approximately Gaussian and in the following a Gaussian charge distribution is assumed.
Furthermore, only the effect of the opposing beam (strong beam) on a single beam particle (weak beam), referred to as weak-strong interaction, will be described in the following section. In this case the distribution of the strong beam remains unchanged. For strong-strong beam-beam interactions where the change of the distributions of both beams is taken into account it is referred to the literature.

#### 1.7.4.1 Incoherent head-on beam-beam effects

As the weak beam passes through the field of the strong beam it receives a transverse kick while the strong beam remains unchanged. For small amplitudes the kick obtained with the Basetti-Erskin formula (Eqn. 1.100) can be linearized and the transformation of the phase space coordinates $(x, x')$ and $(y, y')$ can be described by the thin-lens matrix of a quadrupole with focal strength [29]

$$\frac{1}{f_z} = \frac{2Nr_0}{\gamma\sigma_z(\sigma_x + \sigma_y)}, \quad z = x, y\,, \tag{1.118}$$

where $N$ is the number of particles in the strong beam, $\sigma_z$ the beam size of the strong beam and $r_0$ the classical radius of the particles of the weak beam. Taking the case of only one collision point, the transformation from one collision to the next is then given by the one-turn matrix[8]

$$\begin{pmatrix} 1 & 0 \\ -\frac{1}{2f_z} & 1 \end{pmatrix} \cdot \begin{pmatrix} \cos(\phi_{0z}) & \beta^*_{0z}\sin(\phi_{0z}) \\ -\frac{1}{\beta^*_{0z}}\sin(\phi_{0z}) & \cos(\phi_{0z}) \end{pmatrix} \cdot \begin{pmatrix} 1 & 0 \\ -\frac{1}{2f_z} & 1 \end{pmatrix} = \begin{pmatrix} \cos(\phi_{0z} + \Delta\phi_z) & \beta^*_z\sin(\phi_{0z} + \Delta\phi_z) \\ -\frac{1}{\beta^*_z}\sin(\phi_{0z} + \Delta\phi_z) & \cos(\phi_{0z} + \Delta\phi_z) \end{pmatrix}, \quad z = x, y\,, \tag{1.119}$$

where the kick from the strong beam has been split in half due to symmetry reasons. The unperturbed parameters $\phi_{0z}$ and $\beta^*_{0z}$ and the perturbed ones $\phi_z = \phi_{0z} + \Delta\phi_z$ and $\beta^*_z$ are related by

$$\cos(\phi_{0z} + \Delta\phi_z) = \cos(\phi_{0z}) - \frac{\beta^*_{0z}}{2f_z}\sin(\phi_{0z}), \quad z = x, y\,, \tag{1.120}$$

$$\beta^*_z = \beta^*_{0z}\frac{\sin(\phi_{0z})}{\sin(\phi_z)}, \quad z = x, y\,. \tag{1.121}$$

Hence, in linear approximation the change of the beta-function and tune depends on the phase advance between the collisions and the beam-beam parameter

$$\xi_z = \frac{\beta^*_{0z}}{4\pi f_z} = \frac{Nr_0\beta^*_{0z}}{2\pi\gamma\sigma_z(\sigma_x + \sigma_y)}, \quad z = x, y\,, \tag{1.122}$$

which is a measure for the beam-beam strength. Note that $\beta^*_{0z}$ is the beta-function of the optics of the weak beam at the IP and $\sigma_z$ the beam size of the strong beam at the IP. For highly relativistic ($\beta \approx 1$) round beams with $\sigma_x = \sigma_y = \sigma = \sqrt{\gamma\beta^*_0\epsilon_N}$ and $\beta^*_{0x} = \beta^*_{0y} = \beta^*_0$ Eqn. 1.122 simplifies to

$$\xi_z = \frac{Nr_0}{4\pi\epsilon_N}\,, \tag{1.123}$$

and depends only on the number of particles $N$ and the normalized emittance $\epsilon_N$. In hadron machines the normalized emittance is energy independent and so is the beam-beam parameter, while in electron machines the normalized rms emittance depends on the beam energy (Eqn. 1.65) due to the influence of synchrotron radiation and thus also the beam-beam parameter.

[8] This can be easily extended to multiple collision points by just substituting the one turn matrix by the transport matrix from one collision point to the next.

For $\xi_z < 1$ and for $\phi_z$ not close to a multiple of $\pi$ the beam-beam parameter is approximately equal to the tune-shift $\Delta\nu_z = 2\pi\Delta\phi_z$ caused by the beam-beam interaction

$$\Delta\nu_z \approx \xi_z = \frac{N r_0 \beta^*_{0z}}{2\pi\gamma\sigma_z(\sigma_x + \sigma_y)}, \quad z = x,\, y \tag{1.124}$$

referred to as beam-beam tune-shift.

#### 1.7.4.2 Coherent beam-beam effects

In addition to the incoherent beam-beam effects, the beam is also effected as a whole by the opposing beam known as coherent beam-beam effects. A good measure for the strength of the coherent effect is similar to the incoherent case, the coherent beam-beam parameter. In the case of two beams, denoted with + and −, colliding head-on and with no displacement of their barycenters it is given by [14]:

$$\Xi^{\pm}_z = \frac{N_{\mp} r_0 \beta^{*\pm}_z}{2\pi\gamma_{\pm}\Sigma_z(\Sigma_x + \Sigma_y)}, \quad z = x, y\,, \tag{1.125}$$

where $\Sigma_z = \sqrt{(\sigma^+_z) + (\sigma^-_z)}$ is the effective beam size. Thus for small amplitudes the effect on the entire beam is half the one of the effect on a single particle given by the incoherent beam-beam parameter. For larger amplitudes the effects become equal. This is clear as for large amplitudes the two beams can be considered as point like charges. Equivalent to the incoherent beam-beam tune-shift, the coherent beam-beam tune-shift is equal to the coherent beam-beam parameter.

In general the motion of the two beams becomes coupled by the beam-beam interaction and collective effects can appear. The most important ones are orbit effects, coherent modes and multi-bunch coupling.

#### 1.7.4.3 Dynamic beta, emittance and beam size

In Sec. 1.7.4.1, only the change of the phase advance has been discussed, but the head-on beam-beam interaction also changes the beta-function at the IP where the expression given in Eqn. 1.121 can be rewritten to depend only on the unperturbed parameters

$$\beta^*_z = \beta^*_{0,z}\frac{\sin(\phi_{0z})}{\sin(\phi_z)} = \frac{\beta^*_{0,z}}{\sqrt{1 + 4\pi\xi_{0,z}\cot\phi_{0z} - 4\pi^2\xi^2_{0,z}}}, \quad z = x, y\,. \tag{1.126}$$

Including synchrotron radiation effects the change of the beta-function at the IP results in a change of the beam envelope inducing a change of the equilibrium rms emittance [14]

$$\epsilon_{\mathrm{rms},z} = \frac{(1 + 2\pi\xi_{0z}\cot(\phi_{0z}))\epsilon_{\mathrm{rms},0z}}{\sqrt{1 + 4\pi\xi_{0z}\cot(\phi_{0z}) - 4\pi^2\xi^2_{0z}}}\,. \tag{1.127}$$

The dynamic beam size is then just given by $\sigma_z = \sqrt{\beta^*_z\epsilon_{\mathrm{rms},z}}$. The dependence of all three parameters is illustrated for the case of the LHeC in Fig. 2.29. For lepton colliders like e.g. LEP the tunes were optimized by placing them close to the half integer resonance to explore the reduction of the beam size at the IP and thus increase the luminosity by exploiting the dynamic beta effect.

#### 1.7.4.4 Hourglass effect

For small values of the beta-function $\beta^\star$ at the IP the beta-function increases rapidly with the distance $s$ to the interaction point

$$\beta(s) = \beta^\star + \frac{s^2}{\beta^\star}\,. \tag{1.128}$$

In the case where the bunch length lies in the range or is larger than $\beta^\star$ the beta-function can no longer be considered constant along the bunch leading to a reduction of the luminosity. Explicit expressions for the luminosity reduction factor are given in e.g. [30].

#### 1.7.4.5 Long range beam-beam effects

In order to have only one crossing of the beams at the center of the detector, the beams are often separated with a small crossing angle which is illustrated in Fig. 1.10. Since the bunches travel in a common beam pipe in the interaction region, they still feel the electromagnetic field of the bunches of the opposite beam called long-range interactions. In general, these long-range interactions are much weaker than head-on interactions but they are much more frequent[9].

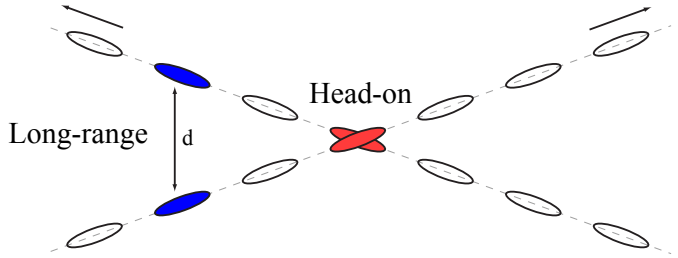


**Figure 1.10:** Schematic plot of head-on and long-range beam-beam interactions.

The main properties of the beam-beam long-range interactions are summarized in the subsequent list [31].

- Large amplitude particles are mainly effected.
- The tune-shift is proportional to the number $N$ of long-range interactions and inversely proportional to the square of the beam separation $d$ and has the opposite sign than the head-on beam-beam tune-shift

  $$\Delta\nu_{\mathrm{lr}} \propto \pm\frac{N}{d^2}\,, \tag{1.129}$$

  where the $+$ is for equally charged beams and the $-$ for oppositely charged beams. The change of sign of the tune-shift can be understood from Fig. 1.11 which shows the derivative of the Lorentz force in respect to the amplitude. For large amplitude particles the sign changes and with it the sign of the tune-shift, leading to a folding of the tune footprint of the beam.
- The symmetry between the planes is broken, resulting in an excitation of also the odd resonance.

[9] For example, in the LHC the beams experience about 30 long-range interactions per IP.

- The closed-orbit is changed.
- Enhancement of the PACMAN effect[10].

### 1.7.5 Non-linearity of the space-charge force for Gaussian beam distributions

The instantaneous tune-shift of a single particle caused by the space-charge field is proportional to the derivative of the Lorentz force in respect to the amplitude $r = \sqrt{x^2 + y^2}$ and averaged over the same. The space-charge force for round Gaussian beams given by Eqn. 1.106

$$F_r = \frac{2\lambda}{4\pi\epsilon_0} q f_q (1 + \beta^2 f_v) \frac{1}{r} (1 - e^{-\frac{r^2}{2\sigma^2}})$$

is then non-linear in $r$.

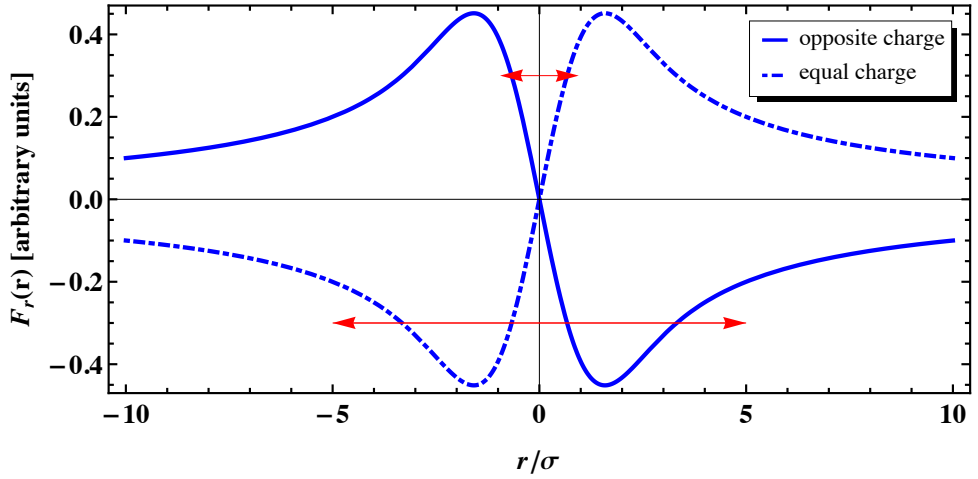


**Figure 1.11:** Space-charge force for round Gaussian beams for equally (dashed) and oppositely (solid) charged particles. The red arrows indicate the oscillation range of small and large amplitude particles.

Its shape is illustrated in Fig. 1.11 from which one can draw the following conclusions:

- for small amplitude particles ($\lesssim 1.5\,\sigma$) the space-charge force is approximately linear in $r$ and results in an amplitude independent tune-shift of the core of the beam.
- for particles with larger amplitudes ($\gtrsim 1.5\,\sigma$) the space-charge force becomes non-linear, in particular it decreases and changes the sign of its slope. Large amplitude particles thus experience a smaller but amplitude dependent tune-shift which tends to 0 for very large amplitudes.

[10] In most colliders the bunches are not equidistantly spaced, but grouped together in bunch trains, providing longer time gaps to allow for e.g. the rise time of the injection and extraction kickers. The bunches of one beam usually encounter the bunches of the other beam only at the interaction point. As the bunches are now grouped in trains of bunches the bunches at the beginning and end of the train experience less long-range interactions, leading to differences in closed-orbit and position and dimension of the tune-spread of the bunches. This effect is known as PACMAN effect.

Briefly, the non-linearity of the space-charge force leads to a detuning with amplitude. For head-on beam-beam effects it can be expressed analytically [29]

$$\begin{aligned}\Delta\nu_x &= \xi\left(\tfrac{1+\frac{1}{a}}{2}\right)\int_0^\infty \tfrac{du}{(1+u)^{3/2}(1+\frac{u}{a^2})^{1/2}} Z_1\left(\tfrac{\alpha_x}{1+u}\right) Z_2\left(\tfrac{\alpha_y}{1+\frac{u}{a^2}}\right) ,\\ \Delta\nu_y &= \xi\left(\tfrac{1+a}{2}\right)\int_0^\infty \tfrac{du}{(1+u)^{3/2}(1+a^2u)^{1/2}} Z_2\left(\tfrac{\alpha_x}{1+a^2u}\right) Z_1\left(\tfrac{\alpha_y}{1+u}\right) ,\end{aligned} \tag{1.130}$$

where $a = \frac{\sigma_y}{\sigma_x}$ is the aspect ratio of the strong beam, $\sqrt{\alpha_x}$ and $\sqrt{\alpha_y}$ are the amplitudes normalized by $\sigma_x$ and $\sigma_y$ respectively and $Z_1$ and $Z_2$ are defined by

$$\begin{aligned}Z_1(x) &= e^{-x}\left(J_0(x) - J_1(x)\right) ,\\ Z_2(x) &= e^{-x} J_0(x) ,\end{aligned} \tag{1.131}$$

where $J_0$ and $J_1$ are the Bessel functions. As an example Fig. 1.12 shows the amplitude dependence of the tune-shift from head-on beam-beam effects in the case of the LHeC High Acceptance (HA) option.

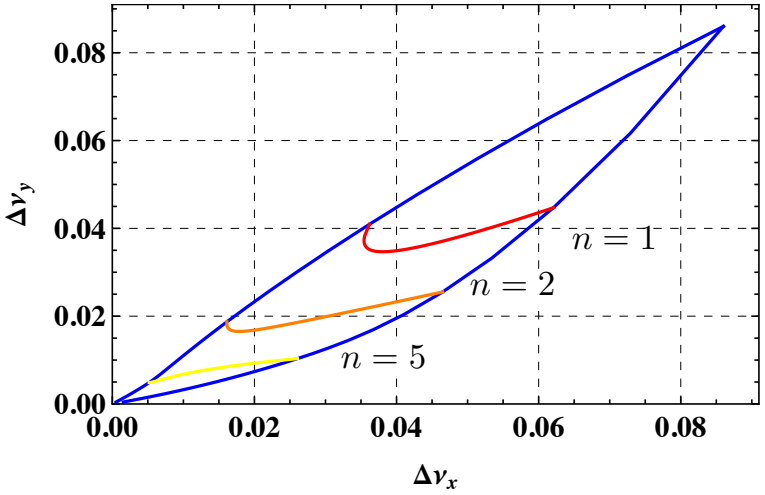


**Figure 1.12:** Detuning with amplitude due to head-on beam-beam for the LHeC High Acceptance (HA) option. The parameter $n$ denotes the amplitude in number of sigmas of the rms beam size.

In general, as the beam-beam interaction represents a strong localized non-linear kick, it influences many aspects of the non-linear beam dynamics, which are not subject of this thesis and for further details it is instead referred to the literature.
In the case of space-charge effects, the non-linear space-charge self-field of the beam introduces non-linearities in the whole machine. The impact of these non-linearities can be many-sided. One aspect investigated in the framework of this thesis is the dependence of the beam stability on the variation of the beam size and the symmetry of the lattice (Sec. 3.6). The idea behind this study is that the strength of the non-linear kick depends on the beam size and the ratio between the beam sizes. For small variations of the beam size the variation of the defocusing effect of the space-charge self-field and its non-linear part are small and the emittance blow-up is expected to be smaller than for a lattice with large variations of the beam size. Furthermore, a high symmetry of the lattice could be

advantageous in the case of space-charge effects as the space-charge force has the same "symmetry" as the lattice[11] and thus resonances are suppressed due to the symmetry of the lattice.

## 1.8 The Optics and Tracking Codes MAD-X and PTC

Most machines at CERN and also the lattices investigated in the framework of this thesis are designed with the optics and tracking code MAD-X [32] which offers a larger variety of different matching routines and an easy-to-use element definition - both essential in the first design phases and further optics development of an accelerator. The strength of PTC [33], [34] lies in the modeling and analysis of the non-linear optics and beam dynamics and an interface to PTC is implemented in MAD-X for this purpose. The tools provided by PTC and used in this thesis are:

- **fully symplectic tracking routines:**
  In MAD-X, conventional thin-lens tracking routines are implemented which correspond to a "drift-kick-drift" model with a second order symplectic integrator. The advantage of this tracking method is its speed which makes it preferable for extensive tracking campaigns but it is non-trivial to create an adequate linear and non-linear model of the machine. Furthermore it is known that MAD-X might not give correct tracking results for large momentum errors. PTC on the other hand offers a relatively precise model of all machine non-linearities and a correct tracking also for large momentum errors providing that the exact Hamiltonian is used.

- **normal form analysis:**
  Higher order chromaticities (detuning with momentum) and anharmonicities (detuning with amplitude) can be directly obtained with PTC via a normal form analysis of the one turn map.

At its core PTC is a symplectic integrator and the user has to provide the correct integrator settings for his purpose. These settings explicitly are:

- the number of integration steps

- the integration model: the "drift-kick-drift" model splits the integration step using drifts, while for the "matrix-kick-matrix" matrices are used. The "matrix-kick-matrix" model has the advantage of producing the correct phase advance.

- the order of the symplectic integrator: "method 2" for a simple second order integrator with one kick per integration step, "method 4" for the Ruth-Neri-Yoshida fourth order integrator with 3 kicks per integration step and "method 6" for the Yoshida sixth-order integrator with seven kicks per integration step

[11] In this context the term "symmetry" is used for the reoccurrence of the same non-linear field after each equivalent part of the lattice.

- the use of an expansion in the momentum error $\delta$ of the Hamiltonian, e.g. for a drift space:

$$H = -\sqrt{(1+\delta)^2 - p_x^2 - p_y^2} \quad \text{(exact)}, \quad H = \frac{p_x^2 + p_y^2}{2(1+\delta)} - \delta \quad \text{(expanded)}\,. \tag{1.132}$$

The accelerator model gains precision with the number of integration steps, the order of the integrator and with the use of the exact Hamiltonian at the cost of CPU time. As PTC is in general a rather slow tracking code, it is essential to find a model precise enough for the corresponding purpose.
For the theory about symplectic integration and Lie algebra techniques see [35].

# 2. LHeC Ring-Ring Option

The current Ring-Ring option design foresees a 10 GeV recirculating linac as injector and the installation of a 50-70 GeV main electron ring on top of the existing LHC proton magnets (Fig. 2.1). In order to ensure simultaneous proton-proton and electron-proton

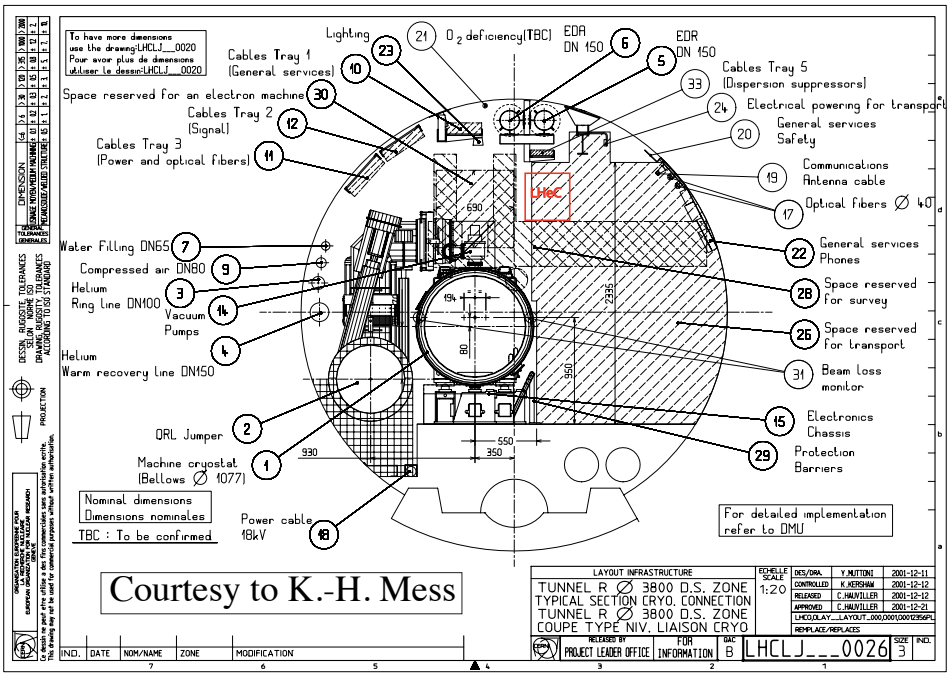


**Figure 2.1:** Representative cross section of the LHC tunnel with the original space holder for the electron beam installation directly above the LHC magnets. The new shifted location of the electron ring due to the additional bypasses in Point 1 and Point 5, and the need to keep the cirucmference of both rings the same, is indicated in red.

operation, the lattice also includes bypasses with separate tunnels around the then existing proton-proton LHC experiments. These bypasses are in addition used to house the full RF of the LHeC as well as the injection and extraction region. The LHeC experiment will either be installed in Point 2 or Point 8. For the design study presented in the LHeC Conceptional Design Report (CDR) [10], Point 2 has been chosen as collision point. In the

following the LHeC CDR, of which the geometry, layout and optics part of the Ring-Ring collider has been elaborated in the framework of this thesis, will serve as a baseline, and is referred to for general information and technical details important for the actual design of the accelerator, but not relevant for the more general description given in this thesis.

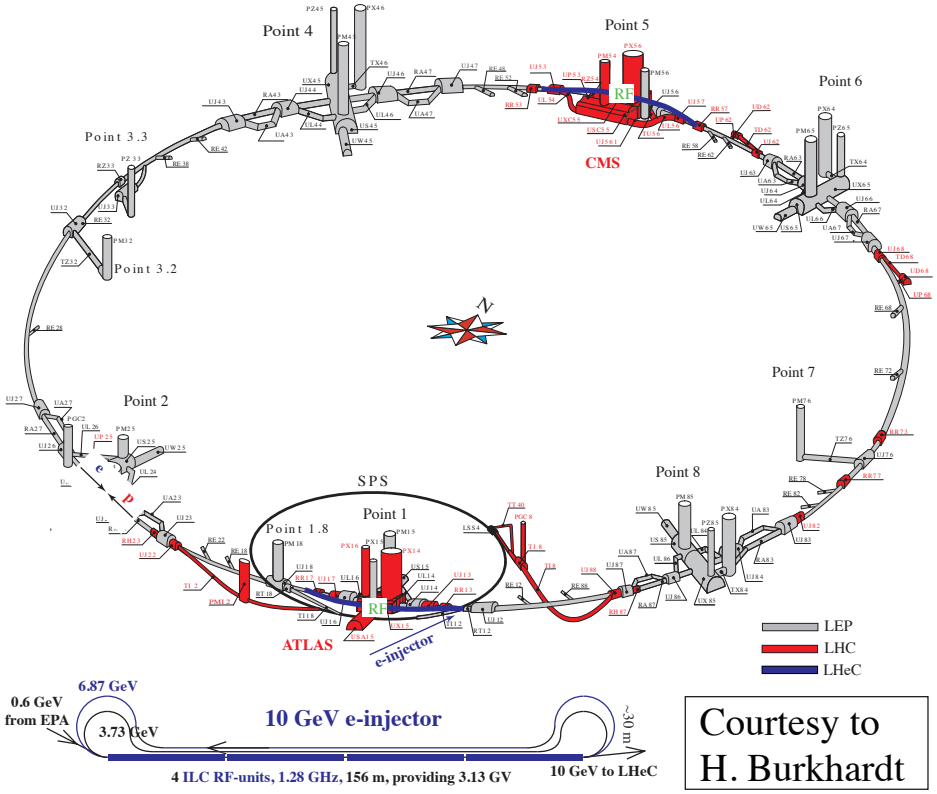


**Figure 2.2:** Schematic layout of the LHeC: In grey the LEP tunnel now used for the LHC, in red the LHC extensions. The two LHeC bypasses are shown in blue. The RF is installed in the central straight section of the two bypasses. The bypass around Point 1 hosts in addition the injection.

The overall layout of the LHeC is shown in Fig. 2.2 and the baseline beam parameters as defined in the LHeC CDR [10] are summarized in Table 2.1 assuming LHC ultimate

| | **electron beam** | **proton beam** |
|---|---|---|
| beam energy [GeV] | 60 | 7000 |
| number of particles per bunch [$10^{10}$] | 1.98 | 17 |
| number of bunches | 2808 | |
| bunch spacing [ns] | 25 | |
| hor./vert. normalized emittance $\gamma\epsilon_{x/y}$ [mm] | 0.59/0.29 | 3.75/3.75 |
| synchrotron radiation power [MW] | 44 | negligible |

**Table 2.1:** Proton and electron beam parameters for the Ring-Ring option. For the proton beam the LHC ultimate parameters [36] have been assumed.

parameters [36] for the proton beam. A critical review of the design parameters performed in the framework of this thesis is given in Sec. 2.1.

In general, the same parameters can be assumed for positrons as for electrons and in the following the electron beam is described representative for both. The electron beam energy and intensity has been set to limit the synchrotron radiation losses to less than 50 MW which is considered to be a safe limit in order to stay below 100 MW total power consumption and at the same time deliver a luminosity of over $10^{33}$ $\mathrm{cm}^{-2}\mathrm{s}^{-1}$. This leads to an energy of 60 GeV and $2 \times 10^{10}$ particles per bunch with the same bunch pattern as the LHC, still leaving some margin for an increase in intensity and energy.
Furthermore, experiences from HERA advise to match the naturally flat electron beam to the round proton beam at the Interaction Point (IP) as a mismatch could result in a reduction of the proton beam lifetime [37]. The difference of the ratio of the horizontal to the vertical emittance between the proton and electron beam is too large in order to adjust the beam sizes over the beta-function at the IP. One possibility of converting the flat electron into a round beam is to introduce coupling in the interaction region or to couple the full electron ring. The different possibilities studied in this thesis are discussed in more detail in Sec. 2.4.3. For the baseline parameters, the option of a fully coupled ring has been chosen and an emittance ratio of 2:1 assumed.
For the interaction region two options have been considered [10], the High Luminosity (HL) option with a detector acceptance of 10° and the High Acceptance (HA) option with a detector acceptance down to 1°. The HL option delivers a higher luminosity as the final focus quadrupoles are placed only 1.2 m from the IP allowing for smaller beta-functions at the IP compared to the HA option where the distance from the first quadrupole to the IP is 6.2 m. Both options foresee a crossing of the beams in the horizontal plane with a crossing angle of 1 mrad ensuring a minimum separation of $5\sigma_e + 5\sigma_p$ at all parasitic encounters which is considered to be sufficient based on experiences from HERA and LHC [10]. The interaction region parameters are summarized in Table 2.2.

| | **HA** | | **HL** | |
|---|---|---|---|---|
| | electron | proton | electron | proton |
| luminosity [$10^{32}\mathrm{cm}^{-2}\mathrm{s}^{-1}$] | 9 | | 18 | |
| syn. rad. power (interaction region) [kW] | 51 | | 33 | |
| critical energy [keV] | 163 | | 126 | |
| crossing angle [mrad] | 1 | | | |
| hor./vert. beta-function at IP [m] | 0.4/0.2 | 4.0/1.0 | 0.18/0.1 | 1.8/0.5 |
| hor./ver. rms beam size at IP [$\mu$m] | 45/22 | | 30/16 | |

**Table 2.2:** Parameters of the Ring-Ring interaction region.

In the framework of this thesis, the complete electron ring geometry, layout and optics, except the interaction region, have been designed which are described in Sec. 2.2 and 2.3. In addition, different beam dynamical aspects regarded to be relevant have been studied in this thesis and are presented in Sec. 2.4. The main parameters of the complete lattice are compiled for a better overview in Appendix G.

## 2.1 Review of Design Parameters

The aim of every or rather most colliders is to achieve the highest possible luminosity and energy. In the case of the LHeC the luminosity is given by

$$\mathscr{L}(\theta) = \underbrace{\frac{N_e N_p N_b f_{\mathrm{rev}}}{2\pi\sqrt{(\sigma_{xe}^2+\sigma_{xp}^2)\cdot(\sigma_{ye}^2+\sigma_{yp}^2)}}}_{\mathscr{L}_0} \cdot \underbrace{\frac{1}{\sqrt{1+\left(\frac{\sigma_{se}^2+\sigma_{sp}^2}{\sigma_{xe}^2+\sigma_{xp}^2}\right)\tan^2\frac{\theta}{2}}}}_{S(\theta)}, \tag{2.1}$$

where the index $e$ indicates the electron and the index $p$ the proton beam parameters. The parameter $N_b$ is the number of bunches, $N_i$ the number of particles per bunch, $\sigma_{xi/yi}$ the horizontal and vertical rms beamsize, $\sigma_{si}$ the rms bunchlength and $\theta$ the crossing angle at the IP. $\mathscr{L}_0$ denotes the luminosity for head-on collisions and $S(\theta)$ the geometric luminosity reduction factor which expresses the decrease of the luminosity due to the crossing angle. Beside the geometric loss factor, a reduction in luminosity can also occur due to the hourglass effect. An estimation of the strength of this effect can be obtained from the analytical formula for head-on collisions [30]

$$R(u_x,u_y) = \frac{\mathscr{L}}{\mathscr{L}_0} = \int_{-\infty}^{\infty}\frac{du}{\sqrt{\pi}}\frac{e^{-u^2}}{\sqrt{(1+u^2/u_x^2)(1+u^2/u_y^2)}}, \tag{2.2}$$

where $u$ is a integration variable depending on $s$ and $u_x$ is defined by

$$u_x^2 = \frac{2(\sigma_{xp}^2+\sigma_{xe}^2)}{(\sigma_{sp}^2+\sigma_{se}^2)((\frac{\sigma_{xp}}{\beta_{xp}^*})^2+(\frac{\sigma_{xe}}{\beta_{xe}^*})^2)} \tag{2.3}$$

with a corresponding expression for $u_y$.

In addition, the achievable luminosity can also be limited by beam-beam effects. A measure for the limit arising from head-on collisions is the incoherent beam-beam tune-shift given by Eqn. 1.119

$$\Delta\nu_{xe,ye} = \frac{\beta_{xe,ye}^* r_e}{2\pi\gamma_e}\cdot\frac{N_p}{\sigma_{xp,yp}(\sigma_{xp}+\sigma_{yp})}, \tag{2.4}$$

$$\Delta\nu_{xp,yp} = \frac{\beta_{xp,yp}^* r_p}{2\pi\gamma_p}\cdot\frac{N_e}{\sigma_{xe,ye}(\sigma_{xe}+\sigma_{ye})}. \tag{2.5}$$

The impact of the beam-beam long-range interactions is more difficult to estimate. For the LHeC the number of long-range encounters is just given by the bunch spacing and the distance from the IP to the first proton quadrupole, where the three beams each enter their dedicated beam pipe. For 25 ns bunch spacing there is one parasitic encounter every approx. 3.75 m resulting in $2\times 6$ long-range interactions over the whole IP assuming a distance of 22.96 m from the IP to the first proton quadrupole. The strength of the long-range interactions is according to Eqn. 1.129 proportional to $1/d^2$ with $d$ being the distance between the beams. Thus a sufficient separation of the beams must be ensured in order to avoid an instability of the beams. From HERA and LHC experience a minimal separation of $5\sigma_e + 5\sigma_p$ is considered to be acceptable in the case of the LHeC [10]. This separation is provided by choosing the crossing angle large enough.

In the case of the LHeC also the synchrotron radiation losses at the interaction region have to be taken into account as the necessary beam separation is achieved by bending

the electron beam, resulting in considerable synchrotron radiation losses in the interaction region. Due to the high proton beam energy of 7 TeV, a separation by bending the proton beam is not possible, as very strong dipoles would be required in order to achieve even a small separation. The bending of the electron beam is realized by passing off-center through the final focus quadrupoles of the electron ring and afterwards an additional separator dipole. The emitted synchrotron radiation power can be calculated with the following analytical formula [38]

$$P_{\text{quad}} = \frac{C_\gamma}{2\pi} k^2 E_0^4 f_{\text{rev}} N_e N_b \left( \epsilon_x \int_0^L \beta_x(z) dz + \epsilon_y \int_0^L \beta_y(z) dz \right) , \tag{2.6}$$

$$P_{\text{dip}} = \frac{C_\gamma}{2\pi} \frac{L}{\rho^2} E_0^4 f_{\text{rev}} N_e N_b , \tag{2.7}$$

where $E_0$ is the beam energy, $k$ the normalized quadrupole strength, $\rho$ the bending radius and $L$ the magnet length. In general, synchrotron radiation losses in the interaction region can contribute considerably to the background in the detector and can heat up the vacuum system, both effects which definitely want to be avoided.

### 2.1.1 Number of bunches and bunch intensity

The beam intensity in lepton colliders, thus also in the case of the LHeC electron accelerator, is primarily limited by the power loss due to synchrotron radiation (Eqn. 1.54)

$$P_{\text{Beam}} = U_0 N_b N_e f_{\text{rev}} , \tag{2.8}$$

which scales linearly with the number of bunches $N_b$ and the bunch intensity $N_e$. As the luminosity scales quadratically with the bunch intensity $N_e N_p$ but only linearly with the number of bunches $N_b$ and assuming the same synchrotron radiation loss budget, a higher luminosity is therefore reached by increasing the bunch intensity and reducing the number of bunches by the same factor.

Beside the luminosity and the synchrotron radiation losses over the whole ring, the other three parameters to be considered are the synchrotron radiation losses in the interaction region, the beam-beam tune-shift and the number of long-range interactions. As the synchrotron radiation losses in the interaction region scale linearly with the bunch intensity and number of bunches (Eqn. 2.6 and 2.7), the same argument holds for the synchrotron radiation losses over the whole ring. The incoherent beam-beam tune-shift (Eqn. 2.4 and 2.5) scales as well linearly with the bunch intensity, representing a possible upper limit for the same, but is independent of the number of bunches. On the other hand the number of long-range interactions increases with the number of bunches, explicitly if the number of bunches is increased by $n$ the number of long-range interactions increases as well by $n$. Summarizing the above arguments, a higher luminosity can be reached with a smaller number of bunches and a higher bunch intensity without increasing the total synchrotron radiation losses in the whole ring and the interaction region. Furthermore the number of long-range interactions is reduced. On the other hand a higher bunch current results in a larger incoherent beam-beam tune-shift.

Nevertheless, in the case of the LHeC the bunch intensity and number of bunches of the proton beam is fixed by the LHC proton physics parameters. Therefore, the luminosity

of the LHeC is determined by the fixed bunch pattern of the LHC, which is not optimal for a lepton collider due to its high number of bunches and resulting small electron beam bunch intensity.

### 2.1.2 Luminosity, beam energy and beam intensity

As shown in Sec. 2.1.1, the optimal luminosity for the LHeC is reached with the same bunch pattern for the electron beam as for the LHC proton beam. Under this assumption the luminosity and beam energy $E_0$ for a total synchrotron radiation power of $P_{\mathrm{Beam}}$ are related by

$$\mathscr{L} = \mathrm{const} \cdot P_{\mathrm{Beam}} E_0^4 \,. \tag{2.9}$$

This dependence is illustrated in Fig. 2.3 for the LHeC, where the HA optics have been assumed. In addition, the geometric luminosity reduction factor arising from the crossing angle of 1 mrad has been included. For the LHeC an energy of 60 GeV has been chosen

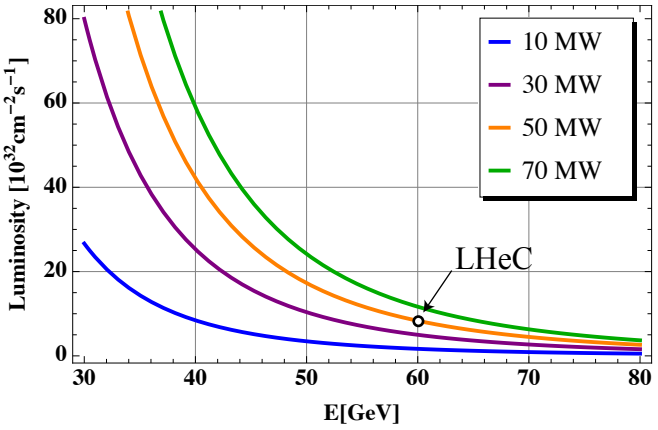


**Figure 2.3:** Maximum luminosity versus beam energy for different synchrotron radiation power loss assuming LHeC HA parameters.

leading to a luminosity in excess of $10^{33}$ cm$^{-2}$s$^{-1}$. However, a higher luminosity could be obtained by lowering the beam energy.

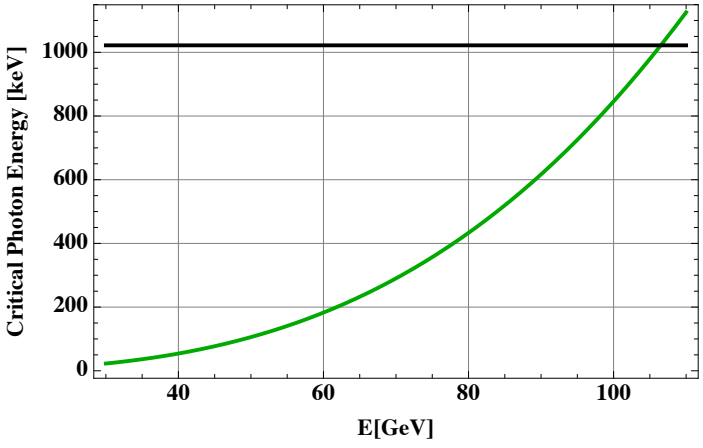


**Figure 2.4:** Critical photon energy versus beam energy. The black line indicates the energy necessary for pair production ($\epsilon_c = 2m_e c^2 = 1.022$ MeV)

For very high beam energies the energy of the emitted photons can reach the threshold for the production of $e^+e^-$ pairs. In this case, background and also machine protection become considerably more challenging. The maximum photon energy is given by the critical photon energy [12]

$$\epsilon_c = \frac{\hbar c \gamma^3}{\rho}\,, \tag{2.10}$$

where $\rho$ is the bending radius. The critical photon energy versus the beam energy is shown in Fig. 2.4 assuming the LHeC optics described in [10] with a main dipole bending radius of 2622.56 m. The limit for pair production is reached at a beam energy of 106.5 GeV.

### 2.1.3 Luminosity and beam-beam effects

As described in the previous chapters the highest luminosity in combination with the smallest synchrotron radiation losses is reached if the LHeC electron beam has the same bunch pattern as the proton beam and the bunch intensity is adjusted in order to ensure a synchrotron radiation power smaller than 50 MW. With a fixed bunch pattern and bunch intensity, the luminosity can be further improved by a reduction of:

- the crossing angle
- the beam size at the IP i.e. a reduction of the emittance or beta-function

It is known from experience at HERA that unequal beam sizes at the IP lead to a reduction of the proton beam life time [37]. Therefore, the beam sizes must be matched at the IP. Furthermore, the LHC ultimate parameters (Table 2.1) are assumed for the proton beam and a horizontal uncoupled electron emittance $\epsilon_{xe}$ with $J_x = J_s = 1.5$ and $J_y = 1$ delivering the design values of 5.0 nm in the horizontal and 2.5 nm in the vertical plane for the electron beam. All parameters are summarized in Table 2.3.

| | **electron beam** | **proton beam** |
|---|---|---|
| beam energy | 60 GeV | 7 TeV |
| number of particles per bunch $N_{p/e}$ | $1.98 \times 10^{10}$ | $1.7 \times 10^{11}$ |
| number of bunches $N_b$ | 2808 | |
| bunch spacing | 25 ns | |
| hor. rms emittance $\epsilon_{xe,0}(J_{x/s} = 1.5, J_y = 1, \kappa = 0)$ | 6.67 nm | - |
| hor./ver. rms emittance $\epsilon_{xp/yp} =: \epsilon_p$ | - | 0.5/0.5 nm |
| minimum beta-function at IP $\beta^*_{xp/yp,\mathrm{min}}$ | - | 0.5/0.5 m |
| bunch length $\sigma_{sp/se}$ | 5.7 mm | 7.5 cm |

**Table 2.3:** Proton and electron beam parameters assumed for the review of design parameters. For the proton beam the LHC ultimate parameters [36] have been used.

In order to simplify the equations, the following parameters are defined:

$$\kappa = \frac{\epsilon_{ye}}{\epsilon_{xe}} \quad \text{the ratio between the e-beam emittances}\,, \tag{2.11}$$

$$n = \frac{\beta^*_{xp}}{\beta^*_{yp}} \quad \text{the ratio between the beta-functions of the p-beam at the IP}\,. \tag{2.12}$$

In addition, under the approximation of no vertical dispersion, a negligible vertical emittance in the uncoupled case and the same damping partition in the coupled and uncoupled case, the electron beam emittances are related by Eqn. 1.69, leading to the following relations between the electron and proton beam beta-function at the IP (under the assumption of equal beam sizes):

$$\beta^*_{xe} = \frac{2}{3}\frac{\beta^*_{yp}\epsilon_p n(\frac{3}{2}+\kappa)}{\epsilon_{xe,0}}\,, \tag{2.13}$$

$$\beta^*_{ye} = \frac{2}{3}\frac{\beta^*_{yp}\epsilon_p(\frac{3}{2}+\kappa)}{\epsilon_{xe,0}\kappa}\,. \tag{2.14}$$

The expression Eqn. 2.1 for the luminosity then reduces to

$$\mathscr{L}(\theta) = \frac{1}{4\pi}\frac{f_{\mathrm{rev}}N_bN_eN_p}{\sqrt{n}\beta^*_{yp}\epsilon_p\sqrt{1+\frac{\frac{1}{2}\left(\sigma^2_{se}+\sigma^2_{sp}\right)\tan^2\frac{\theta}{2}}{n\epsilon_p\beta^*_{yp}}}}\,, \tag{2.15}$$

and becomes independent of the ratio $\kappa$ between the electron beam emittances. As illustrated in Fig. 2.5, the maximum luminosity is reached in the case of $n = 1$ when the beams are squeezed in both planes to the minimum $\beta^*$ of $\beta^*_{p,\mathrm{min}} = 0.5$ m. The luminosity

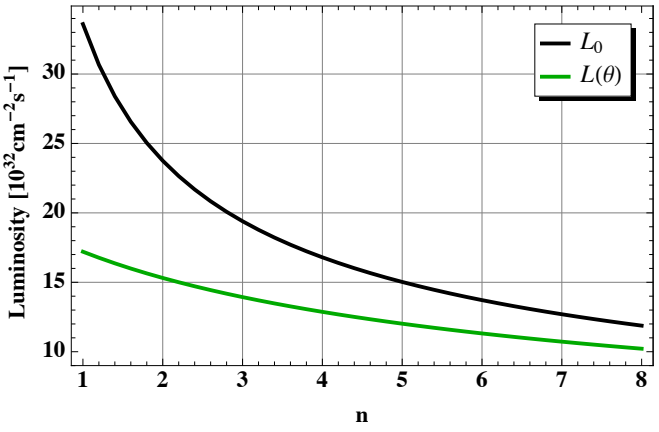


**Figure 2.5:** Maximum luminosity with ($L(\theta)$) and without ($L_0$) geometric reduction factor $S(\theta)$ versus ratio $n$ between horizontal and vertical proton beam beta-functions at the IP assuming $\beta_{yp}* = \beta^*_{p,\mathrm{min}}$ and a constant crossing angle of $\theta = 1$ mrad.

decreases slower with $n$ if the effect of the crossing angle is taken into account, where the same crossing angle of 1 mrad has been assumed for all $n$. This assumption is somewhat unrealistic, as the angle would have to be increased for values of $n < 8$[1].

[1]Here the limit of $n = 8$ is an educated guess based on the 1 mrad crossing angle being sufficient in the case of the HA option and the following reasoning: The value of $n = 8$ for $\beta^\star_{yp} = 0.5$ and $\kappa = 0.35$ - the parameters of the HA* option proposed later - yields a $\beta^\star_{xe/xp}$ equal to $\beta^\star_{xe/xp}(\mathrm{HA}) = 0.4/4.0$ m. As the crossing angle depends on the required minimum separation at the first parasitic encounter, here $5\sigma_e + 5\sigma_p$, and the beam size in turn indirectly on $\beta^\star_x$ as $\beta_x(s) = \beta^*_x + \frac{s^2}{\beta^*_x}$ and $\sigma_x = \sqrt{\beta_x\epsilon_{x,\mathrm{rms}}}$, the same $\beta^*_x$ should lead to approximately the same separation at the first parasitic encounter. Summing up, the required crossing angle for $n = 8$ and $\beta^\star_{yp} = 0.5$ should be approximately the same as for the HA-option. For smaller values of $n$ the horizontal beta-function at the IP $\beta^\star_x$ decreases and consequently the beam size at the first parasitic encounter increases, making an increase of the crossing angle eventually necessary.

The hourglass reduction factor $R(u_x, u_y)$ of Eqn. 2.2 also takes a simpler form

$$R(u_x, u_y) = \int_{-\infty}^{\infty} \frac{du}{\sqrt{\pi}} \frac{e^{-u^2}}{\sqrt{\left(1 + \bar{u}_x^2 u^2\right)\left(1 + \bar{u}_y^2 u^2\right)}} \tag{2.16}$$

with

$$\bar{u}_x^2 = \frac{1}{4}\left(\sigma_{se}^2 + \sigma_{sp}^2\right)\left(\frac{1}{\kappa^2 n^2 {\beta_{ye}^*}^2} + \frac{1}{n^2 {\beta_{yp}^*}^2}\right), \tag{2.17}$$

$$\bar{u}_y^2 = \frac{1}{4}\left(\sigma_{se}^2 + \sigma_{sp}^2\right)\left(\frac{1}{{\beta_{ye}^*}^2} + \frac{1}{{\beta_{yp}^*}^2}\right), \tag{2.18}$$

and depends only on the vertical beta-function at the IP, where $\beta_{ye}^*$ is given by Eqn. 2.14. The dependence of the hourglass effect on $n$ and $\kappa$ is illustrated in Fig. 2.6. Only for $n = 1$ a strong reduction is visible. For $\kappa \to 0$ the reduction factor tends to 1. In this case the vertical beta-function tends to infinity $\beta_{ye} \to \infty$ and the hourglass effect - mainly from the protons - in the vertical plane becomes negligible, while the effect only slightly increases in the horizontal due to the stronger squeeze of the electron beam. For $\kappa \to 1$ the hourglass loss factor reaches its minimum for all values of $n > 1$, as it implies a maximum squeeze in the vertical plane, which is the plane with the smaller beta-function and therefore stronger hourglass effect. It has to be kept in mind that in the above formula the effect of the crossing angle is not taken into account. In general it is possible that the hourglass effect is reduced if the effect of the crossing angle is included.

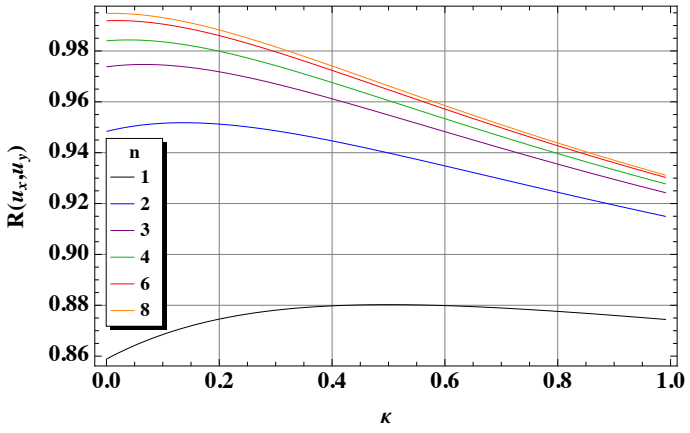


**Figure 2.6:** Hourglass reduction factor $R(u_x, u_y)$ for different ratios $n$ between proton beam beta-functions at the IP assuming $\beta_{yp}* = \beta_{p,\min}^*$ versus the ratio $\kappa$ between electron beam emittances.

Using the assumption of equal beam sizes at the IP, the incoherent beam-beam tune-shift (Eqn. 1.124) reduces to the following expressions for the electron beam

$$\Delta\nu_{xe} = \frac{r_e}{2\pi\gamma_e}\frac{N_p}{\epsilon_{xe,0}\left(1 + \sqrt{\frac{\beta_{ye}^*\kappa}{\beta_{xe}^*}}\right)} \overset{(2.13),(2.14)}{=} \frac{r_e}{2\pi\gamma_e}\frac{N_p\left(1 + \frac{2}{3}\kappa\right)}{\epsilon_{xe,0}\left(1 + \sqrt{\frac{1}{n}}\right)}, \tag{2.19}$$

$$\Delta\nu_{ye} = \frac{r_e}{2\pi\gamma_e}\frac{N_p}{\kappa\epsilon_{xe,0}\left(1 + \sqrt{\frac{\beta_{xe}^*}{\beta_{ye}^*\kappa}}\right)} \overset{(2.13),(2.14)}{=} \frac{r_e}{2\pi\gamma_e}\frac{N_p\left(1 + \frac{2}{3}\kappa\right)}{\kappa\epsilon_{xe,0}\left(1 + \sqrt{n}\right)}, \tag{2.20}$$

and the proton beam

$$\Delta\nu_{xp} = \frac{r_e}{2\pi\gamma_p}\frac{N_e}{\epsilon_p(1+\sqrt{\frac{1}{n}})}, \tag{2.21}$$

$$\Delta\nu_{yp} = \frac{r_e}{2\pi\gamma_p}\frac{N_e}{\epsilon_p(1+\sqrt{n})}. \tag{2.22}$$

The dependence on $n$ and $\kappa$ is shown in Fig. 2.7 and 2.8. In the case of the electron beam, the ratio between the emittances can always be chosen to deliver the same beam-beam tune-shift in both planes. This is considered to be best for the beam stability, as the beam-beam tune-shift then takes on moderate values in both planes. The difference

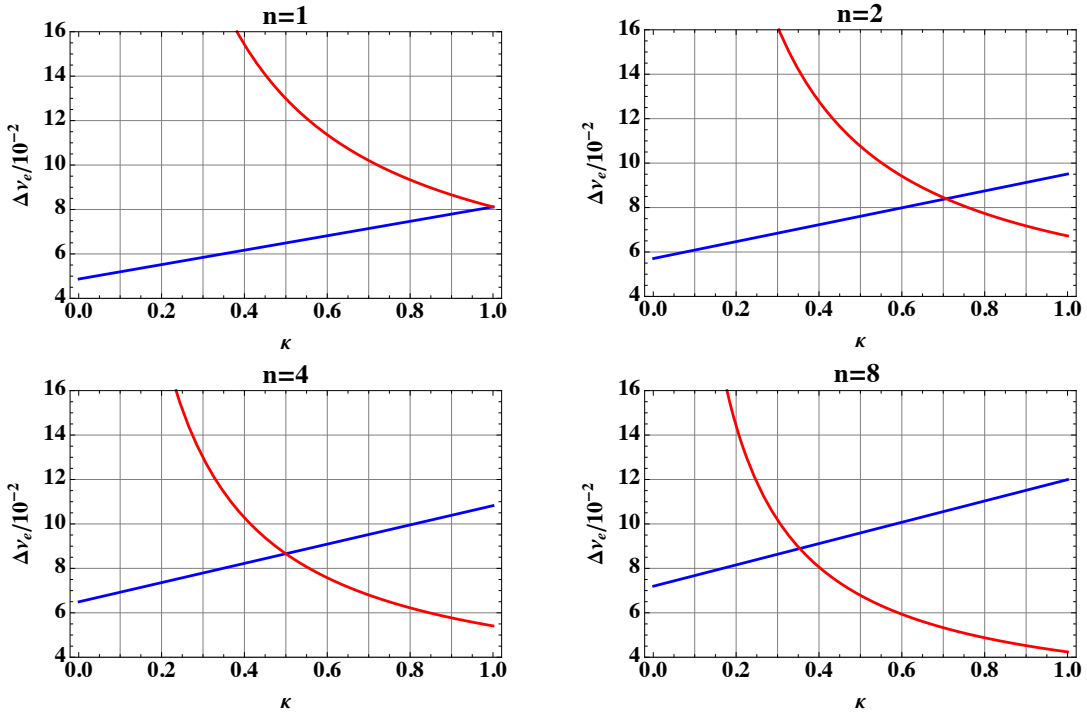


**Figure 2.7:** Horizontal (blue) and vertical (red) electron beam-beam tune-shift $\Delta\nu_{ie}$ for different ratios $n$ between proton beam beta-function at the IP, assuming $\beta_{yp}* = \beta^*_{p,\min}$ versus the ratio $\kappa$ between electron beam emittances.

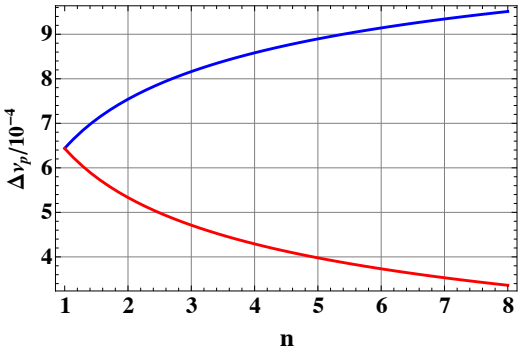


**Figure 2.8:** Horizontal (blue) and vertical (red) proton beam-beam tune-shift $\Delta\nu_{ip}$ versus the ratios $n$ between proton beam beta-functions at the IP assuming $\beta_{yp}* = \beta^*_{p,\min}$.

between the horizontal and vertical proton beam-beam tune-shifts increases with $n$ and, correspondingly, the best beam stability is reached for $n = 1$.
In general, an increases in luminosity is always obtained by decreasing the emittance, which is theoretically possible in the case of the proton beam and also in the case of the electron beam, for latter by for example further increasing the bending radius. Another benefit would be a reduction of the synchrotron radiation losses in the interaction region due to the smaller electron beam emittances.
Another possibility to increase the luminosity without changing the beam parameters is to change the ratio $n$ of the proton beta-functions at the IP to higher values of $n$ as the luminosity (Eqn. 2.15) is only linear in $\frac{1}{\sqrt{n}}$ but quadratic in $\frac{1}{\sqrt{\beta^*_{yp}}}$

$$\mathscr{L}(\theta) \sim \frac{1}{\sqrt{n\beta^{*\,2}_{yp} + \frac{1}{2}\tan^2\frac{\theta}{2}(\sigma^2_{se} + \sigma^2_{sp})\beta^*_{yp}}}\,, \tag{2.23}$$

where $\frac{1}{2}\tan^2\frac{\theta}{2}(\sigma^2_{se} + \sigma^2_{sp}) = 1.41$ for $\theta = 1$ mrad. Explicitly considering the LHeC HA option, a gain in luminosity could be achieved by reducing $\beta^*_{yp}$ from 1 m to the minimal value of $\beta^*_{p,\mathrm{min}} = 0.5$ m. Furthermore, in order to keep the same beam separation and therefore crossing angle in the horizontal plane $n$ is increased to 8, so that $\beta^*_{xp}$ and therefore $\beta^*_{xe}$ are kept unchanged. To obtain the same incoherent electron beam-beam tune-shifts, $\kappa$ is changed from 0.5 to 0.35, leading to only slightly higher tune-shifts. The horizontal proton beam-beam tune-shift still stays well below the nominal LHC tune-shifts and only changes slightly compared to the HA option. All values are summarized in Table 2.4.

| | **electron beam** | | **proton beam** | | |
|---|---|---|---|---|---|
| | LHeC | | LHeC | | LHC |
| | HA* | HA | HA* | HA | nominal |
| $\Delta\nu_x$ | 0.089 | 0.086 | 0.00095 | 0.00086 | 0.0037 |
| $\Delta\nu_y$ | 0.089 | 0.086 | 0.00034 | 0.00043 | 0.0034 |

**Table 2.4:** Comparison of incoherent beam-beam tune-shifts. The proposed option with $\beta^* = 0.5$ m, $n = 8$, $\kappa = 0.35$ and a crossing angle of $\theta_{\mathrm{HA}^*} = \theta_{\mathrm{HA}} = 1$ mrad is referred to as HA* option.

This option, which is in the following referred to as HA* option, then delivers a luminosity by a factor of 1.4 higher:

$$\mathscr{L}(\mathrm{HA}^*) = 1.4 \times \mathscr{L}(\mathrm{HA}) = 10.2 \times 10^{32}\ \mathrm{cm}^{-2}\mathrm{s}^{-1}\,. \tag{2.24}$$

A disadvantage of the new HA* option might be the higher synchrotron radiation losses in the interaction region due to the stronger squeeze in the vertical plane and the larger horizontal emittance for $\kappa = 0.35$. The change due to the smaller $\kappa$ and, therefore, higher horizontal electron beam emittance is considered to be small, as the radiation losses in quadrupoles scale linearly with the horizontal emittance and $\frac{\epsilon_{xe}(\kappa=0.35)}{\epsilon_{xe}(\kappa=0.5)} = 1.08$. As the radiation loss in the quadrupoles scales quadratically with the beam size, an estimate of

the additional radiation losses due to the smaller vertical beta-function at the IP can be obtained by comparing the beam size at the first electron final focus quadrupole given by

$$\sigma_{ye} = \sqrt{\epsilon_{ye}(\kappa)(\beta^*_{ye} + \frac{s^2}{\beta^*_{ye}})}\,. \tag{2.25}$$

Because the radiation loss in dipoles is independent of the beam size, the relative change of the total synchrotron radiation loss $P_{\mathrm{Syn}}$ of the HA$^*$ option compared to the HA option is then estimated to be in the range of

$$\sigma_{ye}(\mathrm{HA}^*) = 0.74 \text{ mm},\ \sigma_{ye}(\mathrm{HA}) = 0.69 \text{ mm} \Rightarrow \frac{P_{\mathrm{Syn}}(\mathrm{HA}^*)}{P_{\mathrm{Syn}}(\mathrm{HA})} \sim \frac{\sigma_{ye}(\mathrm{HA}^*)^2}{\sigma_{ye}(\mathrm{HA})^2} = 1.14 \tag{2.26}$$

In the case of the HA option optics the vertical maximum beta-function in the final focus quadrupoles is already quite large. Therefore, a reduction from $\beta^*_{ye}(\mathrm{HA}) = 0.2$ to $\beta^*_{ye}(\mathrm{HA}^*) = 0.13$ could result in an unacceptably large vertical beta-function, consequently large beam size and higher synchrotron radiation losses. The latter could be reduced by changing from a QF-QD doublet to a QD-QF doublet. An alternative QD-QF optics for

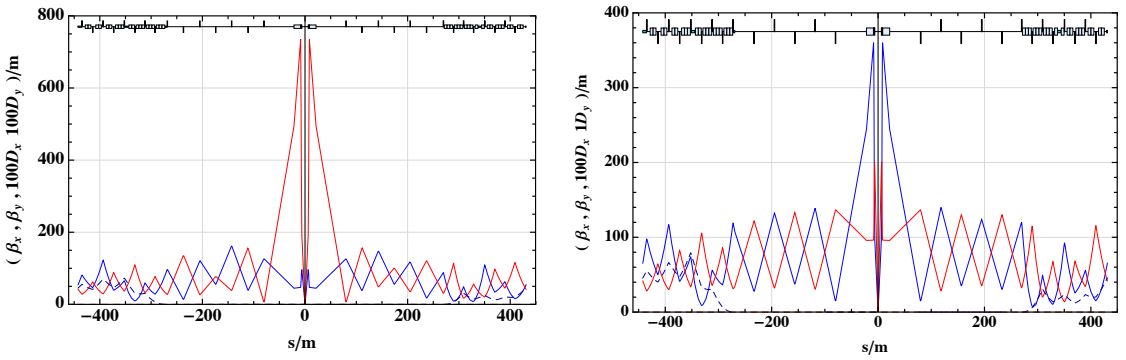


**Figure 2.9:** Optics of the LHeC HA option [10] (left) and the alternative HA (QD-QF) solution (right) with a QD-QF doublet instead of a QF-QD doublet. The horizontal/vertical beta-function is shown in blue/red and the horizontal/vertical dispersion in dashed-blue/dashed-red.

the LHeC HA option (HA (QD-QF) option) developed in the framework of this thesis and shown in Fig. 2.9, already delivers comparable synchrotron radiation losses (Table 2.5), indicating smaller losses with a QD-QF optics than a QF-QD optics in the case of the HA$^*$ option.

| | **HA** | **HA (QD-QF)** |
|---|---|---|
| Q1 | 5.4 kW | 5.6 kW |
| Q2 | 6.2 kW | 6.4 kW |
| Separation Dipole | 14.1 kW | 14.1 kW |
| Total | 51.4 kW | 52 kW |

**Table 2.5:** Synchrotron Radiation Losses in the interaction region for the HA option with a QF-QD doublet and the alternative HA (QD-QF) option with a QD-QF doublet. The losses are calculated analytically using Eqn. 2.6 and 2.7

### 2.1.4 Polarization

In the case of the LHeC a high polarization of the electron beam is desired by the experiments as it allows to investigate different polarization dependent phenomena relevant in particle physics. Two examples are the dependence of the cross section of neutral and charged current and of the weak mixing angle $\sin^2\Theta$ on the polarization [10]. A general study of the achievable electron beam polarization in the case of the LHeC Ring-Ring option is presented in [10] and [39], which is referred to for further details. In the following only a short summary of the main points will be given.

The polarization in the LHeC is obtained by using the Sokolov-Ternov polarizing process. The inverse time constant of the exponential build up of the polarization is given by [40]:

$$\tau_{\mathrm{st}}^{-1} = \frac{5\sqrt{3}}{8} \frac{r_e \gamma^5 \hbar}{m_e |\rho|^3}\,, \tag{2.27}$$

and depends on the beam energy - $\gamma$ is the Lorentz factor - and the radius of curvature $\rho$ of the bending magnets. This polarizing process is counteracted by a depolarizing process which occurs if the invariant spin field $\hat{n}(s)$ is not perfectly aligned to the vertical field of the bending magnets. This "misalignment" is mainly caused by a misalignment of the ring, by spin rotators or by uncompensated skew quadrupoles or solenoids. Furthermore, the depolarization can increase significantly near spin-orbit resonances

$$\nu_0 = m_0 + m_1 Q_1 + m_2 Q_2 + m_3 Q_3\,, \tag{2.28}$$

where $m_0$, $m_1$, $m_2$, $m_3$ are integers, $Q_1$, $Q_2$, $Q_3$ the three tunes of the synchro-betatron motion and $\nu_0$ the spin tune, which is very nearly the number of precisions of the spin vectors around the invariant axis on the closed-orbit $\hat{n}_0(s)$. The spin tune $\nu_0$ is given by $a\gamma$, where $\gamma$ is the Lorentz factor and roughly increases by 1 every $\frac{m_e}{(g-2)/2} = 440.648$ MeV for $e^{\pm}$ rings. The increase of the energy spread (Eqn. 1.61) with the beam energy in general leads to a stronger depolarization for higher energies.

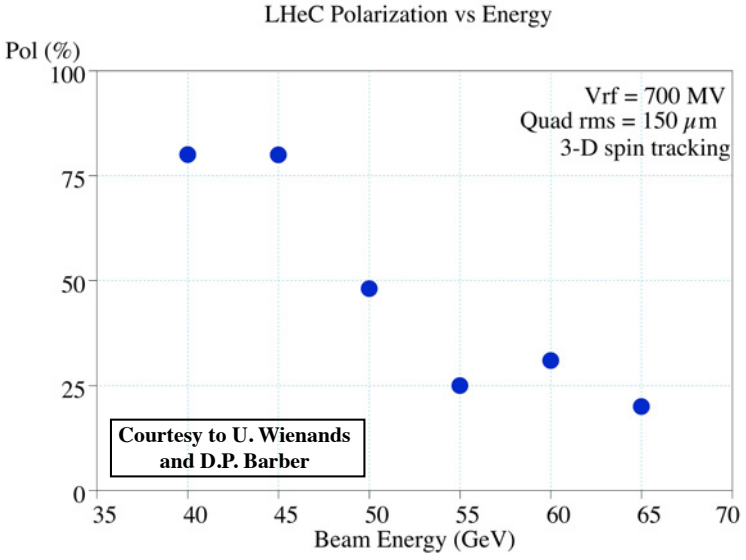


**Figure 2.10:** Dependence of the equilibrium polarization on the beam energy. The polarization falls steeply with increasing energy. Figure is taken from [10].

In order to estimate the polarization attainable in the case of the LHeC, an early version of the LHeC lattice has been studied and presented in [10], which is a flat ring without bypass, interaction region and spin rotators and a working point of $Q_x/Q_y = 123.83/85.62$. Furthermore, an rms vertical alignment error of the quadrupoles of 150 $\mu$m and one orbit corrector per quadrupole has been assumed. Fig. 2.10 shows the polarization obtained for different beam energies. The polarization decreases steeply for beam energies larger than 50 GeV, as the energy spread increases beyond 441 MeV. Note that the simulation results of the polarization level illustrated in Fig. 2.10 are based on one machine per energy value and can vary significantly for different misaligned rings, e.g. for the nominal beam energy of 60 GeV and a synchrotron tune of $Q_s = 0.1$ between 10% and 40% [10]. Furthermore, this early LHeC lattice represents a kind of best case scenario as neither coupling, so the introduction of skew quadrupoles, nor the interaction region with a separation scheme including vertical bends and spin rotators are included in this lattice. The effect of the skew quadrupoles could possibly be undone by a careful "linear spin matching" [41]. In order to limit the effect of the spin rotators and especially vertical beam separation, the interaction region would have to be carefully designed and studied in detail.

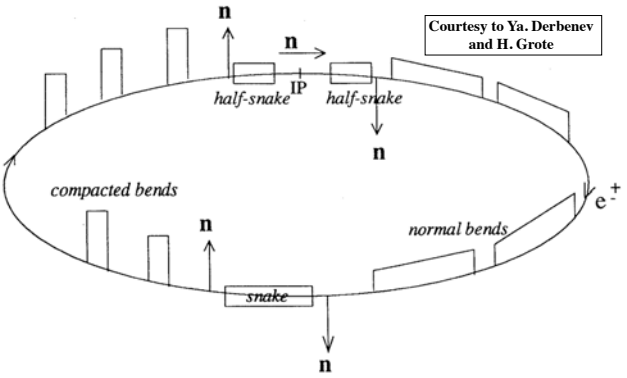


**Figure 2.11:** Schematic view of the proposed scheme to increase the polarization for high energies in the LHeC using Siberian snakes. Figure is taken from [42].

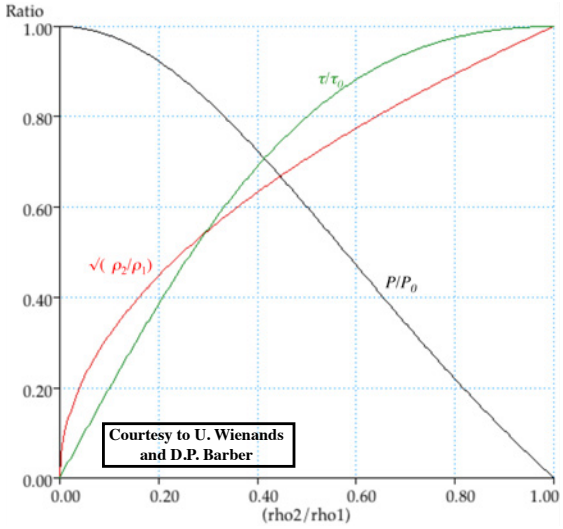


**Figure 2.12:** Polarization and synchrotron radiation losses depending on the ratio between the bending radius of the two halfs of the ring using the scheme sketched in Fig. 2.11. Figure is taken from [43].

An alternative approach to increase the polarization at high energies is to use "Siberian snakes" and "half-snakes" which rotate the spin field by 180° and 90° respectively. By decreasing the bending radius in one half of the ring and rotating the spin field by 180° after each half (Fig. 2.11), the polarization could be increased in exchange for additional synchrotron radiation losses due to the decreased bending radius in one half of the ring. Fig. 2.12 shows the gain in polarization and increase in synchrotron radiation depending on the ratio between the bending radius of the two halves of the ring. For further explanation of this scheme see [43].

## 2.2 General Layout and Geometry

One of the first steps in the design of a new accelerator is the geometry and general layout. This is especially important in the case of the LHeC, where the electron ring has to be installed on top of the already existing LHC which implies that the LHeC electron ring must follow the LHC geometry and symmetry. The layout of this first idealized LHeC ring developement in this thesis is described in Sec. 2.2.1 and 2.2.3. Furthermore, to allow for parallel *pp* and *ep* collisions, bypasses around the active *pp* experiments are needed. The different bypass options and geometries studied in the framework of this thesis are discussed in Sec. 2.2.4. Assuming an ideal electron ring following exactly the LHC geometry, the bypasses will either increase or decrease the circumference of this ring and the circumference will differ from the LHC circumference. Possibilities to adjust the electron ring circumference, including the effect of the bypasses, are presented in Sec. 2.2.2.

### 2.2.1 LHC symmetries

In the LHC two proton beams, i.e. beams of the same charge, collide, which implies that separate beam pipes and opposite magnetic fields have to be provided for the beam guidance. For this purpose, special superconducting magnets with two individual apertures have been designed [44]. In order to match the circumference of both beams, the two beams alternate between the inner and outer beam pipe and cross at the four experimental insertions illustrated in Fig. 2.13 (left). Averaging over the position of beam 1 and beam 2, one obtains the following symmetries shown in Fig. 2.13 (right):

- **Arcs**: One LHC arc would ideally consist of 23 equal arc cells with a length of 106.9 m taking the average between the two beams. Geometrically this is the case, but as more degrees of freedom were needed for the matching of the LHC dispersion suppressor (DS) [44], approximately one arc cell is used in addition for the DS. This leads to an arc length of $L(\text{LHC arc}) = 2452.23$ m which is smaller than 23 times the arc cell length of $23 \cdot L(\text{LHC arccell}) = 2458.7$ m.

- **Insertions**: The LHC hosts eight insertions in total, where the even insertions have a length of $L(\text{even insertions}) = 879.7$ m and the odd insertions a length of $L(\text{odd insertions}) = 880.6$ m. The different length of the even and odd insertions goes back to the design of LEP, where the high luminosity experiments - requiring

less space - were situated in the even insertions and the small angle experiments - needing more free space - were placed in the odd insertions [45]. As the LHC was built in the old LEP tunnel, it had to adopt the insertions length and the four fold LEP symmetry.

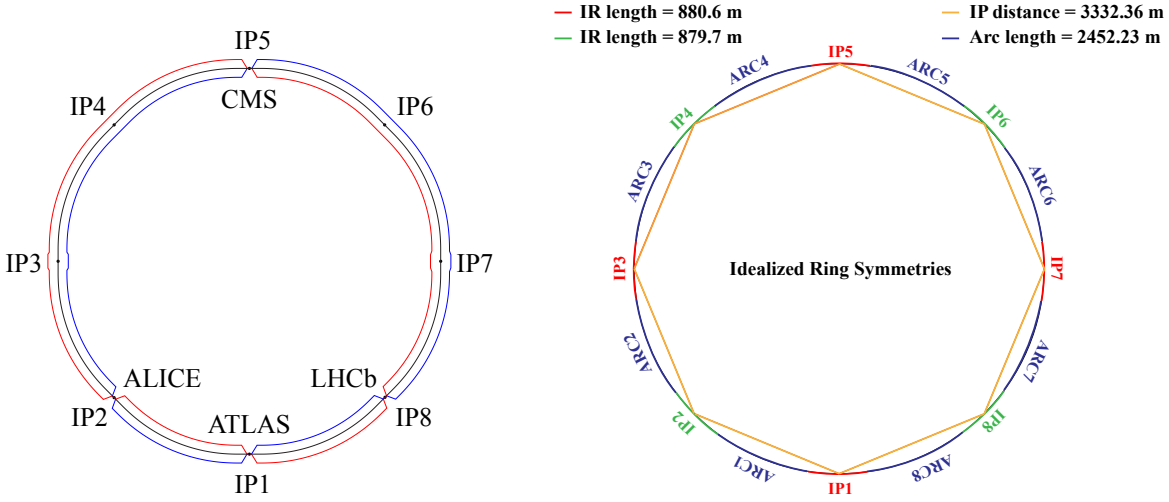


**Figure 2.13:** (left) Position of the two LHC proton beams. The distance between the beams is exagerated by a factor 2000. Both beams alternate between the inner and outer magnet aperture and cross at the four experimental insertions.
(right) LHC symmetries obtained by taking the average between beam 1 and beam 2.

### 2.2.2 LHeC electron ring circumference

Adding one bypass to an ideal electron ring lattice following exactly the LHC geometry will necessarily change its circumference and lead to a circumference mismatch between the LHC proton and LHeC electron ring. As the LHeC electron beam collides only in one point with the protons of the LHC, the circumferences can be either exactly matched or they can differ by a multiple of the LHC bunch spacing. It might occur that in the case of different circumferences the proton beam could become unstable due to beam-beam interactions with the electrons [46], [47]. In order to avoid possible performance limitations arising from this effect, the electron ring circumference is chosen to be equal to the LHC circumference in the current design. Two different possibilities are considered in order to achieve this:

1. Different bypass designs, e.g. one inner and one outer bypass, which compensate each other in length.

2. Compensation of the path length difference caused by the bypasses by a radial displacement of the electron ring to the inside or outside of the LHC in places where the two rings share the same tunnel.

### 2.2.3 Idealized ring

A first step in the LHeC electron ring design is to create a ring which follows the LHC proton ring, where the average between beam 1 and beam 2 is taken as reference. As

described in Sec. 2.2.4.2, this ring must be radially displaced by approximately 61 cm to the inside of the LHC in order to compensate the path length difference arising from the bypasses. Furthermore, to minimise the interference with the LHC elements, the electron ring is set 1 m above the LHC magnets. A representative cross section of the LHC tunnel with the electron ring indicated in red is shown in Fig. 2.1. In the following this ring is referred to as the Idealized Ring.
The main remaining conflicts with the LHC are the QRL service modules in the arc[2] and the DFBs [3] in the insertions. In the main arcs the QRL service modules have a length of 6.62 m and are installed at the beginning of each LHC arc cell. The insertions host a different number of DFBs with a varying placement and length. The idealised ring lattice, the construction of which is described in this section, is designed to avoid overlaps of magnet elements with all service modules in the main arcs. To show that it is possible to create an optics with no electron ring elements at the positions of the DFBs in the insertions, dispersion suppressors fulfilling this criterion were designed for IR2 and IR3 representatively for all even (Point 2, 4, 6, 8) and odd insertions (Point 1, 3, 5, 7). For simplicity, all straight sections are filled with a regular FODO cell structure which would have to be adapted at a later stage to the respective integration constraints.

### 2.2.3.1 Arc cell length

To adjust the beam optics to the regular reappearance of the service modules at the beginning of each LHC arc cell, the LHeC FODO cell length is chosen to be a multiple $n$ or sub-multiple $1/n$ ($n \in \mathbb{N}$) of the LHC arc cell length. In addition to the integration constraints, the cell has to provide the right emittance which is the case for a LHeC FODO cell length of half the LHC arc cell length, approximately 53.4 m (Sec. 2.3.1).

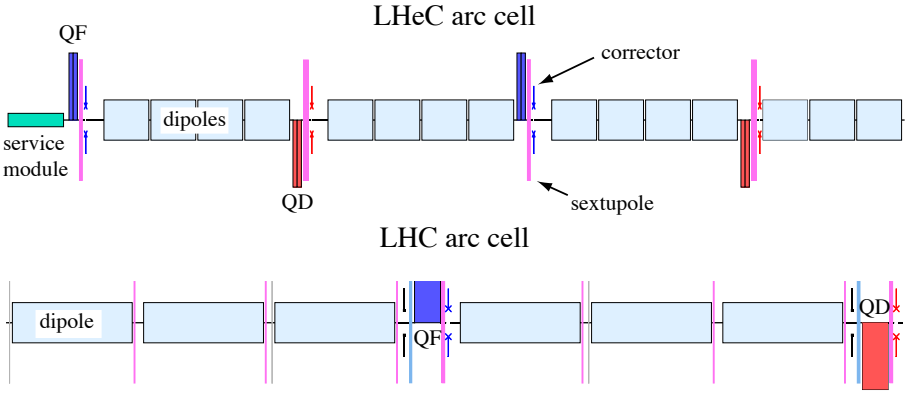


**Figure 2.14:** Layout of the LHeC arc cell in comparison to the standard LHC arc cell.

[2]QRL are the cryogenic installations in the LHC tunnel with the QRL service modules being the cryogenic connection between the superconducting machine and the cryogenic distribution line. The jumper connections of the service modules extend vertically above the LHC cryostat and into the path of the LHeC electron ring. There is enough space available to pass the service module, but no electron ring elements can be placed at this location. For further details see [10].

[3]The DFBs are the cryogenic electrical distribution feedboxes that feed the electric current (room temperature) into the cold mass. The DFBs are installed on the outer left and right in each insertion to supply the special quadrupoles of each insertion. For further details see [10].

As the LHC arc cell is symmetric, the best geometrical alignment with the LHC main arc would be achieved with an also symmetric layout of the LHeC cell. Because of the service modules, no elements can be placed in the first 6.9 m of two consecutive cells. If all cells had the same layout, another 6.9 m would be lost in the second FODO cell. This would result in additional unwanted synchrotron radiation losses as the energy loss in a dipole magnet is proportional to the inverse of the length of the dipole (Eqn. 2.7). In order to avoid this, the LHeC arc cell is a double FODO cell, symmetric in the positioning of the quadrupoles but asymmetric in the placement of the dipoles. The final LHeC FODO cell design is shown in Fig. 2.14 together with the standard LHC arc cell.

#### 2.2.3.2 Main dipoles

The bending angle in the arc cells and in the dispersion suppressors (DSs) is determined by the LHC geometry. Geometrically, the LHC DS starts at the end of the arc (E.ARC.12.B1 in Fig. 2.15) and ends at the long straight section (E.DS.L2.B1 in Fig. 2.15) and is used as "definition" for the DS in this chapter. With this definition the LHC DS consists of two

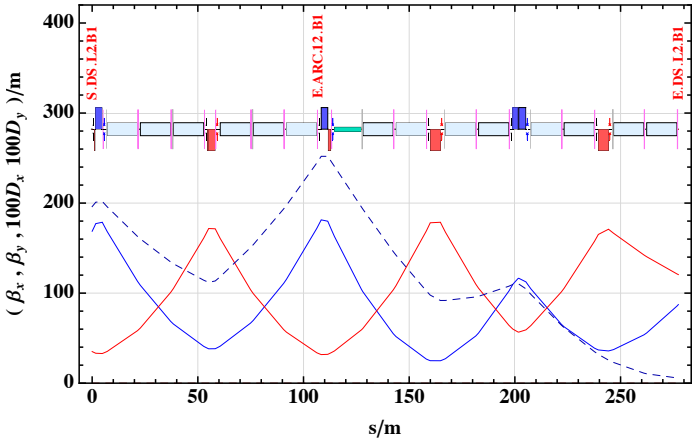


**Figure 2.15:** Optics and layout of the LHC dispersion suppressor.

cells. Applying the same conversion rule as in the arc (one LHC FODO cell corresponds to two LHeC FODO cells), the LHeC DS would then ideally consist of 4 equal cells with the same ratio between the LHeC DS and arc cell lengths as between the LHC DS and arc cell. For the LHC this ratio is 2/3, leaving the following choices for the number of dipoles in the arc and DS cell:

$$N_{\text{Dipole, arc cell}} = \frac{3}{2} N_{\text{Dipole, DS cell}} = 3, 6, 9, 12, 15 \ \ldots \tag{2.29}$$

A good compromise between a reasonable dipole length and optimal use of the available space for the bending is 15 dipoles per arc cell. The dipoles are then split up in packages of $3+4+4+4$ in one arc cell and $2+3$ in one DS cell. With the constraint that the electron ring should keep the same symmetry as the idealized LHC ring (see Fig. 2.13 (right)), i.e. an eightfold symmetry, the bending angle of the main dipoles is given by

$$\theta_{\text{MB}} = \frac{2\pi}{8 \cdot (23 \cdot 15 + 2 \cdot 4 \cdot 5)} \,. \tag{2.30}$$

#### 2.2.3.3 Module length

Beside the bending angle, the module length of the electron ring has to be matched to the LHC geometry taking the radial displacement into account, leading to slightly shorter electron ring modules compared to their proton ring equivalents. All module lengths are listed in Table 2.6.

| | **proton ring** | **electron ring** |
|---|---|---|
| arc celllLength | 106.9 m | 106.881 m |
| DSL length (even Points) | 172.80 m | 172.78 m |
| DSR length (even Points) | 161.60 m | 161.57 m |
| DSL length (odd Points) | 173.74 m | 173.72 m |
| DSR length (odd Points) | 162.54 m | 162.51 m |

**Table 2.6:** Proton and electron ring module lengths.
DSL=Dispersion Suppressor Left side, DSR=Dispersion Suppressor Right side

#### 2.2.3.4 Geometric fine adjustment

As described above, the bending angle and module length have been fixed to best fit the LHC geometry. Ideally the dipole length would be chosen as long as possible, but because of the asymmetry of the LHeC arc cell, the dipoles have to be shortened and moved to the right in order to fit the LHC geometry illustrated in Fig. 2.14 (top).
In the case of the dispersion suppressor the LHeC DS layout would ideally be similar to the LHC DS layout shown in Fig. 2.15, but has to be modified in order to avoid the DFBs in the DS region and to follow the LHC geometry. In the final design the dipoles are placed as symmetrically as possible between the regular arrangement of the quadrupoles. Fig. 2.16 shows the final dispersion suppressor layout.

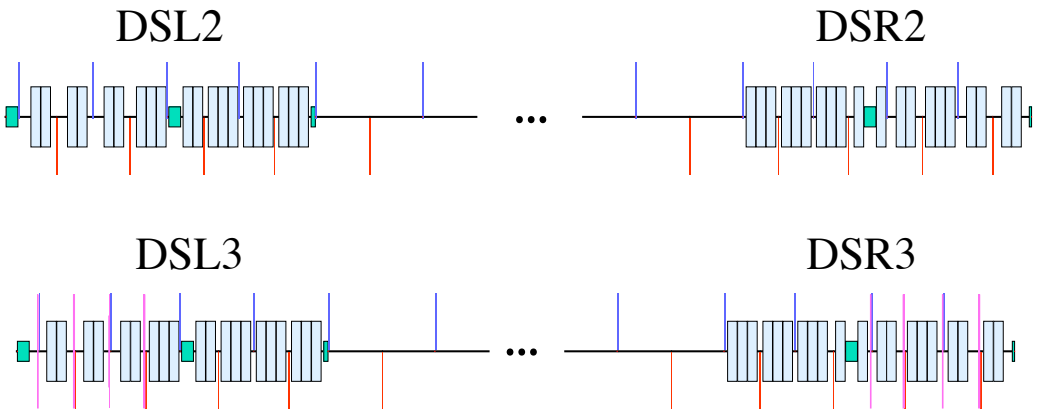


**Figure 2.16:** LHeC dispersion suppressor layout. The DFBs are shown in turquoise.
(top) Even Points (bottom) Odd Points

Using the design of the different modules presented in this section, the LHeC geometry follows almost exactly the ideal radial displacement of 61 cm in respect to the LHC and diverts only by a few centimetres from this ideal geometry (Fig. 2.17).

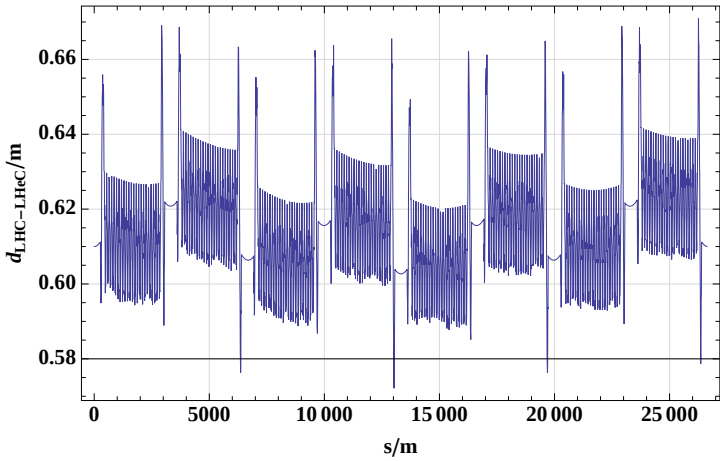


**Figure 2.17:** Radial distance between the LHC and the LHeC idealized ring.

### 2.2.4 LHeC bypasses

The current LHeC electron ring design foresees bypasses around the LHC experiments in Point 1 and Point 5. The main requirements for both bypasses are that all integration constraints are respected, synchrotron radiation losses are not significantly increased and that the change in circumference can be compensated. The present ATLAS and CMS cavern including the final bypass design highlighted in blue and green respectively are shown in Fig. 2.18. The different bypass options studied in this thesis are discussed in Sec. 2.2.4.1 and the final design presented in Sec. 2.2.4.2

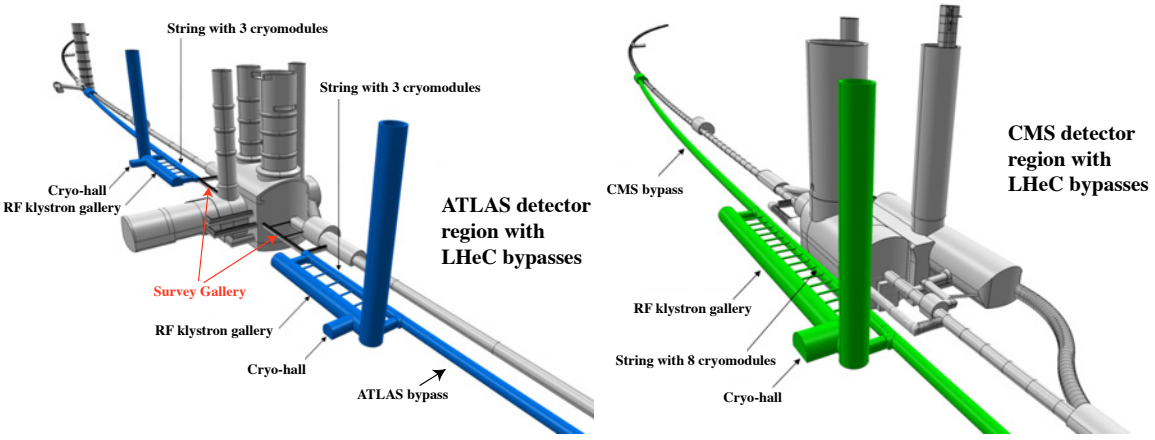


**Figure 2.18:** ATLAS (left) and CMS (right) cavern. The final bypass design is shown in blue and green respectively. Pictures are taken from [10].

#### 2.2.4.1 Bypass design

Three different options are considered as basic bypass designs with different advantages and disadvantages

**Vertical bypass:** In practice only vertically upward bypasses would be feasible in respect to integration as in the case of a vertically downward bypass the electron ring would have to cross the LHC elements and, in addition, 1 m of solid concrete floor. A vertically upward bypass would require a separation of about 20 to 25 m [48] and would feature the following advantages:

1. Vertical shafts are by a factor of 10 more expensive than horizontal tunnels [48]. The construction of additional vertical shafts could be avoided by building vertical bypasses and using the existing access shafts of ATLAS and CMS and thus reduce the tunnel costs.
2. In order to fully bypass the ATLAS cavern horizontally a separation of more than 80 m is required, while for a vertical bypass a separation of 20 to 25 m is sufficient in both cases (ATLAS and CMS).
3. Interference with only very little of the existing LHC equipment. Especially no crossing of the transport zone on the inside of the LHC tunnel.

and disadvantages

1. It would be necessary to remove the tunnel ceiling for several tenths of meters. It is questionable if the tunnel stability would allow such an intervention as the ceiling is already quite unstable in some parts of the current tunnel.
2. As the natural horizontal curvature of the ring cannot be employed, the necessary separation can only be achieved by additional vertical bends. To get an estimate for the length of such a bypass, the necessary separation of 20 to 25 m could be achieved with 5 to 5.5 standard LHeC cells accounting for a length of 550 to 600 m (Fig. 2.19). Including 100 m of straight section just above the cavern, the total bypass length would lie between 1.2 and 1.3 km. The long straight section at the IP would not be sufficient to host such a bypass.

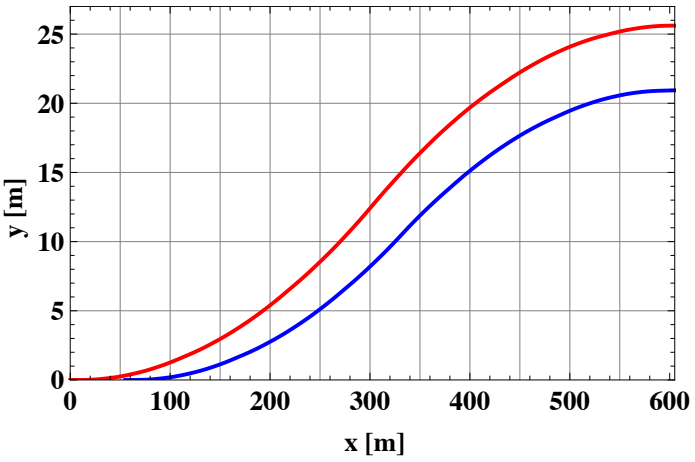


**Figure 2.19:** Left half of a vertical bypass constructed out of standard LHeC cells, where the bypass with 25 m separation is shown in red and with 20 m in blue.

The additional synchrotron radiation losses of a bypass constructed in this way would amount to approximately 1.1-1.2 MW. The emitted synchrotron radiation could represent a major challenge as it would increase the background in the detector, if not sufficiently shielded.

3. Creation of vertical dispersion, which implies a dispersion suppressor for both planes and probably a reduction of the polarization of the electron beam.

**Horizontal inner bypass:** A horizontal inner bypass around ATLAS would require a minimum separation of 39 m for a length of about 100 m, which could be in the extreme case still reduced to 33.5 m [49]. A possible layout of a bypass with a separation of approx. 39 m is shown in Fig. 2.20. In this version the bending angle

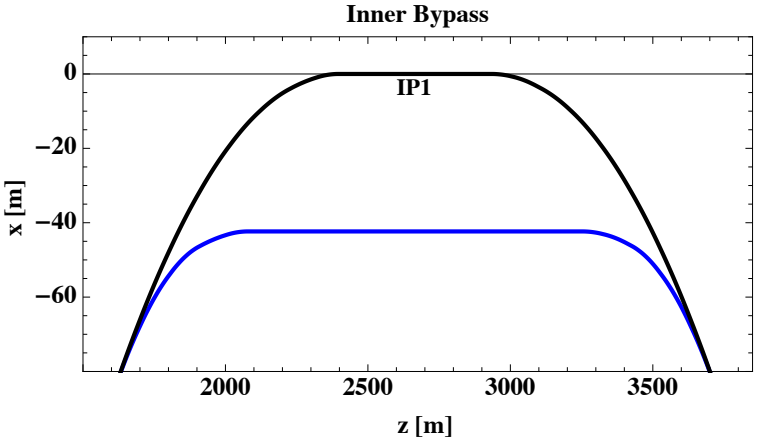


**Figure 2.20:** Inner Bypass ATLAS with a separation of 39 m.

of the dipoles has been doubled compared to the bending angle of the standard arc cell dipoles. The total length of the bypass is approx. 2 km with a long straight section of around 1 km in the center. The total radiation losses amount to about 3 to 4 MW. Similar values are expected for an inner bypass around CMS, but this option has not been studied in detail. The general advantages are

1. The increase in circumference due to an outer bypass could be compensated by an inner bypass
2. The bypass is completely decoupled from the LHC and would allow an almost complete construction during LHC operation.
3. One long dispersion free straight section for the installation of RF, wiggler(s) etc.

and disadvantages:

1. The LHeC electron ring crosses the transport zone on the inner side of the LHC tunnel for approximately 130 m.
2. The bending angle has to be increased, causing additional and harder synchrotron radiation losses. Furthermore, the direction of the synchrotron radiation is tangential to the beam direction and would therefore be emitted in the direction of the LHC tunnel.

**Horizontal outer bypass:** A horizontal outer bypass can be either constructed with additional bends in the same way as a vertical bypass or by inserting a straight section in the arc and using the existing curvature of the ring to obtain the necessary separation [50]. In this thesis, only the latter case with no additional bends has been studied as the necessary separation could be achieved with this method. The design without extra bends has the following advantages:

1. No crossing of the transport zone on the inside of the LHC tunnel.
2. No additional synchrotron radiation losses and no radiation emitted in the direction of the detector.
3. Dispersion free straight sections for the installation of RF, wiggler(s) etc.

and disadvantages:

1. Long bypasses due to the small bending angle.
2. Opening of the outer tunnel wall over several tenths of meters.

The cavern in Point 1 reaches far to the outside of the LHC, so that a separation of about 100 m would be necessary in order to fully bypass the experimental hall and therefore does not represent a feasible option. A detailed integration study [49], [51] revealed that it is possible to use the existing survey gallery shown in Fig. 2.18 (left), to reduce the separation to 16.25 m. For a bypass on the inside, a separation of about 39 m would be required, resulting in a bypass length of more than 2 km length. Therefore the outer bypass through the survey gallery represents the best option for Point 1. Due to the compact design of the cavern in Point 5, a separation of only about 20 m is needed to completely bypass the experiment on the outside. The separation in the case of an inner horizontal bypass or a vertical bypass would be the same or larger and therefore the horizontal outer bypass is also the preferred option.

#### 2.2.4.2 Final bypass design and adjustment of the ring circumference

Both bypasses in Point 1 and Point 5 require approximately the same separation, explicitly 16.25 m in Point 1 and 20 m in Point 5 [49], [51]. To obtain the necessary separation $\Delta_{\mathrm{BP}}$ a straight section of length $s_{\mathrm{BP}}$ is inserted into the lattice of the idealized ring (see Sec. 2.2.3) in front of the last two arc cells. The separation $\Delta_{\mathrm{BP}}$, the remaining angle $\theta_{\mathrm{BP}}$ and the inserted straight section $s_{\mathrm{BP}}$ are related by (Fig. 2.21):

$$\Delta_{\mathrm{BP}} = s_{\mathrm{BP}} \sin\theta_{\mathrm{BP}} \,. \tag{2.31}$$

As indicated in Fig. 2.21, the separation could be increased by inserting an S-shaped chicane including negative bends. The advantage of additional bends would be a possible

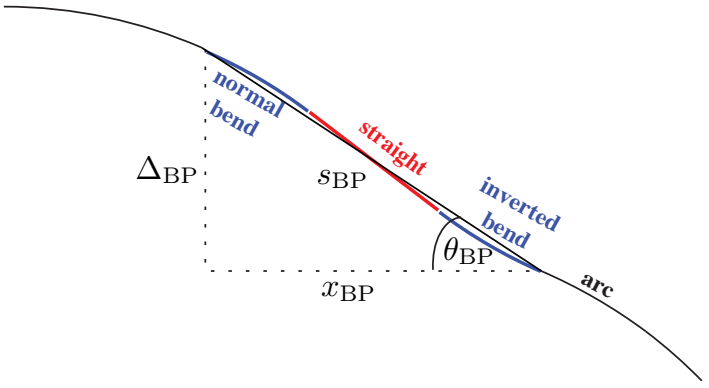


**Figure 2.21:** Horizontal outer bypass: a straight section is inserted to obtain the required separation. The separation can be increased by inserting inverted bends.

reduction of the bypass length and a faster separation of the electron and proton ring. On the other hand, the additional bends would need to be placed in the LHC tunnel, the straight sections of the bypass would be reduced and the synchrotron radiation produced by these bends would be emitted in the direction of the LHC tunnel. One could now consider shortening the bypass by inserting the straight section just one arc cell before the end of the arc and using negative bends to obtain the necessary separation, but the reduction of the bypass length is only a couple of 100 m and does not make up for the considerably shorter straight sections which are needed for the installation of additional equipment.
In summary, both bypasses can be constructed by inserting a straight section of the right length two arc cells before the end of the arc. The angle $\theta_{\mathrm{BP}}$ is then just given by the total angle over the two arc cells plus the angle of the dispersion suppressor, explicitly

$$\theta_{\mathrm{BP}} = (\underbrace{2 \cdot 15}_{\text{2 arc cells}} + \underbrace{20}_{\text{dispersion suppressor}}) \cdot \theta_{\mathrm{MB}}\,, \tag{2.32}$$

where $\theta_{\mathrm{MB}}$ is the bending angle of the LHeC dipoles. As both bypasses are outer bypasses, the only possibility to compensate the resulting increase in circumference is a radial displacement of the electron ring to the inside of the LHC (Sec. 2.2.2). Given the separation $\Delta_{\mathrm{BP}}$, angle $\theta_{\mathrm{BP}}$ and length of the inserted straight section $s_{\mathrm{BP}}$, the induced change in circumference is just the difference between $s_{\mathrm{BP}}$ and $x_{\mathrm{BP}}$, given by

$$\Delta s_{\mathrm{BP}} = s_{\mathrm{BP}} - x_{\mathrm{BP}} \overset{(2.31)}{=} 2\Delta_{\mathrm{BP}} \tan\left(\frac{\theta_{\mathrm{BP}}}{2}\right). \tag{2.33}$$

As for both bypasses the straight section is inserted at the same position in the arc, the total change in circumference from both bypasses is

$$\Delta s_{\mathrm{BP,tot}} = \Delta s_{\mathrm{BP,IP1}} + \Delta s_{\mathrm{BP,IP5}} \overset{(2.33)}{=} 2(\Delta_{\mathrm{BP,IP1}} + \Delta_{\mathrm{BP,IP5}}) \tan\left(\frac{\theta_{\mathrm{BP}}}{2}\right), \tag{2.34}$$

and can be compensated by a change in radius $\Delta R$ of the idealised ring by

$$\Delta s_{\mathrm{BP,tot}} = 2\pi\Delta R\,. \tag{2.35}$$

Taking the change in radius into account, the separation $\Delta_{\mathrm{BP}}$ has to be substituted by $\Delta_{\mathrm{BP,tot}} := \Delta_{\mathrm{BP}} + \Delta R$. The radius change and the total separation are then related by

$$\Delta R = \frac{\Delta_{\mathrm{BP}}}{\pi \cot\left(\frac{\theta_{\mathrm{BP}}}{2}\right) - 2}\,, \quad \text{with } \Delta_{\mathrm{BP}} = \Delta_{\mathrm{BP,IP1}} + \Delta_{\mathrm{BP,IP5}}\,, \tag{2.36}$$

yielding an ideal radius change of the idealized ring of

$$\Delta R_{\mathrm{ideal}} \approx 61 \text{ cm} \tag{2.37}$$

According to this reference, the idealized ring described in the preceding section Sec. 2.2.3 has been designed. As it is very difficult to obtain exactly this radius change at all positions of the ring, the idealized ring only follows approximately the reference value of 61 cm and the circumference increase of the bypasses is not precisely compensated. The fine adjustment of the circumference is then performed by changing the length of

| | Point 1 | Point 5 |
|---|---|---|
| total bypass length | 1303.3 m | 1303.7 m |
| separation $\Delta_{\mathrm{BP}}$ | 16.25 m | 20.56 m |
| dispersion free straight section $2(s_{\mathrm{BP}} + x_{\mathrm{BP}})$ | 172 m | 297 m |
| ideal radius change of the idealised ring $\Delta R$ | 61 cm | |

**Table 2.7:** Lengths characterising the bypasses.

the inserted straight section of the bypass in Point 5, where the necessary change can be calculated with Eqn. 2.33. Point 5 is chosen for the adjustment, as the bypass in Point 1 passes through the existing survey gallery fixing its geometry and thereby the separation. The final values for both bypasses are summarized in Table 2.7 and the geometry shown in Fig. 2.22.

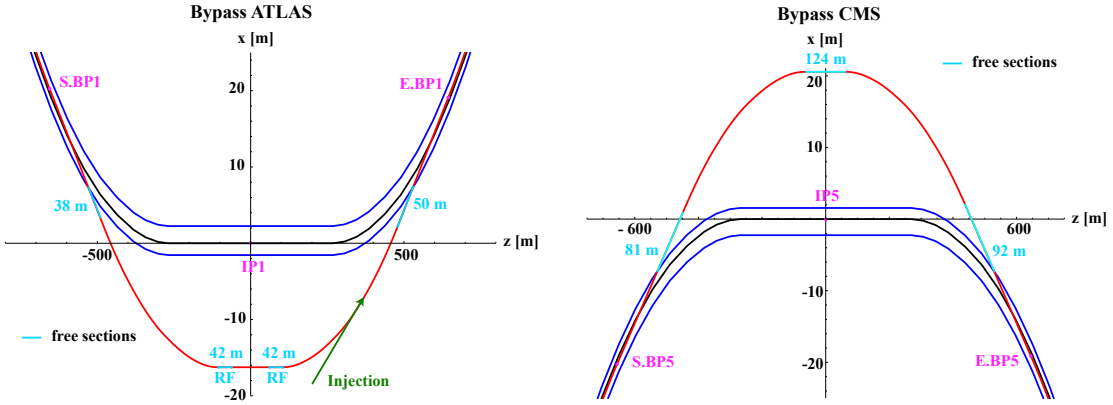


**Figure 2.22:** Final bypass design: The LHC proton ring is shown in black, the electron ring in red and the tunnel walls in blue. Dispersion free sections reserved for the installation of RF, wiggler(s), injection and other equipment are marked in light blue. Beginning and end of the bypass are marked with S.BP and E.BP.
(left) Bypass around Point 1 using the survey gallery. The injection is marked in green and is located in the right arc of the bypass.
(right) Bypass around Point 5. The cavern is completely bypassed.

## 2.3 Layout and Linear Optics

The optics of the electron ring lattice are strongly influenced by the geometrical constraints and the shortage of space in the LHC tunnel. The main interference with the LHC beside Point 1 and Point 5, which have to be bypassed, are the QRL service modules and DFBs in the tunnel, where no electron ring elements can be placed. The complete optics, which has been developed in the framework of this thesis except the interaction region optics at Point 2, consists of different building blocks, addressed in the corresponding sections: Sec. 2.3.1 describes the arc cell optics, Sec. 2.3.2 the insertion optics - except Point 2 which hosts the interaction region with a dedicated optics design (for the optics see [10]) - and Sec. 2.3.3 the bypass optics.

Furthermore, in order to facilitate the matching of the naturally flat electron beam to the round proton beam, the design parameters defined in the LHeC CDR [10] assume a fully coupled electron ring, leading to an emittance ratio of

$$\kappa = \frac{\epsilon_y}{\epsilon_x} = 0.5 \tag{2.38}$$

Different possibilities to create the coupling and match the beamsize of electron and proton beam at the IP are described in Sec. 2.4.3. In order to get an estimate for the emittances in the case of a fully coupled ring, but using only the optics of the uncoupled lattice, Eqn. 1.69 is used in this section:

$$\epsilon_x = \frac{\epsilon_{0x} J_x}{J_x + \kappa}, \qquad \epsilon_y = \frac{\epsilon_{0x} J_x \kappa}{J_x + \kappa} \text{ with } \kappa = \frac{\epsilon_y}{\epsilon_x}, \tag{2.39}$$

where $\epsilon_i$ are the emittances in the coupled and $\epsilon_{0i}$ the emittances in the uncoupled case. Note that this equation is only valid under the assumption of a vanishing vertical emittance in the uncoupled case ($\epsilon_{0y} = 0$), no vertical dispersion in both cases ($D_y = D_{y0} = 0$) and no change of the horizontal damping partition ($J_x = J_{0x}$).

### 2.3.1 Arc cell

As pointed out in Sec. 2.2.3.1, the LHeC arc cell length has to be a multiple or sub-multiple of the LHC FODO cell length in order to find a periodic optics solution respecting the non-interference constraint with the LHC QRL service modules. Furthermore, the synchrotron radiation losses and emittance of the electron beam are mainly determined by the choice of the arc cells representing the major part of the whole ring with dipoles and therefore non-vanishing dispersion.

As basic arc cell design a FODO cell has been chosen, as it features a high dipole filling factor compared to other standard cells like DBA or TME, and thus minimizes the synchrotron radiation losses, considered to be more crucial than a smaller emittance for which other cells like the DBA or TME cell are optimized. The horizontal emittance of a FODO cell is approximately given by Eqn. A.11 [14]

$$\epsilon_x(J_x) = \frac{(2 - \frac{3}{2}\sin^2(\frac{\phi}{2}) + \frac{1}{15}\sin^4(\frac{\phi}{2}))}{\sin^2(\frac{\phi}{2})\sin\phi} \frac{\theta^3}{J_x}, \tag{2.40}$$

and depends on the phase advance and bending angle of the dipoles and the horizontal damping partition, which as a first step is set fixed. In order to ensure the closure of the ring, the total dipole bending angle must equal $2\pi$ and thereby relates the total number of cells $N_{\text{arccell}}$ to the dipole bending angle $\theta$, i.e.

$$\theta = \frac{2\pi}{2 \cdot N_{\text{arccell}}}. \tag{2.41}$$

Consequently the emittance decreases with the number of arc cells. Independent of the cell length, the minimum emittance is reached for a phase advance of 136° (see Appendix A). In the case of the LHeC, a FODO cell length equal to the LHC FODO cell length leads to a too large emittance, as the minimum reachable emittance is $\epsilon_x(\kappa = 0.5) = 9.29$ nm, assuming the conditions delivering the smallest emittance, explicitly as long as possible

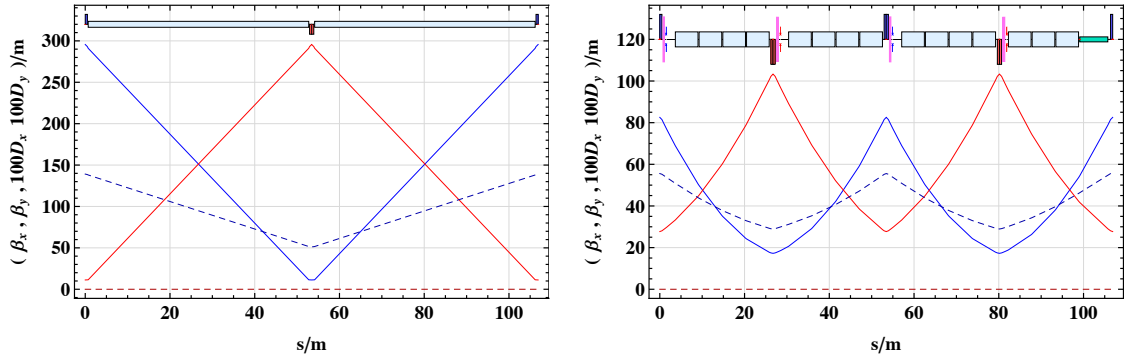


**Figure 2.23:** (left) Layout and optics of a LHeC arc cell with the same cell length as the LHC FODO cell ($L_{\text{FODOcell}} \approx L_{\text{FODO, LHC}} = 106.9$ m) and a phase advance of $\phi_{x/y} = 136°/136°$ delivering the smallest possible emittance for this cell.
(right) Final LHeC arc cell layout and optics with $L_{\text{FODOcell}} \approx \frac{L_{\text{FODO, LHC}}}{2} = 53.45$ m and a phase advance of $\phi_{x/y} = 90°/60°$.

dipoles, a phase advance of $\phi = 136°$ and $J_x = 2$. The optics and layout of this cell are shown in Fig. 2.23 (left).
Taking half the LHC FODO cell length as LHeC FODO cell length delivers a horizontal emittance which is slightly smaller than the design emittance of $\epsilon_x = 5$ nm including the effect of coupling and assuming realistic parameters, explicitly $J_x = 1.5$ and $\phi_{x/y} = 90°/60°$. Thus, half the LHC FODO cell length has been chosen as LHeC FODO cell length. All parameters of the final LHeC arc cell are summarized in Table 2.8 and the optics and layout are shown in Fig. 2.23 (right).

| | |
|---|---|
| cell length | 106.881 m |
| dipole fill factor[4] | 0.75 |
| phase advance per cell | 180°/120° |
| damping partition $J_x/J_y/J_e$ | 1.5/1/1.5 |
| horizontal emittance $\epsilon_{x0}$ | 5.79 nm |
| horizontal emittance $\epsilon_x(\kappa = 0.5)$ | 4.34 nm |
| vertical emittance $\epsilon_y(\kappa = 0.5)$ | 2.17 nm |

**Table 2.8:** Optics parameters of one LHeC arc cell with a phase advance of 90°/60° per FODO cell.

The dipole configuration of the LHeC arc cell is optimized to follow the LHC geometry as close as possible, leave enough space for the QRL service module at the beginning of each arc cell and still reach the highest achievable dipole filling factor under these conditions in order to minimize synchrotron radiation losses. It is not optimized for the smallest emittance, which would be achieved if the dipoles were moved as close as possible to the defocusing quadrupoles and the dipole length increased to fill the entire available space.

[4]The dipole fill factor is defined as $L_{\text{dipoles}}/L_{\text{cell}}$, where $L_{\text{dipoles}}$ is the length of all dipoles in the cell, i.e. in the case of a FODO cell it is two times the length of one dipole.

The phase advance of 90°/60° per FODO cell, hence 180°/120° per arc cell, has been chosen based on LEP experience and is considered to be very stable[5]. Again, the smallest emittance would theoretically be reached for a phase advance of 136° in both planes.
Last but not least, the damping partition has been chosen to minimize the aperture in the focusing quadrupoles for the uncoupled lattice resulting in a $J_x$ of approximately 1.5. In the case of a ratio of $\kappa = 0.5$, the minimum aperture requirements for the focusing quadrupole would be reached for $J_x = 1.31$. This is illustrated in Fig. 2.24, which shows the beam size in the focusing and defocusing quadrupole versus the horizontal damping partition $J_x$ for $\kappa = 0$ and $\kappa = 0.5$. Note that as the focusing and defocusing quadrupoles are built with the same circular aperture in most cases and the horizontal beam size is in general larger than the vertical, due to the non-vanishing dispersion in the horizontal plane, it is important to optimize the beam size at the focusing quadrupole where the horizontal beam size takes its maximum. Though in the case of strong coupling and furthermore large vertical dispersion, this choice of damping partition would have to be reconsidered.

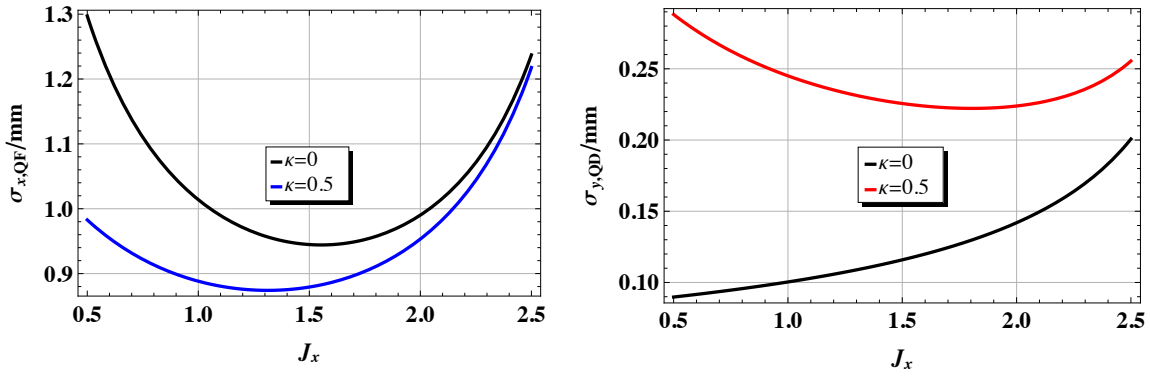


**Figure 2.24:** Horizontal beam size at the focusing quadrupole of the LHeC arc cell (left) and vertical beam size of the defocusing quadrupole of the LHeC arc cell (right) versus the horizontal damping partition $J_x$ for two different emittance ratios $\kappa = 0$ and $\kappa = 0.5$.

### 2.3.2 Insertions

Going back to the design of the LEP tunnel, all even and odd insertions respectively have the same length (see Sec. 2.2.1). For a proof of principle, a dispersion suppressor for the insertion in Point 2, representative for all even, and a dispersion suppressor in Point 3,

[5]The LEP orbit correction system and chromaticity correction scheme has originally been designed for a rather conservative phase advance of 60°/60° per arc cell. At a later stage, the phase advance has been changed to 90° in the horizontal in order to decrease the emittance and thus increase the luminosity. This change in phase advance led to a worse orbit correction, due to the not optimal phase advance between the BPMs whose positions had been optimized for 60°. That the BPM system was under-sampled anyway in LEP was also not helping the situation. Furthermore, the dynamic aperture was worse for a 90° phase advance, due to larger Hamiltonian driving terms arising from the incomplete sextupole families for a correction scheme adjusted to 90° phase advance. A compromise between the design optics with a pure 60°/60° phase advance and a 90°/90° optics were the 90°/60° which were in the end a very stable optics [52], [53]. For the LHeC with a sextupole scheme still free to chose and orbit correction system this might not be the optimal choice and should be reconsidered.

representative for all odd points, has been designed. The Long Straight Section (LSS) in each insertion has been filled with a simple FODO lattice with a phase advance of 90°/60°. In a later phase of the project a detailed design of each insertion would have to be done avoiding all LHC equipment.

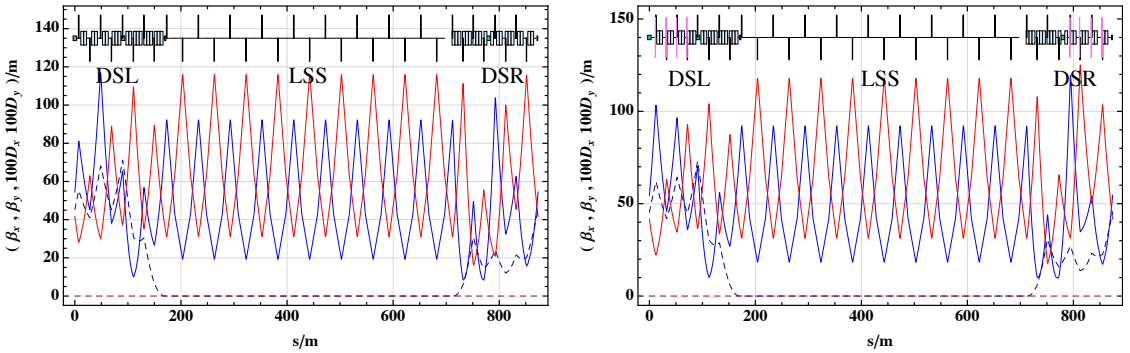


**Figure 2.25:** (left) Even insertions optics. (right) Odd insertion optics.

The insertion layout and optics of all even Points are shown in Fig. 2.25 (left) and of all odd Points in Fig. 2.25 (right). The dispersion suppressors for the even and odd insertions differ slightly in their length but have the same general layout. The dipole positions are optimized to allow for a placement as regular as possible of the 8 matching quadrupoles and to follow the LHC geometry as closely as possible. The Dispersion Suppressor on the Left side (DSL) is split into two dispersion suppressor sections, reaching from the first DFB to the second DFB and from the second to the beginning of the Long Straight Section (LSS). The quadrupoles are distributed equally in each section. In the case of the Dispersion Suppressor on the Right side (DSR), the quadrupoles are placed within equal distance from each other throughout the complete dispersion suppressor. This layout turned out to be better for the right side, due to the different arrangement of the DFBs. The dispersion is matched in all cases using 8 individual quadrupoles for the 8 degrees of freedom $(\beta_{x/y}, \alpha_{x,y}, D_x, D'_x)$. Well known standard dispersion suppressor schemes like the missing bend or half bend scheme could not be applied to the LHeC due to the fixed placement of the dipoles which is not in agreement with any of these schemes.

### 2.3.3 Bypasses

The bypasses are constructed geometrically by inserting a straight section into the idealized ring two arc cells in front of the end of the arc (Sec. 2.2.4.2). It is intended to install the RF cavities and wigglers as well as the injection and dump area in the long straight sections of the bypasses, all requiring dispersion free straight sections. Therefore, the dispersion has to be suppressed with dedicated dispersion suppressors on the left and right side of each straight section.

The resulting layout and chosen nomenclature are illustrated in Fig. 2.26. As dispersion suppressors for the straight section right after the arc (DSLSSL and DSLSSR) the last two arc cells are used, providing exactly the required 8 individual quadrupoles for matching the 8 optics parameters $\beta_{x/y}, \alpha_{x,y}, D_x, D'_x$. In the sections TLIR and TRIR, the same configuration of dipoles as in the idealised ring lattice is kept for geometric reasons. Among

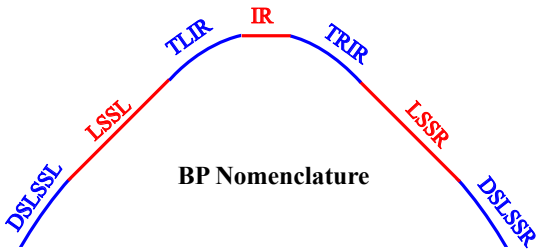


**Figure 2.26:** Bypass nomenclature: The straight sections are named Long Straight Section Left side (LSSL), Interaction Region (IR) - for the straight section parallel to the interaction region of the LHC - and Long Straight Section Right side (LSSR) and are marked in red. The dispersion suppressor sections are Dispersion Suppressor of LSSL (DSLSSL), Transfer line Left of IR (TLIR), Transfer line Right of IR (TRIR) and Dispersion Suppressor of LSSR (DSLSSR) and are indicated in blue.

this fixed arrangement of dipoles, 14 matching quadrupoles per side are placed as equally spaced as possible providing enough knobs to match the twiss functions and dispersion from one dispersion free section to the next. As in the case of the insertions, the straight sections are filled with a 90°/60° FODO cell lattice. The complete bypass optics in Point 1 and Point 5 are shown in Fig. 2.27.

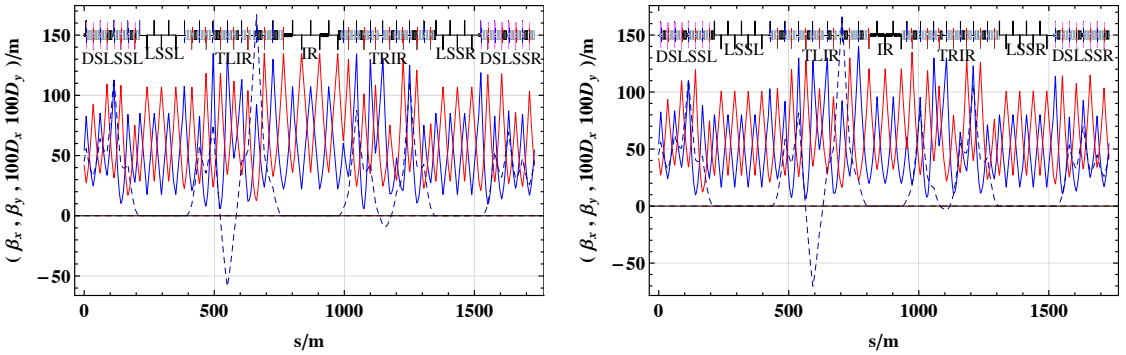


**Figure 2.27:** Bypass optics Point 1 (left) and Point 5 (right).

## 2.4 Beam Dynamics

In this section different beam dynamical aspects investigated in the framework of this thesis and relevant for the LHeC are presented. Sec. 2.4.1 gives a motivation for the LHeC working point used in this thesis, Sec. 2.4.2 describes a possibility to correct the chromaticity and off-momentum beta-beating, Sec. 2.4.3 discusses different possibilities of matching the flat electron beam to the round proton beam and the last section, Sec. 2.4.4 estimates the effect of the circumference errors on the damping partition and a possibility to correct small circumference errors.

### 2.4.1 Beam-beam effects and working point adjustment

The beam stability and performance of every circular accelerator strongly depends on its working point which has to be chosen with great care and the optimization of which is in most machines never finished as it influences the machine performance in many different ways. Therefore, only a rough guess of a good working point is given in this chapter based on the resonance diagram, the detuning of amplitude and the dynamic-beta due to beam-beam effects. Furthermore, only the HA option is considered, but the results can in general be almost directly transferred to the HL option.

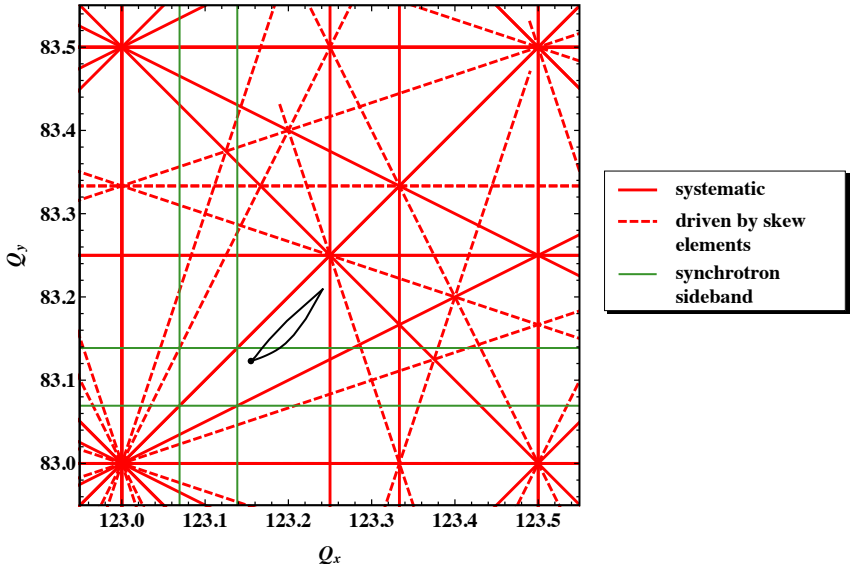


**Figure 2.28:** Resonance diagram for the LHeC HA option up to 4th order. The first two synchrotron sidebands of the integer resonance are indicated in green. Solid lines correspond to resonances associated with normal multipoles and dashed lines to resonances associated with skew multipoles. The detuning with amplitude due to head-on beam-beam is shown in black. Large amplitude particles experience the smallest tune-shift and small amplitude particles (the core of the beam) the largest tune-shift. The working point of $Q_x/Q_y = 123.155/83.123$ is indicated by a black dot.

The LHeC lattice, including the bypasses and the single interaction region, has no symmetries and thus all resonances are systematic. The detuning with amplitude and the resulting tune-spread due to beam-beam effects can be expressed analytically by Eqn. 1.130. Fig. 2.28 shows a possible working point for the LHeC of $Q_x/Q_y = 123.155/83.123$, which lies close to the linear coupling resonance. Taking only resonances up to 4th order into account, the full tune-spread due to head-on beam-beam can be accommodated in the resonance line free area close to the diagonal. The first and second synchrotron sidebands of the integer resonance are indicated in blue. For the chosen working point the first synchrotron sideband is avoided, but the second synchrotron sideband is crossed by high amplitude particles.
Furthermore, the tune is placed below the diagonal in order not to drive the resonance

$$2Q_x - 2Q_y = m \tag{2.42}$$

which can be excited by the octupole component of the beam-beam force [54][6].
The working points of lepton colliders are often optimized to explore the increase in luminosity due to the dynamic beta effect (Sec. 1.7.4.3). The dynamic beta, emittance and beam size depend on the tune $Q_0$ and incoherent beam-beam tune-shift $\Delta\nu_0$. The dependence on the tune is shown in Fig. 2.29 for the case of the LHeC HA option with an incoherent beam-beam tune-shift of $\Delta\nu_{0,x/y} = 0.086$. The working point of $Q_x/Q_y = 123.155/83.123$ is indicated by a red dashed line. For this choice of working

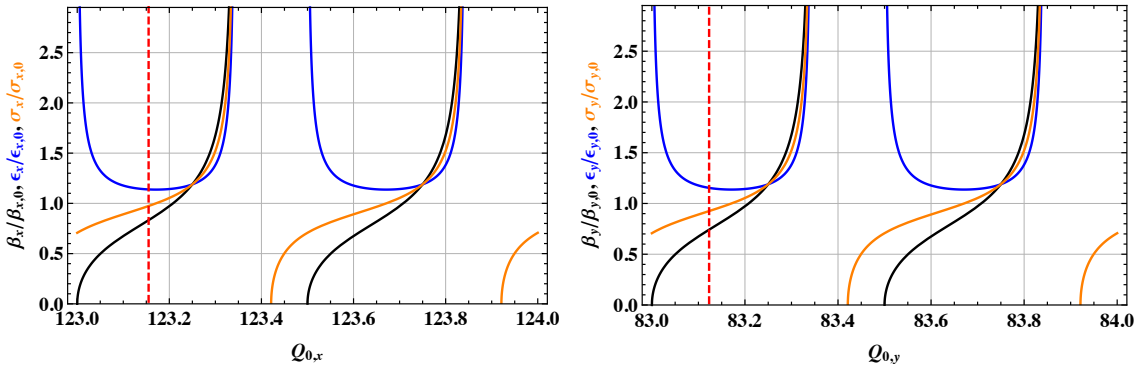


**Figure 2.29:** Horizontal (left) and vertical (right) dynamic beta, emittance and beam size for the HA option with an incoherent beam-beam tune-shift of $\Delta\nu_{0,x/y} = 0.086$. The working point of $Q_x/Q_y = 123.155/83.123$ is indicated as dashed red line.

point, the beta-function, emittance and consequently beam size at the IP only decrease slightly and the luminosity could be hence increased by moving the working point towards the integer or half integer resonance assuming the beam is still stable for this choice of working point. Note that in the current treatment of the dynamic beta effect, the effect of coupling necessary to match the beam spot size of proton and electron beam at the IP, is not considered, and could change the development of all three parameters.

### 2.4.2 Correction of chromatic aberrations

The theoretical background of the correction of chromatic aberrations in large colliders is summarized in Appendix C. In this section, the correction schemes for the LHeC developed in the framework of this thesis will be presented.
In order to design a suited correction scheme, the sections of the ring inducing the largest chromatic error have first to be identified. A measure for the induced chromatic error is the natural chromaticity, and the contributions to the same of the eight insertions for the HA and the HL option are listed in Table 2.9. In general, a relatively large contribution is expected from the low-beta insertion located at IR2 in the case of the LHeC due to the high beta-function at the strong final focus magnets. This is only the case for the vertical

[6]The resonance $2Q_x - 2Q_y = 0$ is known in connection with space-charge dominated machines as Montague resonance and the theory developed in this context has been applied to beam-beam effects in [54]. In the tune range considered for the LHeC higher orders of this resonance fulfilling the condition $2Q_x - 2Q_y = \pm 2q_0$ could be excited where $q_0$ is the integer part of the tune split. In order not to excite this resonance and under the assumption of equal linear beam-beam tune-shifts in the two planes, a working point below the diagonal should be chosen.

| | HA | HL |
|---|---|---|
| IR 1 | 6.9/5.5 | 6.5/6.1 |
| IR 2 | 5.2/18.3 | 9.9/9.3 |
| IR 3/7 | 3.2/2.7 | 3.1/3.1 |
| IR 4/6/8 | 3.2/2.7 | 3.0/3.0 |
| IR 5 | 7.0/5.7 | 6.7/6.4 |

**Table 2.9:** Relative contribution of the insertions to the natural chromaticity multiplied by a factor 100 , i.e. $\frac{\mathrm{d}Q_{x/y}}{\mathrm{d}Q_{x/y,\mathrm{tot}}} \cdot 100$, for the HA option with a total natural chromaticity of $-(144.1/136.2)$ and the HL option with $-(151.8/122.8)$.

plane of the HA option, which can be explained by having a look at the optics of the interaction region shown in Fig. 2.30.

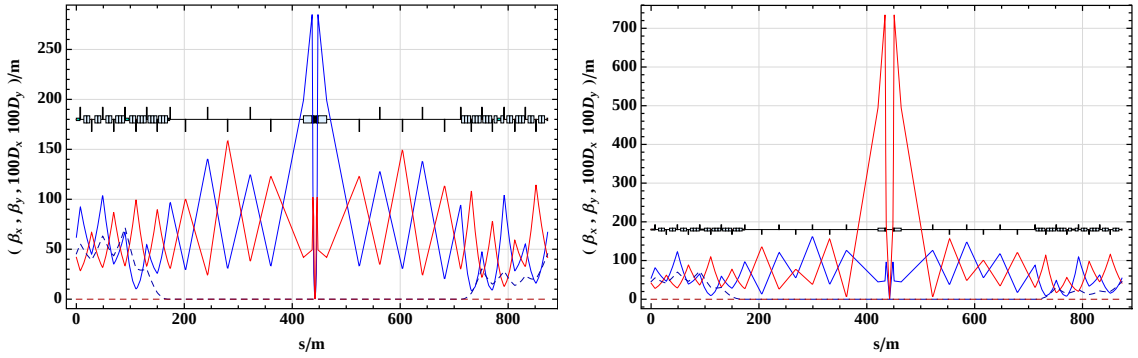


**Figure 2.30:** Optics of the HL option (left) and HA option (right).

In the case of the HL option (Fig. 2.30 (left)), the final focus magnets are located so close to the interaction region that the beta-function in the final focus triplet is very moderate in both planes. This leads to only a slightly higher contribution to the natural chromaticity compared to the other insertions and the resulting, rather equal distribution of the sources of chromatic errors, suggests a global correction of the chromatic aberrations where even an unsophisticated scheme with only two sextupole families could already be sufficient. In the framework of this thesis only the more challenging HA option has been studied. It is expected that the results obtained for this option represent a worst case scenario of the chromatic correction in the case of the HL option.

The HA option (Fig. 2.30 (right) and also previously Fig. 2.9 (left)), which is the option chosen for the CDR, has a QF-QD doublet in order to minimize the synchrotron radiation losses in the interaction region [10]. This choice and the small distance to the IP of only 6.2 m result in a horizontal beta-function in the final focus QF which is even smaller than in the following long straight section and explains the small contribution to the natural chromaticity in the horizontal plane. In the case of the vertical plane, the smaller $\beta^*$ and the larger distance to the IP lead to the high beta-function in the final focus QD typical for low-beta insertions and suggests a local correction with the two adjacent arcs described in Sec. 2.4.2.1. In order to test if the local correction indeed improves the correction of the chromatic aberrations, a global correction scheme has also been studied and a comparison of the two schemes is presented in Sec. 2.4.2.2

#### 2.4.2.1 LHeC chromaticity correction scheme

As described in Appendix C the off-momentum beta-beating and thus second order chromaticity can be corrected by using several sextupole families, where the number of families is determined by Eqn. C.15, and each family has to contain an even number of sextupoles in order to minimize the geometric aberrations. In the case of the LHeC arc cell, which is a double FODO cell with a phase advance of 90°/60° per FODO cell, the condition of Eqn. C.15 is fulfilled for two families in the horizontal and three in the vertical plane. The second condition of an even number of sextupoles per family yields that the number of arc cells, thus double FODO cells, containing sextupoles has to be divisible by 2 and 3. As the standard LHeC contains 23 arc cells and the arcs next to the bypasses only 19 arc cells the latter condition can be fulfilled in two different ways

- Option 1: not placing sextupoles in all arc cells
- Option 2: also placing sextupoles in the dispersion suppressor

A possible scheme using Option 1 is sketched in Fig. 2.31 (left) and using Option 2 in Fig. 2.31 (right).

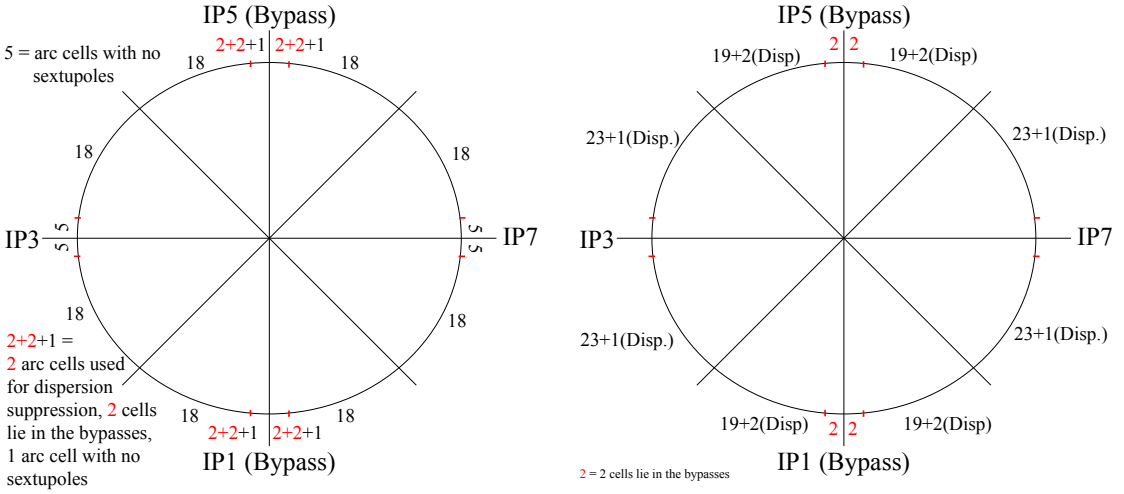


**Figure 2.31:** Chromaticity correction scheme for the LHeC.
(left) Option 1: sextupoles are only placed in the arcs.
(right) Option 2: sextupoles are also placed in the dispersion suppressor.

In general, it is considered to be better to place additional sextupoles in the dispersion suppressors and thus reduce the sextupole strength [55]. Therefore Option 2 has been chosen as the correction scheme for the LHeC. The downside of this choice is that the sextupoles in the dispersion suppressor are not exactly in phase with the other family members and have a stronger or weaker chromatic effect respectively due to the changed dispersion and Twiss function. This could increase the geometric aberrations, as not all sextupoles will have an exactly compensating partner and reduce the effectiveness of the scheme due to phase errors (Appendix C.3).
In the current scheme, the horizontal sextupole families are not completed in the arcs next to the bypasses, as it was considered to be more important to reduce the sextupole strength of the vertically focusing sextupoles by placing sextupoles in the dispersion suppressors

next to the bypasses - especially of the ones in the arc adjacent to the low-beta insertion - than to complete the families in the horizontal plane. This choice could increase the chromatic aberrations in addition, and in case the correction scheme turns out to be dynamically unstable, one would have to revise this choice.
For the local compensation of the low-beta insertion located at Point 2, the two adjacent arcs are used. This leads to a total number of 15 sextupole families, 5 families in the arc left of IP2 (Arc 1) and 5 in the arc right of IP2 (Arc 2) and 5 in the rest of the ring, explicitly in Arc 3 to 8.

#### 2.4.2.2 Matching the chromaticity correction scheme

The first step in matching a correction scheme, including the local correction[7] of a low-beta insertion, is to obtain suited starting values for the sextupole strengths. As described in Appendix C.2, the beta-beating is corrected by an up and down powering of the different sextupole families, where the sextupole strength, needed to correct the natural chromaticity, serves as reference value. This value is obtained by matching the natural chromaticity while the same strength is assigned to all focusing and defocusing sextupoles respectively. The next step is the local correction of the low-beta insertion at IP2 with the sextupoles in the two adjacent arcs. For the most efficient correction, the phase advance $\phi$ between the first sextupole of the correcting family and the IP has to be $2\phi = 0 \,\mathrm{mod}[\pi]$, where the effect of phase errors is not taken into account. In the horizontal plane, this condition must be already fulfilled for the first sextupole family, as then all following horizontally focusing sextupoles add up coherently due to the phase advance of $\frac{\pi}{2}$ per FODO cell (Eqn. C.20). In the vertical plane, with a phase advance of $\frac{\pi}{3}$, the sextupole family, of which the first member has a phase advance $\phi$ closest to $2\phi = 0 \,\mathrm{mod}[\pi]$, is chosen as correcting family (Eqn. C.22). As a first step of the actual matching of the local correction scheme, the phase advance is adjusted to the required $2\phi = 0 \,\mathrm{mod}[\pi]$, using a symplectic transfer matrix - referred to as "phasor" in this thesis - which changes only the phase advance but leaves all Twiss functions and the dispersion unchanged (Appendix B). The applied change in phase advance induces an unwanted change of the tune, which can be compensated in two different ways:

- Option A: changing the phase advance of the arc cells
- Option B: changing the phase advance of another insertion

Changing the phase advance of the arc cells would lead to a phase error which could reduce the efficiency of the correction scheme as discussed in Appendix C.3. Therefore, Option B is the more suited option. The easiest implementation is to change the phase advance of the FODO cells in the straight sections of IR3 and IR7, where IR3 and IR7 have been chosen, as Point 3 and Point 7 do not host an LHC experiment which needs to be bypassed. Furthermore, they lie opposite each other and thus change the optics symmetrically. As an actual change of the phase advance of the FODO cells would entail a

[7] In this context the term "local" is used for the correction of the beta-beating, originating from the low-beta insertion, with the sextupoles located in the two adjacent arcs. The term global refers to the correction of the beta-beating with all sextupoles in the ring.

rematch of the dispersion suppressors, the phase advance is also at first artificially changed with the phasor.
Until now, suitable initial conditions have been set for the sextupole strengths and phase advance constraints, but no actual matching performed. In a first matching step, the $W$-function (Eqn. C.12), being a measure for the off-momentum beta-beating, is matched to 0 at IP2 and IP1 and IP3 respectively, using the sextupole strength of the compensating family and the phase advance $\phi^{L/R}$ between the first family member and the IP as free parameters[8]. With this condition, the off-momentum beta-beating created by the low-beta insertion at IP2 is, as wanted, compensated by the sextupoles of the two adjacent arcs. Ideally, the beta-beating would be corrected by an up and down powering of the sextupoles, which would not change the linear chromaticity. In practice, the linear chromaticity changes slightly, because the matched sextupole strengths differ from the ideal ones. The difference between the ideal and the actual sextupole strength, and the resulting change of the linear chromaticity, is generated by the distortion caused by the sextupoles of one plane on the correction of the other plane and the effect of the sextupoles in the dispersion suppressors, which are not exactly in phase with the other members of their family and have, in addition, other Twiss and dispersion values. Furthermore, the beta-beating is not corrected in the rest of the ring, which yields a non-zero $W$-function at IP2, if the $W$-function is calculated for the complete ring and not just for the section from IP1 over IP2 to IP3. Therefore, in another matching step, using all 15 sextupole families and the phase advance $\phi^{L/R}$ as free parameters, the $W$-function is matched to 0 at IP2 and IP1 and IP3 respectively and, in addition, the linear chromaticity matched to $Q'_{x/y} = 2$. This, for now last step, leads to an optics as wanted, i.e. an optics with a local correction of the low-beta insertion, no change of the tune and an adjustment of the linear chromaticity to $Q'_{x/y} = 2$, but it still contains the artificial phasor element. As a next step, the phasor is removed and the optics rematched to the phase advances obtained for the lattice including the phasor. For the left and right side of IR2 the phase advance $\phi^{L/R}$ is matched by rematching the long straight section and the dispersion suppressor of the interaction region. In IR3 and IR7, the phase advance of the FODO cells is rematched, followed by a rematch of the dispersion suppressor and a final match of the complete insertion to the desired phase advance values. As the rematch of IR1, IR2 and IR3 slightly changes the Twiss parameters compared to the initial optics, the complete lattice is rematched in a final last step with the constraints $W(\text{IP2}) = W(\text{IP3}) = W(\text{IP1}) = 0$ and $Q'_{x/y} = 2$, using the strength of all 15 sextupole families as free parameters, where the strength values obtained for the optics including the phasor are taken as initial values. The detour of the optics including the phasor is taken, as it is usually quite time consuming to rematch an insertion. With the phasor, values for the phase advance can be obtained and also starting values for the strength of the sextupoles, which are very close to the final values. Both are important for a successful final matching.

[8]The matching constraint of $W_{x/y}(\text{IP1/IP3}) = 0$ could also be substituted by $W_{x/y}(\text{P}) = 0$ of any other point P in the lattice which lies closely before the first sextupole of Arc 1 and after the last sextupole of Arc 2 respectively.

#### 2.4.2.3 Comparison of the local correction with global correction schemes

In order to be able to judge if the local correction of the low-beta insertion improves the momentum-dependence of the lattice, the local correction scheme is compared to a global correction scheme. As reference for a global correction scheme, the lattice with the minimum number of sextupole families fulfilling the condition Eqn. C.15, which is necessary for a global beta-beating correction, has been used, i.e. 5 sextupole families - two horizontal and three vertical. The higher order chromaticities of this lattice have been calculated by the normal form analysis available in PTC and afterwards matched with MAD-X, first to $Q'_{x,y} = 2$, then to $Q'_{x,y} = 2$, $Q''_{x,y} = 0$ and last to $Q'_{x,y} = 2$, $Q''_{x,y} = 0$, $Q'''_{y} = 0$ taking advantage of the 5 free parameters. As the vertical plane is more challenging, $Q'''_{y}$ has been matched to 0 instead of $Q'''_{x}$. The sextupole strengths obtained for all four correction schemes are compiled in Table 2.10.

| | **local correction** | $\boldsymbol{Q''_x = Q''_y = 2}$ | $\boldsymbol{Q''_x = Q''_y = 0}$ | $\boldsymbol{Q'''_y = 0}$ |
|---|---|---|---|---|
| $m_{\mathrm{S_{F1}}}$ [1/m$^2$] | 0.449/0.474/0.409 | 0.453 | 0.433 | 0.433 |
| $m_{\mathrm{S_{F2}}}$ [1/m$^2$] | 0.445/0.632/0.472 | 0.453 | 0.477 | 0.478 |
| $m_{\mathrm{S_{D1}}}$ [1/m$^2$] | -0.478/-0.980/-0.390 | -0.445 | -0.390 | -0.250 |
| $m_{\mathrm{S_{D2}}}$ [1/m$^2$] | -0.402/-0.442/-0.377 | -0.445 | -0.528 | -0.524 |
| $m_{\mathrm{S_{D3}}}$ [1/m$^2$] | -1.032/-0.430/-0.387 | -0.445 | -0.415 | -0.559 |

**Table 2.10:** Normalized sextupole strengths for the four different correction schemes. The horizontally focusing sextupoles have a length of $L_{\mathrm{S_F}} = 0.35$ m and the vertically focusing sextupoles a length of $L_{\mathrm{S_D}} = 0.6$ m. In the case of the local correction scheme, the first value denotes the strength of the 5 sextupole families in Arc1, the second in Arc2 and the third the one of the sextupoles in the rest of the ring.

In order to see the effect of the local correction, the $W$-function for all four cases is compared in Fig. 2.32. In the horizontal plane, the $W$-function is globally reduced by the

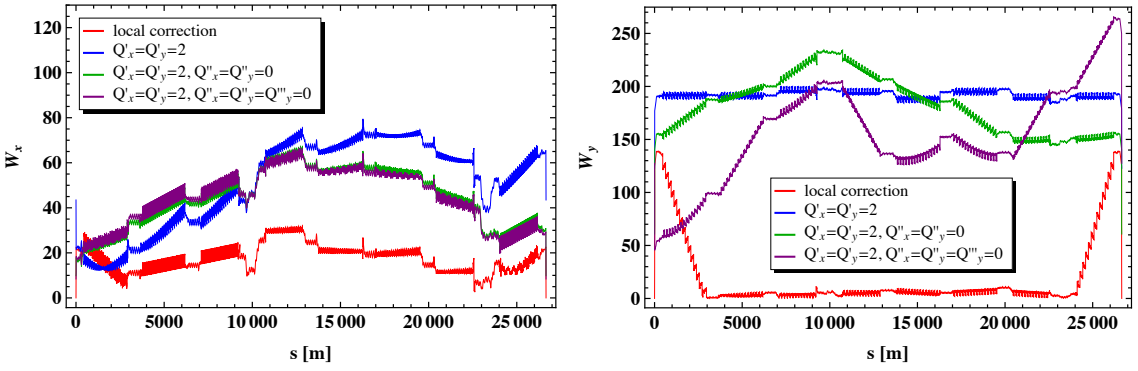


**Figure 2.32:** Horizonal (left) and vertical (right) $W$-function for all four correction schemes. IP2 is located at $s = 0$.

local correction, but does not show the typical strong decrease in the arcs adjacent to the low-beta insertion. This result is not surprising, as in the case of the horizontal plane, the chromatic contribution of the low-beta insertion lies in the same range as for the other insertions. In addition, the horizontal beta-function in the final focus doublet is not higher than in the following long straight section so that the chromatic error is not localized to

the final focus magnets, but distributed over the complete insertion as it is also the case for the other insertions. In the vertical plane, the local correction considerably reduces the $W$-function globally except in the two arcs adjacent to the IP. As expected, the $W$-function is decreased there in steps to almost 0. In contrast, the global correction schemes show a high $W$-function over the complete lattice. Furthermore, the variation of the $W$-function increases in the case of a global correction of $Q''_{x/y}$ and even more in the case of a correction of $Q'''_y$, as the correction of the higher order chromaticities is mainly achieved by a change of the off-momentum beta-beating and thus the $W$-function. At last, as only in the case of the local correction the $W$-function has been matched to 0 at the interaction point IP2, it also only vanishes in this case. This leads to a weaker momentum dependence of the

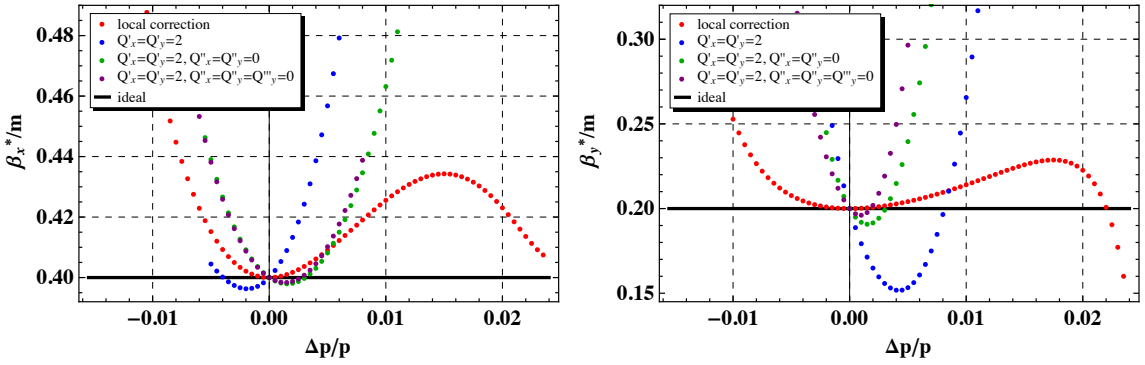


**Figure 2.33:** Horizonal (left) and vertical (right) $\beta^*$ at IP2. The Twiss parameters are calculated with PTC as MAD-X might not deliver correct results for large momentum deviations. Ideally, the beta-function would be independent of the momentum deviation, which is indicated by a black line.

beta-function at the IP in the case of the local correction which is illustrated in Fig. 2.33. Again, the improvement is much larger in the vertical plane where, as mentioned before, the off-momentum beta-beating of the low-beta insertion is successfully corrected with the two adjacent arcs, while in the horizontal plane, the local correction mainly consists of the vanishing $W$-function at the IP.

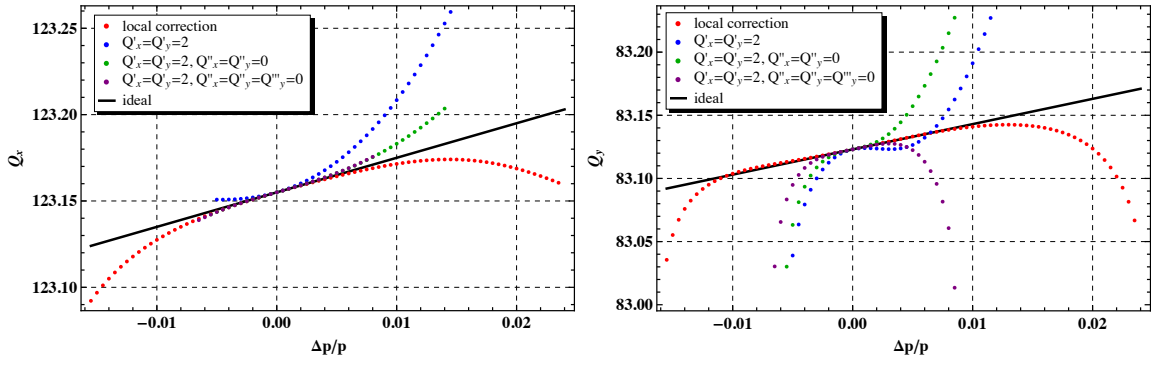


**Figure 2.34:** Dependence of the horizonal (left) and vertical (right) tune on the momentum deviation. The tune is calculated with PTC as MAD-X might not deliver correct results for large momentum deviations. Ideally, the chromaticity would be linear with $Q'_{x/y} = 2$, which is indicated by a black line.

In addition to the direct effect of the local correction on the off-momentum beta-beating, the correction should also, according to Eqn. C.8, theoretically reduce the dependence of the tune on the momentum, explicitly it should lead to a reduction of the second order chromaticity. The dependence of the tune on the momentum for all four correction schemes is shown in Fig. 2.34. The local correction scheme shows, as expected, an almost linear dependence of the tune on the momentum up to momenta almost as large as 10 times the rms momentum spread. Comparing the correction of only $Q'_{x,y} = 2$ with $Q'_{x,y} = 2, Q''_{x,y} = 0$, the second order term is corrected in trade of a third order term in the vertical plane. Similarly, the correction of the third order vertical chromaticity $Q'''_y = 0$ leads to the appearance of a stronger fourth order term.
Comparing the sextupole strengths of the different correction schemes (Table 2.10), the correction of the higher order chromaticities requires an increase of the sextupole strength of certain families, which could lead to a stronger detuning with amplitude. In all three cases, the already small detuning with amplitude does not increase and even decreases

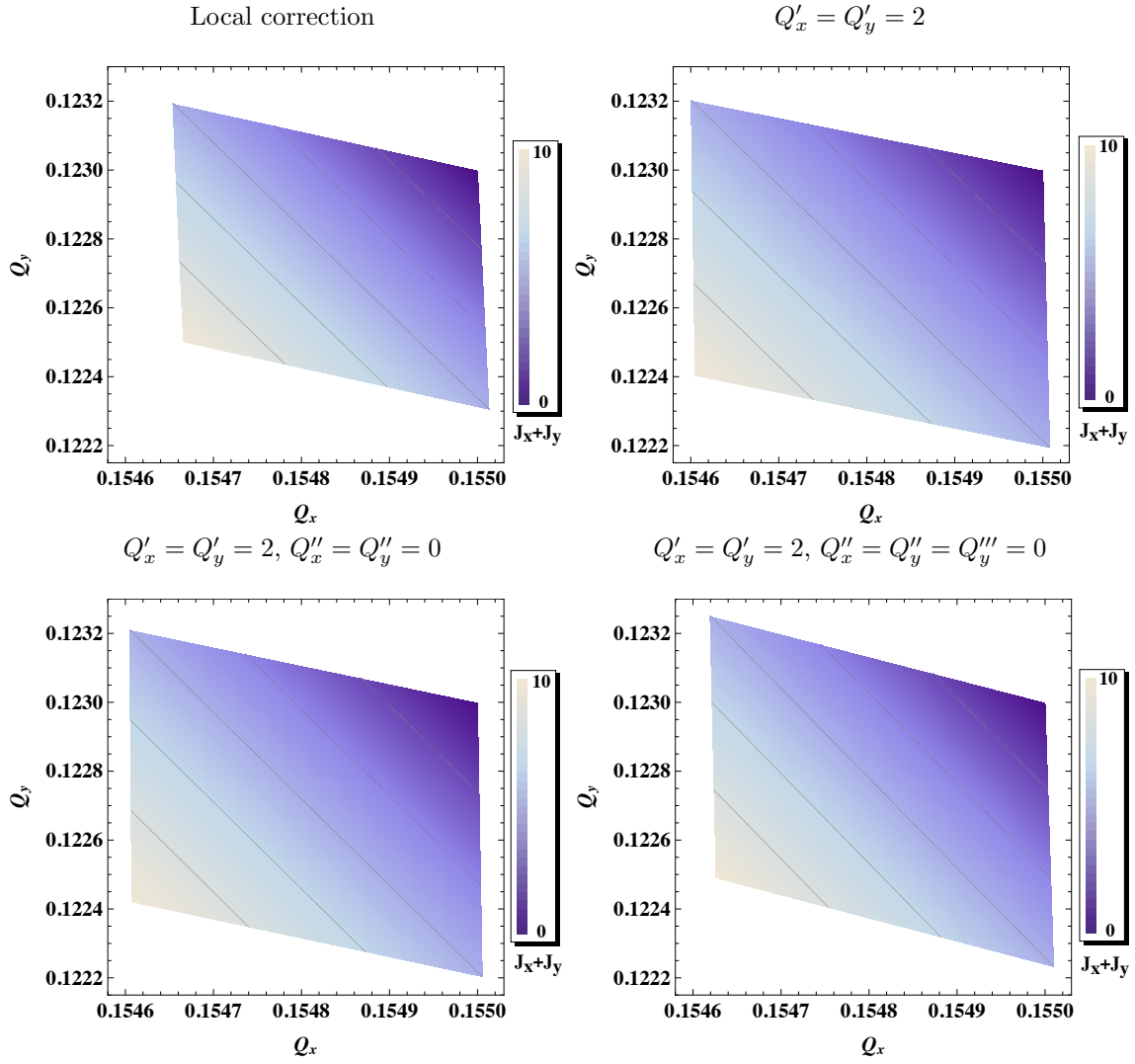


**Figure 2.35:** Detuning with amplitude until second order for the four different correction schemes and for actions $J_{x/y}$ with $0 < J_{x/y} < 5$. The anharmonicities $\alpha_{z,ij}$ have been obtained by using the normal form analysis available in PTC.

slightly in the case of the local correction (Fig. 2.35), where terms until second order in the horizontal and vertical action $J_{x/y}$ have been considered (Eqn. 1.87)

$$Q_z(J_x, J_y) \approx Q_z + \alpha_{z,10} J_x + a_{z,01} J_y + \frac{1}{2}\left(\alpha_{z,20} J_x^2 + 2\alpha_{z,11} J_x J_y + \alpha_{z,02} J_y^2\right),\ z = x, y\,, \quad (2.43)$$

and the anharmonicities $\alpha_{z,ij}$ have been obtained using the normal form analysis implemented in PTC.

At last, the dynamic aperture for on-momentum and for a momentum offset of one rms momentum spread $\pm\,(\Delta p/p)_{\mathrm{rms}} = \pm 0.0012$ of the four different lattices has been compared in order to investigate the effect of a momentum offset on the beam stability. The chosen stability criterion is, that the particle being tracked is not lost. The particle with the smallest amplitude, which is lost during the tracking, then determines the dynamic aperture. Particles with an initial amplitude of $n(\sigma_x \cos\phi + \sigma_y \sin\phi)$ have been tracked for 1024 turns using the tracking module of PTC and not including synchrotron radiation effects[9]. The parameter $n$ has been increased in steps of 0.1 and $\phi$ in steps of 2°. The small

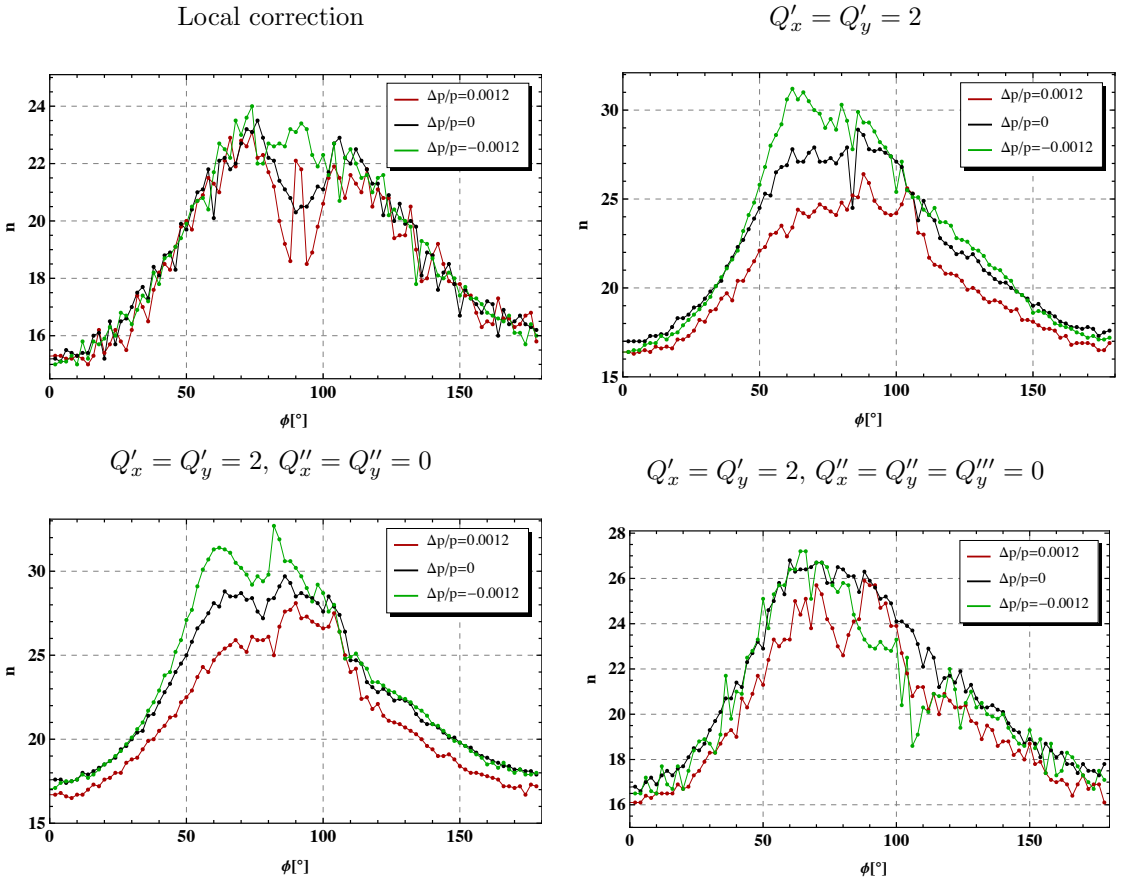


**Figure 2.36:** Dynamic aperture of the four correction schemes for $\Delta p/p = 0.0012$, $\Delta p/p = 0$ and $\Delta p/p = -0.0012$. The parameter $n$ and $\phi$ define the initial amplitude $a$ of the particle with $a = n(\sigma_x \cos\phi + \sigma_y \sin\phi)$. All particles have been tracked over 1024 turns. As expected, the dependence of the dynamic aperture on the momentum is reduced by the local correction scheme.

[9] The dynamic aperture is expected to increase if synchrotron radiation with its damping effect is included and thus the tracking without synchrotron radiation should deliver a lower limit on the dynamic aperture.

number of turns of 1024 corresponds to approximately four synchrotron radiation damping times at 60 GeV and is considered to be sufficient, so that all initial oscillations are damped after this time. The dynamic aperture of all four correction schemes is shown in Fig. 2.36. The global correction of only the linear and second order chromaticity exhibits a strong momentum dependence, which is then reduced in the case of the global correction of the third order chromaticity. Compared to all three global correction schemes, the local correction features the least momentum dependence and thus, as desired, a comparable beam stability for on- as well as off-momentum particles. The absolute values of the dynamic aperture are sufficient in all cases, but decrease in the case of the local correction and with the global correction of the higher order chromaticities. This is probably due to the presence of one stronger sextupole family. The comparison of the absolute values should be taken with caution, as the lattices are all matched to the working point of $Q_x = 123.155$, $Q_y = 83.123$ chosen in Sec. 2.4.1, which is not optimized for dynamic aperture studies, but well enough suited to investigate the momentum dependency of the dynamic aperture being the aim in this section.

### 2.4.3 Coupling and matching electron and proton beam size at the IP

Experiences from HERA show that it is essential to match the beam sizes of the proton and electron beam at the interaction point in order to avoid a reduction of the proton beam lifetime [37]. As the proton beam parameters are fixed by the parameters required for LHC p-p physics, the only possibility to adjust the beam size is to change the interaction region optics. For the current interaction region design an optics with a ratio of 4:1 between the horizontal and vertical proton $\beta^*$, and thus horizontal and vertical beam size, has been matched [10]. In this thesis, three different possibilities to achieve an electron beam size matched to the proton beam size of the current interaction region design have been studied, which are presented in the three subsections of this section. For all options, the proton beam optics are assumed to be fixed. As electron beam optics only the HA option, considered to be the preferred option, has been studied, whereas the same methods could be applied to the HL option.

#### 2.4.3.1 Global coupling in the complete ring

Global coupling can be obtained by simply introducing one skew quadrupole at any position in the ring. If the skew quadrupole is placed in a dispersion free region, only the betatron motion is coupled. Vertical emittance is then generated by betatron coupling in dipoles. The placement in a region with horizontal dispersion results in coupling of the betatron as well as dispersive part, and vertical emittance is in addition generated by vertical dispersion in dipoles. The placement of the skew quadrupole in a dispersion free region is in general preferable, as no change of the dispersion suppressors is required in this case. In both cases, the Twiss parameters in the interaction region are changed due to the coupling. If the change is unacceptably large, a coupling correction scheme or matching section including skew quadrupoles would have to be installed around the interaction region.

As an example for the case of a skew quadrupole in a dispersion free region, one skew quadrupole of 0.5 m length has been inserted in the long straight section of Point 2,

| | $\delta = 0$ | $\delta = -0.0022$ |
|---|---|---|
| $k_{\text{skew}}$ [1/m] | 0.014 | 0.010 |
| $\epsilon_1$ [nm] | 5.8 | 4.1 |
| $\epsilon_2$ [nm] | 2.9 | 2.0 |
| $\epsilon_3$ [$\mu$m] | 5.0 | 7.5 |
| $J_1$ | 1.0 | 1.5 |
| $J_2$ | 1.0 | 1.2 |
| $J_3$ | 2.0 | 1.3 |

**Table 2.11:** Equilibrium emittances and damping partition numbers calculated with MAD-X for the case of one skew quadrupole of 0.5 m length inserted in the dispersion free region at Point 2 for on-momentum and off-momentum yielding $J_1 = 1.5$.

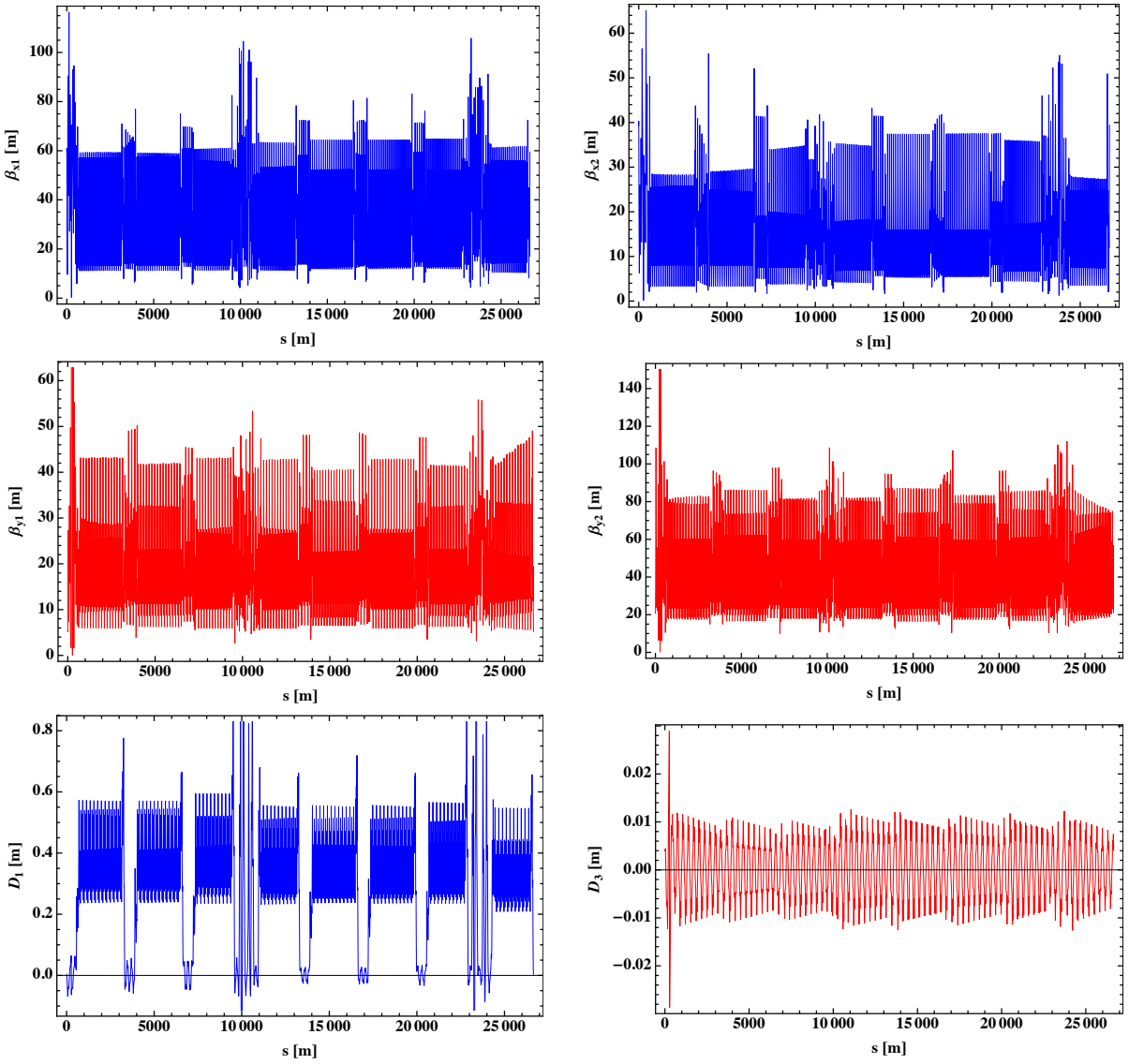


**Figure 2.37:** Ripken parameters for the case of one skew quadrupole inserted in the dispersion free region at Point 2 for on-momentum and including synchrotron radiation.

and its strength adjusted to yield a ratio of 2:1 between the equilibrium emittances $\epsilon_i$, defined in Eqn. E.11 of mode 1 and mode 2 respectively[10]. Table 2.11 summarizes the results obtained with MAD-X for zero momentum offset $\delta$ - so on-momentum - and for a momentum offset yielding the design value of $J_1 = 1.5$ as set in the CDR [10]. The second case of an adjustment to $J_1 = 1.5$ serves to show that the damping partition and emittance ratio can be changed by adjusting the strength of the skew quadrupole and the momentum offset.

In the case of no synchrotron radiation and no momentum offset, no vertical dispersion is created by the inserted skew quadrupole. Both the synchrotron radiation and the momentum offset, result in a change of the closed-orbit and therefore, in the case of coupling, a non-vanishing vertical dispersion. Nevertheless, the vertical dispersion due to the changed closed-orbit is expected to be small. Exemplary Fig. 2.37 shows the Ripken parameters [15] $\beta_{kj}$, $D_1$ and $D_3$ along the ring for the case of $\delta = 0$ and $k_{\text{skew}} = 0.014\ \frac{1}{\text{m}}$, including the effect of synchrotron radiation, where the index $k = 1, 2, 3$ of $\beta_{kj}$ refers to the plane $x$, $y$, $z$ and the index $j = 1, 2, 3$ to the eigen-mode, $D_1$ is the horizontal and $D_3$ the vertical dispersion. As expected, the vertical dispersion is small compared to the horizontal one.

As an example for the second case of a skew quadrupole in a dispersive region, one skew quadrupole of 0.5 m length has been inserted in the section TLIR of the bypass around Point 5. Table 2.12 summarizes the rms emittances and damping partition numbers calculated with MAD-X for on-momentum and for a momentum offset yielding $J_1 = 1.5$ and Fig. 2.38 shows the Ripken parameters for $k_{\text{skew}} = 0.0077\ \frac{1}{\text{m}}$ and on-momentum including the effect of synchrotron radiation. For the on-momentum case $J_2$ differs from 1.0 due

| | $\boldsymbol{\delta = 0}$ | $\boldsymbol{\delta = -0.00175}$ |
|---|---|---|
| $k_{\text{skew}}$ [1/m] | 0.0077 | 0.0077 |
| $\epsilon_1$ [nm] | 6.6 | 4.5 |
| $\epsilon_2$ [nm] | 3.3 | 2.3 |
| $\epsilon_3$ [$\mu$m] | 7.0 | 23.5 |
| $J_1$ | 1.0 | 1.5 |
| $J_2$ | 1.5 | 2.1 |
| $J_3$ | 1.5 | 0.4 |

**Table 2.12:** Equilibrium emittances and damping partition numbers calculated with MAD-X for the case of one skew quadrupole of 0.5 m length inserted in the dispersive region TLIR of the bypass around Point 5 for on-momentum and off-momentum yielding $J_1 = 1.5$.

to the non-zero vertical dispersion. Furthermore, an adjustment of $J_1$ leads to a small $J_3$ and therefore a large emitance $\epsilon_3$ of the third mode. In general, the emittances are larger than for the previous case where the skew quadrupole was located in a non-dispersive section which can be explained by the increase of the curly H-function due to the vertical dispersion in the dipoles.

[10] The emittances of mode 1 and mode 2 respectively correspond to the horizontal and vertical emittance in the uncoupled case.

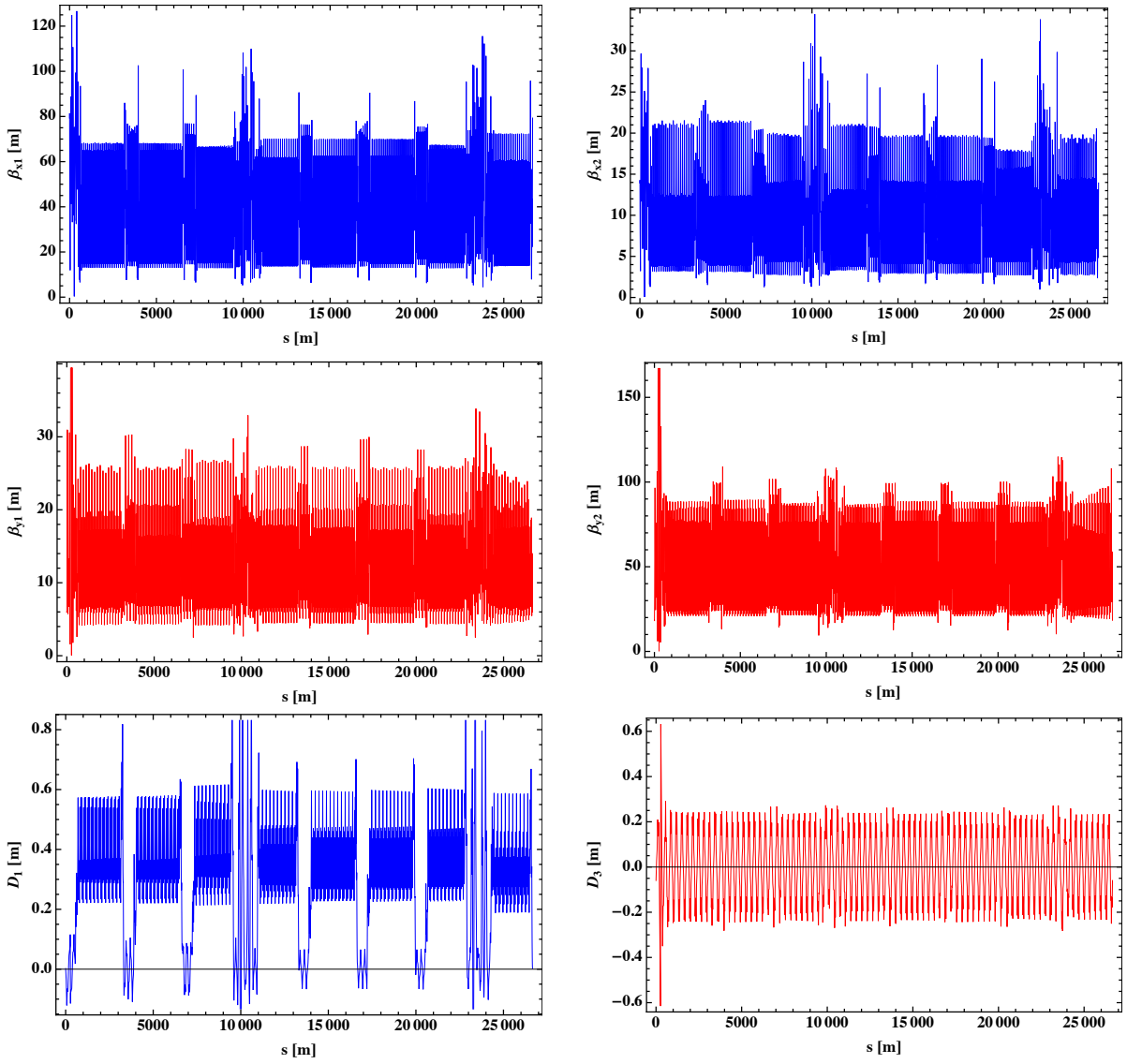


**Figure 2.38:** Ripken parameters for the case of one skew quadrupole inserted in the dispersive region TLIR of the bypass around Point 5 for on-momentum and including synchrotron radiation.

### 2.4.3.2 Decoupled interaction region using two times four skew quadrupoles.

The adjustment of the emittances by introducing global coupling, in particular also in the interaction region, discussed in the preceding section implies that a coupling correction or matching section including skew quadrupoles is needed around the interaction region in order to match the electron beam size to the proton beam size at the IP. Therefore, the second possibility considered and presented in this section is to create coupling with skew quadrupoles on one side of the IP (right side) and correct it on the other side (left side) with skew quadrupoles, so that the region around the interaction point is decoupled. For small perturbations, a correction scheme can be calculated using perturbation theory, but as will be shown later in this section, fails for larger skew quadrupole strength necessary to achieve the desired emittance ratio of 2:1. The theoretical background is outlined in Appendix F.

In first order, the difference $Q_x - Q_y = m$ and the sum resonance $Q_x + Q_y = m$ can be excited. The contribution of one skew quadrupole to the sum resonance is given by Eqn. F.8:

$$K_s = \kappa_i e^{i\psi_i}, \text{ with } \psi_i = \Phi_x(s_i) + \Phi_y(s_i)\,, \tag{2.44}$$

and to the difference resonance by Eqn. F.9

$$K_d = \kappa_i e^{i\varphi_i}, \text{ with } \phi_i = \Phi_x(s_i) - \Phi_y(s_i) \tag{2.45}$$

with

$$\kappa_i = \frac{N_i}{2\pi\sqrt{\beta_x(s_i)\beta_y(s_i)}} \tag{2.46}$$

and $N_i$ the integrated quadrupole strength and $\Phi_{x/y}$ the phase advance in the horizontal and vertical plane. The total contribution from different quadrupoles is then just given by the sum of all contributions:

$$K_s = \sum_i \kappa_i e^{i\psi_i}, , \tag{2.47}$$

$$K_d = \sum_i \kappa_i e^{i\varphi_i}\,. \tag{2.48}$$

As the LHeC working point of $Q_x/Q_y = 123.155/83.123$ is placed close to the difference resonance (Fig. 2.28), it is best to produce the required coupling with an arrangement of skew quadrupoles, resulting in a compensation of the difference resonance and an excitation of the sum resonance, in order to ensure the stability of the beam. This can be achieved by four skew quadrupoles on each side of the IP grouped in two pairs, Q1/Q2 and Q3/Q4, where each pair is orthogonal in the case of the sum resonance, i.e. $\Delta\psi = \pi/2$ and each quadrupole has a difference resonance compensating partner in the other pair i.e. $\Delta\varphi = n \cdot \pi$. If $\Delta\varphi = 2n \cdot \pi$ the quadrupoles compensating each other must have opposite strength and equal strength for $\Delta\varphi = (2n+1) \cdot \pi$. For the LHeC, a scheme with $\Delta\psi = \pi/2$ and $\Delta\varphi = 0$ illustrated in Fig. 2.39 has been chosen, as in this case all quadrupoles could be placed in the long straight section around IP2.

$$\begin{aligned}
\Delta\varphi &= (\Phi_x(s_2) - \Phi_y(s_2)) - (\Phi_x(s_1) - \Phi_y(s_1)) \\
&= (\Phi_x(s_4) - \Phi_y(s_4)) - (\Phi_x(s_3) - \Phi_y(s_3)) \\
\Delta\psi &= (\Phi_x(s_2) + \Phi_y(s_2)) - (\Phi_x(s_1) + \Phi_y(s_1)) \\
&= (\Phi_x(s_4) + \Phi_y(s_4)) - (\Phi_x(s_3) + \Phi_y(s_3))
\end{aligned}$$

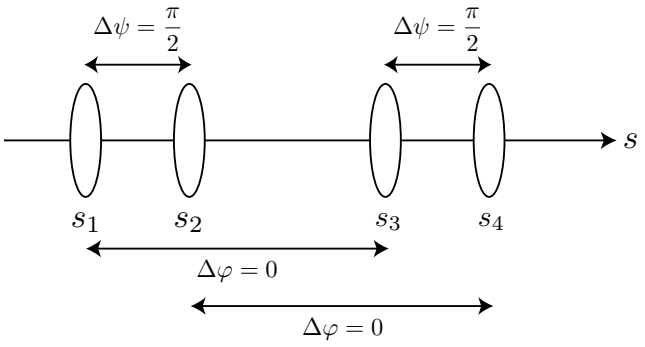


**Figure 2.39:** Excitation of the sum resonance and compensation of the difference resonance with four skew quadrupoles.

With this compensation scheme, the condition for the compensation of the difference resonance becomes

$$K_d = (\kappa_1 + \kappa_3)e^{i\varphi_1} + (\kappa_2 + \kappa_4)e^{i\varphi_2}\,, \tag{2.49}$$

where $\kappa_1 = -\kappa_3$ and $\kappa_2 = -\kappa_4$, and the condition for the orthogonality of each pair in the case of the sum resonance

$$K_s = (\kappa_1 + e^{i\frac{\pi}{2}}\kappa_2)e^{i\psi_1} + (\kappa_3 + e^{i\frac{\pi}{2}}\kappa_4)e^{i\psi_3}\,. \tag{2.50}$$

In reality, these conditions can never be exactly met. In order to have an automatic compensation of the difference resonance, the constraint on the phase $\Delta\varphi = 0$ between the quadrupoles compensating each other is a "strong constraint", while the orthogonality of the pairs, thus on the phase $\psi = \pi/2$, is only a "weak constraint".
To fulfil the condition of $\Delta\varphi = \Phi_x - \Phi_y = 0$ between the compensating pairs, one has to find four positions of the quadrupoles with the same value of $\varphi$. These four positions are indicated in Fig. 2.40 with black lines. The skew quadrupoles on both sides of the

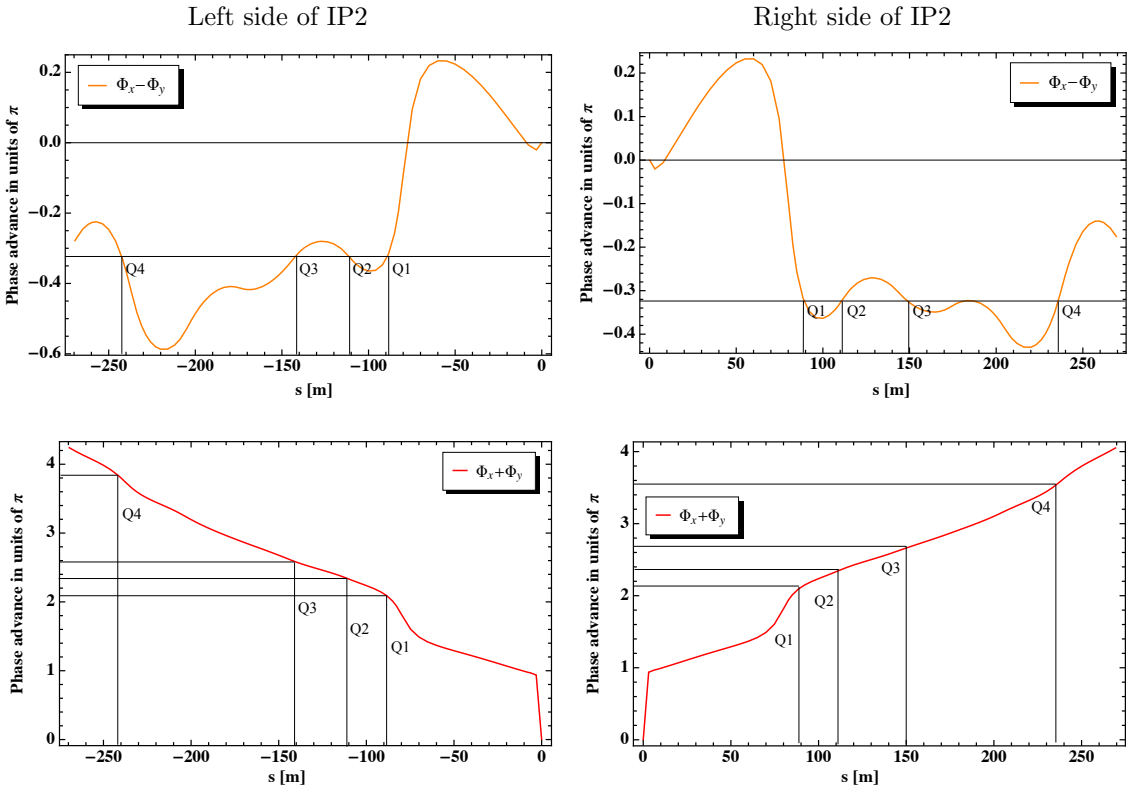


**Figure 2.40:** Difference (top) and sum (bottom) of the horizontal and vertical phase advance and positions of the skew quadrupoles Q1 to Q4.

interaction region are placed more or less symmetrically in respect to the IP, due to the (approximate) mirror symmetry of the interaction region. Furthermore, it turned out to be better to compensate Q1 with Q4 and Q2 with Q3, as the beta-function at the position of the skew quadrupoles Q1/Q4 and Q2/Q3 is comparable, while the beta-function at the position of Q1/Q3 and Q2/Q4 differs, leading to approximately the same strength of the compensating pairs in the case of a compensation of Q1 with Q4 and Q2 with Q3.

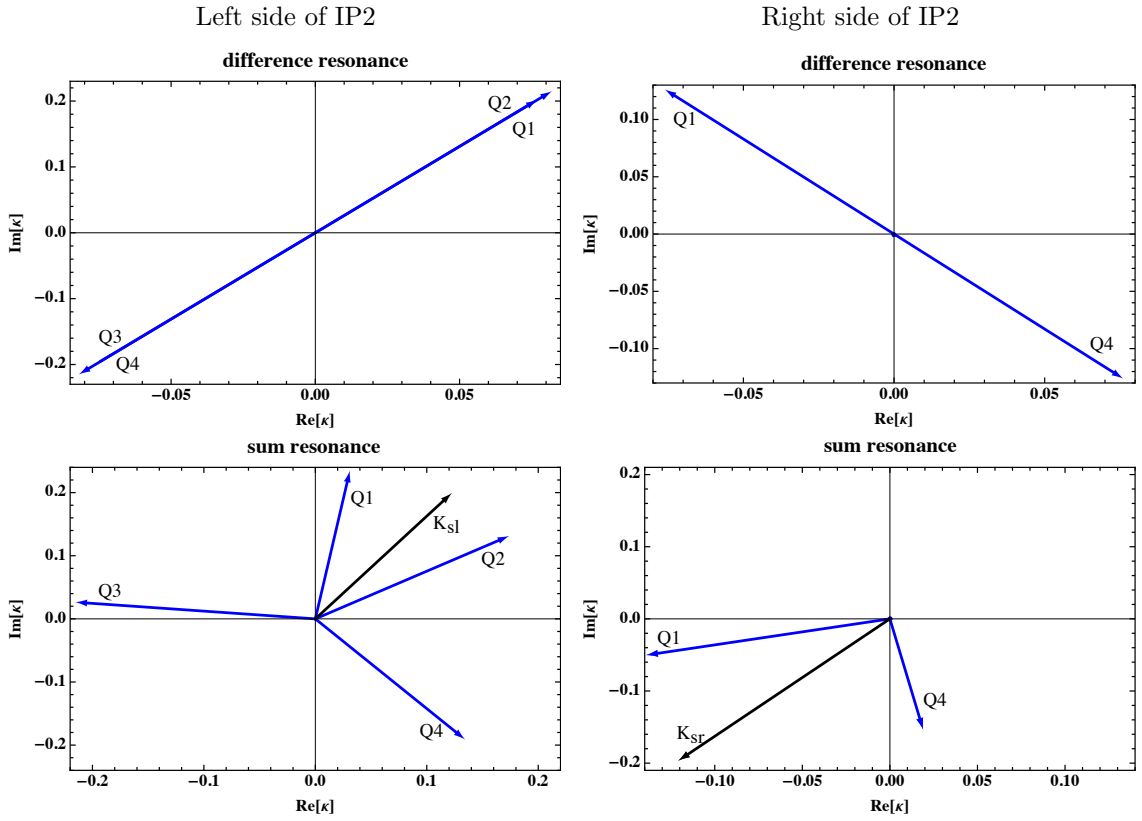


**Figure 2.41:** Representation of the skew quadrupoles in the complex plane. The strength values of the skew quadrupoles are listed in Table 2.13.

| | $k_{Q1}\,[\frac{1}{m}]$ | $k_{Q2}\,[\frac{1}{m}]$ | $k_{Q3}\,[\frac{1}{m}]$ | $k_{Q4}\,[\frac{1}{m}]$ |
|---|---|---|---|---|
| **left side** | 0.0622 | 0.0331 | -0.0326 | -0.0628 |
| **right side** | -0.0385 | 0 | 0 | 0.0377 |

**Table 2.13:** Skew quadrupole strength of the correction scheme yielding an emittance ratio of 2:1. All skew quadrupoles have a length of 0.2 m

| | | | |
|---|---|---|---|
| $\epsilon_1$ | 6.8 nm | $J_1$ | 1.0 |
| $\epsilon_2$ | 3.4 nm | $J_2$ | 1.0 |
| $\epsilon_3$ | 5.0 $\mu$m | $J_3$ | 2.0 |

**Table 2.14:** Equilibrium emittances and damping partition numbers calculated with MAD-X for the correction scheme with $k_{Q1,\,\mathrm{right}} = 0.0385\ \frac{1}{m}$ and on-momentum.

For the adjustment of the emittances, the strength of Q4 and Q3 on the right side of IP2 have been chosen as free parameters. Knowing the beta-function and the quadrupole strength of these two quadrupoles, the strength of the compensating quadrupoles on the right side, i.e. Q1 and Q2, can be calculated by solving Eqn. 2.49. The strength of the skew quadrupoles on the left side are then given by Eqn. 2.49 and 2.50, yielding an exact compensation, if $K_{sr}$ created on the right side is equal to the negative value of the compensating vector $K_{sl}$ on the left side. An emittance ratio of 2:1 is reached for the quadrupole strengths compiled in Table 2.13. The resulting compensation scheme is illustrated in Fig. 2.41 by representing the skew quadrupoles as vectors in the complex plane and the emittances and damping partition numbers of the three eigenmodes for on-momentum are summarized in Table 2.14.
To check if the compensation scheme decouples the interaction region, the Ripken parameters $\beta_{jk}$ at IP2 with and without correction and with and without synchrotron radiation are compared in Table 2.15 with the negative result, that no correction of the coupling is achieved, even not in the idealistic case of no synchrotron radiation. An explanation for the failure of the correction is, that the calculation is based on a perturbative treatment and the approximations made are not valid for the skew quadrupole strength necessary to obtain an emittance ratio of 2:1.

| | $\boldsymbol{\beta^*_{11,IP2}}$ [m] | $\boldsymbol{\beta^*_{12,IP2}}$ [m] | $\boldsymbol{\beta^*_{21,IP2}}$ [m] | $\boldsymbol{\beta^*_{22,IP2}}$ [m] |
|---|---|---|---|---|
| ideal | 0.4 | 0 | 0 | 0.2 |
| correction, no syn. radiation | 0.261 | 0.040 | 0.031 | 0.229 |
| no correction, no syn. radiation | 0.331 | 0.067 | 0.047 | 0.162 |
| correction, syn. radiation | 0.229 | 0.063 | 0.050 | 0.206 |
| no correction, syn. radiation | 0.311 | 0.082 | 0.060 | 0.148 |

**Table 2.15:** Ripken parameters $\beta_{kj}$ at IP2 calculated with MAD-X for the correction scheme with $k_{\mathrm{Q1,\,right}} = 0.0385\ \frac{1}{\mathrm{m}}$ and on-momentum. Also in the idealistic case of no synchrotron radiation the correction scheme fails.

To investigate, if the correction scheme works for small quadrupole strength, a compensation scheme with approximately one third of the skew quadrupole strength has been studied. The resulting skew quadrupole strengths are listed in Table 2.16. The Ripken parameters $\beta_{jk}$ at IP2 with and without correction for this scheme are compared in Table 2.17 and the emittances and damping partition numbers listed in Table 2.18. In this

| | $\boldsymbol{k_{Q1}}$ $[\frac{1}{\mathrm{m}}]$ | $\boldsymbol{k_{Q2}}$ $[\frac{1}{\mathrm{m}}]$ | $\boldsymbol{k_{Q3}}$ $[\frac{1}{\mathrm{m}}]$ | $\boldsymbol{k_{Q4}}$ $[\frac{1}{\mathrm{m}}]$ |
|---|---|---|---|---|
| **left side** | 0.0200 | 0.0106 | -0.0105 | -0.0202 |
| **right side** | -0.0124 | 0 | 0 | 0.0121 |

**Table 2.16:** Skew quadrupole strength yielding an emittance ratio of 75:1, but with a full compensation of the coupling at IP2. All skew quadrupoles have a length of 0.2 m

case, the Ripken parameters $\beta_{jk}$ at IP2 are corrected by the calculated correction scheme, as the skew quadrupole strengths are small enough to be treated, without making a too large error, as a small perturbation.

| | $\boldsymbol{\beta^*_{11,IP2}}$ [m] | $\boldsymbol{\beta^*_{12,IP2}}$ [m] | $\boldsymbol{\beta^*_{21,IP2}}$ [m] | $\boldsymbol{\beta^*_{22,IP2}}$ [m] |
|---|---|---|---|---|
| ideal | 0.4 | 0 | 0 | 0.2 |
| correction, no syn. radiation | 0.390 | 0.00011 | 0.0001 | 0.204 |
| no correction, no syn. radiation | 0.380 | 0.01987 | 0.0122 | 0.189 |
| correction, syn. radiation | 0.381 | 0.0023 | 0.00120 | 0.202 |
| no correction, syn. radiation | 0.363 | 0.0311 | 0.01911 | 0.181 |

**Table 2.17:** Ripken parameters $\beta_{kj}$ at IP2 calculated with MAD-X for the correction scheme with $k_{\mathrm{Q1,\,right}} = 0.0124\ \frac{1}{\mathrm{m}}$ and on-momentum.

| | | | |
|---|---|---|---|
| $\epsilon_1$ | 8.3 nm | $J_1$ | 1.0 |
| $\epsilon_2$ | 0.11 nm | $J_2$ | 1.0 |
| $\epsilon_3$ | 5.0 $\mu$m | $J_3$ | 2.0 |

**Table 2.18:** Equilibrium emittances and damping partition numbers calculated with MAD-X for the compensation scheme with $k_{\mathrm{Q1,\,right}} = 0.0124\ \frac{1}{\mathrm{m}}$ and on-momentum.

#### 2.4.3.3 Local coupling of the interaction region

Another option is to only couple a small area around the IP using one skew quadrupole on each side of the IP. For a full compensation and an optimal conversion of the flat electron beam into a round beam at the IP, these two skew quadrupoles must respect certain conditions on the phase advance which will be derived in the following and then applied to the case of the LHeC.
The transfer matrix of a skew quadrupole in the transverse plane is given by:

$$R_{\mathrm{skew}} = \begin{pmatrix} 1 & 0 & 0 & 0 \\ 0 & 1 & -\frac{1}{f} & 0 \\ 0 & 0 & 1 & 0 \\ -\frac{1}{f} & 0 & 0 & 1 \end{pmatrix} . \tag{2.51}$$

As for the LHeC electron beam, the vertical beam size can be assumed to be negligible compared to the horizontal one in the absence of coupling, the vertical position $y$ can be set to 0. In this case a skew quadrupole simply gives a kick in $y'$ depending on the horizontal position $x$:

$$\left(x,\, x',\, y,\, y'\right) \mapsto \left(x,\, x',\, y,\, y' - \frac{1}{f}x\right) . \tag{2.52}$$

The maximum vertical beam size at the IP is then obtained by tilting the phase ellipse in the $y - y'$ phase space by $\pi/2$, explicitly

$$\Delta\phi_y(s(\mathrm{skew1}), s(\mathrm{IP2})) = \frac{\pi}{2} . \tag{2.53}$$

In addition, the mismatch introduced by the skew quadrupole (skew1) should be canceled by a second skew quadrupole (skew2). No distortion is caused, if the transfer matrix $T$

from skew1 to skew2 is equal to the identity matrix. The transfer matrix $T$ for the transformation from skew1 to skew2 is given by

$$T = R_{\text{skew2}} R(\Delta\phi_x, \Delta\phi_y) R_{\text{skew1}} = \tag{2.54}$$
$$\begin{pmatrix} \frac{(\mathrm{C_x}+\mathrm{S_x}\alpha_{x_1})\beta_{x_2}}{\beta_{x_{12}}} & \mathrm{S_x}\beta_{x_{12}} & -\frac{\mathrm{S_x}\beta_{x_{12}}}{f_1} & 0 \\ \frac{\mathrm{S_y}\beta_{y_{12}}}{f_1 f_2} - \frac{\mathrm{C_x}(\alpha_{x_2}-\alpha_{x_1})+\mathrm{S_x}(\alpha_{x_{12}}+1)}{\beta_{x_{12}}} & \frac{(\mathrm{C_x}-\mathrm{S_x}\alpha_{x_2})\beta_{x_1}}{\beta_{x_{12}}} & \frac{(\mathrm{S_x}\alpha_{x_2}-\mathrm{C_x})\beta_{x_1}}{f_1\beta_{x_{12}}} - \frac{(\mathrm{C_y}+\mathrm{S_y}\alpha_{y_1})\beta_{y_2}}{f_2\beta_{y_{12}}} & -\frac{\mathrm{S_y}\beta_{y_{12}}}{f_2} \\ -\frac{\mathrm{S_y}\beta_{y_{12}}}{f_1} & 0 & \frac{(\mathrm{C_y}+\mathrm{S_y}\alpha_{y_1})\beta_{y_2}}{\beta_{y_{12}}} & \mathrm{S_y}\beta_{y_{12}} \\ \frac{(\mathrm{S_y}\alpha_{y_2}-\mathrm{C_y})\beta_{y_1}}{f_1\beta_{y_{12}}} - \frac{(\mathrm{C_x}+\mathrm{S_x}\alpha_{x_1})\beta_{x_2}}{f_2\beta_{x_{12}}} & -\frac{\mathrm{S_x}\beta_{x_{12}}}{f_2} & \frac{\mathrm{S_x}\beta_{x_{12}}}{f_1 f_2} - \frac{\mathrm{C_y}(\alpha_{y_2}-\alpha_{y_1})+\mathrm{S_y}(\alpha_{y_{12}}+1)}{\beta_{y_{12}}} & \frac{(\mathrm{C_y}-\mathrm{S_y}\alpha_{y_2})\beta_{y_1}}{\beta_{y_{12}}} \end{pmatrix}$$

The index 1/2 stands for the Twiss parameters at the location of the first/second skew quadrupole, $C_{x/y} = \cos\left(\Delta\phi_{x/y}\right)$ and $S_{x/y} = \sin\left(\Delta\phi_{x/y}\right)$, where $\Delta\phi_{x/y}$ is the phase advance from skew1 to skew2. The Twiss parameters have been abbreviated with $\beta_{x_{12}/y_{12}} = \sqrt{\beta_{x_1/y_1}\beta_{x_2/y_2}}$ and $\alpha_{x_{12}/y_{12}} = \alpha_{x_1/y_1}\alpha_{x_2/y_2}$ and $f_{1/2}$ is the skew quadrupole focal strength. The matrix is already considerably simplified by requiring

$$\sin\left(\Delta\phi_x\right) = \sin\left(\Delta\phi_y\right) = 0 \Leftrightarrow \Delta\phi_x = \Delta\phi_y = n\pi \tag{2.55}$$

leading to $T_{13} = T_{24} = T_{31} = T_{42} = 0$. After this simplification, the matrix is then given by

$$T = \begin{pmatrix} -\frac{\beta_{x_2}}{\beta_{x_{12}}} & 0 & 0 & 0 \\ \frac{\alpha_{x_2}-\alpha_{x_1}}{\beta_{x_{12}}} & -\frac{\beta_{x_1}}{\beta_{x_{12}}} & \frac{\beta_{x_1}}{f_1\beta_{x_{12}}} + \frac{\beta_{y_2}}{f_2\beta_{y_{12}}} & 0 \\ 0 & 0 & -\frac{\beta_{y_2}}{\beta_{y_{12}}} & 0 \\ \frac{\beta_{x_2}}{f_2\beta_{x_{12}}} + \frac{\beta_{y_1}}{f_1\beta_{y_{12}}} & 0 & \frac{\alpha_{y_2}-\alpha_{y_1}}{\beta_{y_{12}}} & -\frac{\beta_{y_1}}{\beta_{y_{12}}} \end{pmatrix}. \tag{2.56}$$

As can be seen from Eqn. 2.56, the transfer matrix $T$ is equal to the identity matrix, if and only if the Twiss functions at both quadrupoles are equal ($\alpha_{x_1} = \alpha_{x_2}$ and $\beta_{x_1} = \beta_{x_2}$) and the skew quadrupoles have opposite focal strength ($f_2 = -f_1$).
In summary, the following conditions must be fulfilled:

- The vertical phase advance $\Delta\phi_y$ between the first skew quadrupole and the IP must be $\Delta\phi_y = \frac{\pi}{2} + n\pi$ in order to obtain a round beam at the IP and not e.g. a tilted ellipse.

- The difference in phase advance $\Delta\phi_{x/y}$ between the skew quadrupoles must be $\Delta\phi_{x/y} = n_{x/y}\pi,\ n_{x/y} \in \mathbb{N}$ in order to achieve a full compensation. In addition, the Twiss parameters at the location of both skew quadrupoles must be equal and the skew quadrupoles must have opposite strength, i.e. $f_2 = -f_1$.

As the interaction region of the LHeC is symmetric in respect to the IP, all conditions are fulfilled if the skew quadrupoles are placed exactly at $\Delta\phi_{x/y} = \frac{\pi}{2}$ from the IP. With the current interaction region optics, this condition can not be fulfilled. In order to demonstrate the principle, the phase advance was adjusted by inserting a transfer matrix, the phasor, which changes the phase advance but not the beta-function (Appendix B). The Ripken parameters of the modified optics are shown in Fig. 2.42, and indicate that the effect of the first skew quadrupole is fully compensated by the second.
With this scheme, the beam size at the IP can be adjusted by changing the skew quadrupole strength. A ratio of 2:1 is achieved with a skew quadrupole strength of $k_{\text{skew}} = 0.0477$ and

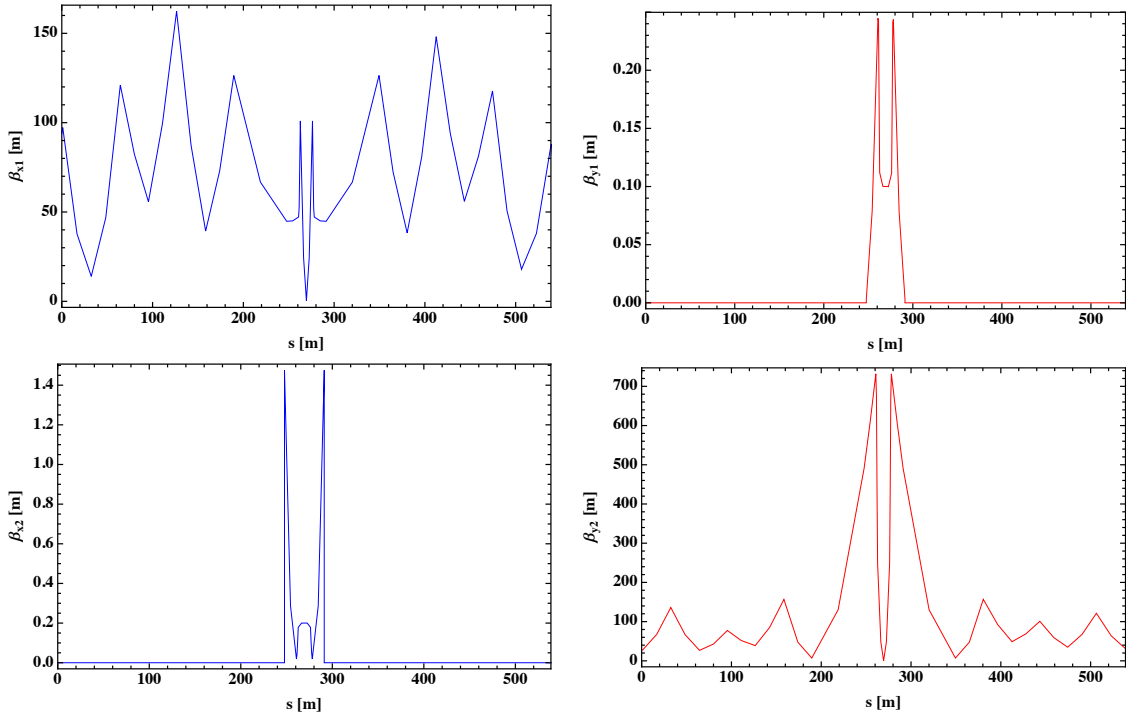


**Figure 2.42:** Ripken parameters $\beta_{kj}$ of the interaction region calculated with MAD-X and for on-momnetum. The coupling introduced by the first skew quadrupole is fully compensated by the second.

length of 0.1 m, yielding the desired beam spot size at the IP of 44.7 $\mu$m in the horizontal and 22.4 $\mu$m in the vertical plane with the assumption of a horizontal rms-emittance of $\epsilon_x = 5.0\,\text{nm}$ and a vanishing vertical emittance, i.e.

$$\begin{aligned} \sigma_{x,\text{IP2}} &= \beta_{x1}\epsilon_x = 44.7\,\mu\text{m} \\ \sigma_{y,\text{IP2}} &= \beta_{y1}\epsilon_x = 22.4\,\mu\text{m} \end{aligned} \tag{2.57}$$

The transformation of the initially flat electron beam into an almost round beam at the IP and back into a flat electron beam is illustrated in Fig. 2.43.

As the coupling is localized at the interaction region, the horizontal emittance is in the case of an uncoupled rest of the LHeC electron ring larger than 5.0 nm, and in general, the vertical emittance is unequal 0, due to magnet imperfections and alignment errors. Assuming more realistic parameters, i.e. a ratio of 100 between the horizontal and vertical emittance $\epsilon_y = \frac{1}{100}\,\epsilon_x$ and an emittance of 5.55 nm for a damping partition of $J_x/J_y/J_s = 1.5/1/1.5$ and no coupling, one obtains a larger beam spot size at the IP:

$$\begin{aligned} \sigma_{x,\text{IP2}} &= \beta_{x1}\epsilon_x + \beta_{x2}\epsilon_y = 50.4\,\mu\text{m} \\ \sigma_{y,\text{IP2}} &= \beta_{y1}\epsilon_x + \beta_{y2}\epsilon_y = 26.9\,\mu\text{m} \end{aligned} \tag{2.58}$$

In reality, it is also not possible to place the skew quadrupoles at exactly the correct phase advance, while equal Twiss functions are quite feasible, as the interaction region is symmetric and, placing the skews at the same position in respect to the IP, automatically fulfils this condition. The coupling has then, in this more realistic case, to be created and corrected with several skew quadrupoles before and after the IP. In [56] it is shown that it is possible to transform an arbitrary planar mode into a circular mode - the "round beam"

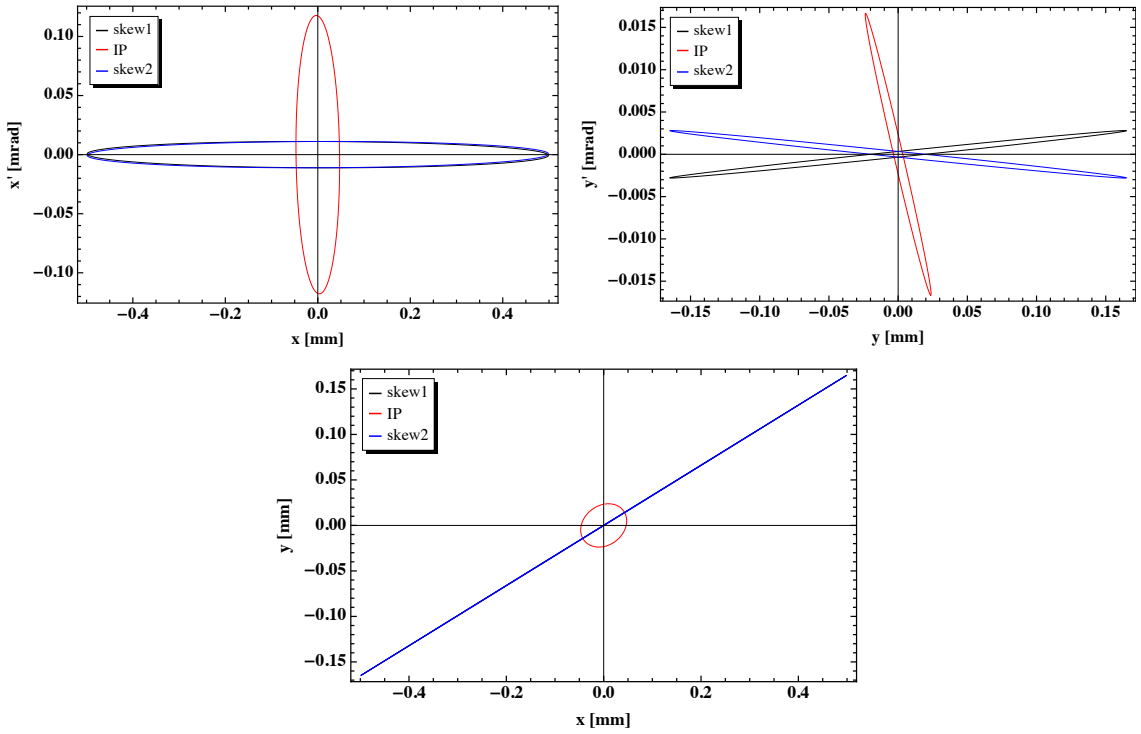


**Figure 2.43:** Transverse phase space and beam envelope at the first skew quadrupole (skew1), the IP and the second skew quadrupole (skew2) assuming a horizontal emittance of $\epsilon_x = 5.0\,\text{nm}$ and a vanishing vertical emittance. The initially flat electron beam at the first skew quadrupole is transformed into a round beam at the IP and back into a flat beam after the second skew quadrupole.

at the IP - and vice versa, using three skew quadrupoles and three normal quadrupoles for matching. The arrangement of those six quadrupoles is called a Derbenev adapter. It would be therefore sufficient to install three skew quadrupoles at each side of the IP and rematch the interaction region in order to obtain the required Twiss functions at the skew quadrupoles and beam size at the IP. With this scheme the electron beam could be also transformed into an entirely round beam with an aspect-ratio of 1:1, perfectly matching the round proton beam and allowing to eventually reduce the beta-function at the IP and hence increase the luminosity. In addition, round beams at the interaction point could be beneficial in order to reduce beam-beam effects as stated in [56].

#### 2.4.3.4 Conclusion

In this section, three different ways to match the flat electron beam to the round proton beam at the IP, i.e.

- global coupling (Sec. 2.4.3.1)
- no coupling in the interaction region, but in the rest of the ring (Sec. 2.4.3.2)
- local coupling of the interaction region (Sec. 2.4.3.3)

have been presented.

The option of global coupling in the complete ring by placing one skew quadrupole either in a dispersive or non-dispersive region (Sec. 2.4.3.1) would have the advantage of

being a very simple scheme, but would have more important disadvantages. First of all, a matching section including skew quadrupoles would have to be included in the long straight sections of the interaction region in order to match the electron beam size to the proton beam size. This would lead to a correction scheme similar to the one considered in Sec. 2.4.3.2, but including matching quadrupoles and not using the perturbation theory approach. In addition, the operation of the electron ring would become more difficult as most beam instrumentation devices are designed for uncoupled lattices. For example, the horizontal and vertical tune could be measured, but the results would have little value, as the important parameters are the tunes of the eigenmodes, which can not be measured with the usual methods used in uncoupled machines.
For the second option, the decoupled interaction region (Sec. 2.4.3.2), the correction scheme had been calculated using an approach based on perturbation theory. For the skew quadrupole strengths, needed in the case of the LHeC in order to obtain an emittance ratio of 2:1, the perturbative treatment is not valid any more and the correction scheme fails. This implies, that additional quadrupoles would be needed for a matching of the Twiss functions and the beam sizes of proton and electron beam at the IP and the new correction scheme would have to be calculated in a more exact way by e.g. using a matrix approach. This more sophisticated correction scheme would then have a similar layout as the one with coupling only in the interaction region (Sec. 2.4.3.3), but it would have the same operational problems as the option of global coupling in the ring (Sec. 2.4.3.1).
The third scheme, which only couples the interaction region (Sec. 2.4.3.3)), is the preferred option as the coupling is localized to the interaction region and the operation of the electron ring would be like the one of an uncoupled machine. In addition, the electron beam could be transformed in an entirely round beam, which would allow for a further squeeze of the proton beam and increase in luminosity. In this thesis, only the principle of such a scheme has been presented. A realistic scheme could be to install of Derbenev adapters [56] on each side of the IP. Such a scheme has not been tried out, as a rematch of the entire interaction region would have been required, being out of the scope of this thesis.

### 2.4.4 Effect of circumference errors

The actual circumference of LEP and LHC both differed by ±5 mm to ±10 mm from the ideal design circumference and a similar error can be expected for the LHeC electron ring. In order to have collisions with the LHC proton beam, the revolution times of both beams have to be equal. A change in circumference in general changes the revolution time of the beam, and thus an error in the electron ring circumference would lead to unequal revolution times of the same and the LHC proton beam. Without doing any physical changes to the machine, the revolution time $T$ can only be adjusted by running off-momentum with $T$ given by:

$$T(\delta) = \frac{C}{c} \frac{1}{\sqrt{1 - \frac{1}{\gamma^2}}} \left(1 + \left(\alpha_c - \frac{1}{\gamma^2}\right) \delta\right) , \tag{2.59}$$

where $\delta = \frac{\Delta p}{p_0}$ is the momentum offset, $C$ the machine circumference, $\gamma$ the relativistic $\gamma$-factor and $\alpha_c$ the momentum compaction factor.

This change in momentum results in an orbit change $d$ with

$$d = D_i \delta \,, \tag{2.60}$$

where $D_i$ is the dispersion in the corresponding plane.
Furthermore, in the case of the electron beam, the change in momentum also causes a change of the 4th synchrotron radiation integral according to Eqn. 1.67 and 1.68

$$\Delta I_{4i} = 2 I_{8i} \delta, \text{ with } I_{8i} = \oint k^2 D_i^2 ds \,, \tag{2.61}$$

and therefore the damping partition (Eqn. 1.56-1.58)

$$\begin{aligned} J_x &= 1 - \tfrac{I_{4x}}{I_2} \,, \\ J_y &= 1 - \tfrac{I_{4y}}{I_2} \,, \\ J_s &= 2 + \tfrac{I_{4x}+I_{4y}}{I_2} \,. \end{aligned} \tag{2.62}$$

A negative $J_i$ leads to anti-damping instead of damping and in this case the beam would most probably not survive much more than a few turns.
The question to be answered in this chapter is whether a circumference difference of about $\pm 10$ mm can still be compensated by running off-momentum with both beams. In the case of the LHC, the largest tolerable orbit shift for machine protection reasons is about 1 mm in the arcs QFs leading to a momentum offset of $\pm 5 \times 10^{-4}$ [57]. Assuming equal revolution times for on-momentum beams, the ideal electron ring circumference is given by

$$C_e(\delta_e = 0) = \frac{C_p \sqrt{\frac{\gamma_e^2 - 1}{\gamma_e^2}}}{\sqrt{\frac{\gamma_p^2 - 1}{\gamma_p^2}}} \,. \tag{2.63}$$

The requirement of equal revolution times then leads to a relation between the proton and electron beam momentum offset $\delta_p$ and $\delta_e$ for a given difference in circumference $\Delta C = C_e(\delta_e) - C_e(\delta_e = 0)$, explicitly:

$$\delta_e(\delta_p, \Delta C) = \frac{\alpha_{cp} \delta_p C_p \sqrt{1 - \frac{1}{\gamma_e^2}} - \Delta C \sqrt{1 - \frac{1}{\gamma_p^2}}}{\alpha_{ce} \left( C_p \sqrt{1 - \frac{1}{\gamma_e^2}} + \Delta C \sqrt{1 - \frac{1}{\gamma_p^2}} \right)} \,, \tag{2.64}$$

where $C_e(\delta_e = 0)$ has been replaced by Eqn. 2.63. As illustrated in Fig. 2.44, a circumference difference of $\pm 10$ mm could not be compensated by only a momentum offset of the LHC proton beam, but would imply a minimum electron beam momentum offset of $\delta_e = \mp 2.7 \times 10^{-3}$. Using the LHeC lattice presented in [10] as optics reference, the maximum dispersion in the arcs is 0.56 m and over the full ring 1.68 m, resulting in an orbit change for $\delta_p = 0$ of

$$\begin{aligned} d_{\text{max,arc}} &= 2.6 \text{ mm} \\ d_{\text{max,tot}} &= 7.8 \text{ mm} \end{aligned} \tag{2.65}$$

which is still tolerable with the current LHeC magnet apertures.
The change in horizontal and longitudinal damping partition, $J_x$ and $J_s$, is shown in Fig. 2.45. In the absence of coupling, the vertical dispersion is 0 throughout the ring and $J_y$

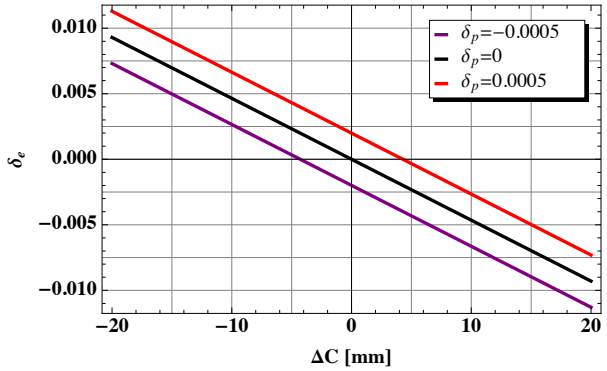


**Figure 2.44:** Required electron beam momentum offset in order to compensate a cirucumference difference of $\Delta C$.

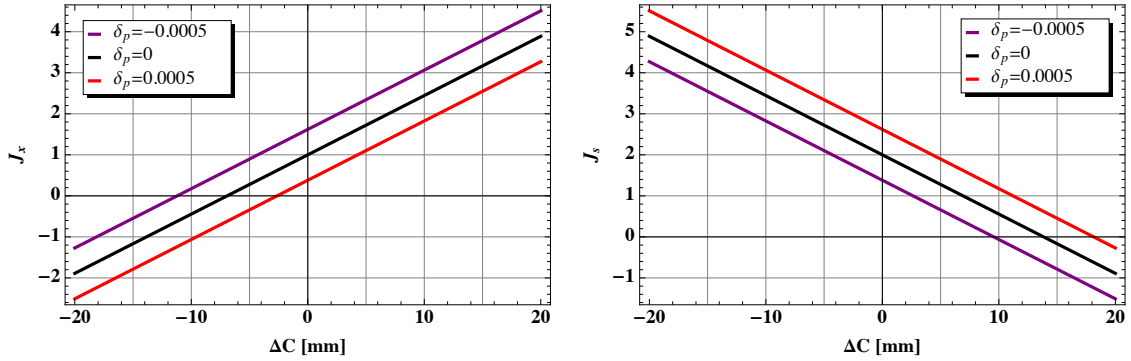


**Figure 2.45:** Change of damping partition $J_x$ (left) and $J_s$ (right) due to an electron beam momentum offset $\delta_e$ required to compensate a circumference difference $\Delta C$. In the absence of coupling, the vertical dispersion is close to 0 throughout the ring and $J_y$ stays unchanged.

stays unchanged. A circumference error smaller than $\pm^{18}_{10}$ mm could still be compensated by running off-momentum with both beams without reaching the anti-damping regime, but leaving no flexibility for any adjustment of the momentum offset of both beams and fixing the damping partition of the electron beam. In case of a circumference error larger than $\pm^{18}_{10}$ mm, $J_x$ or $J_s$ would be smaller than 0 and the electron beam would become anti-damped. A standard way to change the damping partition is to use wigglers, but this is only an option at injection, as at top energy the emitted synchrotron radiation power becomes too large. Another, but time consuming option, would be a physical change of the electron ring circumference, after determining the circumference error by a detailed survey study or indirectly by measuring the damping partition of the electron ring during the commissioning of the same. The change in circumference could be either obtained by displacing parts of the ring, preferably the arcs, or by using the bypasses as large doglegs. As the bypass in Point 1 uses the survey gallery and the bypass in Point 5 fully bypasses the experiment in a separate tunnel, it will be easier to make adjustments in Point 5. According to Eqn. 2.33, a change in circumference $\Delta s = \Delta C$ is achieved by a

simultaneous change in the bypass separation $\Delta_{\mathrm{BP}}$, the inserted straight section $s_{\mathrm{BP}}$ and the straight section $x_{\mathrm{BP}}$ parallel to the interaction region given by

$$\begin{aligned} \Delta_{\mathrm{BP}}(\Delta C) &= \frac{1}{2\tan(\frac{\theta_{\mathrm{BP}}}{2})}\Delta C\,, \\ \Delta s_{\mathrm{BP}}(\Delta C) &= \frac{1}{2\sin(\frac{\theta_{\mathrm{BP}}}{2})}\Delta C\,, \\ \Delta x_{\mathrm{BP}}(\Delta C) &= \frac{1}{2\tan(\frac{\theta_{\mathrm{BP}}}{2})\tan\theta_{\mathrm{BP}}}\Delta C\,. \end{aligned} \tag{2.66}$$

As shown in Fig. 2.46 a change of circumference of $|\Delta C| < 10$ mm would then result in $|\Delta_{\mathrm{BP}}| < 9.8$ cm, $|\Delta s_{\mathrm{BP}}| < 96.2$ cm and $|\Delta x_{\mathrm{BP}}| < 95.7$ cm, which are all tolerable values. Therefore, an adjustment over the bypass in Point 5 appears to be a feasible option.

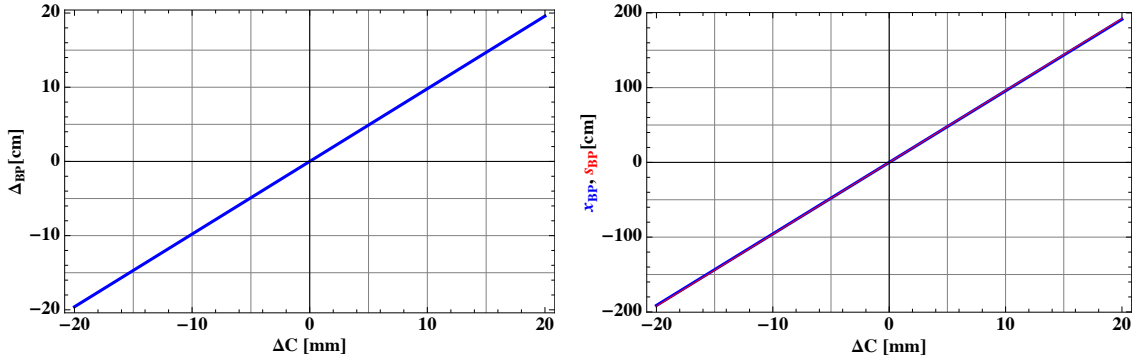


**Figure 2.46:** Change in bypass separation $\Delta_{\mathrm{BP}}$ (left), length of inserted straight section $s_{\mathrm{BP}}$ and the straight section $x_{\mathrm{BP}}$ parallel to the interaction region (right) in Point 5, in order to compensate a circumference difference of $\Delta C$

After a successful realignment of the electron ring, the circumference differences should be small enough that a synchronization between the electron and proton beam could be achieved by adjusting the RF frequency of both beams. The feasibility of this method was demonstrated with proton lead in the LHC [58] and also for electrons and protons in HERA [59].

## 2.5 Summary

One of the main challenges, maybe even the main challenge, of the LHeC project is the installation of the electron ring on top of the already existing LHC proton ring. A detailed survey study revealed [10], that the main challenges are the experiments in Point 1 and Point 5, the QRL jumper connections in the arc and the DFBs in the insertions. In this thesis (Sec. 2.2 and 2.3), it could be demonstrated, that it is possible to design an electron ring layout and optics which avoids the main interferences with the LHC proton ring and also reaches the design parameters defined in the LHeC CDR [10]. Furthermore, a critical review of the design parameters (Sec. 2.1) revealed, that a higher luminosity could possibly be reached, without an increase of the synchrotron radiation losses in the interaction region, by decreasing the vertical proton beam $\beta^*$ to 0.5 m, and a corresponding change of the electron beam optics and parameters.
Subsequent to the design of the layout and linear optics of the electron ring, different beam dynamical aspects relevant for the LHeC electron ring design (Sec. 2.4) have been studied, explicitly a local and three global chromaticity and off-momentum beta-beating correction schemes, different coupling schemes to match the electron and proton beam size at the IP and the effect of circumference errors on the damping partition.
The local chromaticity and off-momentum beta-beating correction scheme (Sec. 2.4.2) featured almost in all points a better performance than the global correction schemes, explicitly an almost linear chromaticity, a small off-momentum beta-beating - in particular a small momentum dependence of the beta-function at the IP - and a small dependence of the dynamic aperture on the momentum, and is therefore the preferred option.
To create the coupling in the electron ring, three different possibilities have been proposed:

1. global coupling of the complete ring, in which case the coupling is created with one skew quadrupole (Sec. 2.4.3.1)

2. “global coupling” but with a decoupled interaction region, for which the correction scheme is calculated using a perturbative approach (Sec. 2.4.3.2)

3. local coupling of the interaction region which is achieved by using two skew quadrupoles installed close to the IP (Sec. 2.4.3.3)

The main disadvantage of the schemes with coupling in the main part of the electron ring (Sec. 2.4.3.1 and Sec. 2.4.3.2) is that a fully coupled ring might be more difficult to operate. Therefore, the local coupling of the interaction region is considered to be the best option, as with this scheme the coupling is limited to the same.
At last, as the electron beam has to be synchronized with the LHC proton beam, the circumferences of both rings have to be matched. The circumference errors of the LEP and LHC rings were in the range of $\pm 5$ mm to $\pm 10$ mm and a similar error can be expected for the LHeC electron ring. The standard approach to adjust the circumference is to run off-momentum, which results in a change of the damping partition. The estimates of the effect of the compensation of the circumference error on the damping partition (Sec. 2.4.4) showed, that circumference errors smaller than $\pm^{18}_{10}$ mm could still be compensated by running off-momentum with the electron and proton beam, but leaving no flexibility in the

adjustment of the damping partition. For larger circumference errors, the electron beam would experience a anti-damping effect. In this case, the circumference of the electron ring could be changed by, for example, displacing parts of the ring or using the bypasses as large doglegs.

Most lattice studies presented in this thesis are based on the ideal case of an unperturbed linear lattice. In reality, the beam optics are distorted by various effects like for example the non-linearities originating from magnet imperfections and alignment errors, the momentum deviation due to the localized restoration of the synchrotron radiation losses (energy sawtooth), the linear and non-linear beam-beam kick the beam experiences at the interaction point, orbit deviations due to long-range beam-beam and impedance effects and many more. These perturbations could be particularly harmful for all optics and optics corrections sensitive to deviations of the phase advance like e.g. the chromatic correction and local coupling schemes presented in Sec. 2.4.2, 2.4.3.2 and 2.4.3.3.

The next steps in the design of the LHeC electron ring layout and linear optics could be a refinement of the layout and optics developed in this thesis, which would respect also all smaller integrations constraints. Furthermore, skew and matching quadrupoles need to be integrated in the interaction region for the matching of electron and proton beam size at the IP and, in addition, spin rotators for further polarization studies. Some continuative beam dynamical aspects to be studied are optics perturbations linked to dynamic aperture and beam survival studies and relevant collective effects, in particular beam-beam effects.

# 3. Design of Space-Charge Dominated Lattices

In low energy machines like the PS Booster at CERN one of the dominant performance limitations is the direct space-charge effect, which was introduced in Sec. 1.6.4. As the space-charge effect is the influence of the self field of the beam on itself, the optics determining amongst others the beam size can considerably influence emittance growth and beam loss along the cycle[1], which are both desired to be as small as possible.
At the time of the design of the PS Booster, a smooth variation of the beam size generated by a triplet structure and a high symmetry and periodicity was considered advantageous and the PS Booster was built accordingly. Modern machines like the CERN RCS [60] proposed as alternative to the PS Booster 2 GeV energy upgrade [8], in general favour FODO lattices, as the required focusing strength is smaller and in consequence the space requirements are also. Furthermore, modern lattices tend to have a three or four fold symmetry, as usually three to four dispersion free sections are required for injection, extraction, RF and sometimes additionally collimation. Examples of modern lattices can be found in e.g. [61], [62] and [63]. A short summary of the PS Booster and PS Booster 2 GeV energy upgrade is given in Sec. 3.1. The lattice and optics options developed in the framework of this thesis and considered for the CERN RCS, or short RCS, feasibility study [60] are presented in Sec. 3.2.
The study of the RCS and the obvious difference of its lattice and optics to the PS Booster lattice and optics, motivated a more general study of lattices and their performance if direct space-charge effects - in the following abbreviated with space-charge effects - are included. At the start of the studies, it was suspected that the following lattice characteristics might have an influence on the machine performance:

- variations of the beam size
- symmetry of the lattice and optics
- periodicity of the lattice and optics equivalent in this thesis to the number of lattice cells

[1] A cycle is the time from one injection to the next.

- phase advance per cell
- inserted straight sections connected to dispersion suppressor schemes and in general the influence of dispersion

The initial expectation was that a small variation of the beam size, a high lattice symmetry and periodicity, a small phase advance per cell and no inserted straight section would be advantageous.
With regard to the above assumptions, different lattices have been studied in this thesis which are summarized in Table 3.1. Some studies with an initially different motivation revealed other aspects. These aspects will be discussed in the corresponding sections and are listed in Table 3.1 together with the initial motivation.

| **lattice characteristic** | | **section** | **lattices** |
|---|---|---|---|
| **initial motivation** | **observed effect** | | |
| variation | | 3.6.1 | regular 16 cell lattice with different cell types, explicitly a FODO, doublet, triplet, long doublet, collapsed triplet and inverted triplet cell structure |
| symmetry | | 3.6.3 | regular 16 cell triplet lattice with symmetry 1, 2, 3, 4 and 16 |
| phase advance, symmetry and periodicity | symmetry | 3.6.4 | regular 15, 16, 18, 21 and 24 cell FODO lattice |
| phase advance and periodicity | weak/strong symmetry | 3.6.5 | regular 15, 16, 18, 21 and 24 cell FODO lattice with symmetry 1 |
| phase advance | chromatic detuning | 3.6.6 | regular 16 cell triplet lattice with symmetry 1 and different working points |
| dispersion | | 3.6.7 | 24 cell FODO lattice with $4 \times 1$ and $2 \times 2$ cells of straight section and 21 cell FODO lattice with $3 \times 2$ cells of straight section and half missing bend or $2\pi$ dispersion suppression |

**Table 3.1:** Overview of lattices studied in this thesis with regard to lattice characteristic suspected to have an influence on the machine performance. The following abbreviations are used: "variation" for variation of the beam size, "symmetry" for symmetry of the lattice and optics, "weak/strong symmetry" for the effect of weak and strong symmetry breaking discussed in Sec. 3.6.5, "phase advance" for phase advance per cell, "dispersion" for the effect of inserted straight sections, connected to dispersion suppressor schemes and in general the influence of dispersion, and "$2\pi$ dispersion suppression" for a dispersion suppression by adjusting the phase advance to $n \cdot 2\pi$ over the arc.

The beam and lattice parameters used for the general studies of the different lattices are summarized in Sec. 3.3. The preparatory work for the space-charge simulations, i.e. mainly the choice of simulation parameters expected to deliver reliable results, is summarized in Sec. 3.4. In all simulations, the initial beam distribution has been matched to the linear optics parameters of the unperturbed lattice, which leads to an initial mismatch of the beam under space-charge effects. For the later interpretation of the simulation results it is important to get an estimate of the order of magnitude of the increase of the emittance due to this initial mismatch which is given in Sec. 3.5.

## 3.1 PS Booster Lattice

In this chapter, a short overview of the optics, main characteristics and challenges of the PS Booster after the 2 GeV energy upgrade [8] is given in Sec. 3.1.1. For the studies of the performance of different lattices with regard to space-charge effects a simplified version of the PS Booster lattice has been created and the parameters adjusted to the RCS parameters in order to have an as small as possible interference from effects other than the direct space-charge effect. This simplified version is described in chapter 3.1.2.

### 3.1.1 PS Booster 2 GeV energy upgrade

The PS Booster lattice consists of 16 triplet cells with the defocusing quadrupole in the center. Two bending magnets are installed on both sides close to the triplet followed by a longer straight section. The optics are shown in Fig. 3.1. The working point at injection

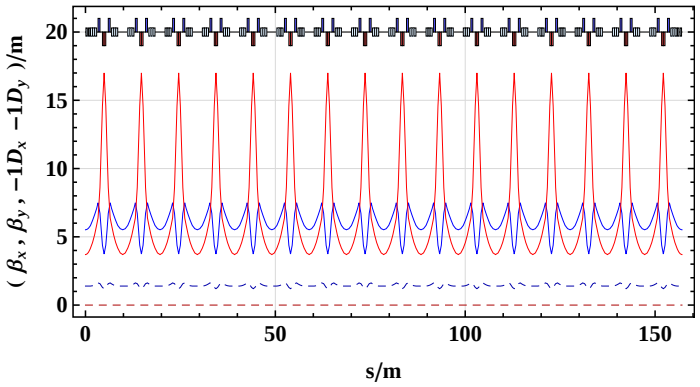


**Figure 3.1:** PS Booster lattice and optics at injection.

for high intensity and brightness beams is $Q_x = 4.28,\ Q_y = 4.55$ and is slowly changed during the ramp from 160 MeV at injection to 2 GeV at extraction. To minimize the emittance blow-up during the ramp, trim quadrupoles are used for a compensation of

| | |
|---|---|
| injection energy | 160 MeV |
| extraction energy | 2 GeV |
| circumference | 1/4 $C_{PS} \approx 157.08$m |
| repetition rate | 0.8 Hz |
| cell type | triplet |
| number of cells | 16 |
| number of straight sections | 0 |
| symmetry | 16 |
| working point | $Q_x = 4.28,\ Q_y = 4.55$ |
| gamma transition | 4.03 |
| injection | $H^-$ charge exchange injection |
| RF system | $V_{RF}(h = 1) = 8$ kV, $V_{RF}(h = 2) = 6$ kV |

**Table 3.2:** PS Booster parameters.

the $2Q_y = 9$ resonance. As a consequence of the high periodicity, the lattice does not contain any dispersion free straight sections and the $H^-$ beam delivered from LINAC4 will therefore be injected in the bend-free section between two triplets. The resulting tight requirements and the non-zero dispersion make the injection region the main challenge of the Booster upgrade[2]. Due to the lack of dispersion free sections, the RF cavities are also installed between two bends of the triplet cells. The PS Booster uses a double harmonic RF system which allows for a larger bunching factor and therefore weaker space-charge effect. Both cavities are operated in antiphase with a RF-voltage of 8 kV for the $h = 1$ cavity and 6 kV for the $h = 2$ cavity. The main parameters are summarized in Table 3.2.

### 3.1.2 Simplified PS Booster lattice

In order to compare the PS Booster lattices with other lattices, a simplified version of the lattice has been created for the studies performed in this thesis including only the main quadrupoles and dipoles. Furthermore, the vertical tune has been lowered by one integer

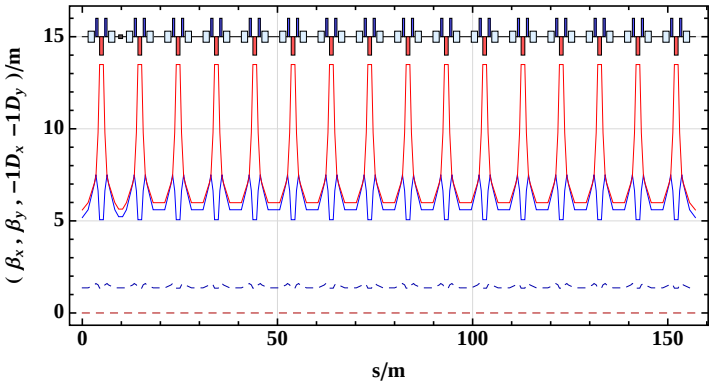


**Figure 3.2:** Simplified PS Booster lattice and optics.

| | |
|---|---|
| injection energy | 160 MeV |
| extraction energy | 2 GeV |
| circumference | 1/4 $C_{PS} \approx 157.08$m |
| repetition rate | 10 Hz |
| cell type | triplet |
| number of cells | 16 |
| number of straight sections | 0 |
| symmetry | 16 |
| working point | $Q_x = 4.28,\ Q_y = 3.55$ |
| gamma transition | 4.20 |
| RF system | $V_{RF}(h = 1) = 50$ kV |

**Table 3.3:** PS Booster parameters for the simplified PS Booster lattice.

[2]Note that most modern lattices therefore contain dispersion free sections for the injection region, RF and extraction. On the other hand such modern lattices require insertions with dispersion suppressors resulting in a low symmetry.

to $Q_y = 3.55$ for a more realistic comparison with lattices with symmetry 3 which is often the preferred symmetry for modern lattices. In the case of symmetry 3 and with a vertical tune of 4.55 the $2Q_y = 9$ resonance is systematic. As a consequence, matching to this working point becomes difficult and large variation of the beta-function and emittance growth have to be expected. Therefore, no machine with symmetry 3 would realistically operate at this working point. Furthermore, the RF settings are adjusted to simplified RCS parameters i.e. a single harmonic RF system with a voltage of 50 kV. The new parameters are summarized in Table 3.3 and the optics shown in Fig. 3.2.

## 3.2 CERN RCS Lattice

A RCS to replace the present PS Booster has been proposed as an alternative to its upgrade [64]. At this time, a circumference of only 1/7th of the PS circumference was considered. The motivation behind this small circumference was to generate the LHC 25 ns and 50 ns beams[3] by operating the RCS with a harmonic number of $h_{\mathrm{RCS}} = 3$, and to fill 18 out of totally $h_{\mathrm{PS}} = 21$ PS buckets with only 6 transfers[4], and thus avoid the triple splitting in the PS. For the LHC 75 ns bunches, the natural choice for the PS would be a harmonic number $h_{\mathrm{PS}} = 14$ and the 12 buckets could then be filled again with 6 transfers from the RCS, now operated at $h_{\mathrm{RCS}} = 2$. Due to the small circumference, a high dipole filling factor was required which suggested a FODO structure and a three-fold symmetry with three arcs and three straight sections for injection, extraction and RF. The number of cells has been chosen as a compromise between a high enough gamma transition, $\gamma_{\mathrm{tr}} > \gamma_{\mathrm{extr}} = 3.13$, and a not too high phase advance per cell. These considerations lead to a lattice, which was first proposed at the Chamonix workshop 2011 [64], with a total number of 15 cells with two quadrupole families and a dispersion suppression by adjusting the phase advance to $2\pi$ over the arc. Furthermore, the horizontal tune had been set between 4 and 5 in order to ensure a gamma transition around or larger than 4, implying a still relatively high phase advance of $> 100°$ per cell.

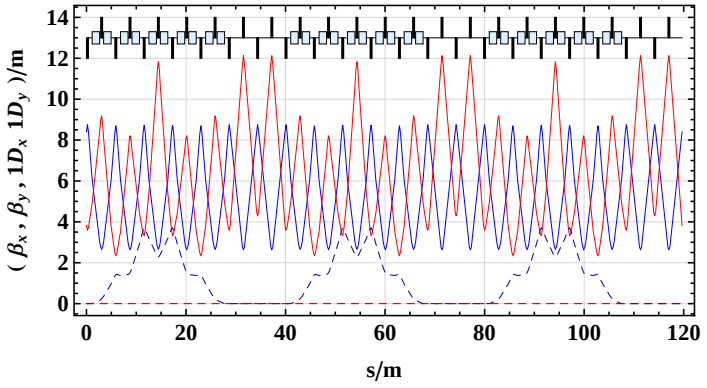


**Figure 3.3:** RCS lattice and optics as proposed in the feasibility study [9].

[3]The LHC 25 ns and 50 ns beams are the beams required in the PS Booster in order to generate in the end LHC beams with a 25 ns and 50 ns bunch spacing.

[4]Here a transfer corresponds to one injection into the PS.

As suspected already at this stage of the study, the space available for correction magnets, instrumentation and other equipment proved to be insufficient and the required dipole field of 1.16 T at extraction could not be increased enough to allow for sufficient space in the arcs [9]. The circumference was then increased to 4/21 of the PS circumference, implying an operation of the RCS with $h = 4$ or $h = 1$. The following feasibility study [9] was performed for $h = 1$ keeping $h = 4$ as possible option. The main parameters used in this study are listed in Table 3.4. As preferred lattice, a 21 cell FODO lattice with three straight sections and a dispersion suppression over a phase advance of $2\pi$ had been chosen, of which the optics are shown in Fig. 3.3. The main reasons for this choice had been integration and space requirements. Instead of concentrating on this one lattice, a more general approach will be taken in the following and all interesting lattice options, proposed for this study and designed in the framework of this thesis, will be discussed.

| | |
|---|---|
| injection energy | 160 MeV |
| extraction energy | 2 GeV |
| circumference | 4/21 $C_{PS} \approx 119.68$m |
| repetition rate | 10 Hz |
| cell type | FODO |
| number of cells | 21 |
| number of straight sections | 3 |
| symmetry | 3 |
| working point | $4 < Q_x,\ Q_y < 5$ |
| gamma transition | $> 3.6$ |
| injection | $H^-$ charge exchange injection |
| RF system | $V_{RF}(h = 1 \text{ to } 4) = 60$ kV |

**Table 3.4:** RCS parameters as proposed in the feasibility study [9].

All lattices considered for the RCS can be classified according to their dispersion suppression scheme:

- dispersion suppression over a phase advance of $n \cdot 2\pi$ along the arc discussed in Sec. 3.2.1.

- a dedicated dispersion suppressor like e.g. a space saving missing half bend scheme as introduced in Sec. 3.2.2.

The reason for this classification is that in a machine with a relatively high RF voltage like the RCS and therefore large momentum spread, the dispersive part considerably contributes to the maximum beam size and thus has to be minimized.
The general quality or suitability of a lattice can be judged by the following main requirements:

- **small quadrupole strength:** A high integrated quadrupole strength leads to longer magnets and leaves less and in the worst case insufficient space for other equipment.

In this case the circumference of the machine would have to be increased, resulting in higher costs.

- **small beta-function and dispersion:** The reachable magnetic field is in general determined by the pole tip field, which is given, e.g. in the case of a quadrupole with a linear field dependency, by the required half aperture times the gradient. The required aperture is in general defined by the beam size, which in turn is given by the twiss parameters. Therefore, small twiss functions are essential for the feasibility of every lattice.

- **high gamma transition:** Gamma transition is given in the case of a FODO lattice and similar lattices approximately by the horizontal tune of the lattice and can be comparatively increased or decreased by changing the lattice structure. In the case of the RCS, it is desired to stay below gamma transition throughout the whole cycle and so a high enough tune has to be chosen to ensure this, specifically $Q_x > 4.0 \approx \gamma_{\text{trans.}} > \gamma_{\text{extr.}} = 3.13$. On the other hand, a low phase advance per cell results in a smaller variation of the beta-function and possibly less emittance blow-up (see Sec. 3.6.6).

### 3.2.1 Dispersion suppression via $n \cdot 2\pi$ phase advance per arc

For lattices with small circumferences like the RCS a triplet structure is in most cases not feasible, as the bend magnet filling factor is considerably smaller than for a FODO or doublet structure and we will therefore limit the discussion in this section to those two structures.

#### 3.2.1.1 Comparison between FODO and doublet structure

To compare the two structures, the example of a 20 cell lattice with 4 straight sections and 2 quadrupole families is used. The magnet lengths are adjusted, so that the maximum dipole field is approximately 1.3 T and the maximum quadrupole field around 10 T/m which are the maximum values assumed for the RCS [9]. The optics are matched to $Q_x/Q_y = 5.40/4.57$, where the horizontal tune is determined by the requirement of a $2\pi$ phase advance per arc and the vertical tune set one integer lower than the horizontal to avoid the Montague resonance [65]. The fractional part of the tune allows for a space-charge tune-shift of approx. 0.5 in the vertical and 0.35 in the horizontal plane.
In general, the required integrated quadrupole strengths for a doublet lattice are twice as large as for a FODO lattice. On the other hand, the doublet gives a higher gamma transition in combination with smaller twiss functions (Fig. 3.4 (left)). In addition, it offers a long continuous straight section, whereas for a FODO lattice the straight section is always split up in two parts. The natural choice would be to place the injection and extraction in one continuous straight section. However, in case of a FODO structure, the kick from a defocusing quadrupole in the center of a straight section can be used beneficially for the beam separation and the required space reduced from 6.2 m for a continuous straight section to $2 \times 2.6$ m [66]. If for other reasons a continuous straight section is desired, a third possibility is a "hybrid" structure with a doublet for the straight section and a FODO

lattice in the arc as shown in Fig. 3.4 (right). In this case, four quadrupole families are used for the matching of one period - two quadrupoles for the doublet structure and two for the FODO.

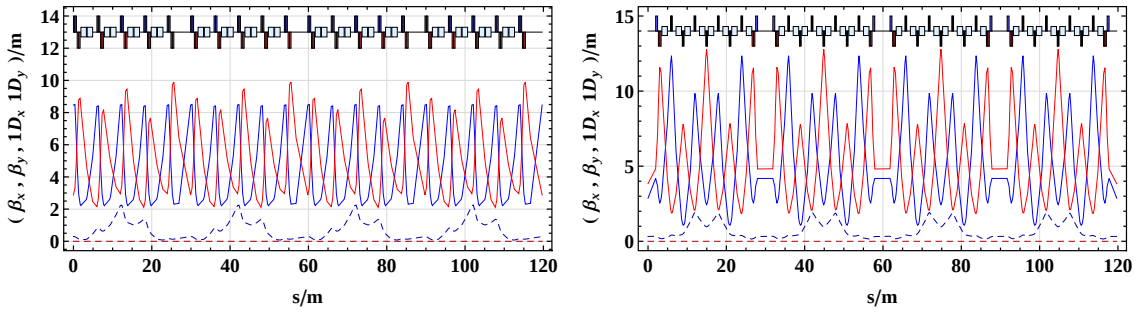


**Figure 3.4:** (left) Doublet lattice and optics.
(right) Hybrid lattice and optics with a FODO structure in the arc and a doublet in the straight section.

As illustrated in Fig. 3.5, the maximum of the dispersion always occurs at a focusing quadrupole and is reduced for the configuration with the defocusing quadrupole in the center of the arc in the case of a FODO lattice. The dispersion can be still slightly reduced by moving the bends as close as possible to the defocusing quadrupoles. Also in the case of the doublet lattice, the dispersion is reduced if the bends are placed next to the defocusing quadrupoles at the cost of more asymmetric lattice functions than for a lattice with the bends in the center of the cell.

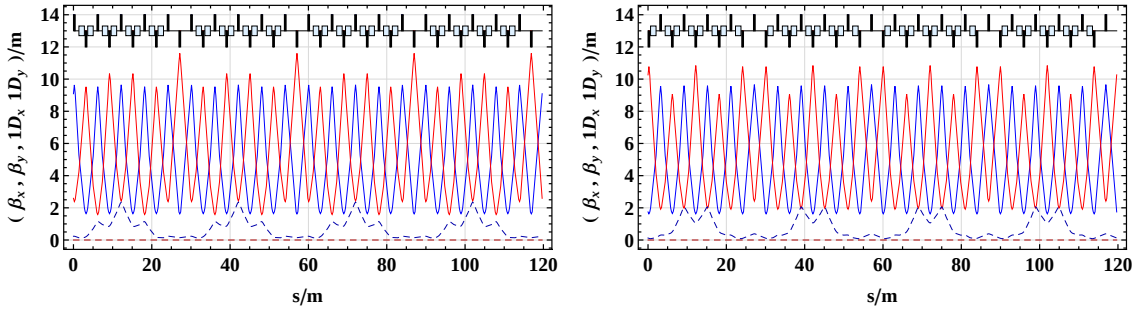


**Figure 3.5:** Optics of (left) QF-0-QD-0-QF FODO lattice. (right) QD-0-QF-0-QD FODO lattice.

### 3.2.1.2 Symmetry and periodicity

Due to the smaller required quadrupole gradient and the new injection scheme which uses the defocusing quadrupole in the center of the straight sections [66], the FODO structure was retained for the RCS proposal and thus this structure will be used as example for the comparison of the different lattice symmetries and periodicities. The lattices discussed in this section all feature a $n \cdot 2\pi$ dispersion suppression scheme fixing the phase advance per arc cell and with it the lattice tune. The number of cells per arc on the other hand is given by the total number of cells and the lattice symmetry, interconnecting all three parameters with each other. To give an idea of this restriction, Table 3.5 gives an overview of all possible options considered for the RCS, where not acceptable parameters are marked in red.

| no. of cells | layout | cells/straight | cells/arc | hor. tune | $\phi_{\text{cell}}$ [deg] |
|---|---|---|---|---|---|
| 15 | triangle | 1 | 4 | 3 3/4 | 90 |
| | | $> 1$ | too high phase advance per cell | | |
| 16 | race | $< 2$ | too tight for inj./extr. | | |
| | | 2 | 6 | 2 2/3 | 60 |
| | | | | 5 1/3 | 120 |
| | | 3 | 5 | 3.2 | 72 |
| | | | | 6.4 | 144 |
| | | $> 3$ | too tight for bending | | |
| 16 | square | 1 | 3 | 5 1/3 | 120 |
| | | $> 1$ | too tight for bending | | |
| 18 | race | $< 2$ | too tight for inj./extr. | | |
| | | 2 | 9 | 2 2/3 | 60 |
| | | | | 5 1/3 | 120 |
| | | 3 | 5 | 3.2 | 72 |
| | | | | 6.4 | 144 |
| | | $> 3$ | too tight for bending | | |
| 20 | race | $< 2$ | too tight for inj./extr. | | |
| | | 2 | 8 | 2.5 | 45 |
| | | | | 5.0 | 90 |
| | | 3 | 7 | 2.86 | 51.4 |
| | | | | 5.71 | 102.9 |
| | | 4 | 6 | $3\frac{1}{3}$ | 60 |
| | | | | $6\frac{2}{3}$ | 120 |
| | | $> 4$ | too tight for bending | | |
| 20 | square | 1 | 4 | 5.0 | 90 |
| | | 2 | 3 | $6\frac{2}{3}$ | 120 |
| | | $> 2$ | too high phase advance per cell | | |
| 21 | triangle | 1 | 6 | 3.5 | 60 |
| | | 2 | 5 | 4.2 | 72 |
| 22 | race | $< 3$ | too tight for inj./extr. | | |
| | | 3 | 8 | 2.75 | 45 |
| | | | | 5.5 | 90 |
| | | 4 | 7 | 3.14 | 51.4 |
| | | | | 6.29 | 102.9 |
| | | $> 4$ | too tight for bending | | |
| 22 | square | $< 2$ | too tight for inj./extr. | | |
| | | 2 | 3.5 | 6.29 | 102.9 |
| | | $> 3$ | too high phase advance per cell | | |
| 24 | race | $< 4$ | too tight for inj./extr. | | |
| | | 4 | 8 | 3.0 | 45 |
| | | | | 6.0 | 90 |

| | | | | | |
|---|---|---|---|---|---|
| | | $> 4$ | too tight for bending | | |
| 24 | triangle | $< 3$ | too tight for inj./extr. | | |
| | | 3 | 5 | 4.8 | 72 |
| | | $> 3$ | too tight for bending | | |
| 24 | square | $< 2$ | too tight for inj./extr. | | |
| | | 2 | 4 | 6.0 | 90 |
| | | 3 | 3 | 8.0 | 120 |
| | | $> 3$ | too tight for tight for bending | | |

**Table 3.5:** Lattice options considered for a dispersion suppression with $n \cdot 2\pi$ phase advance per arc. The layout of the machine, here a racetrack (race), triangular (triangle) and quadratic (square) layout, determines the symmetry of the machine: two-fold in the case of the racetrack layout, three-fold in the case of the triangular layout and four-fold in the case of the square layout. The minimum number of cells per straight section is limited by the space required for injection, extraction and RF (too tight for inj./extr.), whereas the maximum number of cells per straight section is limited by the maximum achievable dipole field (too tight for bending) and the phase advance per cell still considered to be acceptable (too high phase advance per cell)[5]. For some options, the values for the phase advance per cell or the working are just on the edge of being acceptable. These options are marked in red.

In the case of the racetrack option, the phase advance over one arc can be either $2\pi$ or $2 \times 2\pi$. The first value always refers to $2\pi$, the second to $2 \times 2\pi$. In the case of the square and triangle only a $2\pi$ phase advance per arc is possible as otherwise the phase advance per cell becomes too large. All feasible options are summarized in Table 3.6.

| **symmetry** | **no. of cells** | **cells/straight** | **cells/arc** | **hor. tune** | $\phi_{\text{cell}}$ **[deg]** |
|---|---|---|---|---|---|
| race | 20 | 2 | 8 | 5.0 | 90 |
| | 22 | 3 | 8 | 5.5 | 90 |
| | 24 | 4 | 8 | 6.0 | 90 |
| triangle | 15 | 1 | 4 | 3 3/4 | 90 |
| | 21 | 2 | 5 | 4.2 | 72 |
| | 24 | 3 | 5 | 4.8 | 72 |
| square | 20 | 1 | 4 | 5.0 | 90 |
| | 24 | 2 | 4 | 6.0 | 90 |

**Table 3.6:** List of options with dispersion suppression with $n \cdot 2\pi$ phase advance per arc retained for further studies.

#### 3.2.1.3 Correction of the beta-beating with individual quadrupoles

An example for a lattice with a dispersion suppression by adjusting the phase advance to $2\pi$ over the arc is the 21 cell FODO lattice with $3 \times 2$ cells of straight sections, chosen in the RCS feasibility study [9] with the only difference that in the case presented here and studied

[4] As the phase advance per arc has to be a multiple of $2\pi$, the phase advance per arc cell increases, if the number of cells per arc is decreased as is the case if more cells are used as straight section.

further in Sec. 3.6.7, the circumference is adjusted to the PS Booster circumference. The optics of this lattice with a working point of $Q_x/Q_y = 4.47/3.42$ and only two quadrupole families - one focusing and one defocusing - are shown in Fig. 3.6 (left). The working point has been moved away from the one chosen for the simplified PS Booster lattice as in this case the $4Q_y$ resonance was excited, leading to a strong emittance growth. The mismatch

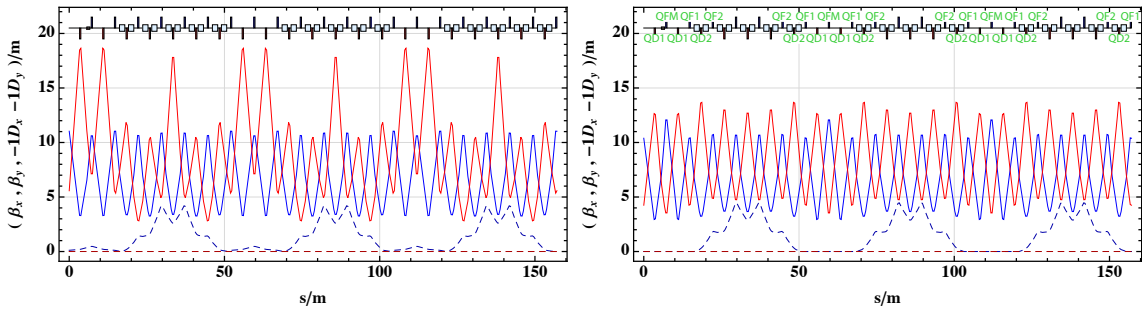


**Figure 3.6:** Example of a 21 cell FODO lattice with $3 \times 2$ cells of straight section using a dispersion suppression by adjusting the phase advance to $2\pi$ over the arc. The mismatch caused by the missing dipoles in the straight section can be considerable reduced by additional individual matching quadrupoles next to the straight section and the dispersion matched to 0 in the straight sections.
(left) Lattice and optics with two quadrupole families
(right) Lattice and optics with additional three focusing and two defocusing quadrupoles marked in green.

introduced by the missing dipoles in the straight sections leads to a strong variation of the vertical beta-function. The variation can be smoothed by allowing for more individual quadrupoles as illustrated in Fig. 3.6 (right), where four focusing and three defocusing quadrupoles were used for the correction. Furthermore, the dispersion can be matched to zero in the straight sections, also in the case of a deviation from the ideal $2\pi$ phase advance per arc, resulting in more flexibility in the choice of a working point. Lattices with only two individual quadrupoles exhibit, in this case, residual dispersion in the straight sections, as can be seen in the case of the 21 cell lattice in Fig. 3.6 (left).

### 3.2.2 Dispersion suppression with a half missing bend scheme

All lattices with a dispersion suppression by adjusting the phase advance to $2\pi$ over the arc show a larger and more irregular dispersion in the arc than the regular lattices. This leads, as described later in Sec. 3.6.7, to a large variation of the horizontal beam size, but also initial instantaneous emittance growth for horizontal working points near the integer resonance, where near means values as large as 0.3. The dispersion beating, being the source of the phenomena listed above, can be reduced with a half missing bend dispersion suppressor scheme. In this scheme, the last dipole before the straight section is shifted by half a cell, making it possible to match the dispersion to the arc with individual quadrupoles, but also reducing the length of the continuous straight section. The reduction of the length of the continuous straight section could make the injection and extraction more challenging, but on the other hand it could also facilitate it if the moved dipole and the quadrupoles in

the straight section could be used for the separation of the incoming and outgoing beam respectively.

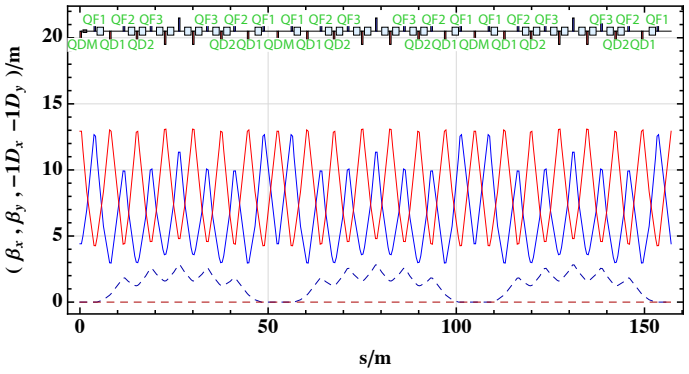


**Figure 3.7:** Example of a 21 cell FODO lattice with $3 \times 2$ cells of straight section and a half missing bend dispersion suppressor. Individual quadrupoles are marked in green.

Exemplary for all lattices with straight sections, in particular also the ones discussed in the preceding section (Sec. 3.2.1), a 21 cell FODO lattice with a half missing bend dispersion suppressor is shown in Fig. 3.7. As expected, the dispersion is regular in the arc and the maximum dispersion is reduced compared to the 21 cell FODO lattice with a dispersion suppression by adjusting the phase advance to $2\pi$ over the arc (Fig. 3.6).

## 3.3 General Beam and Lattice Parameters

Most challenging in respect to the space-charge limit are the ultimate LHC 25 ns beams [44] required for the HL-LHC upgrade [4] due to their small emittance and are thus used as baseline parameters for the simulations presented in this thesis.
The standard assumption for the ultimate LHC 25 ns beam is a parabolic bunchshape with a bunch length of 180 ns at 2 GeV and a longitudinal emittance of $\epsilon_{\text{long}} = 5\pi\sigma_E\sigma_t = 2$ eVs. However, for a PS Booster like machine a parabolic squared distribution in the longitudinal - and also transverse plane - is more realistic [67]. To obtain the corresponding parameters leading to the same bunch length of 180 ns, but under the assumption of a parabolic squared distribution with $\epsilon_{\text{long}} = 7\pi\sigma_E\sigma_t$, the emittance can simply be rescaled, leading to $\epsilon_{\text{long}} = \frac{7}{5} \cdot 2$ eVs. All beam parameters are summarized in Table 3.7.

| | |
|---|---|
| number of particles per bunch | $2.4 \times 10^{12}$ |
| hor./vert. normalized emittance | 2.5/2.5 mm mrad |
| long. emittance | 2.8 eVs |

**Table 3.7:** Ultimate LHC 25 ns beam parameters. The longitudinal emittance is rescaled as a parabolic squared distribution is assumed instead of a parabolic distribution.

The RCS lattices for a machine replacing the existing PS Booster, which have been proposed in [68] and are described in more detail in Sec. 3.2, all had a circumference of 4/21th

of the PS circumference and were all very tight in respect to the available space. For the following more general studies, the circumference was increased to the PS Booster circumference of 1/4th of the PS circumference, also making a direct comparison with the PS Booster lattice possible. The RF parameters were adjusted to the shorter cycle of 10 Hz and the desired longitudinal emittance of 2.8 eVs leading to $V_{\mathrm{RF}} = 50$ kV. To have as simple a system as possible, the double harmonic RF-system foreseen for the RCS and also present in the existing PS Booster is replaced by a single harmonic system with $h = 1$. Furthermore, the magnet length of all lattices is adjusted, so that all lattices have approximately the same dipole strength and quadrupole gradient. All parameters are listed in Table 3.8.

| | |
|---|---|
| injection energy | 160 MeV |
| extraction energy | 2 GeV |
| circumference | 1/4 $C_{\mathrm{PS}} \approx 157.08$m |
| repetition rate | 10 Hz |
| injection | $H^-$ charge exchange injection |
| RF system | $V_{\mathrm{RF}}(h = 1) = 50$ kV |

**Table 3.8:** RCS parameters used for space-charge simulations.

For the general studies performed in this section which have the aim of studying the influence of the space-charge effect, the above simplifications can and should be made, but it also has to be kept in mind that those lattices do not represent realistic machines.

## 3.4 Space-Charge Simulation Method and Settings

For the comparison of the different lattices, the parallel Particle in Cell (PIC) routines of the code PTC-ORBIT were used [69]. PTC-ORBIT combines the fully symplectic Polymorphic Tracking Code PTC [34] with the well tested space-charge calculation routines of ORBIT [70]. The general simulation method is to define regularly spaced points along the lattice, so called nodes, at which the space-charge field of the beam is calculated and the resulting kick then applied to the beam distribution. In between the space-charge nodes the beam is tracked with PTC.

With the current computing power available, a full simulation of all beam particles over several thousand turns is not feasible. Therefore, the beam distribution is modeled by taking a subset of particles called macroparticles. The computing time can be further reduced by simplification of the space-charge field calculation. For all simulations presented in this thesis, a "2 1/2 D" model has been used. In this case, all particles, independent of their longitudinal position, are projected in the transverse plane. The space-charge field is then calculated by extending an equidistant transverse grid over the $2\sigma$ beam envelope and determining the Green's function of the charge distribution of the grid via a Fast Fourier Transformation (FFT). The transverse field is then simply scaled with the longitudinal beam distribution. Using the simplifications described above, the simulation becomes

dependent on the number of macroparticles, the grid-size and the number of space-charge kicks, and a set of adequate simulation parameters has to be found in a "convergence study", which has been carried in this thesis and is described in Sec. 3.4.2.
The simulation time can be further reduced by optimizing the lattice description used for PTC and with it the time required for tracking of the particles. This optimization performed in the framework of this thesis is described in Sec. 3.4.1.

### 3.4.1 Lattice description in PTC

As MAD-X provides powerful tools for matching and lattice design (see Sec. 1.8 about MAD-X and PTC), all lattices were matched with MAD-X. To translate the lattice description from MAD-X to PTC-ORBIT, a dedicated algorithm exists.
Different algorithms, particularly a "drift-kick-drift" or "matrix-kick-matrix" model, are implemented in PTC. In all simulations presented in this thesis, the "matrix-kick-matrix" model has been used, as it produces the same phase advance between elements, and thus tune, as the thick lens model, without costing more CPU time. Furthermore, the number of integration steps for quadrupoles and sextupoles can be specified, and if the exact or expanded Hamiltonian is used. The integration steps are then grouped in ORBIT nodes of a maximum length defined by the user. Between each ORBIT node, a space-charge node is placed.
To ensure that the created lattice description describes the linear and non-linear beam dynamics correctly, the results of the normal form analysis and the dynamic aperture have to be compared to a reference model believed to be a precise description of the lattice. As reference model and final model the parameters listed in Table 3.9 have been used in this thesis. In general, the lattice description has to be checked for each lattice. Exemplary

| | **reference model** | **final model** |
|---|---|---|
| model | "matrix-kick-matrix" | "matrix-kick-matrix" |
| number of integration steps | 10 | - |
| thinlens | - | 0.05 |
| order of symplectic integrator | 6 | 2 |
| Hamiltonian | exact | exact |

**Table 3.9:** Simulation parameters for the reference and final model. The parameter thinlens is the maximum integrated quadrupole strength per integration step. A quadrupole of 1 m and $k = 1/\text{m}$ would be split in 20 integration steps for thinlens=0.05.

for all lattices, the results of the simplified PS Booster lattice (Sec. 3.1.2) with a working point of $Q_x/Q_y = 4.29/3.38$, the working point used for the convergence study described in Sec. 3.4.2, are presented in the following sections.

#### 3.4.1.1 Comparison of the normal form analysis for the simplified PS Booster lattice with $Q_x/Q_y = 4.29/3.38$

The comparison of the higher order chromaticities and anharmonicities defined in Sec.1.6.3 and Sec. 1.6.4 is an excellent way to check that the non-linear part of the lattice is modelled

correctly. The results of the normal form analysis of the reference and final model are given in Table 3.10 and show good agreement. As the lattice does not contain any non-linear elements, the detuning with amplitude is very small. The only non-linearity of the lattice comes from the fringe fields of the dipoles and quadrupoles with a dominating effect from the quadrupoles. For all lattices the chromaticity is uncorrected, as is also the case for the existing PS Booster, leading to a relatively large chromatic detuning.

| | **reference model** | **final model** |
|---|---|---|
| $Q_x/Q_y$ | 4.29/3.38 | 4.29/3.38 |
| $dQ_x/dQ_y$ | $-6.38/-10.84$ | $-6.38/-10.82$ |
| $d^2Q_x/d^2Q_y$ | 172.91/316.78 | 172.85/316.67 |
| $a_{x,10}/a_{y,10}$ | 13.65/47.88 | 13.65/47.88 |
| $a_{x,01}/a_{y,01}$ | 47.88/52.45 | 47.88/52.44 |

**Table 3.10:** Comparison of the higher order chromaticities and anharmonicities of the reference and final model.

It is essential for machines with large bending angles to use the exact Hamiltonian, as otherwise the chromatic behaviour is not modelled correctly. This is also the case for the lattices studied in this thesis. The exact Hamiltonian has thus been used for all lattices. As an example, the results of the normal form analysis of the reference model using the exact and the expanded Hamiltonian are listed in Table 3.11 and show, as expected, a non-negligible difference, in particular in the linear chromaticity.

| | **exact Hamiltonian** | **expanded Hamiltonian** |
|---|---|---|
| $Q_x/Q_y$ | 4.29/3.38 | 4.29/3.38 |
| $dQ_x/dQ_y$ | $-6.38/-10.84$ | $-6.74/-10.18$ |
| $d^2Q_x/d^2Q_y$ | 172.91/316.78 | 171.80/312.72 |
| ... | ... | ... |

**Table 3.11:** Comparison of the higher order chormaticities of the reference model using the exact or expanded Hamiltonian.

#### 3.4.1.2 Comparison of the dynamic aperture for the simplified PS Booster lattice with $Q_x/Q_y = 4.29/3.38$

The dynamic aperture of the final and reference model for $\Delta E = 0$, for half the maximum energy spread ($\Delta E = 1.53$MeV) and for the full energy spread ($\Delta E = 3.05$MeV) are shown in Fig. 3.8 and agree well except for $\sigma_x = 0$ and $\sigma_y = 0$. The disagreement in these points does not really indicate a deficit of the chosen model, as points with $\sigma_{x/y} = 0$ are in general difficult to simulate and results have to be treated with caution [71]. As the lattice contains no non-linear elements, the dynamic aperture is determined by the resonances excited by the dipole and quadrupole fringe fields. Disabling the fringe fields leads to a basically infinite dynamic aperture.

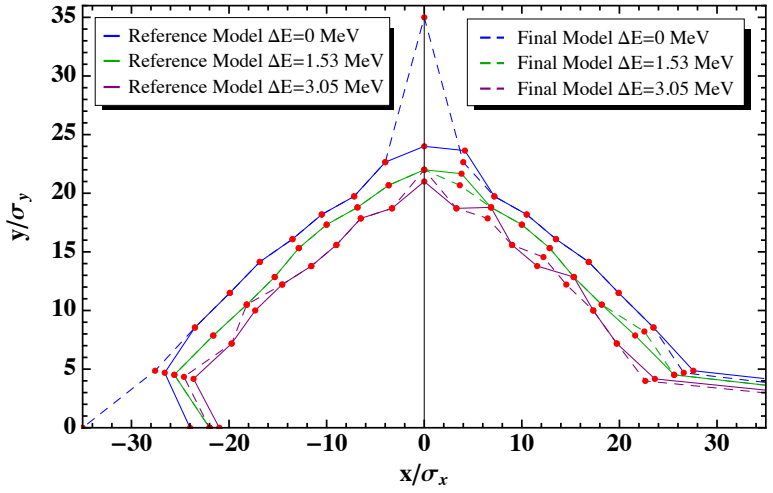


**Figure 3.8:** Dynamic aperture of the reference (solid) and final model (dashed) assuming LHC 25 ns beams (Table 3.7), where $\sigma_{x/y} = \sqrt{\beta_{x,y}\epsilon_{x/y,\mathrm{rms}}}$ denotes the betatron rms beam size given by $\sigma_x/\sigma_y = 4.60/4.96$ mm

### 3.4.2 Dependence on simulation parameters - convergence study

In order to find a good set of simulation parameters delivering credible results in decent computation time, a convergence study has been performed in this thesis for the simplified PS Booster lattice (Sec. 3.1.2).

| | |
|---|---|
| $Q_x/Q_y$ | 4.29/3.38 |
| energy | 160 MeV |
| circumference | 1/4 $C_{\mathrm{PS}} \approx 157.08$m |
| RF system | $V_{\mathrm{RF}}(h=1) = 50$ kV |
| hor./vert. normalized emittance | 2.5/2.5 mm mrad |
| long. emittance | 2.8 eVs |
| number of particles per bunch | $1.2 \times 10^{12}$ |
| number of turns | 2000 |

**Table 3.12:** Simulation parameters used for the convergence study.

A simulation with full beam intensity is in general not suited for a convergence study, as then the emittance behaviour is dominated by the blow-up caused by resonance excitation due to the large space-charge tune-shift. To clearly see only the artefacts of the simulation, the first step is to reduce the beam intensity, typically to half the intensity. With the resulting smaller space-charge tune-spread, the working point is placed such that the tune footprint avoids all resonances possibly causing blow-up. Explicitly in the case of the simplified PS Booster lattice, the working point is moved below the half integer resonance, as for the smaller beam intensity the core of the beam would constantly cross over the resonance. The new working point is considered to be stable, if the emittance is constant at zero beam intensity, so without space-charge. As a last step, the number of turns is chosen large enough, so that all oscillation due to injection mismatch have vanished and the beam distribution has adjusted to the lattice, including all non-linearities. To ensure this, the

beam should be tracked over several oscillation periods. As the longitudinal synchrotron motion is much slower than the transverse, it determines the tracking time and it is usually enough to track over a few synchrotron periods. For the simplified PS Booster lattice, the beam has been tracked over 2 000 turns, which corresponds to approximately eight synchrotron periods which is considered to be sufficient time to test the stability of the beam.
All simulations were performed for the LHC 25 ns beam (Table 3.7), resulting in the corresponding parameters for the convergence study listed in Table 3.12.

#### 3.4.2.1 Stability check of the working point used for the convergence study

The working point of $Q_x = 4.29,\ Q_y = 3.38$ used for the convergence study has been chosen in a safe area well below the half integer resonance. The tune footprint and resonance diagram are shown in Fig. 3.9 (left). The horizontal tune-spread is an artifact from ORBIT where the tune for low amplitude particles is not correctly calculated as illustrated in Fig. 3.9 (right). As the lattice does not contain any non-linear elements, the detuning with amplitude is very small and the tune-spread is only caused by the chromatic detuning due to the large chromaticities in the case of a triplet lattice.

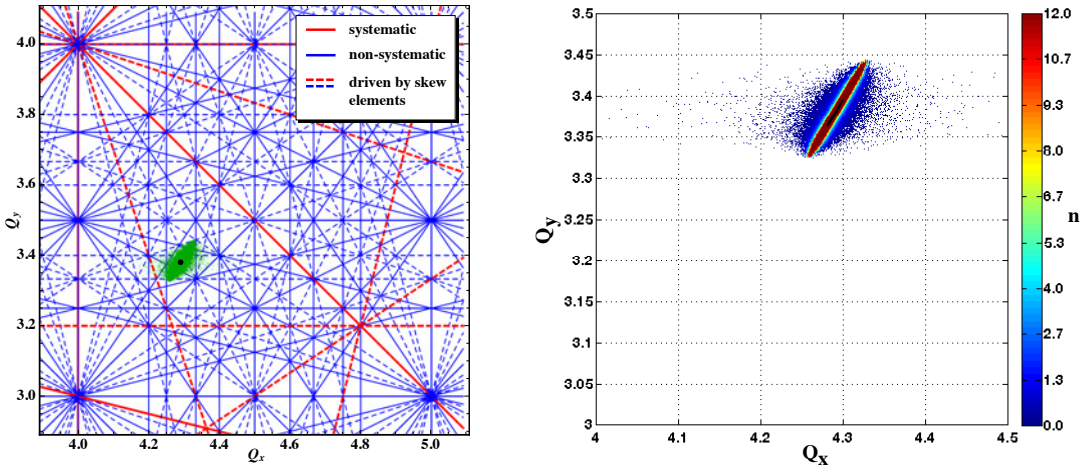


**Figure 3.9:** (left) Resonance diagram with resonances until 5th order and tune footprint from PTC-ORBIT for $Q_x = 4.29,\ Q_y = 3.38$. Systematic resonances are shown in red, non-systematic in blue and resonances due to skew elements are indicated with dashed lines.
(right) Tune footprint from PTC-ORBIT color coded with the horizontal amplitude $n \cdot J_x$ of the individual beam particles, where $J_x$ is the action with $2J_x = \epsilon_{x,\mathrm{rms}} = 4.11\,\mu$m. The tune-spread is mainly caused by the chromatic detuning (indicated in black). The horizontal tune-spread is artificial, due to the fact that the tune is not correctly calculated by ORBIT for particles with small horizontal amplitude particles.

The rms emittance shown in Fig. 3.10 remains constant over several synchrotron periods, indicating that the chosen working point can be considered to be stable.
The difference in the initial rms emittance for different numbers of macroparticles is very small and a statistical phenomenon. The small oscillation with the synchrotron frequency of the horizontal emittance can be explained by the initial longitudinal mismatch, which is also visible as an oscillation of the bunching factor with twice the synchrotron

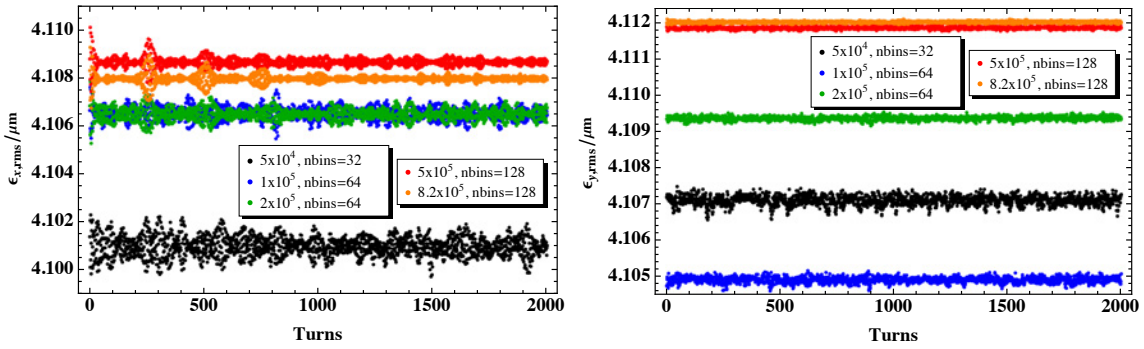


**Figure 3.10:** Time evolution of the horizontal (left) and vertical (right) rms emittance for zero beam intensity and a working point of $Q_x = 4.29,\ Q_y = 3.38$. The oscillations of the horizontal emittance with the synchrotron frequency are caused by the intial longitudinal mismatch.

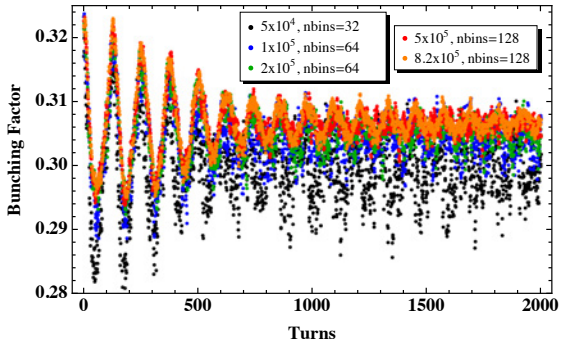


**Figure 3.11:** Bunching factor for zero beam intensity and a working point of $Q_x = 4.29,\ Q_y = 3.38$. The oscillation with twice the synchrotron frequency is caused by the intial longitudinal mismatch.

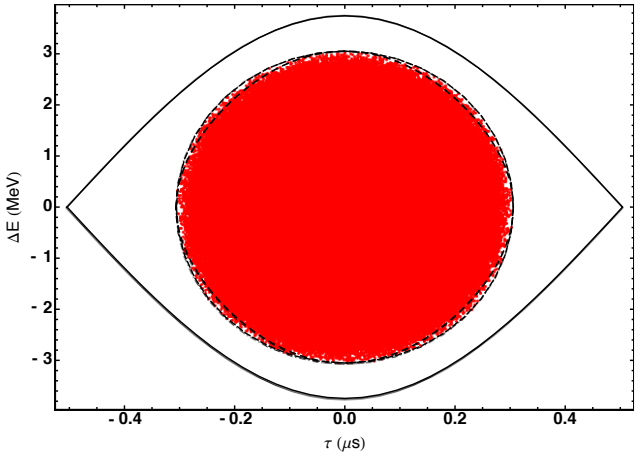


**Figure 3.12:** Longitudinal phase space: The bucket is shown in black, the exact non-linear phase space in dashed and the linear approximation in dashed-dotted. The beam distribution is matched to the phase-space area in linear approximation for simplicity.

frequency (Fig. 3.11). The longitudinal mismatch occurs as the distribution is not matched to the exact non-linear longitudinal phase space - dashed line in Fig. 3.12, but to the linear approximation - dashed-pointed line in Fig. 3.12.

#### 3.4.2.2 Dependence on the number of macroparticles

Because the 2 1/2 D model is a grid based algorithm, the number of macroparticles is linked to the binning of the grid. If the binning of the grid is too large, particles with large amplitudes also experience a strong space-charge kick, leading to an artificial emittance growth. On the other hand, if the bin size is too small, the space-charge calculation is dominated by statistical noise, again leading to artificial blow-up. A rule of thumb for PTC-ORBIT is to use at least 10 macroparticles per gridpoint [72], and as a FFT is used for the space-charge field calculation, the number of bins should be a power of 2 leading to the set of simulation parameters listed in Table 3.13.

| number of bins | number of macroparticles |
|---|---|
| 32 | $5 \times 10^4$ |
| 64 | $1 \times 10^5$ |
| 64 | $2 \times 10^5$ |
| 128 | $5 \times 10^5$ |
| 128 | $8.2 \times 10^5$ |

**Table 3.13:** Simulation parameters used for the investigation of the dependence on the number of macroparticles.

Comparing the development of the rms-emittance (Fig. 3.13) the simulation results converge for a number of bins larger than 128 and more than $5 \times 10^5$ macroparticles, where the criterion for convergence is that the emittance blow-up does not change considerably with a further increase of the number of macroparticles.

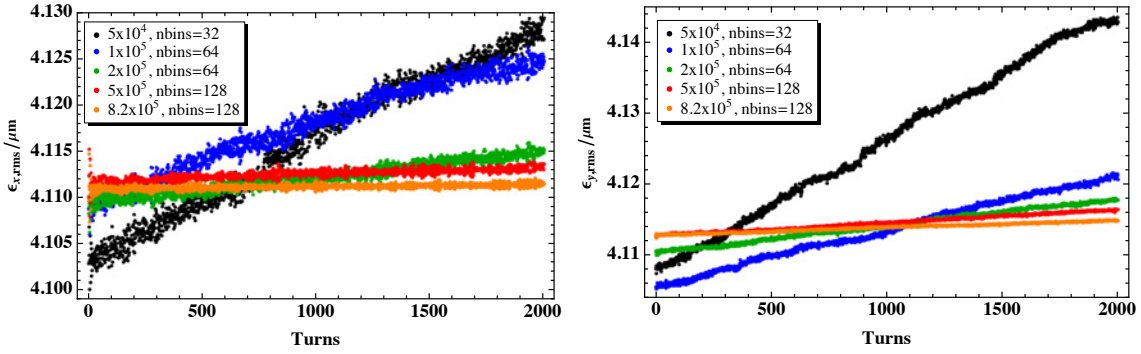


**Figure 3.13:** Time evolution of the horizontal (left) and vertical (right) rms emittance for $1.2 \times 10^{12}$ particles per bunch, a maximum distance of 1 m between space-charge nodes (lmax) and with different number of macroparticles and number of bins.

#### 3.4.2.3 Dependence on the grid binning

In Sec. 3.4.2.2 it has been shown that a minimum of $5 \times 10^5$ macroparticles is necessary. To ensure that for this minimum number of macroparticles the right binning has been

chosen, the number of bins has been varied from $2^4 = 16$ to $2^7 = 128$. Only for the small number of 16 bins, a difference between the simulations is observed and a number of bins of 128 can be considered to deliver reliable simulation results (Fig. 3.14).

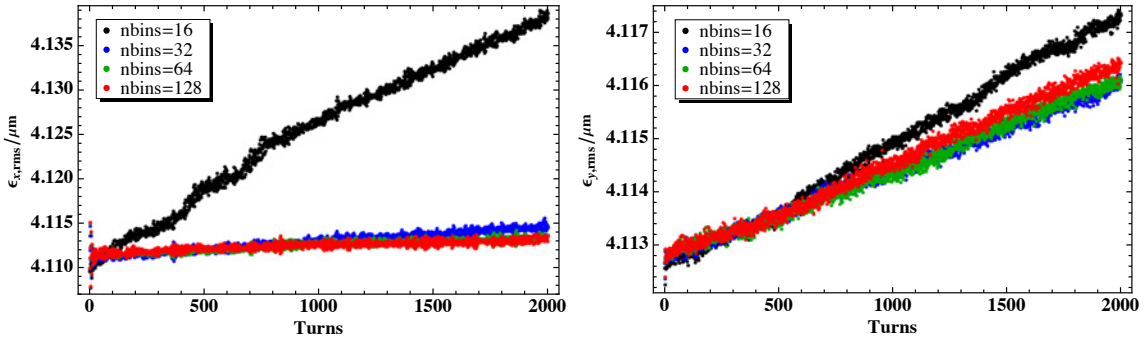


**Figure 3.14:** Time evolution of the horizontal (left) and vertical (right) rms emittance for $1.2 \times 10^{12}$ particles per bunch, $5 \times 10^5$ macroparticles, a maximum distance of 1 m between space-charge nodes (lmax) and different number of bins. Only for the small number of 16 bins the emittance evolution differs from the simulation results with a larger number of bins.

### 3.4.2.4 Dependence on the distance between space charge nodes

An artificial blow-up can not only be caused by an inappropriate choice of the number of macroparticles and bins, but also by too large a distance between the space-charge nodes. A large distance implies strong local non-linear kicks which lead to a stronger excitation of resonances than uniformly distributed kicks. As a rule of thumb more than 10 space-charge nodes per betatron period should be used in the case of PTC-ORBIT [72]. In the case of the simplified PS Booster lattice with a working point around 4 and a length of $50 \cdot \pi$ m, the minimum distance would then be around 4 m. Fig. 3.15 shows the dependence on the distance between space-charge nodes. The emittance behaviour differs only for the largest distance studied (lmax = 4 m).

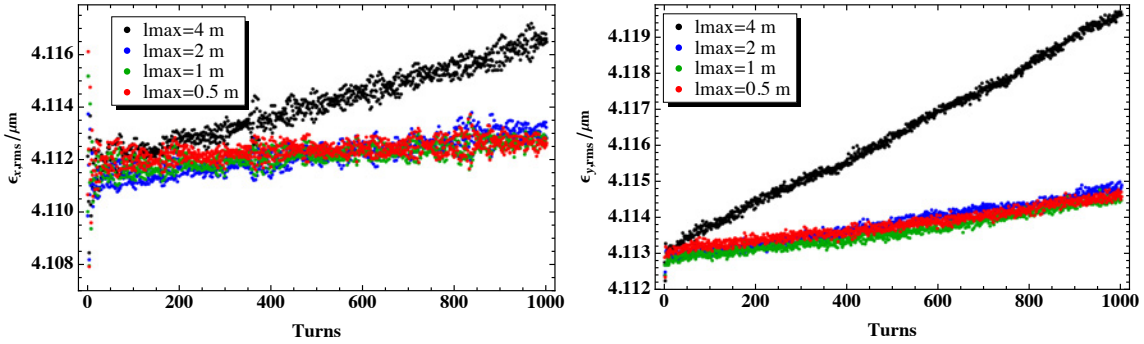


**Figure 3.15:** Time evolution of the horizontal (left) and vertical (right) rms emittance for $1.2 \times 10^{12}$ particles per bunch, $5 \times 10^5$ macroparticles, 128 bins and varying distance lmax between space-charge nodes. Only the largest distance shows a larger emittance growth.

### 3.4.3 Conclusion

In Sec. 3.4.1.1 the final model of the lattice has been compared to a reference model to ensure that the non-linear optics are also described correctly. It is essential to use the exact Hamiltonian in order to obtain the correct chromatic effects.
In Sec. 3.4.2.2 to 3.4.2.4, the dependence of the simulation results on the number of macroparticles, the binning and the distance between space-charge nodes has been investigated. In Sec. 3.4.2.2 it has been shown that a minimum number of $5 \times 10^5$ macroparticles is needed in combination with 128 bins. The 128 bins for $5 \times 10^5$ macroparticles proved to be more than sufficient (Sec. 3.4.2.3). The estimated distance between space-charge nodes of 4 m resulted in an artificial emittanceblow-up (Sec. 3.4.2.4) and the baseline distance has therefore been set to a save value of 1 m, which is significantly smaller than the value expected applying the rule of thumb from [72].
In general, the space-charge calculations need little computation time compared to the PTC tracking time [73]. Thus it is important to reduce the number of macroparticles, but the number of bins and distance between space-charge nodes do not have to be extensively optimized in regard to the CPU time. Therefore, the minimum number of macroparticles of $5 \times 10^5$, a rather large number of bins of 128 and a small distance of only 1 m between the space-charge nodes have been chosen as baseline simulation parameters, summarized in Table 3.14.

| | |
|---|---|
| number of macroparticles | $5 \times 10^5$ |
| number of bins | 128 |
| distance between space-charge nodes | 1 m |

**Table 3.14:** Simulation parameters used in this thesis.

## 3.5 Estimation of Emittance Increase due to Transverse Mismatch

The equations of motion including space-charge are only linear for elliptical transverse profiles (K.V. distribution), and can be analytically solved for the same, but not for any other distribution (see Sec. 1.6.4). This makes it rather difficult and laborious to create a matched initial distribution including all non-linearities introduced by the space-charge field, and usually the initial distribution is only matched to the undisturbed lattice where undisturbed denotes no space-charge nor other sources of non-linearities. For large intensities it could therefore be possible that a different initial blow-up due to filamentation of mismatch occurs for different lattices. This blow-up is expected to be ”fast” compared to the blow-up due to resonance excitation. To get a rough estimate of the increase of the emittance and change of the beta-function due to mismatch, an exemplary study using the simplified PS Booster lattice has been performed in the framework of this thesis. It is expected that the blow-up increases with the intensity. Analytical estimates for the scaling

of emittance and beta function with the beam intensity are derived in Appendix H. Note that Appendix H only treats the linear mismatch and not the non-linear mismatch due to magnet non-linearities and space-charge. To obtain the estimate for the full intensity, the distribution matched to the undisturbed lattice has been tracked for different intensities over 200 turns corresponding to approximately 1 000 betatron oscillations, which is considered to be sufficient to reach the new equilibrium distribution for the lattice with space-charge. The emittance and beta-function were determined from the moments of the distribution using Eqn. 1.18 and Eqn. 1.19

$$\epsilon_{z,\mathrm{rms}} = \sqrt{\sigma_z^2\sigma_{z'}^2 - \sigma_{zz'}^2}\,, \tag{3.1}$$

$$\beta_z = \frac{\sigma_z^2}{\epsilon_{z,\mathrm{rms}}}\,. \tag{3.2}$$

The phase space coordinates $z$ and $z'$ with $z = x, y$ are only the part of the betatron motion and are calculated under the assumption of intensity independent dispersion ($D_z(I) = D_z(I = 0)$)

$$z = z_{\mathrm{tot}} - D_z\frac{\delta p}{p}\,, \tag{3.3}$$

$$z' = z'_{\mathrm{tot}} - D'_z\frac{\delta p}{p}\,. \tag{3.4}$$

The error made due to this assumption is expected to be small.
The simulations have been carried out for the nominal working point of $Q_x/Q_y = 4.28/3.55$ and the working point of $Q_x/Q_y = 4.29/3.38$ used for the convergence study (Sec. 3.4.2). For the nominal high intensity tune of $Q_x/Q_y = 4.28/3.55$ a large emittance blow-up is expected for low intensities due to the excitation of the vertical half integer resonance.

### 3.5.1 Simulation results for $Q_x = 4.29$, $Q_y = 3.38$

In Fig. 3.16 the beta-function as a function of the beam intensity is shown. As derived in Appendix H, the beta-function depends linearly on the beam intensity

$$\Delta\beta_{x,y} = a_{x,y}\cdot I\,.$$

The gradient obtained from the linear fit to the simulation results is

$$a_x = 5.1\times10^{-14}\,\mathrm{m}, \quad a_y = 1.3\times10^{-13}\,\mathrm{m} \tag{3.5}$$

yielding a relative change of the beta function for full intensity of

$$\frac{\Delta\beta_x}{\beta_{x,\mathrm{init}}} = 0.024, \quad \frac{\Delta\beta_y}{\beta_{y,\mathrm{init}}} = 0.053 \tag{3.6}$$

As illustrated in Fig. 3.17, the rms emittance calculated from the beam distribution increases quadratically with the beam intensity. The equation for the emittance growth (Eqn. H.10) derived in Appendix H

$$\frac{\Delta\epsilon}{\epsilon_{\mathrm{init}}} = \frac{(aI)^2}{2\beta_{\mathrm{init}}(\beta_{\mathrm{init}} + a\cdot I)} \tag{3.7}$$

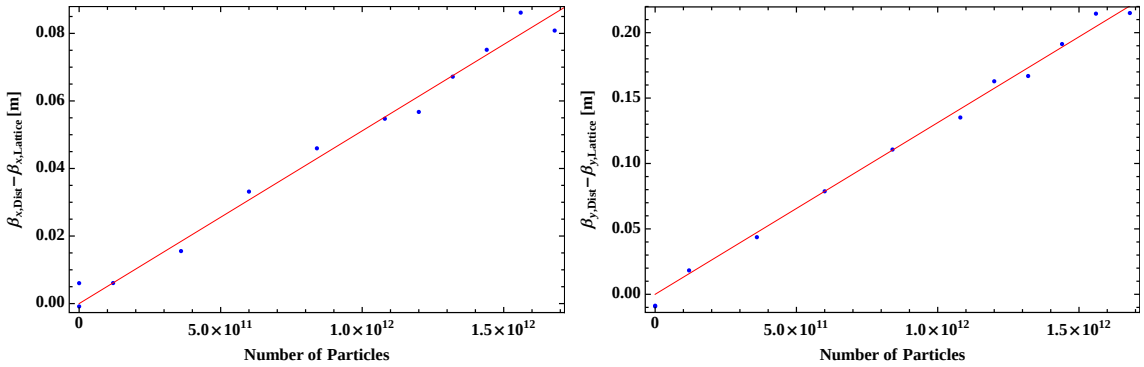


**Figure 3.16:** Difference between horizontal (left) and vertical (right) beta-function of the undisturbed lattice and the beta-function determined from the tracked distribution after 200 turns for a working point of $Q_x/Q_y = 4.29/3.38$. The simulation results are shown in blue and the linear fit in red.

gives the correct order of magnitude, but does not agree exactly with simulation results. The difference could be due to non-linearities or dispersive effects, as the discrepancy is larger in the horizontal plane. The quadratic fit to the emittance increase yields

$$\frac{\Delta\epsilon_x}{\epsilon_{x,\mathrm{init}}} = 4.89 \times 10^{-28}\ I^2, \quad \frac{\Delta\epsilon_y}{\epsilon_{y,\mathrm{init}}} = 1.61 \times 10^{-28}\ I^2 \tag{3.8}$$

Extrapolating to the full beam intensity of $2.4 \times 10^{12}$ one obtains

$$\frac{\Delta\epsilon_x}{\epsilon_{x,\mathrm{init}}} = 0.0028, \quad \frac{\Delta\epsilon_y}{\epsilon_{y,\mathrm{init}}} = 0.00093 \tag{3.9}$$

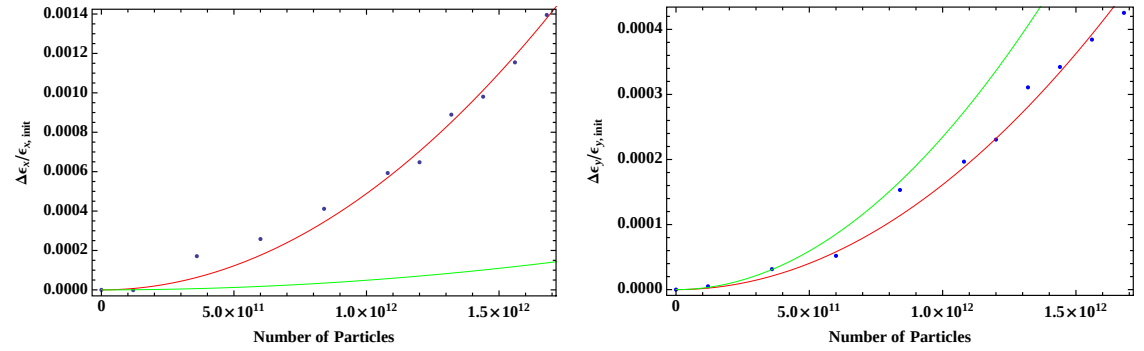


**Figure 3.17:** Difference between horizontal (left) and vertical (right) rms emittance of the undisturbed lattice and the rms emittance determined from the tracked distribution after 200 turns for a working point of $Q_x/Q_y = 4.29/3.38$. In both planes the emittance increases quadratically with the intensity as derived in appendix H. The simulation results are shown in blue, the quadratic fit in red and the analytical estimation using Eqn. H.10 in green.

### 3.5.2 Simulation results for $Q_x = 4.28$, $Q_y = 3.55$

The linear fit to the beta-function as a function of the intensity, shown in Fig. 3.18, yields the following gradients:

$$a_x = 4.73 \times 10^{-14}\,\mathrm{m}, \quad a_y = 1.21 \times 10^{-13}\,\mathrm{m} \tag{3.10}$$

giving a relative change of the beta function for full intensity of

$$\frac{\Delta\beta_x}{\beta_{x,\text{init}}} = 0.022, \quad \frac{\Delta\beta_y}{\beta_{y,\text{init}}} = 0.052 \tag{3.11}$$

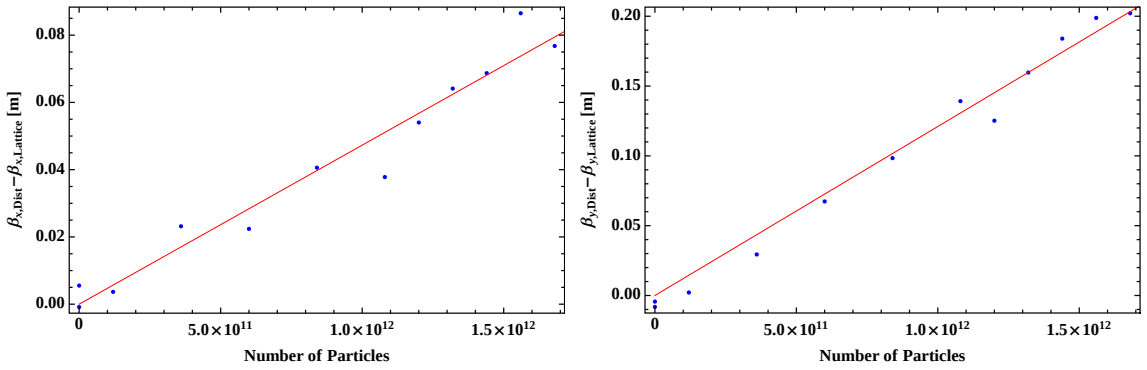


**Figure 3.18:** Difference between horizontal (left) and vertical (right) beta-function of the undisturbed lattice and the beta-function determined from the tracked distribution after 200 turns for a working point of $Q_x/Q_y = 4.28/3.55$. The simulation results are shown in blue and the linear fit in red.

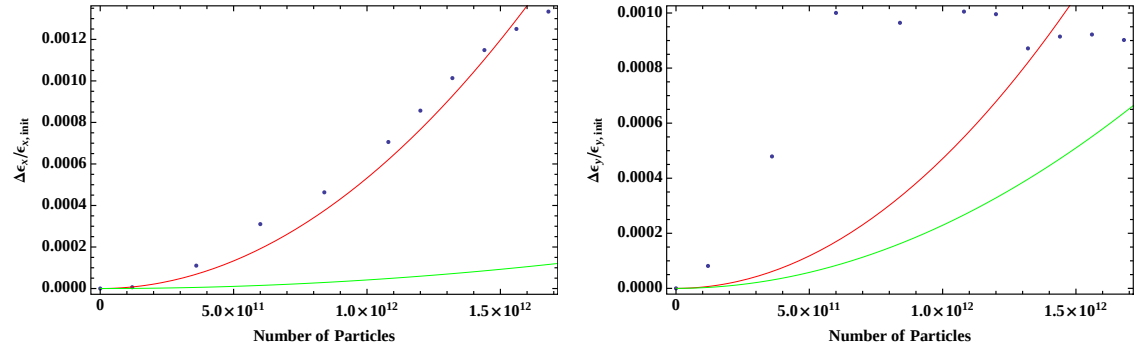


**Figure 3.19:** Difference between horizontal (left) and vertical (right) rms emittance of the undisturbed lattice and the rms emittance determined from the tracked distribution after 200 turns for a working point of $Q_x/Q_y = 4.28/3.55$. In the vertical plane the increase of the emittance is probably not caused by the mismatch but by the excitation of the half integer resonance. The simulation results are shown in blue, the quadratic fit in red and the analytical estimation using Eqn. H.10 in green.

Fig. 3.19 shows the emittance increase with intensity. As suspected, the emittance increase in the vertical plane is dominated by the excitation of the half integer resonance. We therefore estimate the increase of the emittance by using the quadratic fit for the horizontal plane and Eqn. 3.7 for the vertical plane with $a_y$ given by 3.10

$$\frac{\Delta\epsilon_x}{\epsilon_{x,\text{init}}} = 5.32 \times 10^{-28}\ I^2, \quad \frac{\Delta\epsilon_y}{\epsilon_{y,\text{init}}} = 2.34 \times 10^{-28}\ I^2 \quad \text{(analytical)} \tag{3.12}$$

The extrapolation to the full beam intensity of $2.4 \times 10^{12}$ then yields

$$\frac{\Delta\epsilon_x}{\epsilon_{x,\text{init}}} = 0.0031, \quad \frac{\Delta\epsilon_y}{\epsilon_{y,\text{init}}} = 0.0013 \quad \text{(analytical)} \tag{3.13}$$

### 3.5.3 Conclusion

The results of the studies on the mismatch due to generating macroparticle distributions neglecting direct space-charge and lattice non-linearities are summarized in Table 3.15. For both working points the beta-function shows a linear increase with intensity, leading to a relatively small change at full intensity. For $Q_x/Q_y = 4.29/3.38$ the emittance increases quadratically in both planes and an estimate can be obtained from the extrapolation of the quadratic fit to the full intensity, while for $Q_x/Q_y = 4.28/3.55$ a large blow-up of the vertical emittance is observed. This can be explained by the excitation of the vertical half integer resonance in the case of $Q_x/Q_y = 4.28/3.55$. In this case an estimate can only be obtained from Eqn. 3.7. For both planes the initial emittance increase due to mismatch lies in the per-mil range and can thus be neglected in general.

| | $\boldsymbol{Q_x/Q_y = 4.29/3.38}$ | $\boldsymbol{Q_x/Q_y = 4.28/3.55}$ |
|---|---|---|
| $\frac{\Delta\beta_x}{\beta_{x,\mathrm{init}}}$ | 0.024 | 0.022 |
| $\frac{\Delta\beta_y}{\beta_{y,\mathrm{init}}}$ | 0.053 | 0.052 |
| $\frac{\Delta\epsilon_x}{\epsilon_{x,\mathrm{init}}}$ | 0.0028 | 0.0031 |
| $\frac{\Delta\epsilon_y}{\epsilon_{y,\mathrm{init}}}$ | 0.00093 | 0.0013 |

**Table 3.15:** Results of the studies on initial betatron mismatch.

## 3.6 Lattice Studies

In this sections, the studies of the different lattices, investigated in the framework of this thesis, are presented. Motivated by the different design of the PS Booster and RCS, the lattices have been studied with respect to their different cell types, number of cells, symmetries and dispersion suppressor schemes.

The general beam, lattice and simulation parameters used in all simulations are given in Sec. 3.3 and Table 3.14. Assuming a cycle of 10 Hz and a linear ramp-up for 60% of the cycle and 40% for the ramp-down, the full ramp-up would take about 100 000 turns. A simulation of the full ramp-up is therefore unrealistic due to excessive computing requirements. As the space-charge force scales with $1/(\beta\gamma^2)$, the space-charge effect is most relevant at low energy and it is sufficient to simulate only a smaller number of turns with realistic CPU time requirements, explicitly 10 000 turns have been simulated.

In order to compare only the influence of the space-charge effect, no fringe fields except the very weak dipole fringe fields (which can not be disabled) have been simulated (except in Sec. 3.6.2 which is explicitly addressing this subject).

### 3.6.1 Dependence on the lattice cell and variation of the beam size

Many modern lattices are based on a FODO cell structure, which exhibits a relatively large variation of the beam size compared to a doublet or triplet lattice as used for the

PS Booster. A very smooth variation of the beam size, and in particular small variations of the ratio between the two transverse sizes, as featured by triplet focusing, results in an almost uniformly distributed space-charge field, while a large variation of the beam size entails a varying strength of the non-linear space-charge kick. The latter case is expected to lead to stronger resonance excitation.
All lattices presented in this section consist of 16 equal cells and thus have a periodicity and symmetry of 16 and are matched to a working point of $Q_x/Q_y = 4.28/3.55$.

#### 3.6.1.1 Comparison of triplet, doublet, long doublet and FODO

The triplet lattice features the least variation of the beam size, then the doublet, the long doublet (doublet with a larger distance between the quadrupoles) and finally the FODO lattice with the largest variations. The maximum and minimum beam size for all four

| | **unit** | **triplet** | **doublet** | **long doublet** | **FODO** |
|---|---|---|---|---|---|
| $\sigma_{x,\max}/\sigma_{x,\min}$ | mm | 6.02/4.56 | 7.89/4.29 | 8.26/4.00 | 8.46/3.62 |
| $\Delta\sigma_x$ | mm | 1.46 | 3.60 | 4.25 | 4.84 |
| $\sigma_{y,\max}/\sigma_{y,\min}$ | mm | 8.11/4.79 | 7.33/4.44 | 7.82/4.08 | 8.17/3.78 |
| $\Delta\sigma_y$ | mm | 3.32 | 2.89 | 3.75 | 4.39 |

**Table 3.16:** Maximum and minimum rms beam size for triplet, doublet, long doublet and FODO lattice, where the notation $\Delta\sigma_{x/y} = \sigma_{x/y,\max} - \sigma_{x/y,\min}$ was used.

lattices is listed in Table 3.16. The optics are shown in Fig. 3.20 and the one rms beam envelope for all four cell types in Fig. 3.21.

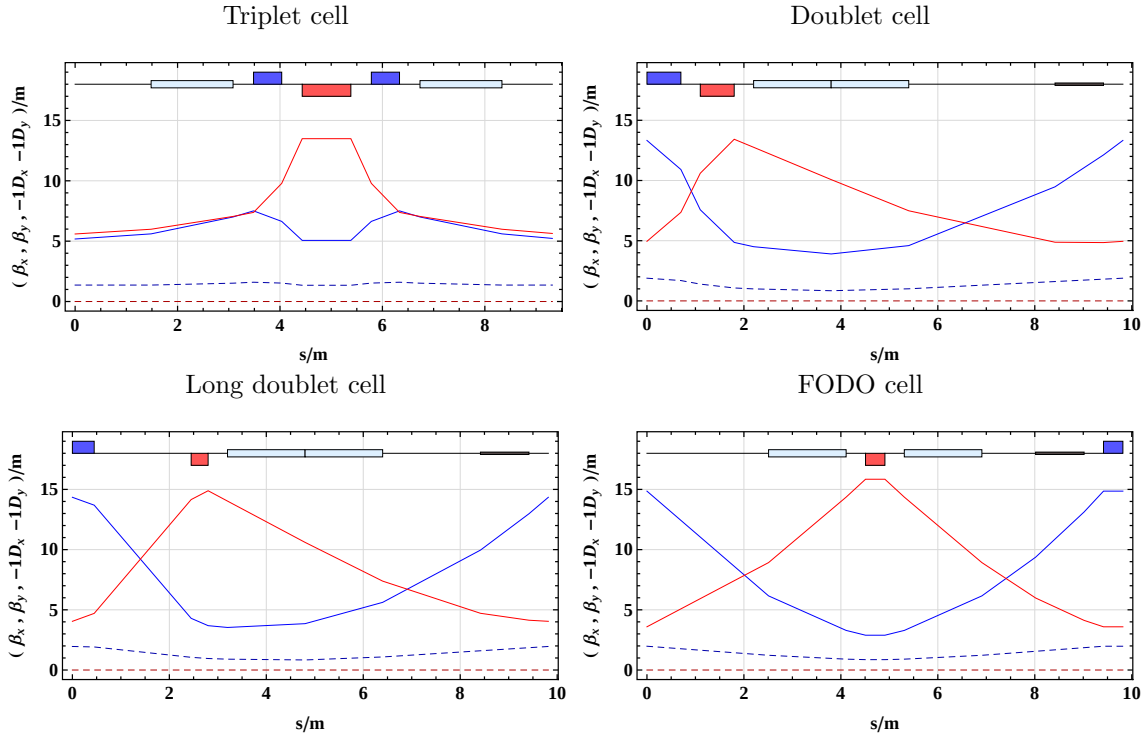


**Figure 3.20:** Optics of the different lattice cells.

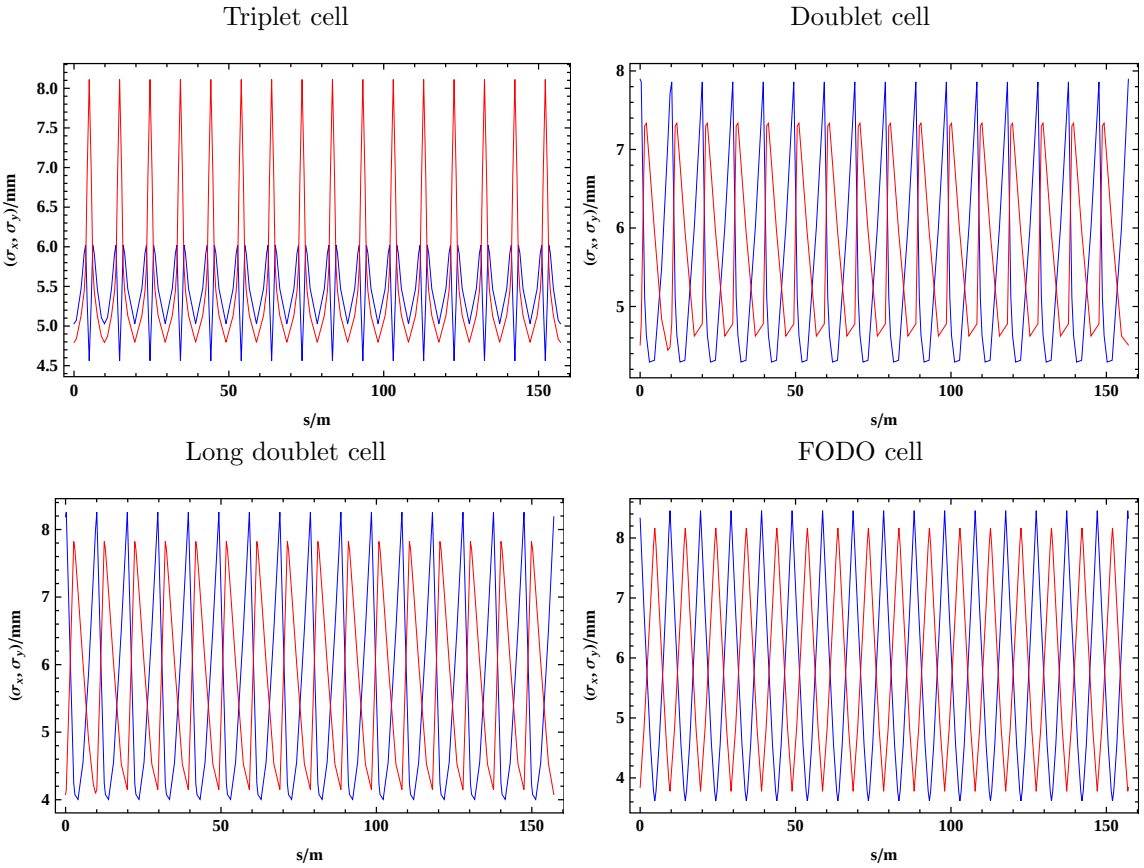


**Figure 3.21:** One rms beam envelope of the 16 cell lattice built of different lattice cells. The beam envelope has been calculated using the design transverse normalized rms emittance of 2.5 $\mu$m and the rms momentum spread corresponding to the design longitudinal emittance of 2.8 eVs.

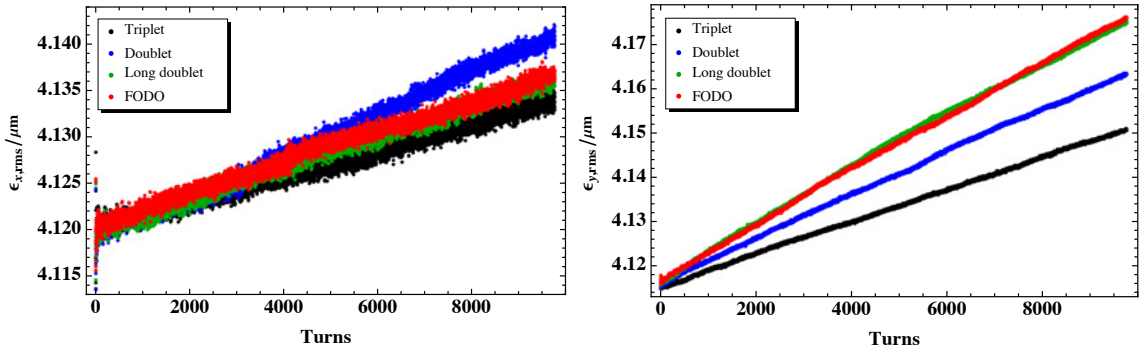


**Figure 3.22:** Time evolution of horizontal (left) and vertical (right) rms emittance for different lattice cells.

Neglecting quadrupole fringe field effects, the least rms emittance growth is observed, as expected, for the triplet lattice, followed by the doublet, while the long-doublet and FODO cell exhibit the same emittance behaviour (Fig. 3.22). Comparing the difference between the maximum and minimum beam size, the triplet has the smallest difference in the horizontal plane, but a large difference in the vertical plane. This large difference occurs only over a small length, which turns out to be of little importance (Sec. 3.6.1.2). For the doublet, long doublet and FODO lattice the large variations are not limited to a small section, as is the case for the triplet, and the difference between the maximum and minimum beam size represents a qualitative measure for the expected emittance growth.

### 3.6.1.2 Variation of the beam size

The results of Sec. 3.6.1.1 indicate that not only the maximum variation of the beam size plays an important role, but also the duration of the variation. To investigate this matter, a triplet cell "collapsed" to almost zero length has been compared to the triplet cell of the simplified PS Booster lattice. Both optics are shown in Fig. 3.23. In particular, the section with a high vertical beta function is shortened in the case of the collapsed triplet cell and with it the length of the large variation of the beam size.

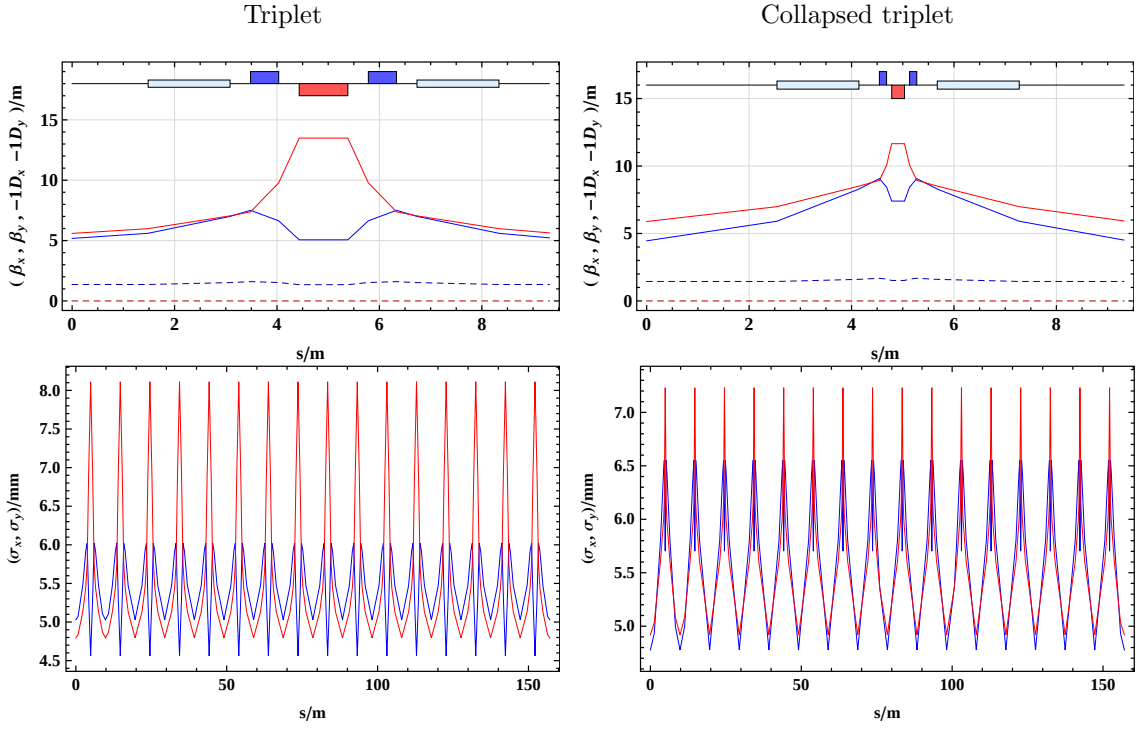


**Figure 3.23:** Optics and one rms beam envelope of the triplet and collapsed triplet cell lattice. The beam envelope has been calculated using the design transverse normalized rms emittance of 2.5 $\mu$m and the rms momentum spread corresponding to the design longitudinal emittance of 2.8 eVs.

Simulations confirm this hypothesis as the emittance growth in the vertical plane for the collapsed triplet is slightly less than for the triplet (Fig. 3.24 (right)) while the horizontal plane stays unchanged (Fig. 3.24 (left)).

For most low energy circular accelerators, the space-charge effect is weaker in the horizontal than in the vertical plane, due to the non-vanishing horizontal dispersion and thus larger

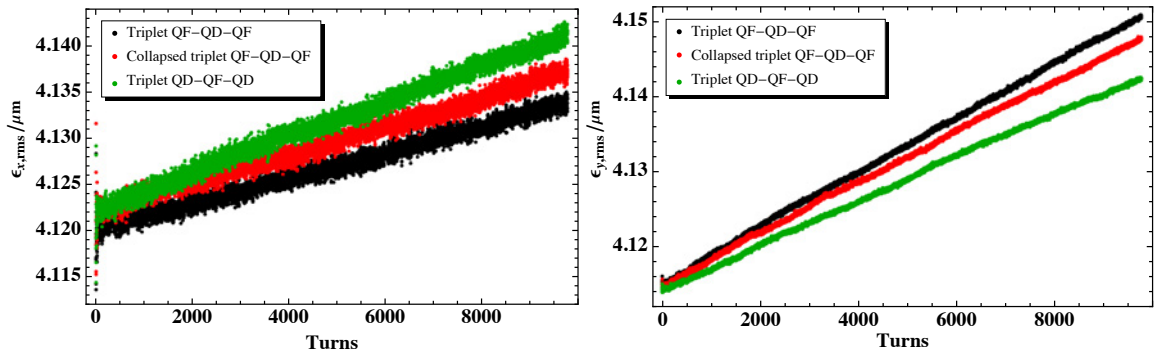


**Figure 3.24:** Time evolution of horizontal (left) and vertical (right) rms emittance for the triplet, collapsed triplet and inverted triplet lattice.

beam size. The comparison of the different cells revealed that the variation of the beam size has a non-negligible influence on the emittance growth. In some cases e.g. the triplet lattice, where a large variation is only given in one plane, it could therefore be advantageous to have the large variation of the beam size in the plane with the larger beam size. Fig. 3.25 shows the optics of a 16 cell lattice with an inverted triplet cell, the QF is in the center of the cell, for which the large variation of the beam size occurs in the horizontal plane. Compared to the triplet, the inverted triplet exhibits a smaller emittance growth in the

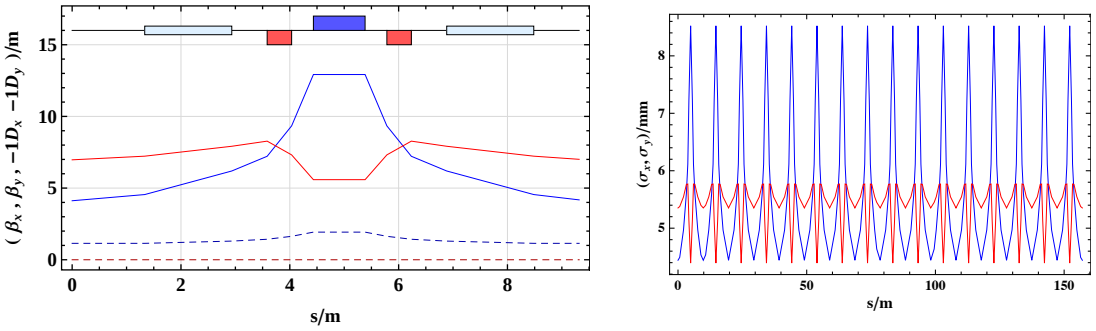


**Figure 3.25:** Optics and one rms beam envelope for the inverted triplet cell (QD-QF-QD). The beam envelope has been calculated using the design transverse normalized rms emittance of 2.5 $\mu$m and the rms momentum spread corresponding to the design longitudinal emittance of 2.8 eVs.

vertical and a slightly larger growth in the horizontal (Fig. 3.24), which is just the desired behaviour. In reality, a larger variation of the horizontal beam size is often not practical as it implies a large beam size at all or some of the focusing quadrupoles, resulting in a large required magnet aperture, limiting the achievable quadrupole gradients.

### 3.6.2 Influence of fringe fields

In all other sections, no fringe fields (only the very weak dipole fringe fields as they cannot be disabled) have been simulated in order to isolate the emittance blow-up caused by the space-charge effect. In reality, fringe fields are always present. To give an example of the influence of fringe fields, Fig. 3.26 shows the emittance evolution for the triplet, doublet and FODO cell lattice of Sec. 3.6.1.1, but now including both dipole and quadrupole fringe fields. First one notes that the emittance blow up, mainly in the vertical plane, is in all

cases considerably higher than for the lattices without fringe fields. Furthermore, the triplet and doublet lattice now show more or less the same emittance growth in contrast to the results obtained in Sec. 3.6.1.1 where the triplet lattice showed the smaller emittance growth. Also including the fringe fields the FODO lattice still shows the largest emittance growth despite the by approximately a factor of two smaller integrated quadrupole strength with regard to the doublet cell lattice.

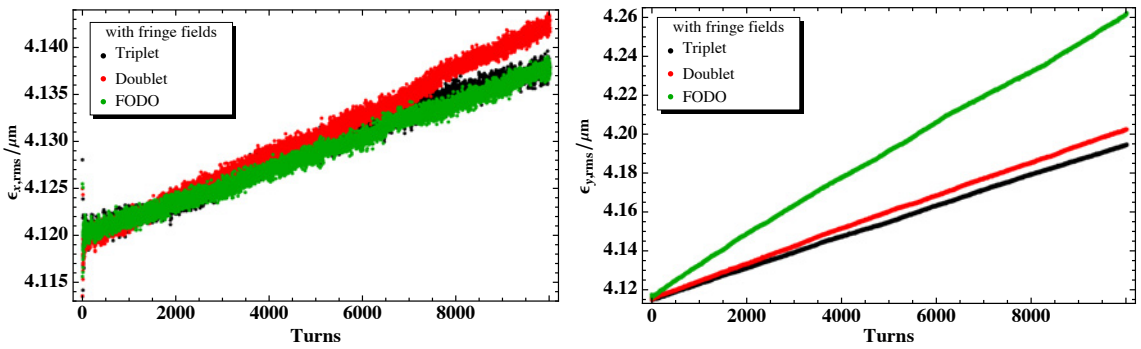


**Figure 3.26:** Time evolution of horizontal (left) and vertical (right) rms emittance for different lattice cells including fringe fields.

A second example is the collapsed triplet cell lattice of Sec. 3.6.1.2. Including the quadrupole fringe fields in the simulation, a very large emittance growth illustrated in Fig. 3.27 is observed for the collapsed triplet due to the very high quadrupole gradients required for this lattice.

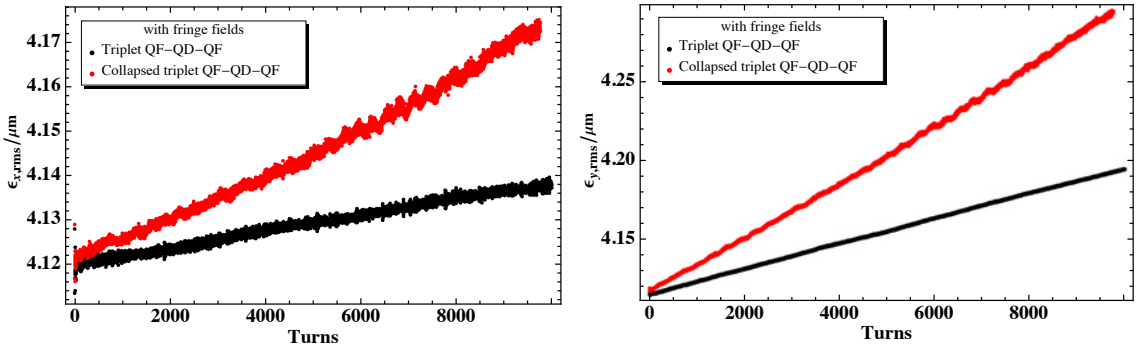


**Figure 3.27:** Time evolution of horizontal (left) and vertical (right) rms emittance for the triplet and collapsed triplet including fringe fields.

In general, a smoother focusing and small variation of the beam size, which is advantageous in the case of strong space-charge effects, can be achieved with a large number of strong focusing magnets, but the effect of the fringe fields would most probably undo the beneficial effect of the small variation of the beam size. For a realistic estimate of the blow-up to be expected in a real machine, the effect of the fringe fields has to be taken into account.

### 3.6.3 Influence of weak symmetry breaking

The lattices proposed for the CERN RCS all possessed a low symmetry of 2, 3 or 4 compared to 16 for the PS Booster. In this section, the importance of symmetries is

studied on the example of variations of the simplified PS Booster lattice (Sec. 3.1.2). The symmetry of the lattice is broken by shortening the bends in one triplet cell. The beta-beating introduced is corrected by matching the modified cell to the arc with the quadrupole triplet next to the shortened bends. The phase advance is then rematched by adjusting the phase advance of the arc cell. This procedure is repeated until the target tune of $Q_x/Q_y = 4.28/3.55$ is reached. Fig. 3.28 shows the optics for the lattice with symmetry 1, with and without beta-beating correction, Fig. 3.29 shows the optics of the lattices with symmetry 2 and 4 and beta-beating correction, and the simplified PS Booster lattice with symmetry 16 is shown in Fig. 3.2.

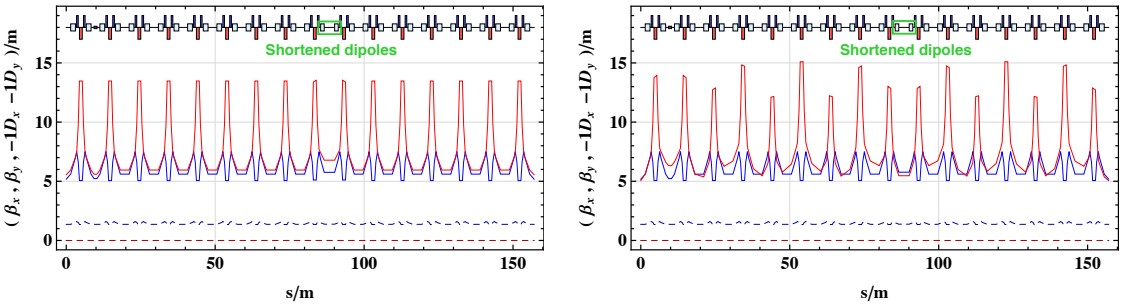


**Figure 3.28:** Optics of the simplified PS Booster lattice with symmetry 1.
(left) With beta-beating correction (right) Without beta-beating correction

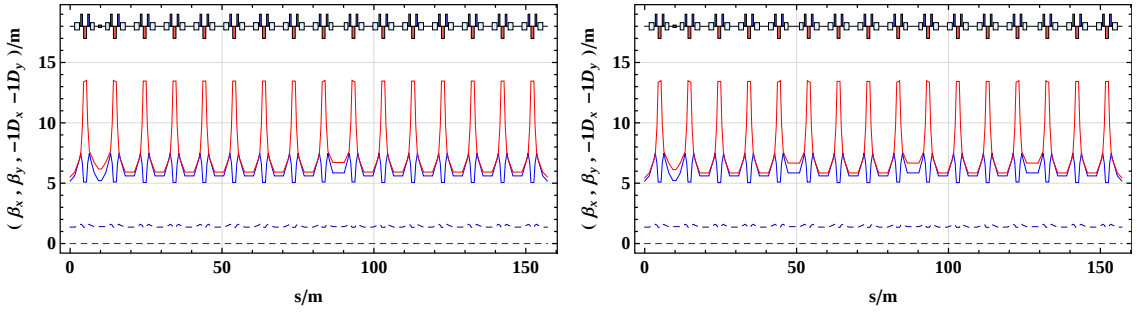


**Figure 3.29:** Optics of the simplified PS Booster lattice with symmetry 2 (left) and symmetry 4 (right) and beta-beating correction in both cases.

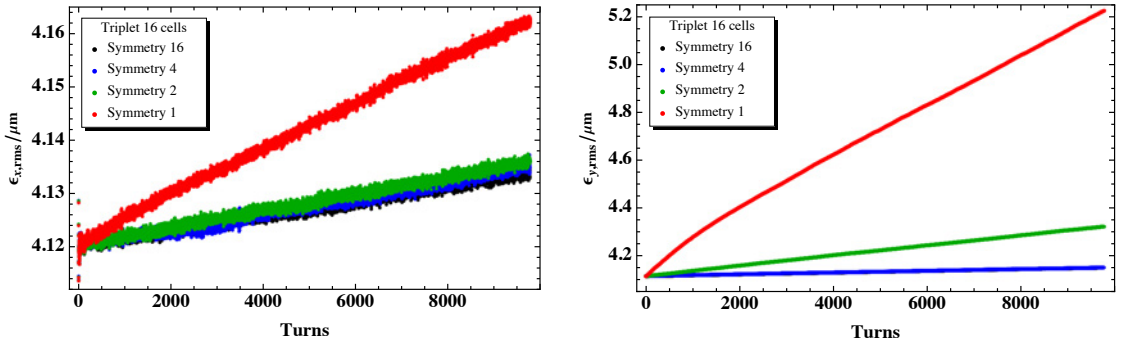


**Figure 3.30:** Time evolution of horizontal (left) and vertical (right) rms emittance for symmetry 1, 2, 4 and 16.

The time evolution of the rms emittance for the different lattice symmetries is plotted in Fig. 3.30. As expected, the lattice with the lowest symmetry (symmetry 1) shows the

largest blow-up. In the case of the lattice with a symmetry of 2 the emittance growth is already considerably reduced and no difference can be seen between symmetry 4 and 16. In order to understand this result better, especially why the lattices with symmetry 4 and 16 feature the same emittance evolution, the tool of an analysis of the beam moments has been used. In general, the rms emittance blow-up in the case of space-charge dominated beams is mostly caused by the coherent excitation of resonances [74]. Which resonances are excited coherently can be obtained by a Fourier analysis of the beam moments [27]. The order of the excited resonance corresponds directly to the coherent oscillation of the corresponding moment of the distribution. For example, the excitation of the $4Q_y$ resonance would appear as a coherent oscillation of the $< y^4 >$ moment and the excitation of the $Q_x + 3Q_y$ resonance as a coherent oscillation of the $< xy^3 >$ moment.

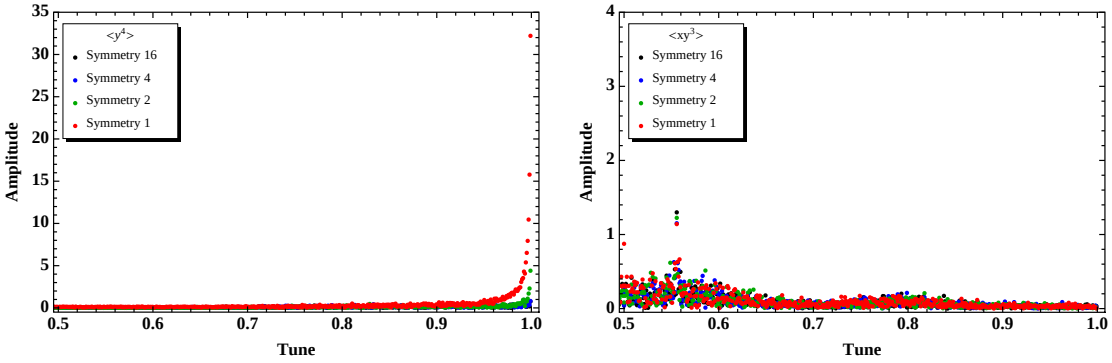


**Figure 3.31:** Discrete Fourier Transformation of the $< y^4 >$ (left) and $< xy^3 >$ (right) moment of the beam after 1024 turns.

Two examples of a Fourier transformation of the $< y^4 >$ and $< xy^3 >$ moment for the different symmetries are given in Fig. 3.31. A coherent oscillation of the $< y^4 >$ moment is visible for symmetry 1 and 2, appearing as a high amplitude at a tune of 1.0, while for $< xy^3 >$ the amplitude is 0 close to a tune of 1.0, but non-zero for the tune of the machine of 0.55.

| | symmetry | | | |
|---|---|---|---|---|
| moment | 16 | 4 | 2 | 1 |
| $< x >$ | 0 | 0 | 0 | 0 |
| $< y >$ | 0 | 0 | 0 | 0 |
| $< x^2 >$ | 2.57 | 2.57 | 2.57 | 2.57 |
| $< xy >$ | 0 | 0 | 0 | 0 |
| $< y^2 >$ | 0 | 0 | 0 | 0 |
| $< x^3 >$ | 0 | 0 | 0 | 0 |
| $< x^2y >$ | 0 | 0 | 0 | 0 |
| $< xy^2 >$ | 0 | 0 | 0 | 0 |
| $< y^3 >$ | 0 | 0 | 0 | 0 |
| $< x^4 >$ | 115.71 | 115.69 | 115.59 | 115.80 |
| $< x^3y >$ | 0 | 0 | 0 | 0 |
| $< x^2y^2 >$ | 11.53 | 11.46 | 11.56 | 12.18 |
| $< xy^3 >$ | 0 | 0 | 0 | 0 |

| | | | | |
|---|---|---|---|---|
| $< y^4 >$ | 0 | 0 | 4.40 | 32.21 |
| $< x^5 >$ | 63.0 | 61.09 | 63.31 | 62.07 |
| $< x^4 y >$ | 5.66 | 4.26 | 6.41 | 3.85 |
| $< x^3 y^2 >$ | 4.78 | 4.52 | 4.92 | 6.52 |
| $< x^2 y^3 >$ | 0 | 1.02 | 0 | 0 |
| $< x y^4 >$ | 3.05 | 2.77 | 4.80 | 12.90 |
| $< y^5 >$ | 0 | 0 | 0 | 0 |

**Table 3.17:** Maximum amplitude close to a tune of 1.0 of the Fourier analysis of the beam moments after 1 024 turns for symmetry 1, 2, 4 and 16 . Raised amplitudes are indicated in red.

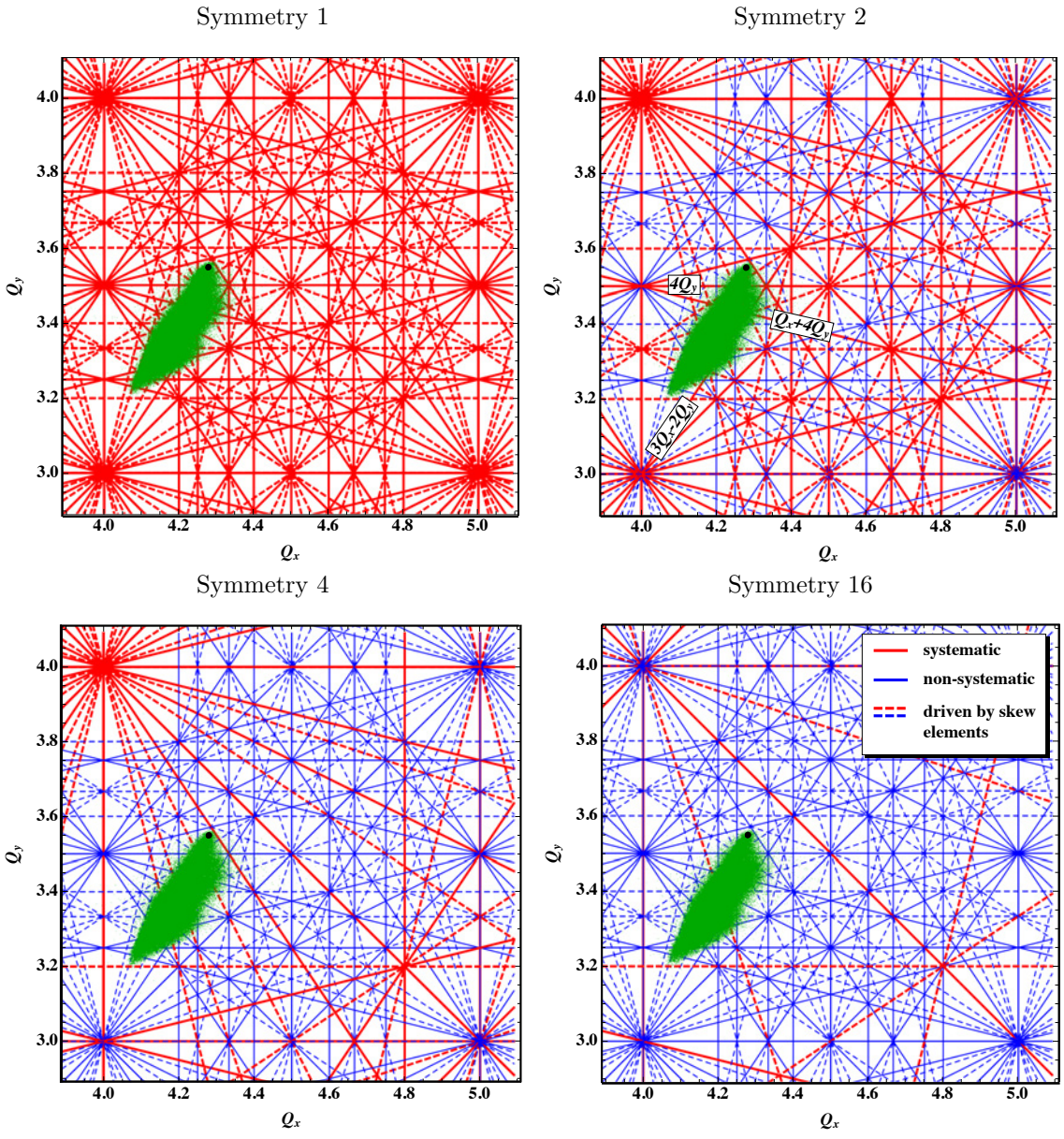


**Figure 3.32:** Resonance diagram until 5th order and tune footprint for symmetry 1, 2, 4 and 16.

The maximum amplitude close to a tune of 1.0 of the beam moments up to 5th order for the different symmetries is listed in Table 3.17. To determine which resonances are excited, only the moments of the first 1 024 turns have been analysed, as the results of the analysis of all turns is dominated by the emittance growth, e.g. an increase of the amplitude of the $< y^2 >$ momentum, erroneously leading to the conclusion of the excitation of the vertical half integer resonance. The moment analysis leads to the conclusion that the emittance growth for symmetry 2 and 1 is caused by the excitation of the $4Q_y$ and $Q_x + 4Q_y$ resonance, which are not excited or less excited for symmetry 4 and 16, as both resonances are systematic for symmetry 2 and 1, but non-systematic for symmetry 4 and 16 (Fig. 3.32), confirming the results of the moment analysis.

### 3.6.4 Dependence on the symmetry and periodicity and relevance of systematic resonances.

To avoid the Montague resonance [65], it is furthermore advisable to choose different integer parts of the tune. In addition, a small phase advance per cell is advantageous (Sec. 3.6.6),

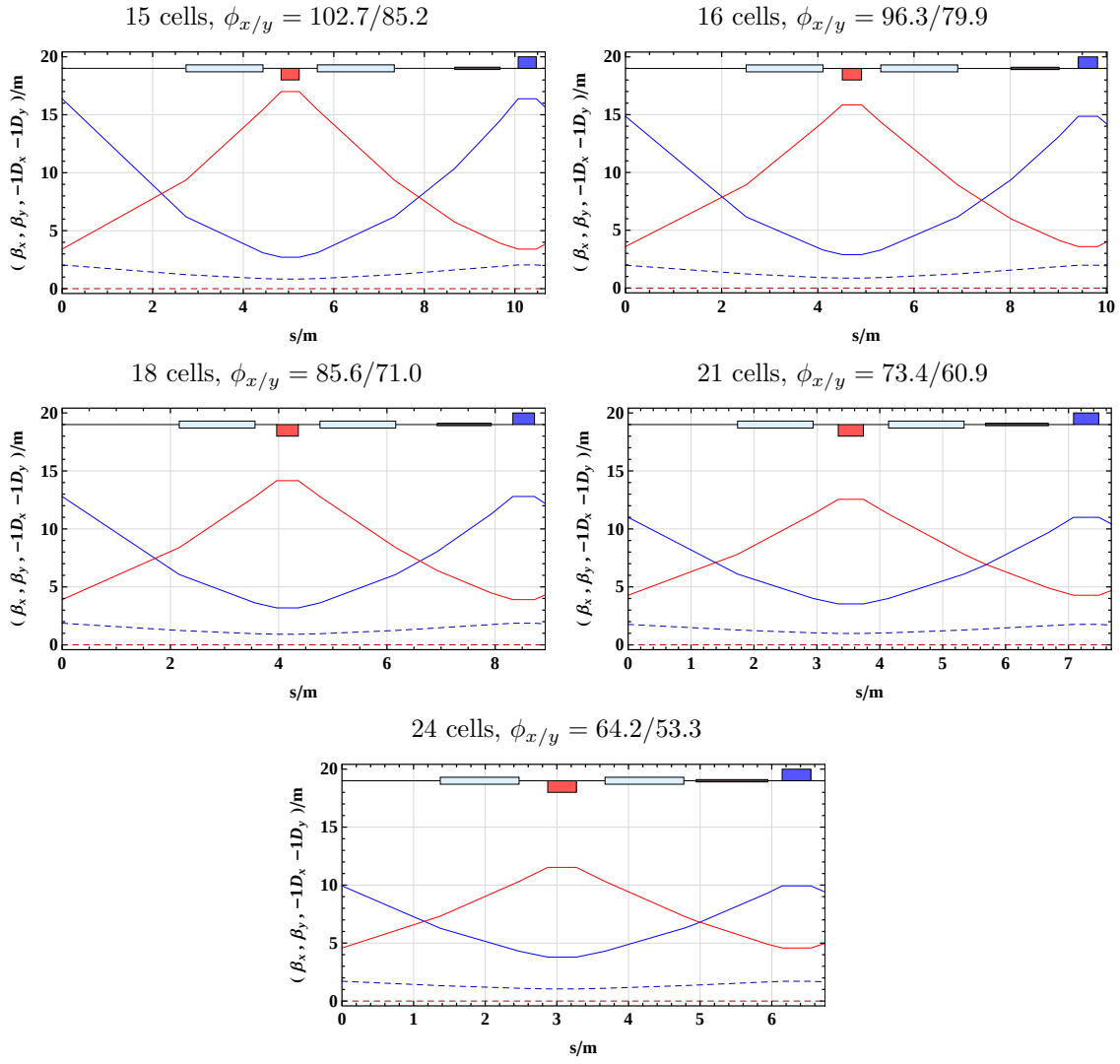


**Figure 3.33:** Optics of one FODO cell for periodicity 15, 16, 18, 21 and 24 and a working point of $Q_x/Q_y = 4.28/3.55$.

implying a preference for a high number of lattice cells. All these constraints often do not leave much choice for the area of possible working points and it is important to choose the symmetry of the machine carefully, as it determines which resonances are systematic or non-systematic. In this section, the importance of systematic resonances is investigated on the example of a FODO cell lattice with a varying number of cells, explicitly 15, 16, 18, 21 and 24 cells and a working point of $Q_x/Q_y = 4.28/3.55$. The same dipole field is assumed for all lattices and the dipole length adjusted accordingly. The length of the quadrupoles is kept constant as the gradient does not change considerably for all lattices. The optics of one lattice cell are shown in Fig. 3.33 for the different number of cells. The maximum dispersion and beta-function depend only weakly on the phase advance for the lattices considered (Appendix A), resulting in a smoother lattice with an increasing number of cells. The emittance growth is expected to decrease with an increasing number of cells (see Sec. 3.6.6), in disagreement with the obtained results shown in Fig. 3.34, revealing strong variations but, at first sight, no correlation with the phase advance per cell, i.e. for the lattices with symmetry 16 and 24 very little blow-up has been found while the lattices with symmetry 15, 18 and 21 show a large blow-up. The emittance development

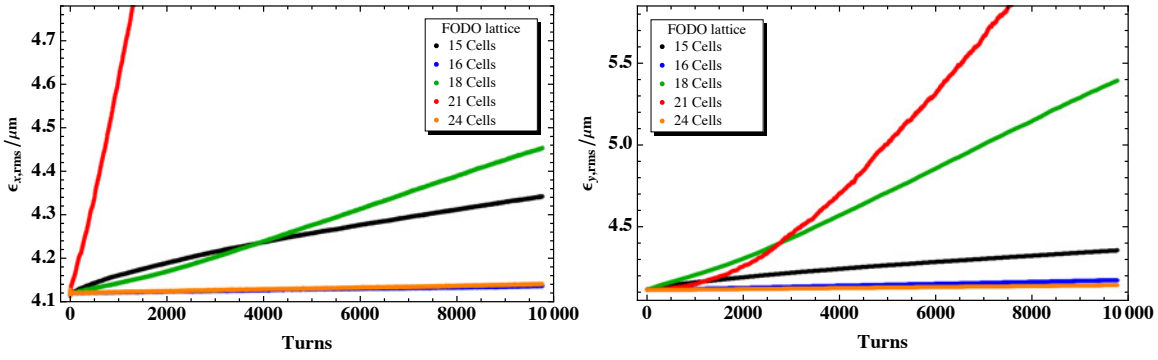


**Figure 3.34:** Time evolution of horizontal (left) and vertical (right) rms emittance for a periodicity and symmetry of 15, 16, 18, 21 and 24.

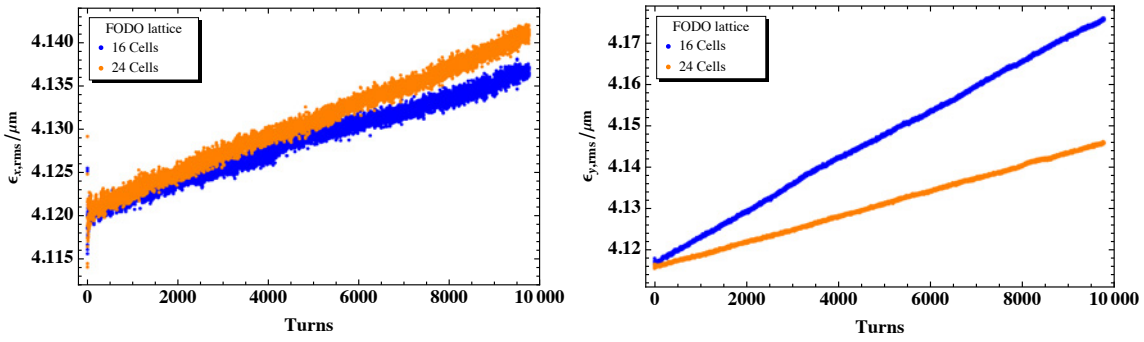


**Figure 3.35:** Time evolution of horizontal (left) and vertical (right) rms emittance for a periodicity/symmetry of 16 and 24.

can be explained by the excitation of systematic resonances of 4th respectively 5th order. Fig. 3.36 shows that the tune foot print crosses the $2Q_x + 2Q_y$ for 15, the $Q_x + 4Q_y$ for 18 and the $5Q_x$ resonance for 21 cells and that no systematic resonances are crossed for 16 and 24 cells for which only a comparably small emittance growth is observed. The results of

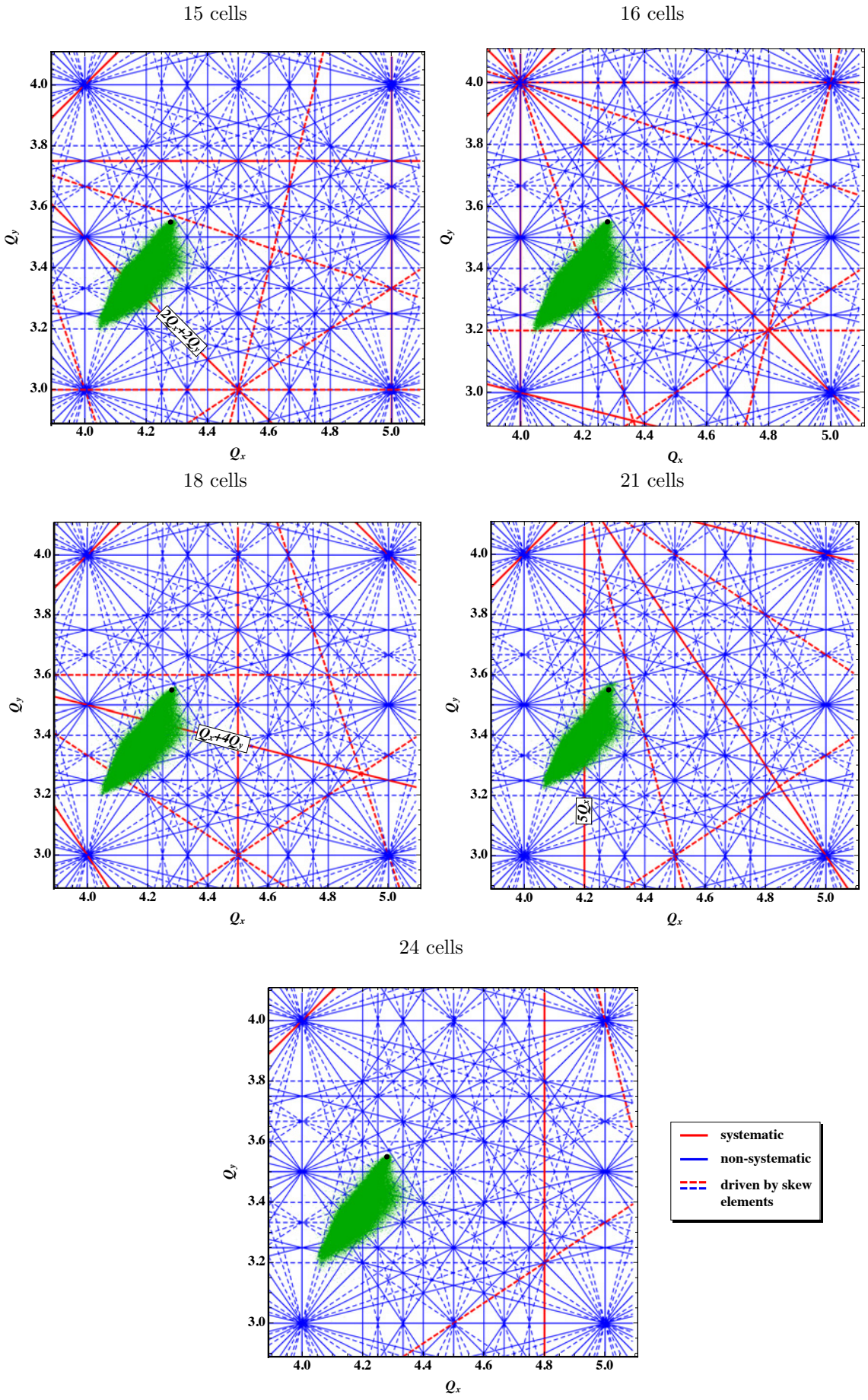


**Figure 3.36:** Resonance diagram and tune footprint for periodicity 15, 16, 18, 21 and 24.

the moment analysis summarized in Table 3.18 confirm that in the case of 18 and 21 cells, the systematic resonance being crossed exhibits a higher amplitude than for the other symmetries and that in the case of 16 and 24 cells, none of the moments show a larger amplitude. For the 18 cell lattice the $4Q_y$ resonance has a higher amplitude in addition to the $Q_x + 4Q_y$ without being systematic. In the case of 15 cells, a large amplitude would be expected for the $x^2y^2$ moment, but instead none of the moments has a particularly high amplitude. Taking a closer look at the 16 and 24 cell FODO lattice where in both cases

| | periodicity | | | | |
|---|---|---|---|---|---|
| moment | 15 | 16 | 18 | 21 | 24 |
| $< x >$ | 0 | 0 | 0 | 0 | 0 |
| $< y >$ | 0 | 0 | 0 | 0 | 0 |
| $< x^2 >$ | 2.30 | 2.36 | 2.45 | 2.57 | 2.62 |
| $< xy >$ | 0 | 0 | 0 | 0 | 0 |
| $< y^2 >$ | 0 | 0 | 0 | 0 | 0 |
| $< x^3 >$ | 0 | 0 | 0 | 1.14 | 0 |
| $< x^2y >$ | 0 | 0 | 0 | 0 | 0 |
| $< xy^2 >$ | 0 | 0 | 0 | 0 | 0 |
| $< y^3 >$ | 0 | 0 | 0 | 0 | 0 |
| $< x^4 >$ | 94.00 | 96.74 | 102.09 | 111.18 | 112.31 |
| $< x^3y >$ | 0 | 0 | 0 | 0 | 0 |
| $< x^2y^2 >$ | 10.55 | 10.70 | 11.45 | 11.55 | 11.70 |
| $< xy^3 >$ | 0 | 0 | 0 | 0 | 0 |
| $< y^4 >$ | 2.16 | 1.11 | 6.01 | 1.37 | 0 |
| $< x^5 >$ | 22.36 | - | 43.80 | 183.78 | 48.99 |
| $< x^4y >$ | 2.80 | - | 2.48 | 3.52 | 2.94 |
| $< x^3y^2 >$ | 3.97 | - | 5.45 | 4.09 | 3.44 |
| $< x^2y^3 >$ | 0 | - | 0 | 0 | 0 |
| $< xy^4 >$ | 0 | - | 6.19 | 2.94 | 1.29 |
| $< y^5 >$ | 0 | - | 0 | 0 | 0 |

**Table 3.18:** Maximum amplitude close to a tune of 1.0 of the Fourier analysis of the beam moments after 512 turns for periodicity 15, 16, 18, 21 and 24, where the periodicity is equal to the number of cells. The analysis is already performed after 512 turns as for 1024 turns the results are already dominated by the influence of the emittance growth. Raised amplitudes are indicated in red.

no systematic resonances are crossed, the emittance growth (Fig. 3.35) is smaller in the case of the 24 cell lattice, in agreement with the assumption that a smaller phase advance per cell and also a smaller variation of the beam size leads to a smaller emittance growth. It should be noted that the smaller variation of the beam size is in this case mainly due to the decrease of the cell length with the number of cells and not primarily due to the phase advance (Appendix A).

### 3.6.5 Weak and strong symmetry breaking and variation of the beam size

In Sec. 3.6.4 it has been shown on the example of a FODO cell lattice with a varying number of cells, that systematic resonances can lead to considerable emittance growth, even if only space-charge effects and no magnet imperfections or random errors are considered. In this section, the focus lies on the symmetry breaking. The symmetry is broken and reduced to 1 in all cases by shortening the bends of one cell. Due to the symmetry of 1, all resonances become systematic. The beta-beating introduced by the shorter bends is corrected by matching the twiss functions of the shorter cell to the arc cell with individual quadrupoles and then readjusting the phase advance per cell.

#### 3.6.5.1 FODO lattices with weak symmetry breaking

In this section, the perturbation and variation of the beam size is kept as minimal as possible. The beam envelope is shown in Fig. 3.37 and Fig. 3.38. All lattices have the same working point of $Q_x/Q_y = 4.28/3.55$. Due to the correction of the beta-beating and the relatively small perturbation introduced by the bends, the symmetry is only weakly broken, visible as an emittance evolution (Fig. 3.39) similar to the lattices with the unbroken symmetry (Fig. 3.34), and therefore suggests a remaining influence of all systematic

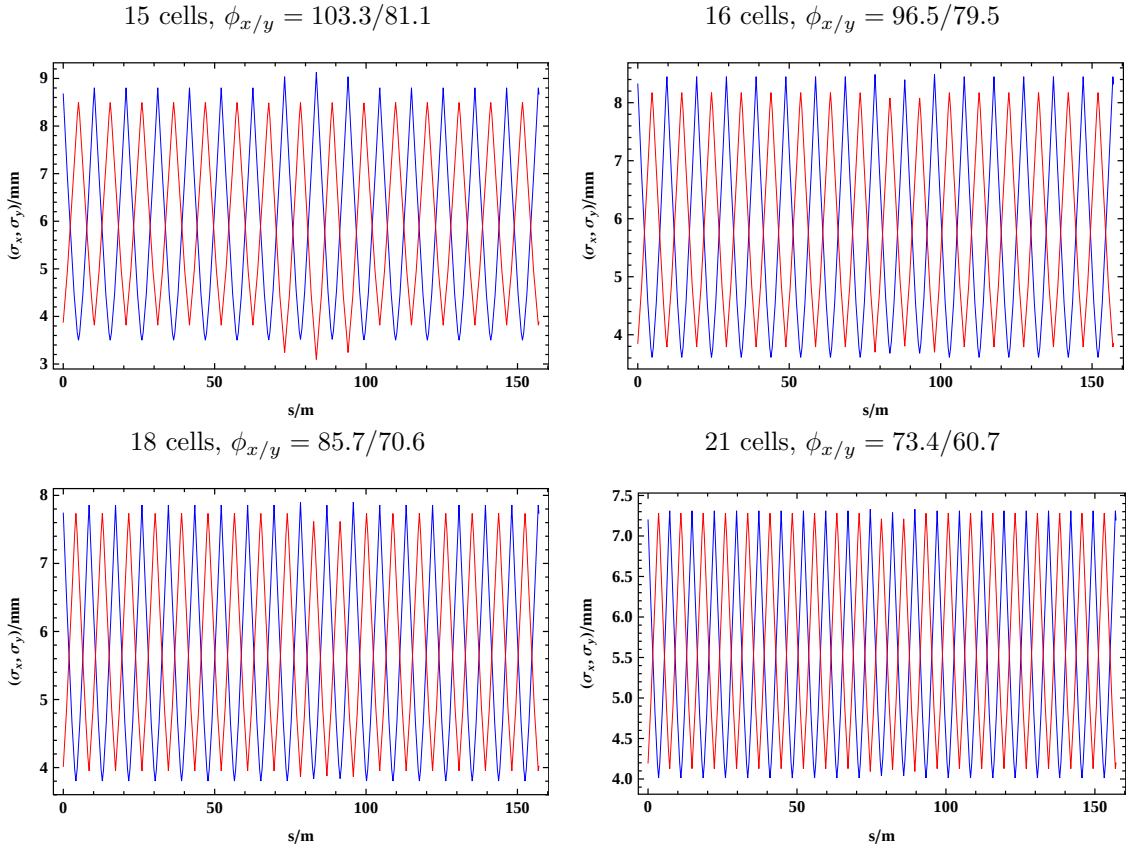


**Figure 3.37:** One rms beam envelope of FODO cell lattices with 15, 16, 18 and 21 cells and symmetry 1. The lattices are matched keeping the variation of the beam size as small as possible. The beam envelope has been calculated using the design transverse normalized rms emittance of 2.5 $\mu$m and the rms momentum spread corresponding to the design longitudinal emittance of 2.8 eVs.

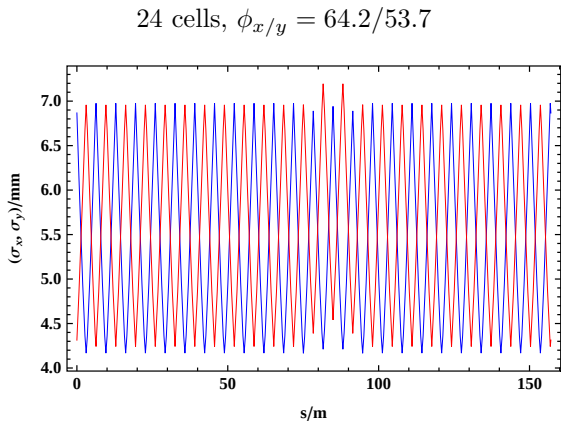


**Figure 3.38:** One rms beam envelope of the 24 cell FODO lattice with symmetry 1. The lattice is matched keeping the variation of the beam size as small as possible. The beam envelope has been calculated using the design transverse normalized rms emittance of 2.5 $\mu$m and the rms momentum spread corresponding to the design longitudinal emittance of 2.8 eVs.

| | number of cells | | | | |
|---|---|---|---|---|---|
| moment | 15 | 16 | 18 | 21 | 24 |
| $< x >$ | 0 | 0 | 0 | 0 | 0 |
| $< y >$ | 0 | 0 | 0 | 0 | 0 |
| $< x^2 >$ | 2.27 | 2.34 | 2.44 | 2.56 | 2.61 |
| $< xy >$ | 0 | 0 | 0 | 0 | 0 |
| $< y^2 >$ | 3.95 | 0 | 0 | 0 | 0 |
| $< x^3 >$ | 0 | 0 | 0 | 1.10 | 0 |
| $< x^2y >$ | 0 | 0 | 0 | 0 | 0 |
| $< xy^2 >$ | 2.02 | 0 | 0 | 0 | 0 |
| $< y^3 >$ | 0 | 0 | 0 | 0 | 0 |
| $< x^4 >$ | 92.29 | 95.91 | 101.55 | 110.64 | 112.17 |
| $< x^3y >$ | 0 | 0 | 0 | 0 | 0 |
| $< x^2y^2 >$ | 41.62 | 10.88 | 11.24 | 11.40 | 11.90 |
| $< xy^3 >$ | 0 | 0 | 0 | 0 | 0 |
| $< y^4 >$ | 692.88 | 4.87 | 6.26 | 1.91 | 5.03 |
| $< x^5 >$ | 24.16 | 35.16 | 43.51 | 170.94 | 48.65 |
| $< x^4y >$ | 2.72 | 2.31 | 3.25 | 4.10 | 2.82 |
| $< x^3y^2 >$ | 33.35 | 2.59 | 4.72 | 3.90 | 3.84 |
| $< x^2y^3 >$ | 4.21 | 0 | 0 | 0 | 0 |
| $< xy^4 >$ | 441.49 | 2.59 | 5.03 | 3.51 | 2.74 |
| $< y^5 >$ | 36.69 | 0 | 0 | 0 | 0 |

**Table 3.19:** Maximum amplitude close to a tune of 1.0 of the Fourier analysis of the beam moments after 512 turns for 15, 16, 18, 21 and 24 cell FODO lattices with symmetry 1 and weak symmetry breaking. Raised amplitudes are indicated in red.

resonances also visible in the moment analysis (Table 3.19). In the case of the 15 cell lattice, a very strong emittance growth is observed, resulting in an increase in amplitude of different moments and no conclusion can be drawn about a single resonance being the cause of the emittance growth. This is in accordance with the results of the lattice with 15 cells and symmetry 15, for which also no resonance seemed to be explicitly excited, in particular, not the systematic $2Q_x + 2Q_y$ resonance (see Sec. 3.6.4).

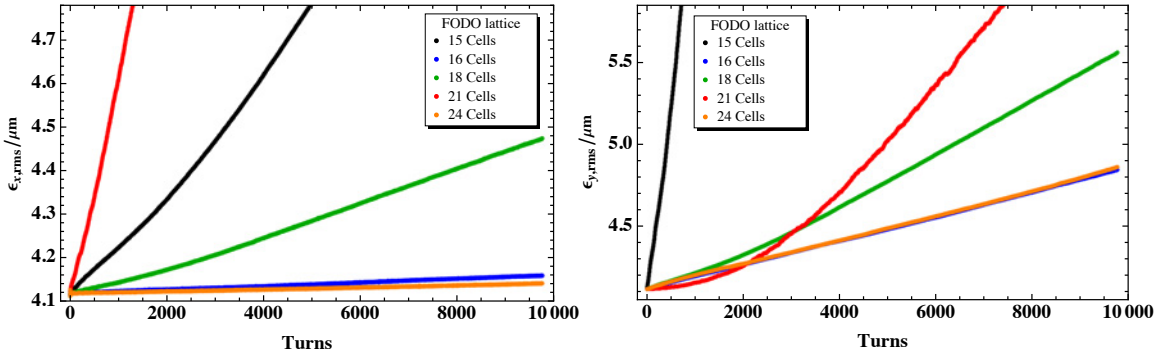


**Figure 3.39:** Time evolution of horizontal (left) and vertical (right) rms emittance for a FODO lattice with 15, 16, 18, 21 and 24 cells and symmetry 1.

#### 3.6.5.2 FODO lattices with strong symmetry breaking

In this section, different 16 cell FODO lattices with symmetry 1 and different integer parts of the tunes matched in two different ways are compared, explicitly $Q_x/Q_y = 2.28/1.55$, $Q_x/Q_y = 3.28/2.55$ and $Q_x/Q_y = 4.28/3.55$. The original motivation was to study the dependence on the phase advance per cell, as with symmetry 1 all resonances are systematic and therefore the resonance diagram independent of the integer part of the tune. It turns out that the emittance growth strongly depends on the way of correcting the beta-beating and if a large variation of the beam size and therefore strong symmetry breaking is introduced or not. Fig. 3.40 and 3.41 show the beam envelope and the horizontal and vertical emittance for the three different working points, each with two different solutions to match the region with the perturbation to the regular cells, where Optics 1 are always the solution leading to smaller variations of the beam size and Optics 2 the one with the larger variations.

For the smallest working point of $Q_x/Q_y = 2.28/1.55$ (Fig. 3.40 (top)), the shorter bends represent a relatively large distortion and the optics of the cell with shorter bends differ considerably from the optics of a normal arc cell. As a consequence, both lattices show a large emittance growth, despite the small phase advance per cell. Furthermore, Optics 2 are an excellent example of an almost uniform focusing around the ring except at the position of the shorter bends, where the vertical beam size is small, resulting in a strong non-linear kick at this position, leading to a large emittance growth.

The intermediate working point of $Q_x/Q_y = 3.28/2.55$ (Fig. 3.40 (bottom)) gives an example of two extreme matching cases. Optics 1 features a good correction of the beta-beating compared to Optics 2, which shows a large variation of the beam size at the location of the shorter bends. Due to the “weaker” symmetry breaking in the case of Optics 1 and the introduction of a large variation of the beam size, thus strong non-linear kick, in the

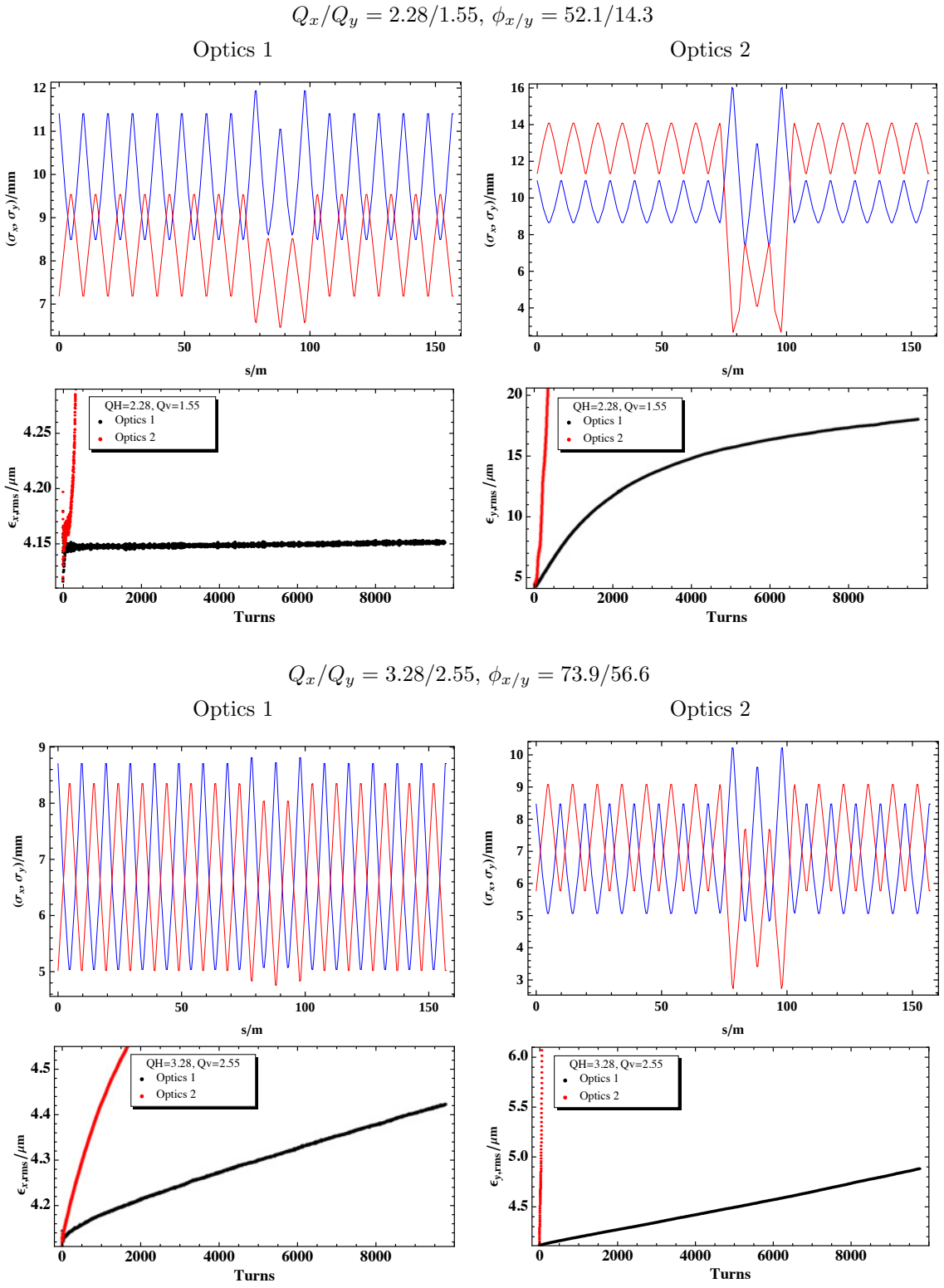


**Figure 3.40:** One rms beam envelope for two different optics (Optics 1 (left) and Optics 2 (right)) and working points ($Q_x/Q_y = 2.28/1.55$ (top) and $Q_x/Q_y = 3.28/2.55$ (bottom)) of a 16 cell FODO lattices with symmetry 1, and time evolution of horizontal (left) and vertical (right) rms emittance of the same. For both working points, Optics 1 is the optics with a relatively small variation of the beam size and weak symmetry breaking, and Optics 2 the optics with a large variation of the beam size and strong symmetry breaking. The beam envelope has been calculated using the design transverse normalized rms emittance of 2.5 $\mu$m and the rms momentum spread corresponding to the design longitudinal emittance of 2.8 eVs.

case of Optics 2, the emittance growth of Optics 1 is considerably smaller compared to Optics 2.

The two optics matched to the highest working point of $Q_x/Q_y = 4.28/3.55$ (Fig. 3.41) are an example for how a slightly different way of matching can already result in a significant change of the time evolution of the emittance.

$$Q_x/Q_y = 4.28/3.55,\ \phi_{x/y} = 96.5/79.5$$

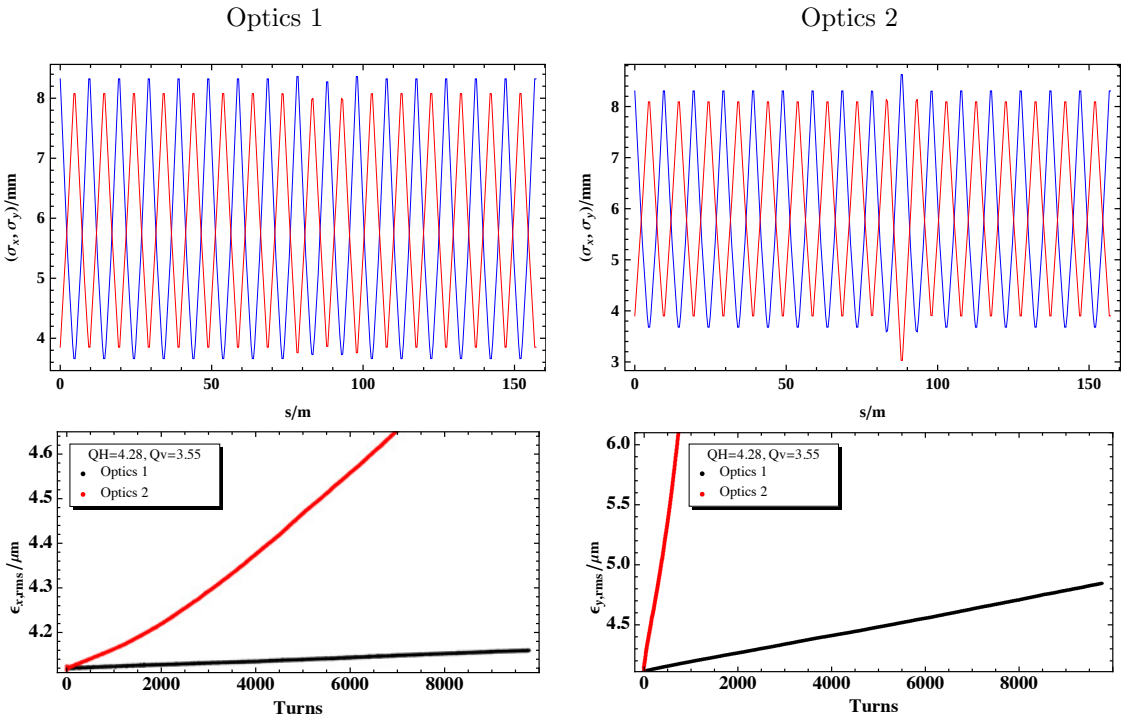


**Figure 3.41:** (top) One rms beam envelope of two different matches of the 16 cell FODO lattices with symmetry 1 and a working point of $Q_x/Q_y = 4.28/3.55$: Optics 1 with a relatively small variation of the beam size and weak symmetry breaking (left) and Optics 2 with a large variation of the beam size and strong symmetry breaking (right). The beam envelope has been calculated using the design transverse normalized rms emittance of 2.5 $\mu$m and the rms momentum spread corresponding to the design longitudinal emittance of 2.8 eVs.
(bottom) Time evolution of horizontal (left) and vertical (right) rms emittance for Optics 1 and Optics 2.

### 3.6.5.3 Beta-beating correction

In all examples of symmetry breaking by shortening the dipoles in certain cells, the beta-beating introduced has been corrected by matching the modified cell to the normal arc cell with individual quadrupoles and so minimizing the variation of the beam size and localizing the resulting irregular twiss functions to the modified cell. The question now is whether this correction is actually beneficial or not.

In the preceding sections it has been shown that the symmetry of the lattice and also how the symmetry is broken plays an important role. This also applies for the beta-beating correction. Fig. 3.42 shows the beam envelope and emittance for a 16 cell triplet lattice with symmetry 1. By not correcting the beta-beating, the weak symmetry breaking, in the

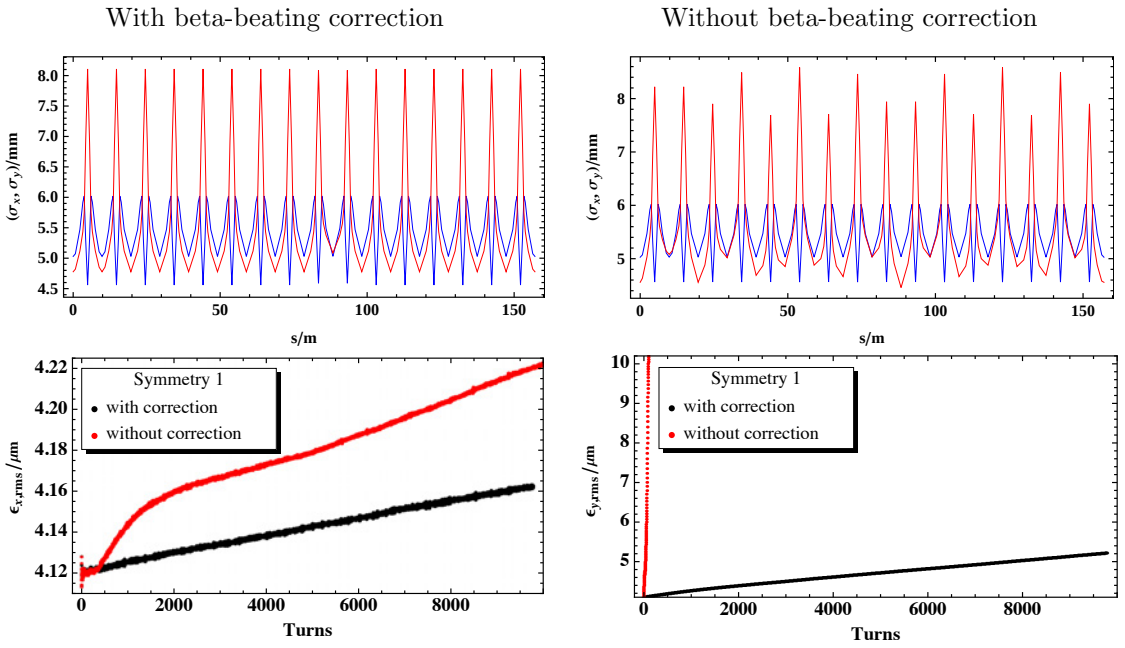


**Figure 3.42:** (top) One rms beam envelope of 16 cell triplet lattice with symmetry 1, a working point of $Q_x/Q_y = 4.28/3.55$ and with (left) and without (right) beta-beating correction. The beam envelope has been calculated using the design transverse normalized rms emittance of 2.5 $\mu$m and the rms momentum spread corresponding to the design longitudinal emittance of 2.8 eVs.
(bottom) Time evolution of horizontal (left) and vertical (right) rms emittance for the optics with and without beta-beating correction.

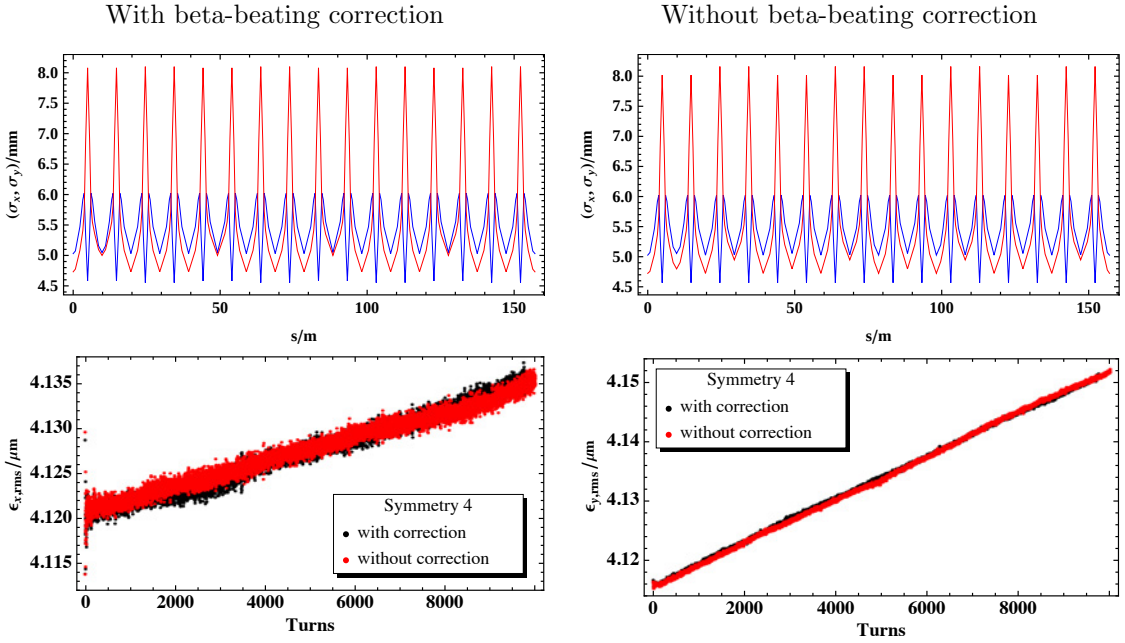


**Figure 3.43:** (top) One rms beam envelope of 16 cell triplet lattice with symmetry 4, a working point of $Q_x/Q_y = 4.28/3.55$ and with (left) and without (right) beta-beating correction. The beam envelope has been calculated using the design transverse normalized rms emittance of 2.5 $\mu$m and the rms momentum spread corresponding to the design longitudinal emittance of 2.8 eVs.
(bottom) Time evolution of horizontal (left) and vertical (right) rms emittance for the optics with and without beta-beating correction.

case of the lattice with correction, turns into a strong breaking of the symmetry, resulting in a large emittance growth.
For comparison, in the case of the 16 cell triplet lattice with symmetry 4, the beta-beating correction does not change the emittance growth (Fig. 3.43). The reason is that the introduced beta-beating preserves the 4-fold symmetry of the lattice, which is the lowest symmetry with no systematic resonances in the region of the tune footprint (Sec. 3.6.3). In addition, the introduced beta-beating is rather small and with it also the variation of the beam size.

### 3.6.6 Dependence on the phase advance per cell and chromatic detuning

In the early design phases of many smaller machines and also for the RCS one of the main issues is to reduce the machine circumference which is mostly done by increasing the magnet filling factor. In addition to driving the magnet strength to the achievable limit, an improvement of the filling factor can also be achieved with a smaller number of cells, as less space is taken by the necessary gaps between the magnets. The drawback of a small number of cells is the resulting high phase advance per cell, which leads to a stronger excitation of all resonances and a larger variation of the beam size. This increase in phase advance can often not be avoided as the horizontal tune at least is limited by the minimum acceptable gamma transition in order to stay below transition throughout the cycle.
To study the effect of a smaller phase advance per cell, the integer part of the tune of the 16 cell triplet lattice with symmetry 1 introduced in Sec. 3.6.3 is varied in integer steps between $Q_x/Q_y = 2.28/1.55$ and $Q_x/Q_y = 5.28/4.55$. The phase advance per cell for the different lattices is listed in Table 3.20 and the beam envelope shown in Fig. 3.44. As the lattice has symmetry 1, all resonances are systematic and the resonance diagram

| **tune** | **phase advance per cell (hor./vert.)** |
|---|---|
| $Q_x = 2.11,\ Q_y = 1.53$ | 47.5/34.5 |
| $Q_x = 2.28,\ Q_y = 1.55$ | 51.3/34.9 |
| $Q_x = 3.28,\ Q_y = 2.55$ | 73.8/57.5 |
| $Q_x = 4.28,\ Q_y = 3.55$ | 96.3/80.3 |
| $Q_x = 5.28,\ Q_y = 4.55$ | 118.9/104.5 |

**Table 3.20:** Phase advance per cell for the different working points

is independent of the integer part of the tune. This applies only partly to the case of the 16 cell triplet lattice, as the symmetry is only weakly broken and resonances being systematic in the case of the full 16 fold symmetry can still have a stronger effect on the emittance growth than non-systematic ones. Comparing the time evolution of the emittance for the different working points (Fig. 3.45) an increase of the emittance growth with the phase advance per cell is in general visible.

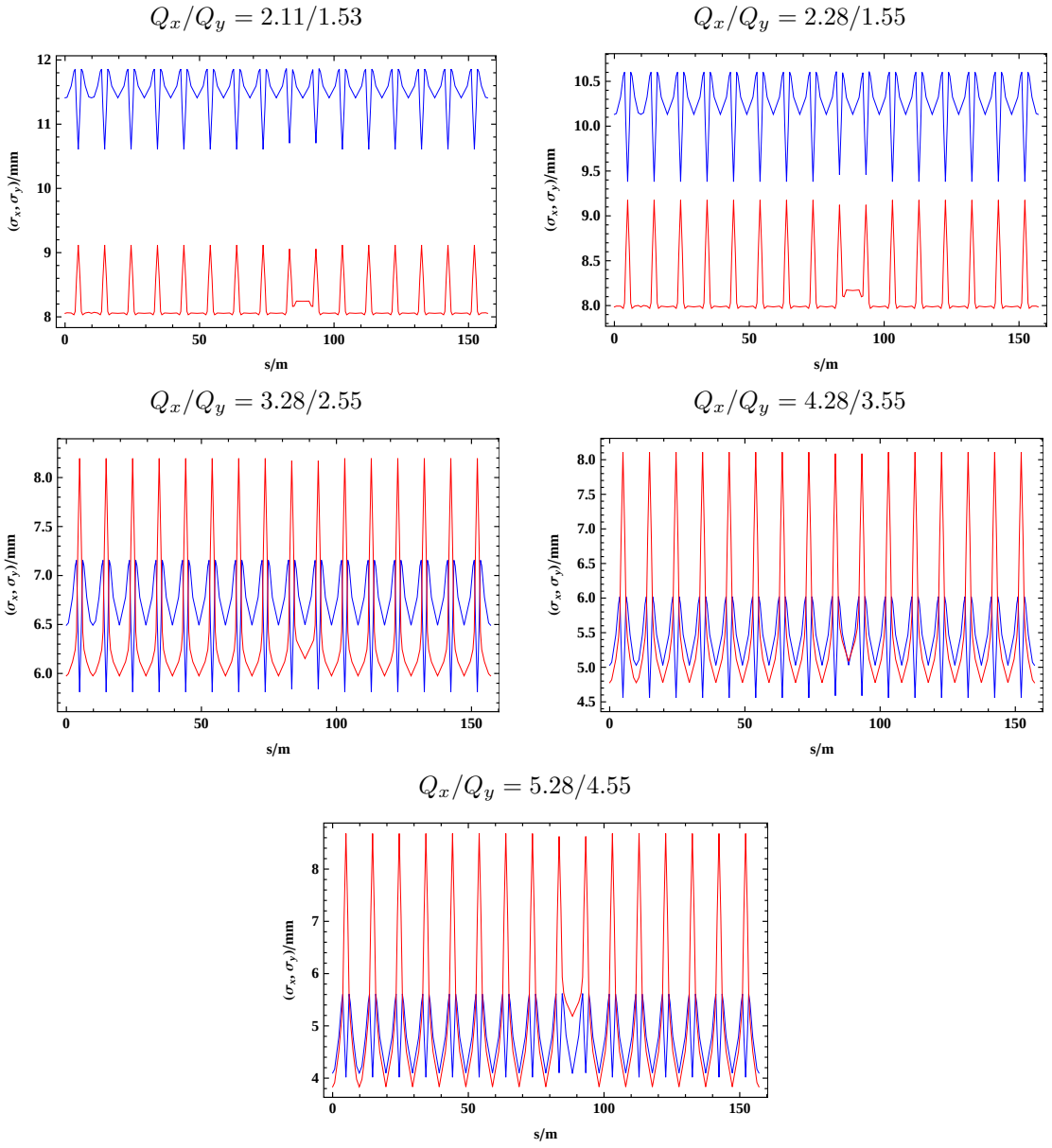


**Figure 3.44:** One rms beam envelope of the 16 cell triplet lattice with symmetry 1 and varying working point. The beam envelope has been calculated using the design transverse normalized rms emittance of 2.5 $\mu$m and the rms momentum spread corresponding to the design longitudinal emittance of 2.8 eVs.

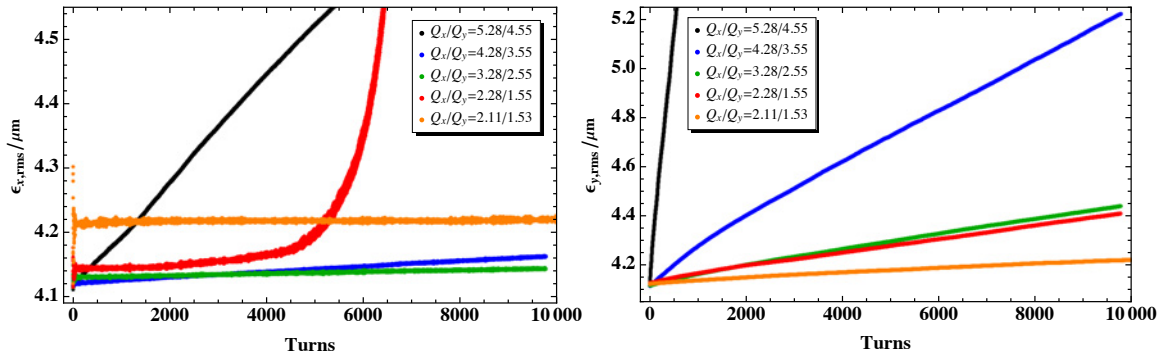


**Figure 3.45:** Time evolution of horizontal (left) and vertical (right) rms emittance for different phase advances per cell. The tune is varied in integer steps between $Q_x/Q_y = 2.28/1.55$ and $Q_x/Q_y = 5.28/4.55$.

Nevertheless, it has to be kept in mind that the growth rate is also influenced by the following two effects:

- **Weak symmetry breaking:** As studied in Sec. 3.6.5, the symmetry is not necessarily fully broken if the bends are shortened in one cell and the beta-beating corrected. Therefore, the resonance diagram and the excitation of the different resonances cannot be assumed to be fully independent of the integer part of the working point. Furthermore, depending on the matching and the beta-beating caused by the shorter bends, the symmetry breaking can have a stronger or weaker effect. The tune footprint and the resonance diagram for the full symmetry of 16 are shown in Fig. 3.46.

- **Chromatic detuning:** Due to the relatively strong quadrupoles of a triplet lattice and the high beta function at the central quadrupole, the chromatic detuning increases rapidly with the phase advance per cell especially for the vertical plane. Table 3.21 lists the chromaticities for the different working points and Fig. 3.46 shows the chromatic detuning for the full momentum spread. The chromatic detuning has two major effects: for small tunes the tune footprint shrinks - especially in the vertical plane - and the core moves closer to the half integer or $4Q_y$ resonance respectively, resulting in a possible instability of the beam core. For a high phase advance per cell, the large detuning with momentum gives rise to a large emittance growth in both planes and makes it difficult to find a stable area accommodating the full tune footprint.

| **tune** | $-\mathbf{Q'_x}$ | $-\mathbf{Q'_y}$ |
|---|---|---|
| $Q_x = 2.11,\ Q_y = 1.53$ | 2.29 | 4.35 |
| $Q_x = 2.28,\ Q_y = 1.55$ | 2.58 | 4.68 |
| $Q_x = 3.28,\ Q_y = 2.55$ | 4.56 | 7.25 |
| $Q_x = 4.28,\ Q_y = 3.55$ | 6.43 | 11.17 |
| $Q_x = 5.28,\ Q_y = 4.55$ | 8.51 | 17.43 |

**Table 3.21:** Chromaticities for the different working points.

For the lowest tune of $Q_x/Q_y = 2.28/1.55$ the beam is stable for the first 4 000 turns but then a large emittance blow-up is observed in the horizontal plane. By moving the working point further away from the $4Q_x$ and $5Q_x$ resonance the beam stays stable at least over the tracked 10 000 turns and the emittance growth is therefore most likely caused by the horizontal 4th or 5th order resonance. A moment analysis could not reveal any further information as the results are probably dominated by the effect of the integer resonance or dispersion respectively in the case of $Q_x/Q_y = 2.11/1.53$. The influence of the integer resonance is visible as an initial oscillation of the horizontal emittance and later stabilization at a higher value compared to $Q_x/Q_y = 2.28/1.55$, as also seen in the case of almost all lattices in Sec. 3.6.7. The straightforward alternative explanation for the oscillation and then stabilization would be a large initial mismatch of the beam. This

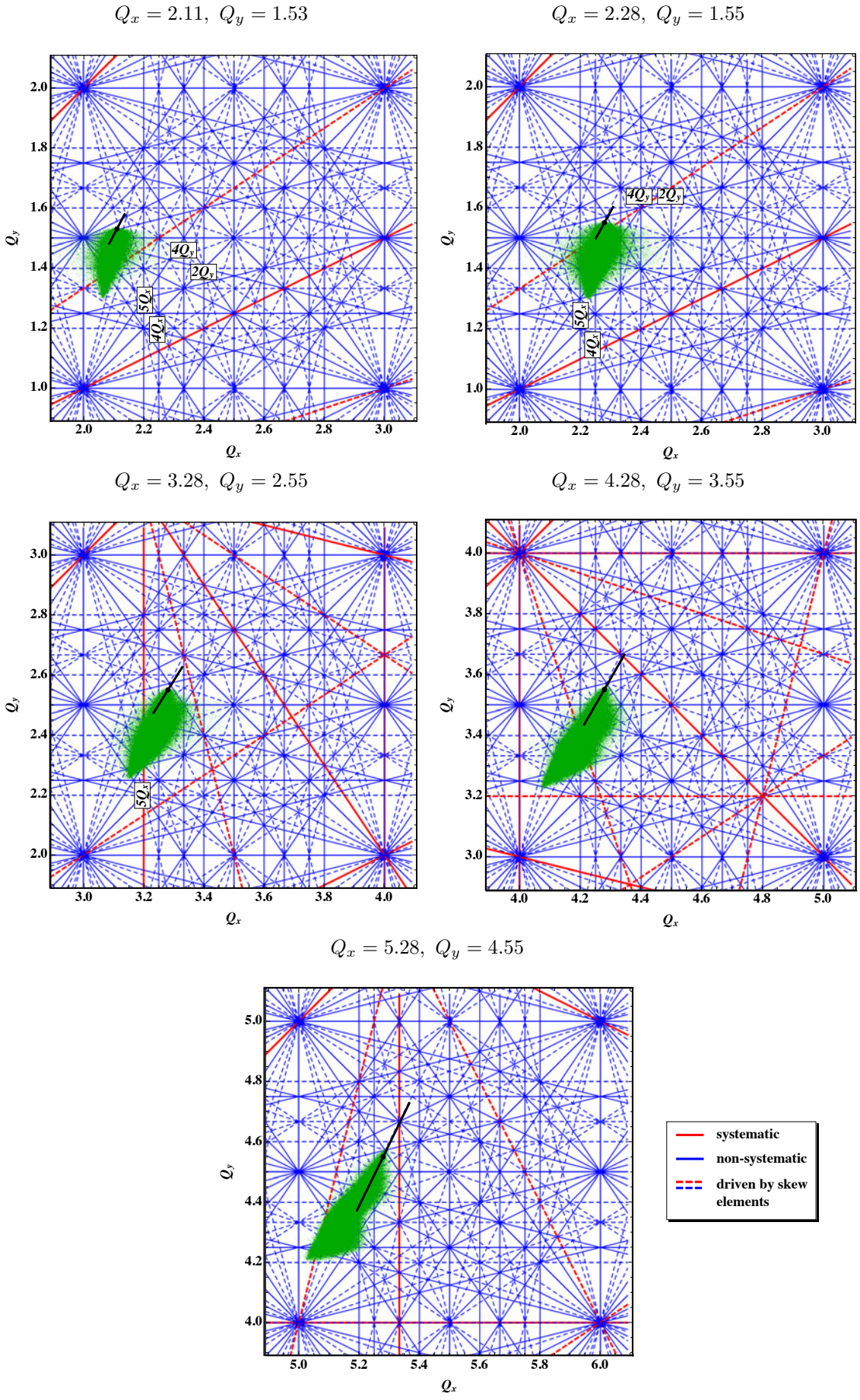


**Figure 3.46:** Resonance diagram until 5th order for symmetry 16 and tune footprint for symmetry 1 of the initial beam distribtution after 1 turn. The chromatic detuning for the full momentum spread is shown in black.

possibility can be excluded, as the same behaviour should then also be visible in the case of $Q_x/Q_y = 2.28/1.55$ and is estimated to be small (Sec. 3.5) anyway.

### 3.6.7 Influence of dispersion

Until now, only lattices without any long straight sections have been studied. This section is devoted to lattices including straight sections, similar to the ones considered for the RCS. Three different lattices, representative for this type, have been studied:

A) 24 cell FODO lattice with symmetry 4 and $4 \times 1$ cell of straight section

B) 24 cell FODO lattice with symmetry 2 and $2 \times 2$ cells of straight section

C) 21 cell FODO lattice with symmetry 3 and $3 \times 2$ cells of straight section

and for each lattice type three different types of optics which can be grouped according to the dispersion suppression scheme

1) dispersion suppression with a phase advance of $2\pi$ over the arc - resulting in dispersion beating in the arc - without correction of the beta-beating.

2) dispersion suppression with a phase advance of $2\pi$ over the arc - resulting in dispersion beating in the arc - with correction of the beta-beating using individual quadrupoles.

3) a half missing bend dispersion suppressor

First, the simulation results of the 24 cell lattices are discussed followed by the 21 cell lattices.

#### 3.6.7.1 Interpretation of tune footprints and time evolution of the rms emittance

The simulation results of the lattices with straight sections are at first sight puzzling due to the following general observations:

- an initial oscillation of the horizontal emittance in the presence of space-charge effects which decreases if the horizontal tune is moved away from the integer resonance[6] (Fig. 3.48)

- the shape of the tune footprint obtained with PTC-ORBIT (Fig. 3.51)

Both results can be explained by the large linear dispersion, a resulting, tune dependent, linear and non linear dispersion mismatch introduced by space-charge and a non-negligible second order dispersion term.

[6]This is not the case for the 21 cell FODO lattice with $3 \times 2$ cells of straight section (see Sec. 3.6.7.4). The different behaviour compared to the 24 cell lattices with straight sections (Sec. 3.6.7.2 and 3.6.7.3) is probably due to the systematic $2Q_x$ and $5Q_x$ resonance between which the particles are "trapped". For more details see Sec. 3.6.7.4.

The contribution of the second order dispersion, illustrated in Fig. 3.47, turned out be an indication for the non linearity of the dispersion and the strength of the dispersion mismatch to be expected due to the space-charge detuning.

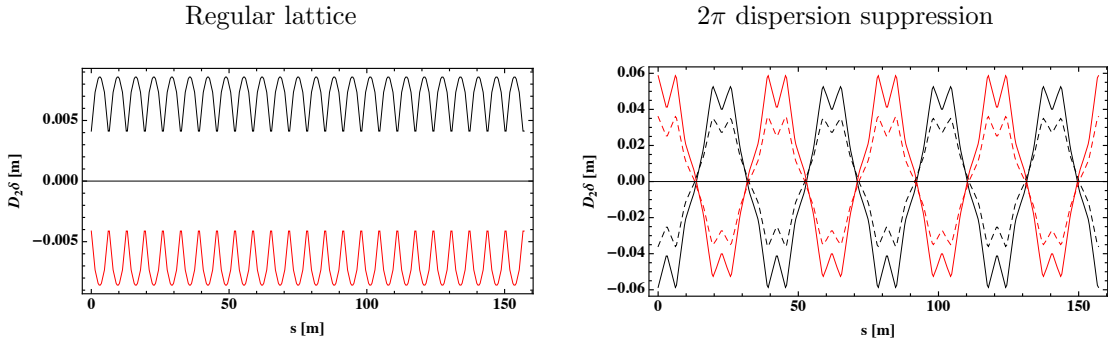


**Figure 3.47:** Contribution of the second order dispersion to the dispersion. The black curve is $D_2\delta$ for $+\delta$ and the red curve for $-\delta$, with $\delta$ being the rms momentum spread. (left) Regular 24 cell FODO lattice with a negligible second order dispersion term. (right) 24 cell FODO lattice with $4 \times 1$ cells of straight section and $2\pi$ dispersion suppression for $Q_x/Q_y = 4.28/3.55$ (solid line) and $Q_x/Q_y = 4.47/3.45$ (dashed line). The second order term is non-negligible and increases if the working point approaches the integer resonance. Similar results are obtained for all lattices with straight sections presented in this thesis.

The initial oscillation of the horizontal emittance, shown in Fig. 3.48, is caused by a dispersion and smaller betatron mismatch introduced by space-charge, which increases for particles with a single particle tune approaching the integer resonance[7]. In the absence of the strong space-charge detuning, the oscillation then vanishes (Fig. 3.49). In addition to the linear dispersion mismatch, the effect of the second order dispersion and its mismatch could become non-negligible (Fig. 3.47). To investigate the influence of a second order dispersion term, the initial distribution has been generated and the emittance calculated, also including the second order dispersion, and compared to the results taking only the linear dispersion into account (Fig. 3.50). Explicitly, the emittance is obtained by subtracting the closed-orbit shift

$$x_{\mathrm{co}} = D_x\delta + \frac{1}{2}D_{2x}\delta^2 \tag{3.14}$$

from the horizontal position. In one case only the linear term is taken into account, as done in PTC-ORBIT (calc. D in Fig. 3.50), and in the other case also the second order term (calc. $D_2$ in Fig. 3.50). Then the emittance is determined from the first and second beam moments, where the dispersion is obtained from the optics calculated with PTC.

[7]The dispersion and second order dispersion both satisfy differential equations similar to the one of a closed-orbit distortion due to dipole field errors, explicitly [75]:

$$\begin{aligned} D'' + \left(k_x + \frac{1}{\rho^2}\right) D &= \frac{1}{\rho} \\ D_2'' + \left(k_x + \frac{1}{\rho^2}\right) D_2 &= \kappa\left(\rho,\, \rho',\, k,\, k',\, D,\, D'\right) \end{aligned}$$

where $\kappa\left(\rho,\, \rho',\, k,\, k',\, D,\, D'\right)$ stands for a polynomial in $\rho$, $\rho'$, $k$, $k'$, $D$ and $D'$. Similar as the closed-orbit distortion due to dipole field errors, the dispersion and second order dispersion are thus most sensitive to tunes close to the integer resonance.

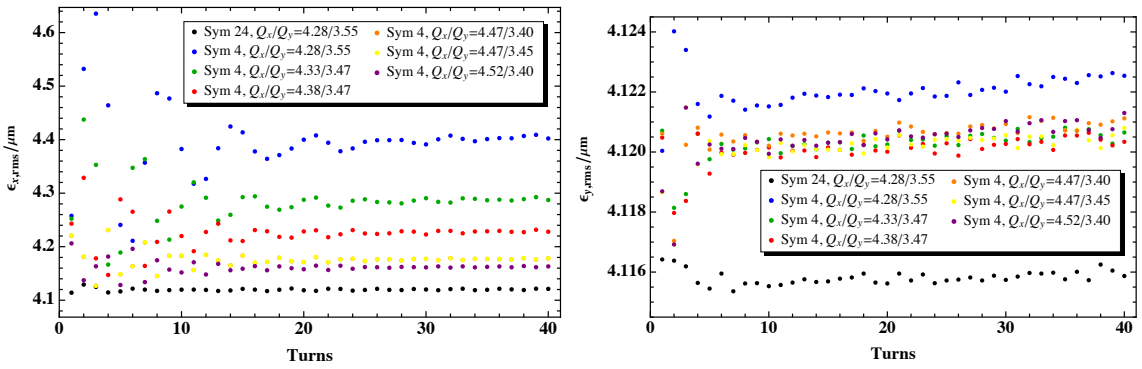


**Figure 3.48:** Time evolution over the first 40 turns of the horizontal (left) and vertical (right) rms emittance calculated with PTC-ORBIT for the regular 24 cell FODO lattice (Sym 24) and the 24 cell FODO lattice with $4 \times 1$ cells straight sections (Sym 4) for different working points. The initial oscillation of the horizontal emittances decreases if the working point is moved away from the integer resonance.

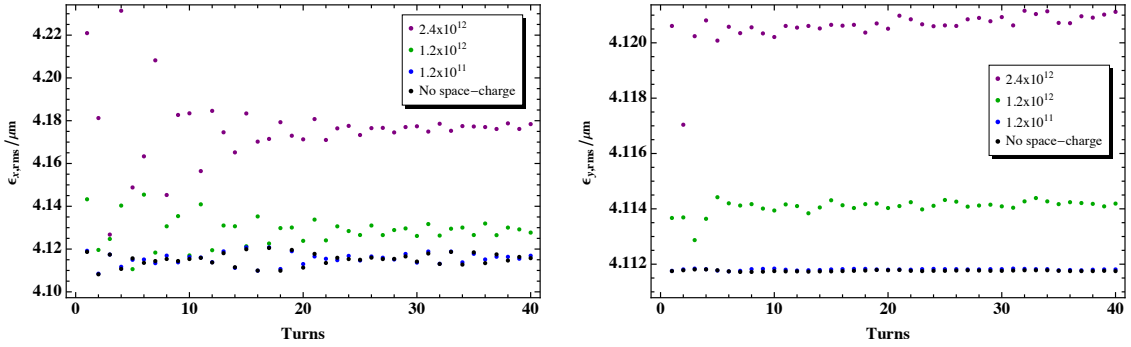


**Figure 3.49:** Time evolution over the first 40 turns of the horizontal (left) and vertical (right) rms emittance calculated with PTC-ORBIT for the 24 cell FODO lattice with $4 \times 1$ cells straight sections with a working point of $Q_x/Q_y = 4.47/3.45$. The initial oscillation of the horizontal emittance decreases with intensity due to the decreasing dispersion mismatch.

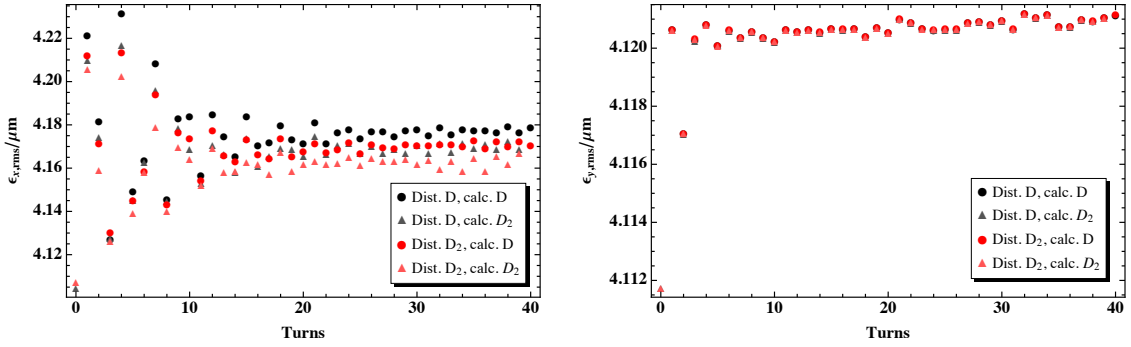


**Figure 3.50:** Time evolution over the first 40 turns of the horizontal (left) and vertical (right) rms emittance for the 24 cell FODO lattice with $4 \times 1$ cells of straight sections with a working point of $Q_x/Q_y = 4.47/3.45$. The initial distribution has been generated taking only the linear dispersion (Dist. D) and the linear and second order dispersion (Dist. $D_2$) into account. The same is valid for the emittance which has been calculated including only the linear dispersion (calc. D) and the linear and second order dispersion (calc. $D_2$).

The initial distribution is generated in a reverse way to the emittance calculation (Dist. D in Fig. 3.50 in case of only linear dispersion terms and Dist. $D_2$ in the case of terms until second order). Including the second order dispersion term in the generation of the initial distribution and in the emittance calculation respectively leads to an very small "reduction" of the emittance. Once the initial oscillation has vanished (roughly after 20 turns) the reduction is approximately constant. As lattices showing a large initial oscillation of the emittance in general also showed a large reduction of the emittance if the second order dispersion was included, the magnitude of the reduction is an indication for the magnitude of the dispersion mismatch due to space-charge detuning.
The second initially puzzling result is the tune footprint obtained with PTC-ORBIT, which is shown in Fig. 3.51.The tune calculation of the individual particles implemented in PTC-ORBIT takes only the linear dispersion into account, resulting in an incorrect calculation of the closed-orbit, and thus tune, due to the non-negligible higher order dispersion terms. This leads to a large artificial horizontal tune-shift for off-momentum beam particles resulting in a large horizontal tune-spread of the beam.

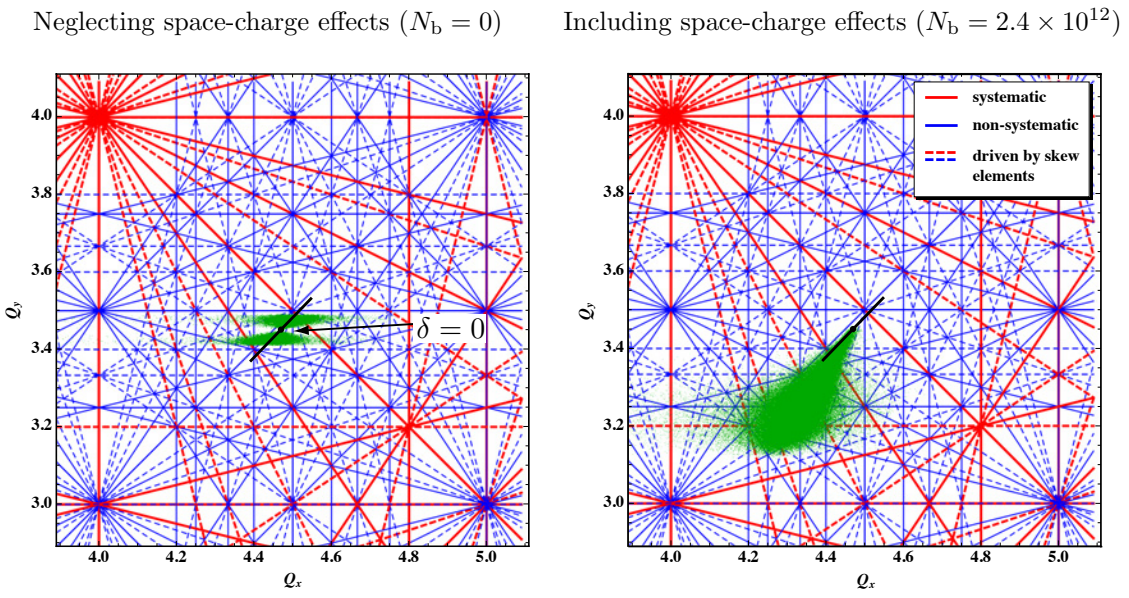


**Figure 3.51:** Resonance diagram until 5th order for symmetry 4 and tune footprint obtained with PTC-ORBIT of the initial distribution for the 24 cell FODO lattice with $4 \times 1$ straight sections, dispersion suppression over $2\pi$, beta-beating correction with individual quadrupoles and a working point of $Q_x/Q_y = 4.47/3.45$. The initial distribution has been matched taking only the linear dispersion into account. The large tune-spread in the horizontal for off-momentum particles is an artefact of the tune calculation performed in PTC-ORBIT, for which only the linear dispersion is taken into account.
(left) The second order (lattice optics) dispersion is non-negligible and thus PTC-ORBIT calculates the wrong closed-orbit for off-momentum particles, resulting in an incorrect calculation of the tune of the same.
(right) The mismatch between the lattice optics dispersion and the dispersion seen by the particles increases for single particle tunes approaching the integer resonance leading to a large tune-spread of the beam in the case of strong space-charge effects.

The results presented in this section are important for the later interpretation of the long-term tracking results, where the emittance is calculated after each turn only with PTC-ORBIT and only each 500 turns including the second order (lattice optics) dispersion term. The increase of the initial oscillation and absolute value of the horizontal emittance for horizontal working points approaching the integer resonance suggests a stronger non-linearity of the dispersion function than given by the pure optics parameters of the lattice. This dependence of the dispersion function on the particle momentum due to the space-charge detuning is not taken into account. Thus, larger emittance values might be obtained just due to the difference between the dispersion obtained from the pure lattice optics without space-charge and the "real" dispersion seen by the beam particles including space-charge. Nevertheless, a good guess of the influence of the higher order dispersion terms caused by the space-charge detuning can be obtained from the "reduction" of the emittance if, in addition, the second order dispersion is taken into account in the calculation. The emittance blow-up of the different lattices can thus be qualitatively compared, but in the case of a comparison of the absolute values the effect of the non-linear dispersion has to be kept in mind.

#### 3.6.7.2 24 cell FODO lattice with $4 \times 1$ cells of straight section

For the 24 cell FODO lattice with $4 \times 1$ cells of straight section the condition of a phase advance of $2\pi$ over the arc for dispersion suppression is fulfilled for a horizontal working

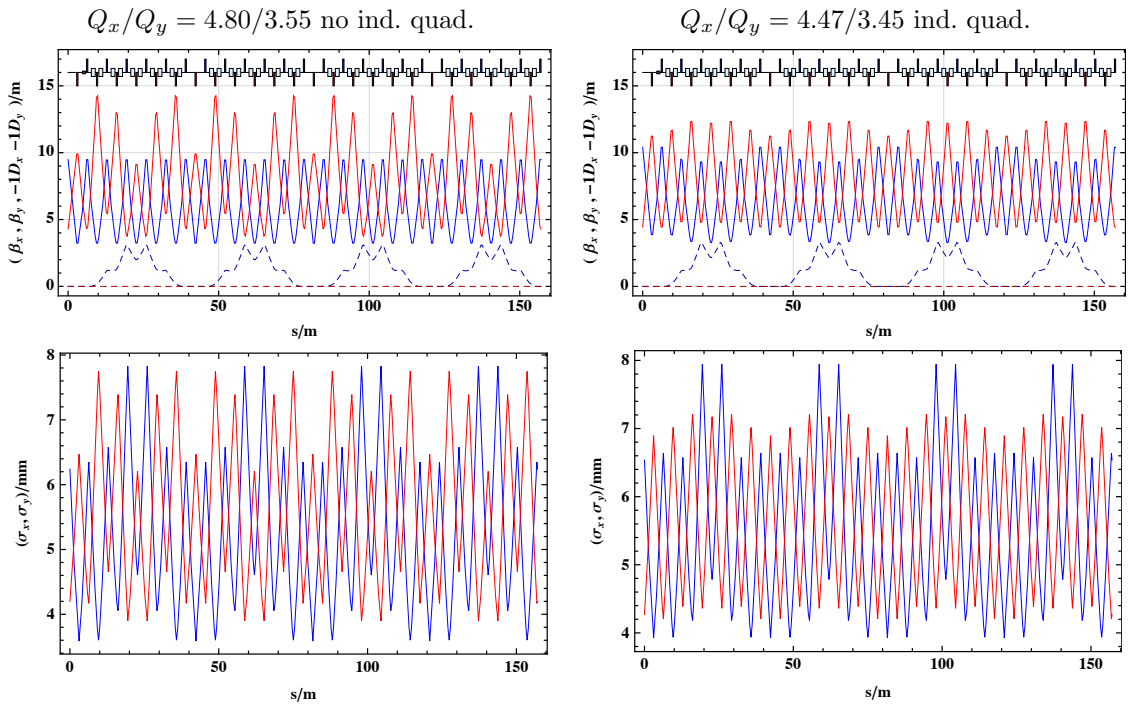


**Figure 3.52:** Optics and one rms beam envelope of the 24 cell FODO lattice with $4 \times 1$ cells of straight section with only two quadrupole families (no ind. quad) and with additional individual quadrupoles for beta-beating correction (ind. quad). The beam envelope has been calculated using the design transverse normalized rms emittance of 2.5 $\mu$m and the rms momentum spread corresponding to the design longitudinal emittance of 2.8 eVs.

point of $Q_x = 4.8$. The optics and beam envelope of this lattice with only one focusing and one defocusing quadrupole family is shown Fig. 3.52 (left). A horizontal working point of 4.8 however is not advisable, as it is located close to the systematic $5Q_x$ resonance (see Fig. 3.51). The option of moving the working point towards the half integer resonance 4.5 is expected to result in a large emittance blow-up. This example points out the dilemma of the limited flexibility due to the restriction to only two quadrupole families. The resulting limited freedom to choose a suitable working point can considerably reduce the machine performance. In addition to the unfortunate working point, the lattice with only two quadrupole families also exhibits a large variation of the beam size (Fig. 3.52 (left)). With more quadrupole families, the working point can be moved and the variation of the beam size reduced. Representative for all lattices with additional individual quadrupoles the optics and beam envelope of the lattice with a working point of $Q_x/Q_y = 4.47/3.45$ are shown in Fig. 3.52 (right). This lattice ($Q_x/Q_y = 4.47/3.45$ ind in Fig. 3.53) also exhibits

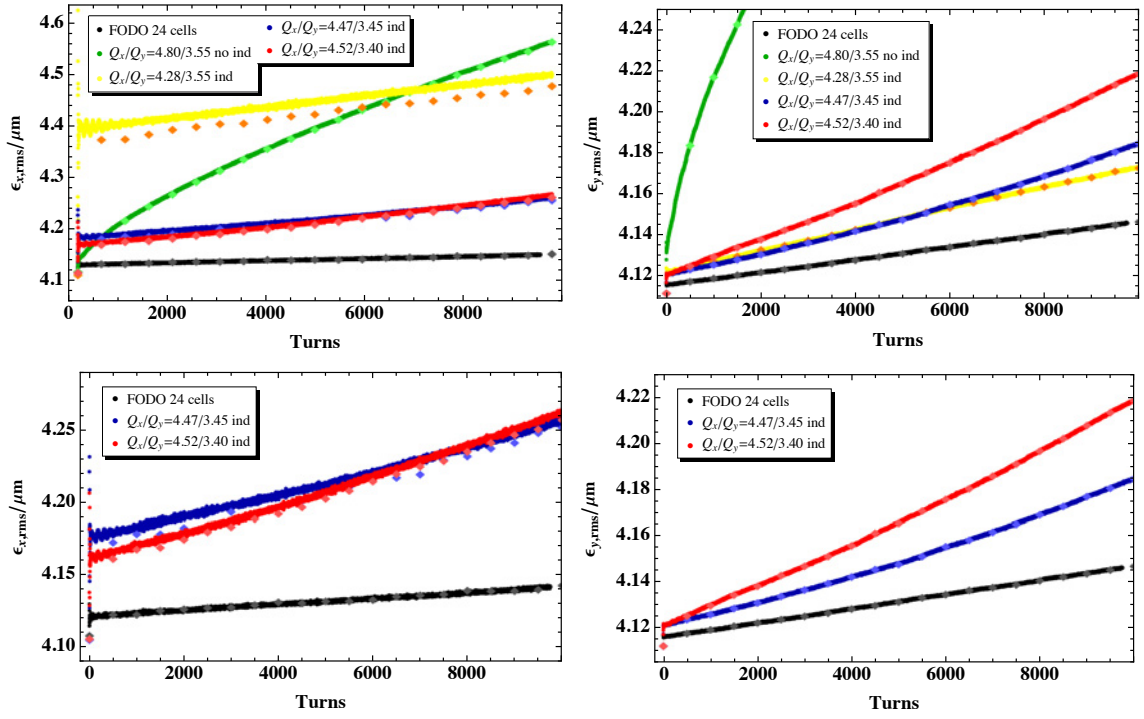


**Figure 3.53:** Time evolution of horizontal (left) and vertical (right) rms emittance for the 24 cell FODO lattice with $4 \times 1$ cells of straight section with only two quadrupole families (no ind) and with additional individual quadrupoles for beta-beating correction (ind) and for the regular 24 cell FODO lattice (FODO 24 cells). The values indicated with diamonds are the emittances calculated including the second order dispersion. For all simulations, the initial distribution has been generated taking only the linear dispersion into account.

the smallest emittance blow-up of the 24 cell lattices with $4 \times 1$ cells of straight straight section. Compared to the lattice with only two quadrupole families ($Q_x/Q_y = 4.80/3.55$ no ind in Fig. 3.53), the emittance blow-up is small, but large in comparison to the regular 24 cell FODO lattice (FODO 24 cells in Fig. 3.53), especially in the horizontal plane. For smaller horizontal tunes, and in particular for $Q_x = 4.28$ ($Q_x/Q_y = 4.28/3.55$ ind

in Fig. 3.53), the horizontal emittance executes large oscillations over the first 20 turns, which are better visible in the emittance development over the first 40 turns shown in Fig. 3.48.

For this lattice type, a missing bend dispersion suppressor is not possible, as the straight section only consists of one cell. Also a significant reduction of the maximum dispersion using more quadrupole families has not been possible.

#### 3.6.7.3 24 cell FODO lattice with $2 \times 2$ cells of straight section

For the 24 cell FODO lattice with $2 \times 2$ cells of straight section, a racetrack layout, the condition for dispersion suppression is fulfilled for $2 \times 2\pi$ phase advance per arc, resulting in a

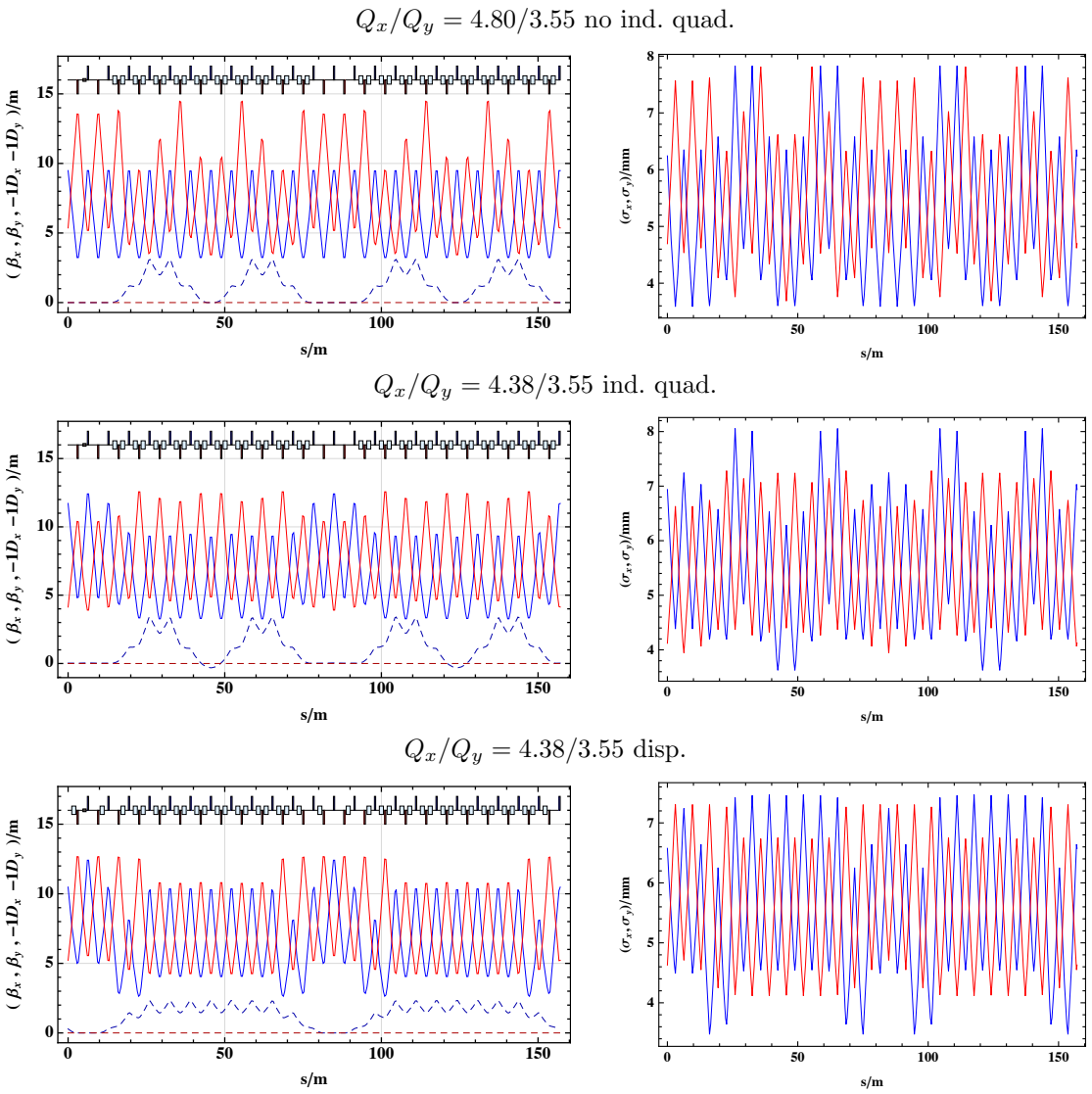


**Figure 3.54:** Optics and one rms beam envelope of the 24 cell FODO lattice with $2 \times 2$ cells of straight section with only two quadrupole families (no ind. quad), with additional individual quadrupoles for beta-beating correction (ind. quad) and with a half missing bend dispersion suppression scheme (disp.). The beam envelope has been calculated using the design transverse normalized rms emittance of 2.5 $\mu$m and the rms momentum spread corresponding to the design longitudinal emittance of 2.8 eVs.

horizontal working point of $Q_x = 4.8$. Fig. 3.54 shows the optics of the lattice with only two quadrupole families ($Q_x/Q_y = 4.80/3.55$ no ind. quad.), a typical lattice with additional individual quadrupole families for beta-beating correction ($Q_x/Q_y = 4.38/3.55$ ind. quad.) and a lattice with a half missing bend dispersion suppressor ($Q_x/Q_y = 4.38/3.55$ disp.). The beta-beating correction with individual quadrupoles already considerably reduces the variation of the beta-function and allows the choice of a better working point. The lattice with a half missing bend dispersion suppressor features a significant reduction of the maximum dispersion, the smallest variation of the beam size and a regular beta-function and dispersion in the arc.

The dispersion matching to the arc has the very positive effect, that the strong oscillation of the horizontal emittance during the first 20 turns almost disappears (Fig. 3.55). As

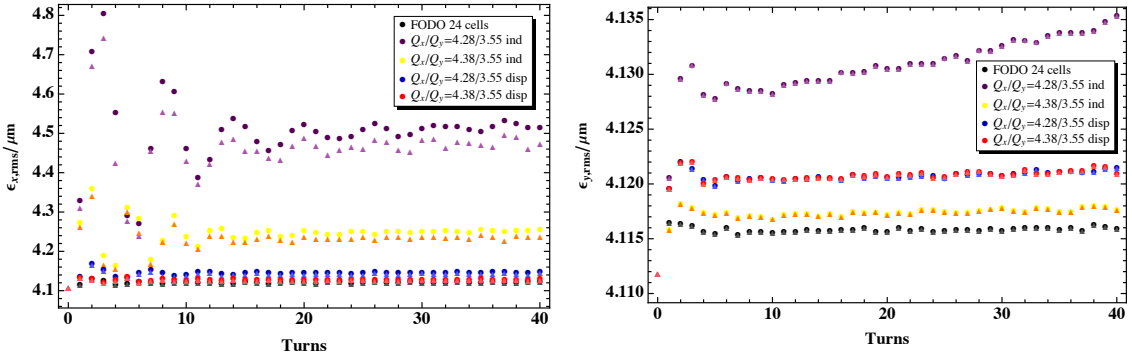


**Figure 3.55:** Time evolution over the first 40 turns of the horizontal (left) and vertical (right) rms emittance for the 24 cell FODO lattice with $2 \times 2$ cells of straight section. The results for the lattices with a dispersion suppression by adjusting the phase advance to $2\pi$ over the arc and individual quadrupoles is indicated with "ind" and the ones for the lattices with a half missing bend dispersion suppressor with "disp". For comparison also the regular 24 cell FODO lattice is shown which is indicated with "FODO 24 cells". The emittances from PTC-ORBIT, including only the linear dispersion, are marked with circles, and the emittances calculated, including the second order dispersion, with diamonds. For all simulations, the initial distribution has been created taking the linear and second order dispersion into account.

expected, the effect is particularly strong for the lattices with a working point closer to the integer resonance ($Q_x/Q_y = 4.28/3.55$). For all lattices with additional individual quadrupoles, horizontal working points larger than $Q_x = 4.4$ have not been included in the study, as they would most likely exhibit a large horizontal emittance growth due to the systematic $5Q_x$ resonances at $Q_x = 4.4$ and several systematic 4th and 5th order resonances for $4.4 < Q_x < 5.0$ (see Fig. 3.32 for the resonance diagram).

The crossing of several systematic resonances also explains the large horizontal emittance growth of the lattice with only two quadrupole families ($Q_x/Q_y = 4.80/3.55$ no ind in Fig. 3.56), while the large variation of the beam size is most likely the cause of the large vertical emittance growth. The large blow-up of the vertical emittance in the case of the lattice with a dispersion suppression by adjusting the phase advance over the arc to $2 \times 2\pi$, additional quadrupole families for beta-beating correction and a working point of $Q_x/Q_y = 4.28/3.55$ is not understood ($Q_x/Q_y = 4.28/3.55$ ind in Fig. 3.56), but seems to

disappear together with the reduction of the initial oscillation of the horizontal emittance by changing the horizontal working point to $Q_x/Q_y = 4.28/3.55$ ($Q_x/Q_y = 4.38/3.55$ ind in Fig. 3.56). The lattices with a half missing bend dispersion suppressor ($Q_x/Q_y = 4.28/3.55$ and $Q_x/Q_y = 4.38/3.55$ disp in Fig. 3.56) feature the smallest emittance growth with a large reduction of the initial and overall blow-up in the horizontal plane. The blow-up in the vertical plane is only slightly reduced.

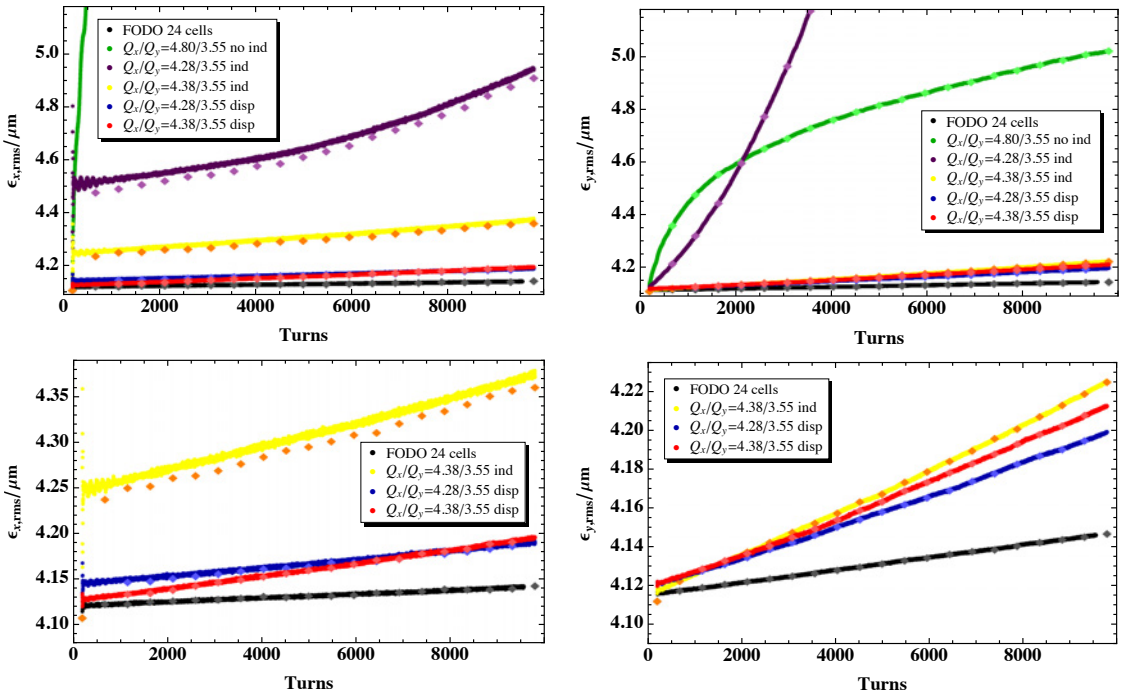


**Figure 3.56:** Time evolution of horizontal (left) and vertical (right) rms emittance for the 24 cell FODO lattices with $2 \times 2$ cells of straight section with only two quadrupole families (no ind), with additional individual quadrupoles for beta-beating correction (ind) and with a half missing bend dispersion suppression scheme (disp) and for the regular 24 cell FODO lattice (FODO 24 cells). The values indicated with diamonds are the emittances calculated, including the second order dispersion. For all simulations the initial distribution has been created taking the linear and second order dispersion into account.

### 3.6.7.4 21 cell FODO lattice with $3 \times 2$ cells of straight section

The regular 21 cell FODO lattice presented in Sec. 3.6.4 exhibits a large emittance blow-up due to the systematic $5Q_x$ resonance at $Q_x = 4.2$. For the studies performed in this section, the working point has been changed to $Q_x/Q_y = 4.47/3.42$, resulting in an emittance growth comparable to the regular 24 cell FODO lattice (Fig. 3.57)[8].

[8]The vertical emittance growth of the 21 cell lattice now lies between the 16 and 24 cell lattice, confirming the assumption that the emittance growth increases with the phase advance per cell (Sec. 3.6.6). Nevertheless, one should be careful with the interpretation of this result as it is quite sensitive to the choice of the working point for the different lattices, as can be seen on the example of the 21 cell lattice matched to $Q_x/Q_y = 4.28/3.55$ and $Q_x/Q_y = 4.47/3.42$.

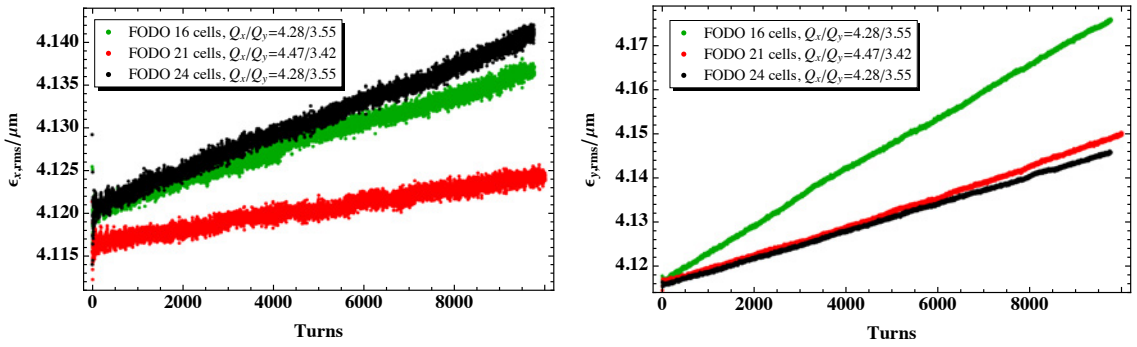


**Figure 3.57:** Time evolution of horizontal (left) and vertical (right) rms emittance for regular FODO lattices with 16, 21 and 24 cells. By changing the working point of the 21 cell lattice, the emittance growth could be reduced to a level comparaple with the 24 cell lattice.

The 21 cell FODO lattices with $3 \times 2$ cells of straight section presented in this section have all been matched to this new working point (or very close to it), in particular also the lattice with only two quadrupole families, resulting in some residual dispersion in the straight sections ($Q_x/Q_y = 4.47/3.42$ no ind. quad. in Fig. 3.58). The optics and beam envelope of two representative 21 cell FODO lattices with $3 \times 2$ cells of straight section

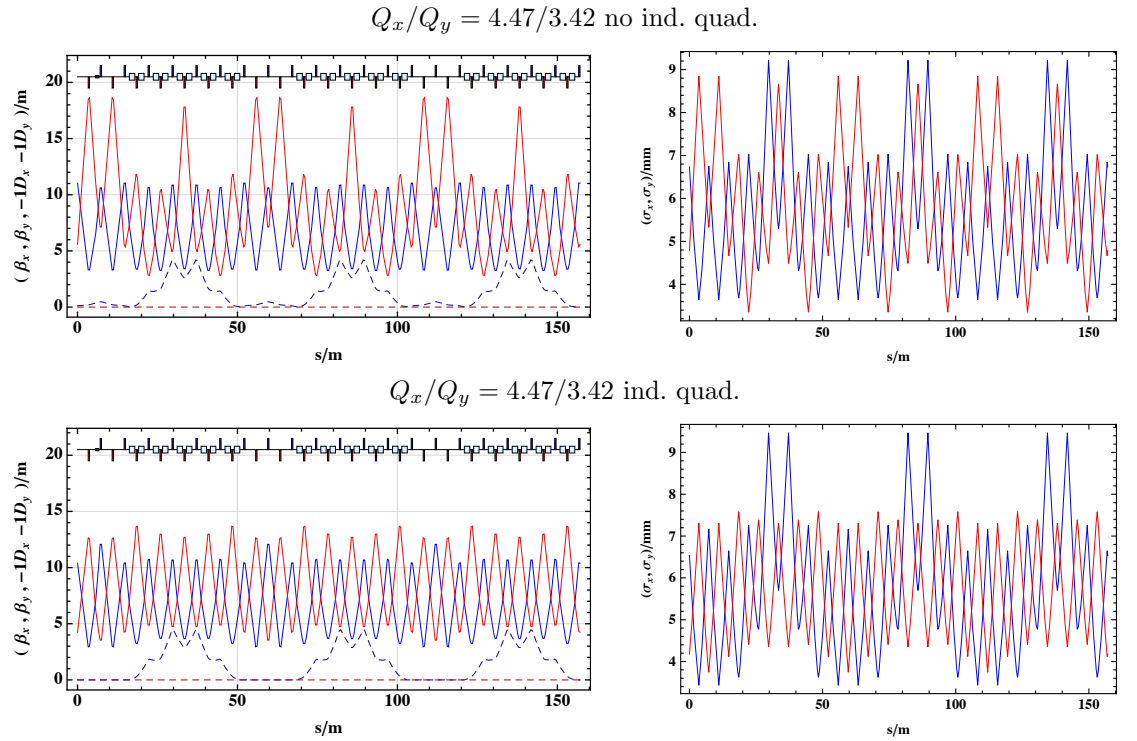


**Figure 3.58:** Optics and one rms beam envelope of the 21 cell FODO lattices with $3 \times 2$ cells of straight section with only two quadrupole families (no ind. quad) and with additional individual quadrupoles for beta-beating correction (ind. quad). The beam envelope has been calculated using the design transverse normalized rms emittance of 2.5 $\mu$m and the rms momentum spread corresponding to the design longitudinal emittance of 2.8 eVs.

and a dispersion suppression by adjusting the phase advance to $2\pi$ over the arc are shown in Fig. 3.58 - one without beta-beating correction ($Q_x/Q_y = 4.47/3.42$ no ind. quad.) and one with beta-beating correction ($Q_x/Q_y = 4.47/3.42$ ind. quad.), and of the lattice with a half missing bend scheme ($Q_x/Q_y = 4.47/3.42$ disp. match 1) featuring the least emittance growth in Fig. 3.59.

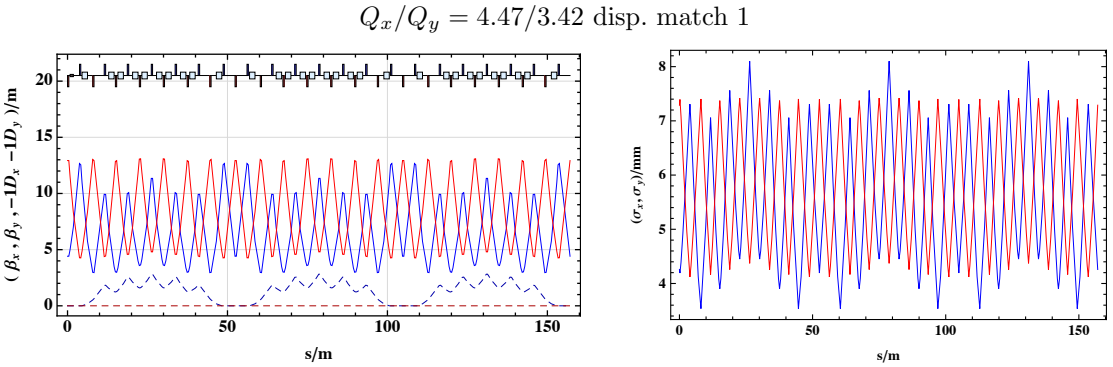


**Figure 3.59:** Optics and one rms beam envelope of the 21 cell FODO lattices with $3 \times 2$ cells of straight section with only two quadrupole families (no ind. quad), with additional individual quadrupoles for beta-beating correction (ind. quad) and with a half missing bend dispersion suppression scheme (disp. match 1). The beam envelope has been calculated using the design transverse normalized rms emittance of 2.5 $\mu$m and the rms momentum spread corresponding to the design longitudinal emittance of 2.8 eVs.

As in the case of the 24 cell FODO lattice with straight sections, the beta-beating is reduced for the lattice with additional quadrupole families ($Q_x/Q_y = 4.47/3.42$ ind. quad.). In addition, the dispersion beating in the arc vanishes by changing to a half missing bend dispersion suppression scheme ($Q_x/Q_y = 4.47/3.42$ disp. match 1).
The time evolution of the emittance for all lattices and the regular 21 cell FODO lattice is shown in Fig. 3.60 and an exemplary tune footprint in Fig. 3.61. First of all, the simulation results differ in three points from the ones obtained for the 24 cell FODO lattice with straight sections:

- The initial oscillations of the horizontal emittance over the first 20 turns are small.
- The agreement of the calculation of the emittance, taking only the linear dispersion into account, with the calculation of the emittance, taking the linear and second order dispersion into account, indicates that higher order dispersion effects have become negligible or at least less relevant.
- The tune footprint does not show the artificially large spread in the horizontal phase-space.

This difference is most probably due to the systematic $5Q_x$ and $2Q_x$ resonances between which the particles are trapped. The proximity of the two systematic resonances makes the system quite sensitive to any small changes and it might be, that the lattices perform quite differently if the working point, or the variation of the beam size, is slightly changed.

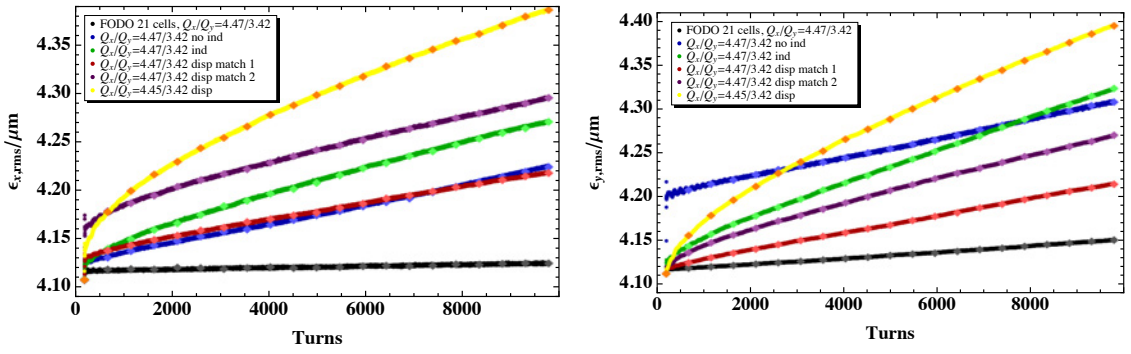


**Figure 3.60:** Time evolution of horizontal (left) and vertical (right) rms emittance for the 21 cell FODO lattices with $3 \times 2$ cells of straight section with only two quadrupole families (no ind), with additional individual quadrupoles for beta-beating correction (ind) and with a half missing bend dispersion suppression scheme (disp) and for the regular 21 cell FODO lattice (FODO 21 cells). The values indicated with diamonds are the emittances calculated including the second order dispersion. For all simulations the initial distribution has been created taking only the linear dispersion into account.

$Q_x/Q_y = 4.47/3.42$, 21 cell FODO lattice $\qquad$ $Q_x/Q_y = 4.47/3.42$, no ind. quad.

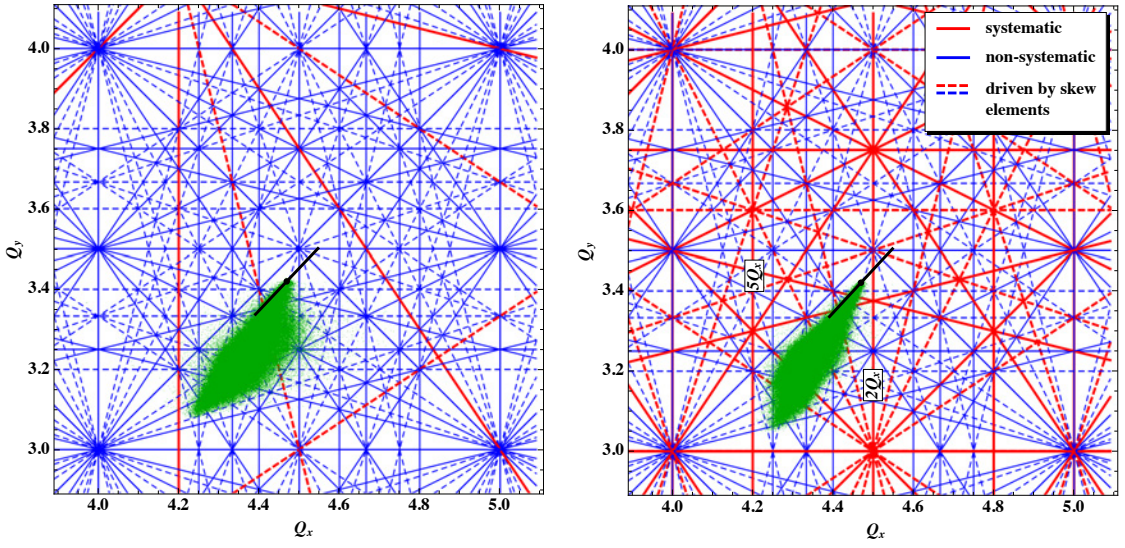


**Figure 3.61:** Resonance diagram until 5th order and tune footprint obtained with PTC-ORBIT of the initial distribution for the regular 21 cell FODO lattice (left) and the 21 cell FODO lattice with $3 \times 2$ cells of straight sections, dispersion suppression by adjusting the phase advance to $2 \times 2\pi$ over the arc and only two quadrupole families. Both lattices are matched to the working point $Q_x/Q_y = 4.47/3.42$. The initial distribution has been matched in both cases, taking only the linear dispesion into account.

Two examples to back up this assumption are two different half missing bend lattices of an earlier matching attempt, one with only a larger variation of the beam size (Fig. 3.62 (left)), and one with a larger variation of the beam size and a very slight change of the horizontal working point to $Q_x/Q_y = 4.45/3.42$ (Fig. 3.62 (right)). All three missing bend

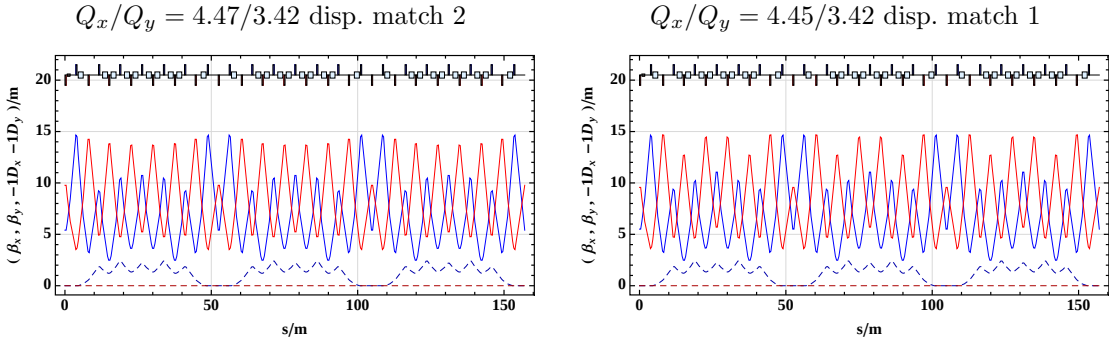


**Figure 3.62:** Optics of two different matches of the 21 cell FODO lattices with $3 \times 2$ cells of straight section and a half missing bend dispersion suppressor scheme.

lattices ($Q_x/Q_y = 4.47/3.42$ disp. match 1, $Q_x/Q_y = 4.47/3.42$ disp. match 2 and $Q_x/Q_y = 4.45/3.42$ disp. in Fig. 3.60) exhibit quite different emittance evolutions.
One explanation for the initial oscillations of the emittance visible in several cases (see Fig. 3.60) could be betatron mismatch. Due to the proximity of the working point to the horizontal and vertical half integer resonance, and in addition that the horizontal half integer resonance is systematic, the beta-beating is suspected to be increased and amplitude dependent, thus leading to an amplitude dependent beta-beating and initial betatron mismatch. Nevertheless, the initial oscillations could still be caused by dispersion mismatch or have an entirely different origin, raising the general question of the cause of emittance blow-up and the reason for the different shapes of emittance growth.
The lattice with a dispersion suppression by adjusting the phase advance to $2\pi$ over the arc and only two quadrupole families ($Q_x/Q_y = 4.47/3.42$ no ind in Fig. 3.60)shows an particularly large sudden increase of the vertical emittance in the beginning. As the $< y^4 >$ moments exhibits a raised amplitude (Table 3.22), the increase could also be, in this case, due to the excitation of the $4Q_y$ resonance.

| | $Q_x/Q_y = 4.47/3.42$ | | | | | $Q_x/Q_y = 4.45/3.42$ |
|---|---|---|---|---|---|---|
| | | disp. over $2\pi$ | | half missing bend | | |
| moment | regular | no ind quad | ind quad | match 1 | match 2 | match 1 |
| $< x >$ | 0 | 0 | 0 | 0 | 0 | 0 |
| $< y >$ | 0 | 0 | 0 | 0 | 0 | 0 |
| $< x^2 >$ | 2.21 | 0 | 0 | 0 | 0 | 0 |
| $< xy >$ | 0 | 0 | 0 | 0 | 0 | 0 |
| $< y^2 >$ | 0 | 0 | 0 | 0 | 0 | 0 |
| $< x^3 >$ | 0 | 0 | 0 | 0 | 0 | 0 |
| $< x^2y >$ | 0 | 0 | 0 | 0 | 0 | 0 |
| $< xy^2 >$ | 0 | 0 | 0 | 0 | 0 | 0 |
| $< y^3 >$ | 0 | 0 | 0 | 0 | 0 | 0 |

| | | | | | | |
|---|---|---|---|---|---|---|
| $< x^4 >$ | 88.14 | 1.12 | 1.61 | 0 | 1.31 | 2.91 |
| $< x^3y >$ | 0 | 0 | 0 | 0 | 0 | 0 |
| $< x^2y^2 >$ | 9.91 | 0 | 0 | 0 | 0 | 1.66 |
| $< xy^3 >$ | 0 | 0 | 0 | 0 | 0 | 0 |
| $< y^4 >$ | 0 | 6.40 | 1.74 | 2.00 | 1.05 | 2.38 |
| $< x^5 >$ | 30.82 | 1.61 | 1.11 | 0 | 0 | 0 |
| $< x^4y >$ | 2.99 | 0 | 0 | 0 | 0 | 0 |
| $< x^3y^2 >$ | 2.01 | 0 | 0 | 0 | 0 | 0 |
| $< x^2y^3 >$ | 0 | 0 | 0 | 0 | 0 | 0 |
| $< xy^4 >$ | 1.12 | 0 | 0 | 0 | 0 | 0 |
| $< y^5 >$ | 1.06 | 1.71 | 0 | 1.41 | 1.11 | 0 |

**Table 3.22:** Maximum amplitude close to a tune of 1.0 of the Fourier analysis of the beam moments after 512 turns for the regular 21 cell FODO lattice (regular) and the 21 cell FODO lattices with $3 \times 2$ cells of straight section with a dispersion suppression by adjusting the phase advance to $2\pi$ over the arc (disp. over $2\pi$) and a half missing bend scheme (half missing bend). Raised amplitudes are indicated in red.

In summary, a reduction of the emittance growth in both planes could be obtained with a half missing bend dispersion suppressor scheme ($Q_x/Q_y = 4.47/3.42$ disp. match 1 in Fig. 3.60). In the case of the dispersion suppression by adjusting the phase advance to $2 \times 2\pi$ over the arc, the decrease of the variation of the beam size leads to an increase in the horizontal and a decrease in the vertical plane, but to no real improvement. In all cases, the origin of the emittance growth is difficult to determine, but good candidates are the excitation of the two systematic resonances - $5Q_x$ and $2Q_x$ - or the horizontal and vertical half integer resonance and betatron or dispersion mismatch.

## 3.7 Conclusion

The main question brought up by the study of a RCS as alternative to the PS Booster upgrade is:

> "Can the RCS lattice, representative for modern high brightness, space-charge dominated lattices, deliver beams with higher brightness than the PS Booster (upgrade), representing the more traditional lattices."

First of all, this question cannot be directly answered, as in this thesis only the influence of the direct space-charge effect on the time evolution of the emittance has been studied and many effects relevant in real machines, like e.g. the effect of the injection process, the ramp and the extraction, fringe fields, magnet imperfections, alignment errors, etc., have been neglected. Nevertheless, the results of the studies of different lattice types obtained in this thesis indicate, that the RCS could probably not deliver as bright beams as the PS Booster after the 2 GeV energy upgrade.

The main results of the studies of different lattice types (Sec. 3.6) can be summarized in a list of lattice and optics characteristics and their influence on the time evolution of the rms emittance, equivalent to the brightness of the beam, as all simulations were carried out for the same beam intensity. These lattice and optics characteristics are:

- **Symmetry**: For all lattices studied in this thesis, the crossing of systematic resonances led to an increase of the rms emittance growth. As the lattice symmetry defines which resonances are systematic and which ones are non-systematic, the symmetry becomes a quite important characteristic of the lattice and optics.
  This was first shown in Sec. 3.6.3 on the example of a 16 cell triplet lattice with symmetry 1, 2, 4 and 16, in which case the symmetry of 16 was (weakly) broken by shortening the bends of 1, 2 and 4 cells respectively. In the following comparison of regular FODO lattices consisting of 15, 16, 18, 21 and 24 cell (Sec. 3.6.4), the increase of the emittance growth due to the crossing of systematic resonances could be further confirmed. The study presented in Sec. 3.6.5 of 15, 16, 18, 21 and 24 cell FODO lattices but now with symmetry 1 revealed that also a weak perturbation of the symmetry leads to an increased emittance blow-up. A much larger emittance growth was though observed for the lattices with a stronger perturbation of the symmetry.

- **Variation of the beam size**: The original assumption was, that a larger variation of the beam size would also result in a larger emittance growth.
  The only clear example identified in this study which backs up this assumption turned out to be the comparison of different cell types (Sec. 3.6.1). In this case, a larger emittance growth was indeed observed for the cells with larger variations of the beam size.
  In the case of the other lattices (Sec. 3.6.3-3.6.5), the difference in emittance growth was mainly caused by the impact of the symmetry of the lattice and optics and the chosen working point. The variation of the beam size was in this case responsible for the breaking of the symmetry: a very localized and large disturbance of the otherwise periodic variation of the beam size, resulted in a strong breaking of the symmetry

and vice versa. The best illustration of the weak and strong symmetry breaking due to the different variation of the beam size is the comparison of the two different optics of the same lattice (Sec. 3.6.5.2).

- **Chromatic detuning**: The variation of the working point of the 16 cell triplet lattice with symmetry 1 (Sec. 3.6.6) made clear that the chromatic detuning, particularly strong in the case of the triplet lattice, represents a non-negligible contribution to the total tune spread. In the particular case of the triplet lattices with large working points, the chromatic detuning leads to an unacceptably large tune spread, (strongly) suggesting a chromaticity correction with sextupole magnets[9].

- **Dispersion suppressor scheme:** Several FODO lattices with straight sections (Sec. 3.6.7) and two dispersion suppressor schemes considered for the RCS, i.e. dispersion suppression by adjusting the phase advance to $n \cdot 2\pi$ over the arc and a half missing bend dispersion suppressor scheme, were studied.
  An obvious disadvantage of lattices with a dispersion suppression by adjusting the phase advance to $n \cdot 2\pi$ over the arc is the fixed working point in the case of the lattices with only two quadrupole families, and in addition large beta-beating. By introducing more quadrupole families, both problems could be mitigated. All lattices with a dispersion suppression by adjusting the phase advance to $n \cdot 2\pi$ over the arc showed initial oscillations and increase of the horizontal emittance, in particular for working points close to the integer resonance. This could be explained by a dispersion and betatron mismatch introduced by space-charge, which increases for particles with a single particle tune approaching the integer resonance. This mismatch is especially strong for the dispersion suppression by adjusting the phase advance to $n \cdot 2\pi$ over the arc, compared to the half missing bend dispersion suppression, due to the large maximum dispersion characteristic for this scheme and the interconnection of dispersion suppression and working point.
  In summary, the lattices with a half missing bend scheme all feature a flexible choice of the working point, a smaller variation of the beam size due to the regular dispersion in the arc and smaller beta-beating in the complete ring and, most importantly, a significant reduction of the initial oscillation of the horizontal emittance.
  In consideration of all the disadvantages of the dispersion suppression by adjusting the phase advance to $n \cdot 2\pi$ over the arc and their mitigation in the case of a dispersion suppression with a missing bend scheme, the dispersion suppression with a half missing bend scheme turned out to be in general the better choice. Nevertheless, for lattices with only one cell of straight section a half missing bend scheme is not feasible and the dispersion suppression by adjusting the phase advance to $n \cdot 2\pi$ over the arc represents the only option. The only drawback of the half missing bend scheme is that the injection and extraction could become more challenging due to

[9] This is only true in the case of the RCS. For slowly cycling machines like the PS Booster the energy spread is significantly smaller due to the smaller required RF voltage. The contribution of the chromatic detuning to the total tune spread is therefore smaller and thus even in the case of a triplet lattice with a high working point, no chromaticity correction would be needed.

the smaller continuous straight sections available and the straight section could not be long enough to host all required RF cavities and eventually collimators.

The assumption that a smaller phase advance per cell would result in a smaller emittance growth turned out to be very difficult to investigate, as the influence of the symmetry and symmetry breaking was, for all lattices studied in regard to this assumption, the dominant effect. The comparison of the 16, 21 and 24 cell lattice (Fig. 3.57) showed the expected behaviour, but it has to be kept in mind that this result depends strongly on the chosen working point.

Coming back to the initial question whether a PS Booster or RCS like lattice would be the better choice, the lattice and optics of both machines are shown in Fig. 3.63 and the most important characteristics compared in Table 3.23.

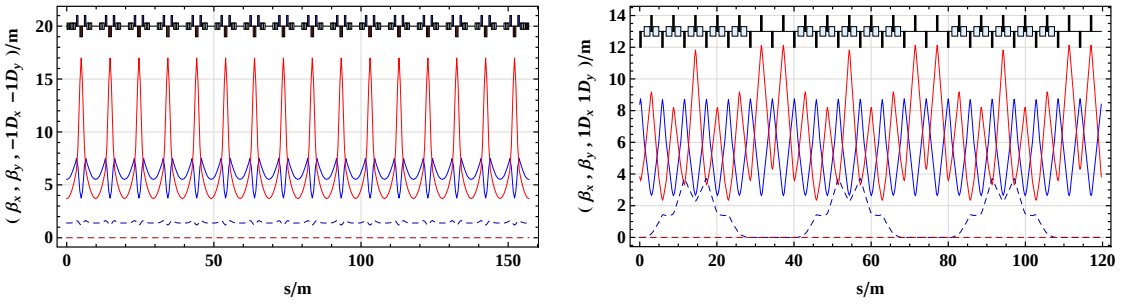


**Figure 3.63:** PS Booster (left) and RCS (right) lattice and optics at injection.

| | **PS Booster** | **RCS** |
|---|---|---|
| cell type | triplet | FODO |
| hor./vert. working point | 4.28/4.55 | 4.20/3.57 |
| number of cells | 16 | 21 |
| hor./vert. phase advance per cell [°] | 96.3/102.4 | 72.0/61.2 |
| symmetry | 16 | 3 |
| dispersion free straight sections | - | 3 |
| dispersion suppressor scheme | - | $2\pi$ over the arc |
| variation of beam size (in comparison) | small | large |

**Table 3.23:** Comparison of the PS Booster and RCS lattice and optics.

Applying the results summarized above, the PS Booster is the better choice in all points except the relatively high phase advance per cell. However, the triplet cell structure of the PS Booster lattice features a very small variation of the beam size compared to a FODO or doublet structure and is thus expected to exhibit a comparably small emittance growth. With a symmetry of 16 and a working point of $Q_x/Q_y = 4.28/4.55$, no systematic resonances are crossed for the PS Booster, while for the RCS with a symmetry of 3 and a working point of $Q_x/Q_y = 4.20/3.57$, the working point is placed right on the systematic $5Q_x$ resonance. By introducing more quadrupole families, the working point of the RCS could be moved and, in addition, also the large beta-beating reduced. Furthermore, because of the dispersion suppression by adjusting the phase advance to $2\pi$ over the arc

and the small fractional horizontal tune of 0.2, a large initial oscillation of the horizontal emittance is to be expected in the case of the RCS.
For the RCS, lattices with a four or two fold symmetry and different number of cells have also been proposed (Sec. 3.2), but the main challenges of all lattices remains the low symmetry and the dispersion suppression.
Besides the practical application to the RCS lattice, the general studies of different lattice types also gave motivation for further general or fundamental studies like for example:

- The investigation of the relevance of coherent and incoherent excitation of resonances.
- The investigation of the cause of the different shapes of the time evolution of the rms emittance.
- The influence of the variation of the beam size on the non-linearity of the optical functions seen by the beam particles.
- The non-linearity of the dispersion seen by the beam particles in the case of lattices with straight sections.

# Summary

After the discovery of a Higg's like particle in 2012, the main objective of the LHC physics is to further investigate its nature and to continue the search for physics beyond the standard model. As the cross section of the processes under study are in general very small, a major upgrade of the LHC, the HL-LHC upgrade, is foreseen around 2020 aiming at a total integrated luminosity of 3000 $fb^{-1}$ during 10-12 years of operation. To reach this goal, the upgrade of the LHC also entails an upgrade of the injector chain delivering the beam to the LHC.

In this thesis, different lattice and optics options of a RCS as alternative to the 2 GeV energy upgrade of the PS Booster - the second accelerator in the LHC injector chain - have been studied. Essential for reaching the performance goal of the HL-LHC is the emittance preservation and minimization of beam losses throughout the injector chain, thus also in the PS Booster or a future RCS. In this respect the PS Booster is currently, and a future RCS would most likely be, mainly limited by space-charge effects. Motivated by the study of the RCS and the obvious differences between the RCS lattice and optics chosen for the technical report [9] and the PS Booster lattice and optics, the performance of different lattice and optics types including space-charge effects has been compared. The studies revealed, that the symmetry of the lattice plays a central role as it determines which resonances are systematic. In general, a larger emittance growth was observed if the tune footprint of the beam crossed a systematic resonance, thus making lattices with a higher symmetry, and consequently less systematic resonances, favourable. Furthermore, a large variation of the beam size entailed in most cases also a larger emittance growth. In the case of lattices with a broken symmetry, which is e.g. the case for lattices with an injection region, a larger variation of the beam size in addition leads to a "stronger" breaking of the symmetry resulting in a larger emittance growth. The lattices with inserted straight sections and a dispersion suppression by adjusting the phase advance to $2\pi$ over the arc all showed a dispersion beating in the arc. This dispersion beating introduces, under the influence of space-charge effects, a dependence of the dispersion seen by the individual beam particles on their tune, which results in turn in a larger emittance growth. This effect can be mitigated with a half missing bend dispersion suppressor, which allows to match the dispersion to the regular dispersion in the arc. In summary, the studies suggest that a PS Booster like lattice would be preferential over the RCS lattice with respect to space-charge effects. However, the performed studies did not include the influence of the injection process and the ramp, possible difficulties during the extraction, the influence of fringe fields, magnetic field and alignment errors, possible resonance compensation schemes

etc., and further studies would be needed to come to a final conclusion about which lattice and optics are the better choice.
In addition to an upgrade of the LHC, also the possibility of deep-inelastic lepton-nucleon scattering at the LHC has been proposed - the LHeC - which would further complement and complete the LHC physics program.
In this thesis, an electron ring lattice and optics of the "Ring-Ring " configuration - except the interaction region - has been designed, which reaches the design parameters detailed in the CDR [10] and which presents a feasible option for the integration of an electron ring in the existing LHC tunnel, considered to be one of the main challenges of the Ring-Ring option. Furthermore, different beam dynamical aspects have been studied: chromatic corrections, different possibilities to create coupling and the influence of circumference errors on the damping partition. In detail, a local chromaticity and off-momentum beta-beating correction scheme has been developed featuring a reduction of the beta-beating, the chromatic detuning and the dependence of the dynamic aperture on the momentum. In contrast to other machines, coupling is needed in the case of the LHeC in order to match the electron beam size to the proton beam size at the interaction point and avoid beam losses and a reduction of the proton beam lifetime [37]. As coupling schemes, three different possibilities have been considered: global coupling created with one skew quadrupole, global coupling of the ring, but with a decoupled interaction region, and localized coupling in the interaction region, where the preferred option is the localized coupling in the interaction region. At last, the estimates of the effect of a circumference errors on the damping partition showed that circumference errors smaller than $\pm^{18}_{10}$ can still be compensated by running off-momentum with the electron as well as proton beam. In the case of larger circumference errors, the electron beam would become anti-damped. In this case, the circumference of the electron ring could be changed by, for example, displacing parts of the ring or using the bypasses as large doglegs. The next steps in the design of the LHeC are a refinement of the lattice and optics with respect to all, and not only the main, integration constraints, the development of an interaction region layout and optics including the beam separation, matching of the electron beam size to the proton beam size at the IP and eventually spin rotators, and further studies of beam dynamics, optics perturbations and collective effects, in particular beam-beam effects.

# Appendix

## A Thin Lens Approximation of a FODO Cell

The most important formulas for a FODO cell in thin lens approximation are summarized in this section. To simplify the formulas the focusing and defocusing quadrupole have equal strength $k$ with $f = \frac{1}{kl} \gg l > 0$. Under these assumptions, the transfer matrix of a quadrupole and a drift space in the transverse plane is then given by

$$M_{\substack{\mathrm{QF}\\\mathrm{QD}}} = \begin{pmatrix} 1 & 0 \\ \mp\frac{1}{f} & 1 \end{pmatrix}, \qquad M_{\mathrm{drift}} = \begin{pmatrix} 1 & s \\ 0 & 1 \end{pmatrix}, \tag{A.1}$$

leading to the following expression for the transfer matrix of one FODO cell of length $L$ without dipoles

$$\begin{aligned} M_{\mathrm{FODO}} &= M_{\mathrm{QFH}} M_{\mathrm{drift}} M_{\mathrm{QD}} M_{\mathrm{drift}} M_{\mathrm{QFH}} \\ &= \begin{pmatrix} 1 - \frac{1}{2}\left(\frac{L}{2f}\right)^2 & L + \frac{L^2}{4f} \\ \left(\frac{L^2}{16f^3}\right) - \frac{L}{4f^2} & 1 - \frac{1}{2}\left(\frac{L}{2f}\right)^2 \end{pmatrix}, \end{aligned} \tag{A.2}$$

where the notation QFH stands for a horizontally focusing half quadrupole.
Including the effect of the dipoles with a bending radius $\theta$, the transfer matrix for the dispersion is given by

$$\begin{aligned} M_{\mathrm{FODO}} &= M_{\mathrm{QFH}} M_{\mathrm{dipole}} M_{\mathrm{QD}} M_{\mathrm{dipole}} M_{\mathrm{QFH}} \\ &= \begin{pmatrix} 1 - \frac{L^2}{8f^2} & \frac{L^2}{4f} + L & \frac{L(8f+L)\theta}{8f} \\ \frac{L(L-4f)}{16f^3} & 1 - \frac{L^2}{8f^2} & \frac{\left(32f^2 - 4Lf - L^2\right)\theta}{16f^2} \\ 0 & 0 & 1 \end{pmatrix}. \end{aligned} \tag{A.3}$$

Using Eqn. A.2 and A.3, expressions for the twiss parameters can be derived. The phase advance is then given by:

$$\sin\left(\phi/2\right) = \frac{L}{4f} \tag{A.4}$$

The motion is stable if $|\mathrm{trace}(M)| < 2$, which is equivalent to

$$f > \frac{L}{4}\,. \tag{A.5}$$

The minimum and maximum beta-function can be expressed by the phase advance and the length of the cell

$$\beta_{\mathrm{max}} = \frac{(1 + \sin\frac{\phi}{2})L}{\sin\phi}, \qquad \beta_{\mathrm{min}} = \frac{(1 - \sin\frac{\phi}{2})L}{\sin\phi}\,. \tag{A.6}$$

Both increase with the length of the FODO cell. The dependence on the phase advance is illustrated in Fig. A.1 (left). The maximum beta-function takes its minimum for 76° while the difference between the maximum and minimum beta-function increases with the phase advance.
Neglecting dispersion - and strictly speaking only valid for large machines - the natural chromaticity (Eqn. 1.38) of one cell is given by

$$\xi_{x,y} = -\frac{1}{4\pi}\left(\frac{\beta_{\max}-\beta_{\min}}{f}\right) \overset{(A.6,\ A.4)}{=} -\frac{1}{\pi}\tan\frac{\phi}{2}\,. \tag{A.7}$$

Assuming that the dipole length is equal to half the cell length $l_{\text{dipole}} = L/2$, and neglecting focusing effects due to the bends (large machine approximation), the maximum and minimum dispersion are given by:

$$D_{\max} = \frac{L\theta(2+\sin\frac{\phi}{2})}{4\sin^2\frac{\phi}{2}}\,, \qquad D_{\min} = \frac{L\theta(2-\sin\frac{\phi}{2})}{4\sin^2\frac{\phi}{2}}\,, \tag{A.8}$$

and decrease with the phase advance (Fig. A.1 (right)).

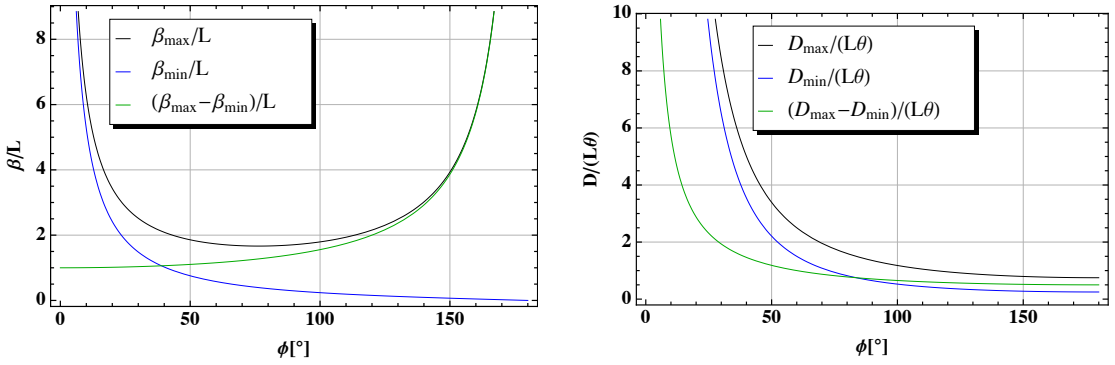


**Figure A.1:** Maximum and minimum beta-function (left) and dispersion (right) as function of the phase advance $\phi$

In thin lens approximation the momentum compaction factor can be approximated by:

$$\alpha_c \approx \sum_i \langle D_i\rangle\theta_i$$

with $\langle D_i\rangle$ the average dispersion function and $\theta_i$ the bending angle in the $i$th dipole leading to

$$\alpha_c \approx \frac{(D_{\max}+D_{\min})}{L} N_{\text{Cell}}\theta \overset{(A.8)}{=} \frac{\theta^2}{\sin^2(\phi/2)} \approx \frac{1}{\nu_x^2}\,, \tag{A.9}$$

where $\nu_x$ is the betatron tune. For gamma transition one then obtains:

$$\gamma_{\text{T}} = \sqrt{\frac{1}{\alpha_c}} \overset{(A.9)}{\approx} \nu_x\,. \tag{A.10}$$

Assuming that the dipoles fill all space between the quadrupoles, the horizontal equilibrium emittance of a synchrotron radiation dominated machine is given by [14]

$$\epsilon_x = \frac{(2-\frac{3}{2}\sin^2(\frac{\phi}{2})+\frac{1}{15}\sin^4(\frac{\phi}{2}))}{\sin^2(\frac{\phi}{2})\sin\phi}\frac{\theta^3}{J_x}\,. \tag{A.11}$$

The emittance decreases with increasing damping partition $J_x$, and the minimum emittance is obtained for 136° independent of $J_x$ (Fig. A.2).

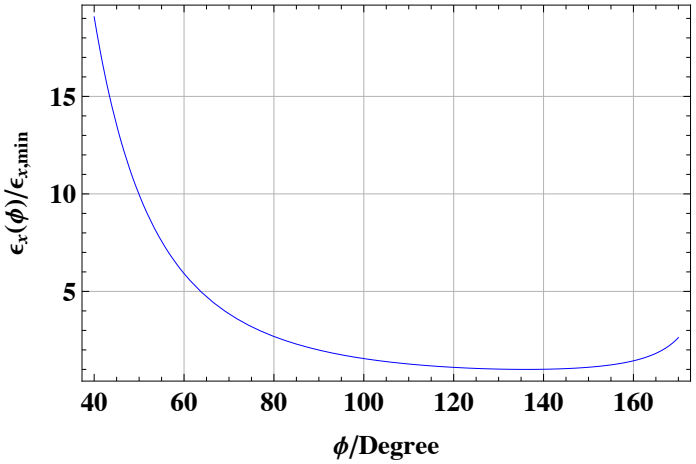


**Figure A.2:** Horizontal equilibrium emittance of a FODO cell as function of the phase advance $\phi$.

# B Phasor

In order to fulfil the phase advance conditions required for some optics, the phase advance can be modulated by inserting a symplectic matrix $R(\Delta\phi_x, \Delta\phi_y)$ which does not change the twiss functions and dispersion but modifies the phase advance within a range of $\pm\pi$. This method is a practical tool to try out some phase advance dependent optics modification without rematching the concerned section or even the complete ring. Assuming no coupling and no vertical dispersion, the constraint of no change of the twiss functions, horizontal dispersion and angular dispersion yields for the matrix $R(\Delta\phi_x, \Delta\phi_y)$ [76]:

$$R(\Delta\phi_x, \Delta\phi_y) = \begin{pmatrix} R_{11} & R_{12} & 0 & 0 & 0 & R_{16} \\ R_{21} & R_{22} & 0 & 0 & 0 & R_{26} \\ 0 & 0 & R_{33} & R_{34} & 0 & 0 \\ 0 & 0 & R_{43} & R_{44} & 0 & 0 \\ R_{51} & R_{52} & 0 & 0 & 1 & 0 \\ 0 & 0 & 0 & 0 & 0 & 1 \end{pmatrix} \text{ with}$$

$$\begin{aligned} R_{11} &= \cos(\Delta\phi_x) + \alpha_x \sin(\Delta\phi_x), & R_{12} &= \beta_x \sin(\Delta\phi_x), \\ R_{21} &= -\gamma_x \sin(\Delta\phi_x), & R_{22} &= \cos(\Delta\phi_x) - \alpha_x \sin(\Delta\phi_x), \\ R_{33} &= \cos(\Delta\phi_y) + \alpha_y \sin(\Delta\phi_y), & R_{34} &= \beta_y \sin(\Delta\phi_y), \\ R_{43} &= -\gamma_y \sin(\Delta\phi_y), & R_{44} &= \cos(\Delta\phi_y) - \alpha_y \sin(\Delta\phi_y), \\ R_{16} &= D_x(1 - R_{11}) - D'_x R_{12}, & R_{26} &= D'_x(1 - R_{22}) - D'_x R_{21}, \\ R_{51} &= D'_x(1 - R_{11}) + D_x R_{21}, & R_{52} &= D_x(R_{22} - 1) - D'_x R_{12}, \end{aligned} \tag{B.1}$$

where $\beta_{x/y}$, $\alpha_{x/y}$, $\gamma_{x/y}$, $D_x$ and $D'_x$ denote the twiss functions, the horizontal dispersion and the horizontal angular dispersion at the location of the matrix.

# C Chromaticity and Off-Momentum Beta-Beating Correction Using Sextupoles

The basic principle of chromaticity correction using sextupole magnets has been introduced in Section 1.4.3. In large lepton machines like the LHeC, the second order chromaticity and the off-momentum beta-beating also play an important role. Uncorrected, they can lead to a large detuning with momentum for large amplitude particles and a strong momentum dependence of the beta-function at the IP and hence loss in luminosity.
In a collider, the low-beta insertions usually significantly contribute to the off-momentum beta-beating and second order chromaticity. A method to correct both parameters by creating a beta-beating wave in the arc is presented in this section. As only a short summary of the theoretical background will be given, it is referred to e.g. [76], [77], [75], [78] and [79] for further details.

## C.1 Off-momentum beta-beating and second order chromaticity

Expressions for the second order chromaticity and off-momentum beta-beating can be derived by treating the chromatic effects as focusing errors in the Hill's equation and calculating the resulting twiss parameters including the distortion [76], leading to

$$Q'_{x,y} = -\frac{1}{4\pi}\int_0^C ds_1\ k^{(1)}_{x,y}(s_1)\beta_{x,y}(s_1)\,, \tag{C.1}$$

$$\begin{aligned} Q''_{x,y} = \frac{1}{2\pi}\int_0^C ds_1\ k^{(2)}_{x,y}(s_1)\beta_{x,y}(s_1) - \\ \frac{1}{8\pi\sin(2\pi Q_{x,y})}\int_0^C ds_1 \int_0^C ds_2\ k^{(1)}_{x,y}(s_1)\beta_{x,y}(s_1)k^{(1)}_{x,y}(s_2)\beta_{x,y}(s_2) \\ \cdot\cos\left(2\left|\phi_{x,y}(s_1)-\phi_{x,y}(s_2)\right|-2\pi Q_{x,y}\right), \end{aligned} \tag{C.2}$$

$$\frac{\beta'_{x,y}}{\beta_{x,y}} = \frac{1}{2\sin(2\pi Q_{x,y})}\int_0^C ds_1\ k^{(1)}_{x,y}(s_1)\beta_{x,y}(s_1)\cos\left(2\left|\phi_{x,y}(s_1)-\phi_{x,y}(s)\right|-2\pi Q_{x,y}\right), \tag{C.3}$$

where $\beta(s)$ is the unperturbed beta-function for an on-momentum particle and $k^{(1)}_{x,y}$ and $k^{(2)}_{x,y}$ are defined as

$$k^{(1)}_x(s) = (k(s)+\frac{1}{\rho^2(s)}) - m(s)D_x(s)\,, \tag{C.4}$$

$$k^{(1)}_y(s) = -k + m(s)D_x(s)\,, \tag{C.5}$$

$$k^{(2)}_x(s) = k^{(1)}_x(s) + m(s)D^{(2)}_x(s)\,, \tag{C.6}$$

$$k^{(2)}_y(s) = k^{(1)}_y(s) - m(s)D^{(2)}_x(s) \tag{C.7}$$

with $\rho$ being the dipole bending radius, $k$ the normalized quadrupole and $m$ the normalized sextupole strength. As the first and second order dispersion $D_x$ and $D^{(2)}_x$ in general satisfy

similar differential equations [75], they are of the same order of magnitude. Hence, the first term of Eqn. C.2, proportional to

$$k_x^{(2)} = k_x^{(1)} + mD_x^{(2)} = (k + \frac{1}{\rho^2}) - mD_x + mD_x^{(2)} \approx k + \frac{1}{\rho^2}\,,$$
$$k_y^{(2)} = k_y^{(1)} - mD_x^{(2)} = -k + mD_x - mD_x^{(2)} \approx -k\,,$$

becomes of the order of the natural chromaticity of the ring and is in general negligible. Under this approximation, the second order chromaticity $Q''$ and the off-momentum beta-beating are related by

$$Q''_{x,y} = -\frac{1}{4\pi}\int_0^C ds\; k^{(1)}_{x,y}(s)\beta'_{x,y}(s)\,. \tag{C.8}$$

Thus, correcting the off-momentum beta-beating indirectly leads to a reduction of the second order chromaticity.

In colliders, the low-beta insertions in general contribute considerably to the off-momentum beta-beating due to the high beta-function and high gradients in the final focus magnets. One way to reduce the beta-beating is to compensate the beta-beating wave originating from one IP with the following IP by choosing a phase of $\frac{\pi}{2}\,\mathrm{mod}[\pi]$ or $2\pi Q + \frac{\pi}{2}\,\mathrm{mod}[\pi]$ between the IPs [76]. As the LHeC only contains one low-beta insertion, this first option is not applicable. The second possibility is to use different sextupole families, which will be described in the following sections and has been applied to the LHeC in the framework of this thesis (Sec. 2.4.2).

## C.2 Concepts of off-momentum beta-beating correction using sextupole families

The off-momentum beta-beating can be described by two chromatic variables and an invariant as introduced by Montague in [77] and implemented in MAD-X [32]. The two chromatic variables $A$ and $B$, omitting in the following the index $x$ and $y$ for the horizontal and vertical plane, are defined by

$$A = \lim_{\delta\to 0}\left(\frac{1}{\delta}\frac{\alpha(\delta)\beta(0) - \alpha(0)\beta(\delta)}{\sqrt{\beta(\delta)\beta(0)}}\right)\,, \tag{C.9}$$

$$B = \lim_{\delta\to 0}\left(\frac{1}{\delta}\frac{\beta(\delta) - \beta(0)}{\sqrt{\beta(\delta)\beta(0)}}\right) = \lim_{\delta\to 0}\left(\frac{1}{\delta}\frac{\Delta\beta}{\beta}\right) \tag{C.10}$$

with $\delta = (p - p_0)/p_0$ and can be seen as the mismatch of the off-momentum betatron envelope in respect to the on-momentum one.

In an achromatic region with $\Delta k = \lim_{\delta\to 0}\left(\frac{1}{\delta}(k(\delta) - k(0))\right) = 0$, $A$ and $B$ oscillate with twice the betatron frequency satisfying the equation

$$\frac{d^2A}{d\phi^2} + 4A = 0, \quad \frac{d^2B}{d\phi^2} + 4B = 0\,. \tag{C.11}$$

Similar to the Courant-Snyder invariant in the case of the linear betatron motion, one can define the chromatic $W$-function

$$W = \frac{1}{2}\sqrt{A^2 + B^2}\,, \tag{C.12}$$

which is a measure of the strength of chromatic perturbations and an invariant in achromatic regions. As in the case of linear coupling, the chromatic variables $A$ and $B$ and the $W$-function can be represented by vectors in the complex plane, where the $W$-function is replaced by the $W$-vector with

$$\mathbf{W} = \frac{1}{2}(A + iB)\,. \tag{C.13}$$

Most important for the concept of this formalism is that in chromatic regions with $\Delta k \neq 0$, the chromatic variable $A$ is changed, but not $B$ and thus also the absolute value of the $W$-vector given by the $W$-function. In the following achromatic regions, all three variables continue to oscillate with twice the betatron frequency until they suffer the next jump in $A$ respectively $W$ in the next chromatic region. This simplified picture of "jumps" is only valid in thin lens approximation, where exemplary the change of $A$ in the case of a quadrupole of strength $kl$ and length $l$ and sextupoles in a dispersive region with strength $ml$ and length $l$ is given by [77]

$$\begin{aligned} \Delta A &= -\beta(0)k(0)l, \qquad \Delta B = 0 \quad \text{for a quadrupole}\,, \\ \Delta A &= -\beta(0)Dm(0)l, \qquad \Delta B = 0 \quad \text{for a sextupole}\,. \end{aligned} \tag{C.14}$$

In the case of a simple FODO lattice, being the building block of the arc in most large collider lattices, the chromatic effect of the FODO cell quadrupoles can be canceled by placing a sextupole with $m(0)l_sD \approx k(0)l_q$ next to each quadrupole, forming an achromatic doublet. In general, it is advantageous to place the sextupoles as close as possible to the quadrupoles as the beta-function takes its extrema at the center of the quadrupoles, making the correction more efficient due to the maximum of the beta-function in the plane to be corrected and minimizing the distortion in the other plane. Furthermore, as the dispersion function fulfills a similar differential equation as the beta-function, it also takes its maximum respectively minimum at the location of the quadrupoles, leading to a more efficient correction if the sextupoles are placed as close as possible to the quadrupoles[10]. As a rule of thumb, the strength of individual sextupoles should be kept as small as possible in order to reduce geometric aberrations and resonance excitation.
In the case of insertions, a local correction is in most cases not advisable as

- most insertions are required to be dispersion free, resulting in a rather inefficient chromatic correction in this region due to the vanishing dispersion
- the low-beta insertions with their strong final focus quadrupoles and high beta functions induce large chromatic errors, which would require strong individual sextupoles

Instead, the chromatic error induced by the insertion can be corrected by using the arc sextupoles. In this case, a $W$-vector compensating the $W$-vector of the insertion is slowly built up in the arc by reducing or increasing the strength of different arc sextupoles. For this purpose, the arc sextupoles are grouped into $2(N+1)$ interleaved families

$$\begin{aligned} &\underbrace{(S_\mathrm{F},\, S_\mathrm{D};\, S_{\mathrm{F}1},\, S_{\mathrm{D}1};\ldots;\, S_\mathrm{FN},\, S_\mathrm{DN})}_{\text{1st group}}\underbrace{(S_\mathrm{F},\, S_\mathrm{D};\, S_{\mathrm{F}1},\, S_{\mathrm{D}1};\, S_{\mathrm{F}2},\, S_{\mathrm{D}2};\ldots;\, S_\mathrm{FN},\, S_\mathrm{DN})}_{\text{2nd group}} \\ &\underbrace{(S_\mathrm{F},\, S_\mathrm{D};\, S_{\mathrm{F}1},\, S_{\mathrm{D}1};\ldots;\, S_\mathrm{FN},\, S_\mathrm{DN})}_{\text{3rd group}}\ldots\underbrace{(S_\mathrm{F},\, S_\mathrm{D};\, S_{\mathrm{F}1},\, S_{\mathrm{D}1};\ldots;\, S_\mathrm{FN},\, S_\mathrm{DN})}_{\text{last group}}, \end{aligned}$$

[10] Usually the lattice only includes horizontal bends and thus only the strength of the sextupoles correcting the horizontal plane is reduced.

where initially all focusing and defocusing sextupoles have the same strength and compensate the natural chromaticity of the machine. By incrementing the strength of e.g. the $S_F$ family by $\Delta m_{S_F}$, the chromatic variable $A$, and thus the $W$-vector, changes and oscillates with double the betatron frequency until it reaches the next member of its family $(N+1)$ cells later. In order to now coherently increase the $W$-vector, the phase advance $2\phi$ of the second member of the sextupole family should be an exact multiple of $2\pi$. This is illustrated in Fig. C.3.

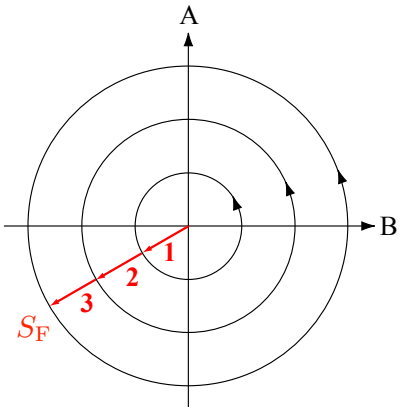


**Figure C.3:** Coherent built-up of the $W$-vector in the arc. The phase advance $2\phi$ between members of one family has to be a multiple of $2\pi$.

This principle holds for all $2(N+1)$ sextupole families, leading to the following relation between the number of sextupole families $2(N+1)$ and the phase advance $\phi_0$ per arc cell

$$2n\pi = 2(N+1)\phi_0, \text{ with } n,\, N \in \mathbb{N}\,. \tag{C.15}$$

Furthermore, as shown in [80], the geometric aberrations up to second order, induced by two equal sextupoles, spaced by a phase advance of $\pi$, exactly cancel each other out[11]. Thus, in order to reduce the geometric aberrations induced by the sextupoles, each family should contain an even number of sextupoles.

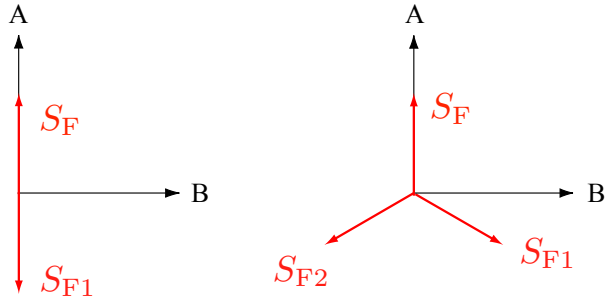


**Figure C.4:** $W$-vectors of the focusing sextupoles in the case of 90° (left) and 60° (right) phase advance per cell.

Taking the above two conditions into account, 4 families are needed for a 90° and 6 families for a 60° phase advance per cell . The resulting $W$-vectors of the sextupole families are

[11] More precise the transfer matrix of two equal sextupoles separated by a phase advance of $\pi$ is minus unity.

shown for both cases in Fig. C.4. For a full compensation, a minimum of 6 independent families is needed, two for $W_x$, two for $W_y$ and two for the linear chromaticities $\xi_x$ and $\xi_y$. In principle, the sextupoles could also be arranged in a non-interleaved or partly interleaved scheme, which has been tried out for some LEP lattice [78]. In this case, the non-interleaved scheme provided a better correction with a larger dynamic aperture for small momentum offsets, but failed for larger momentum offsets as present in a lepton collider like LEP. Therefore, the interleaved schemes are in general considered to be the better choice.
Until now, only the build-up of the $W$-vector in the arc has been discussed. In addition, the correction can be further improved in the case of a low-beta insertion by not only imposing constraints on the phase advance between the arc sextupoles, but also between the final focus magnets and the first arc sextupole. As the final focus magnets as well as the arc sextupoles only change $A$, the $W$-vector should rotate by

$$2\phi_{\mathrm{FF,S}} = 0 \,\mathrm{mod}[\pi] \tag{C.16}$$

between the first sextupole of the correcting family (S) and the final focus magnets (FF) in order to add up coherently (Fig. C.5). In general, the final focus magnets extend over

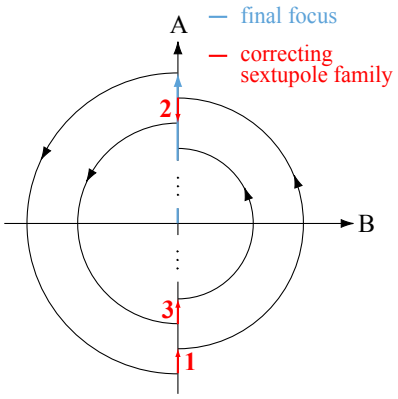


**Figure C.5:** Correction of the $W$ vector created in a low-beta insertion. For an optimal correction the phase advance between the final focus magnets and the first sextupole of the correcting family has to be a multiple of $2\phi = 0 \,\mathrm{mod}[\pi]$.

a larger area and thus are not suited for the practical matching of the phase advance. It is easier to take the IP as a point of reference instead. As the phase advance between the final focus magnets and the IP is approximately $\pi/2$, the condition C.16 is fulfilled if

$$2\phi_{\mathrm{IP,S}} = 0 \,\mathrm{mod}[\pi]\,, \tag{C.17}$$

and can also be used for a first adjustment of the phase advance, followed by an actual matching of the $W$-function to $W = 0$ for a fine adjustment of the beta-beating correction as done in the case of the LHeC in the framework of this thesis (Sec. 2.4.2).

## C.3 Phase sensitivity of the off-momentum beta-beating correction using the arc sextupole families

A critical aspect of the correction of the chromatic error induced by a low-beta insertion with the arc sextupoles is the phase sensitivity, meaning the sensitivity to the deviation of

the phase advance between members of one family to the optimal one. Exemplarily, the case of the LHeC with a phase advance of 90° in the horizontal and 60° in the vertical plane will be investigated in this section. In this case, the off-momentum beta-beating induced by the final focus magnets on the left side $I_{x,y}^{L,\mathrm{IR}}$ is corrected with the adjacent arc to the left, and equally for the right side, leading in the case of the left side of the IP to

$$\begin{aligned} I_{x,y}^{L,\mathrm{IR}} &= I_{x,y}^{L,\mathrm{arc}} \\ &\overset{(C.3)}{=} \frac{1}{2\sin(2\pi Q_{x,y})} \int_{s(\mathrm{arc})}^{s(\mathrm{IP})} ds_1 \; k_{x,y}^{(1)}(s_1)\beta_{x,y}(s_1) e^{i(2|\phi_{x,y}(s_1)-\phi_{x,y}(s)|-2\pi Q_{x,y})} \,, \end{aligned} \tag{C.18}$$

where $s(\mathrm{arc})$ denotes the s-coordinate of the beginning of the arc and $s(\mathrm{IP})$ the s-coordinate of the IP, and the $\cos(\ldots)$ term has been substituted by the exponential function $e^{i(\ldots)}$. A similar expression is obtained for the right side of the IP. Assuming that $\phi_x(s) < \phi_x(s_1)$, that the natural chromaticity is corrected by the arc sextupoles and that the beta-function and dispersion are the same at all focusing and defocusing sextupoles, one obtains for the horizontal plane

$$\begin{aligned} I_x^{L,\mathrm{arc}} &= \underbrace{\frac{e^{-i2(\pi Q_x+\phi_x(s))}}{2\sin(2\pi Q_x)}}_{C_x(s)} \left( \sum_{k=0}^{N_c-1} (-1)^k \Delta m_{S_\mathrm{F}} \beta_{x,S_\mathrm{F}} D_{x,S_\mathrm{F}} e^{i2(k\phi_x^c+\phi_x^L)} \right) + I_x(\Delta m_{S_{\mathrm{D}_i}}) \\ &= C_x(s) \Delta m_{S_\mathrm{F}} \beta_{x,S_\mathrm{F}} D_{x,S_\mathrm{F}} \frac{\sin(N_c \delta\phi_x^c)}{\sin(\delta\phi_x^c)} e^{i((N_c-1)\delta\phi_x^c+2\phi_x^L)} + I_x(\Delta m_{S_{\mathrm{D}_i}}) \,, \end{aligned} \tag{C.19}$$

where $N_c$ is the number of arc cells, $\phi_{x,y}^c$ the phase advance per cell, $\delta\phi_{x,y}^c$ the deviation of the arc cell phase advance per cell from 90° in the horizontal respectively 60° in the vertical plane, $\phi_{x,y}^L$ the phase advance from the IP to the first focusing sextupole $S_\mathrm{F}$ and $\Delta m_{S_{\mathrm{F}_i,\mathrm{D}_i}} = m_{S_{\mathrm{F,D}}} - m_{S_{\mathrm{F}_i,\mathrm{D}_i}}$ the up and down excitation of the $i$th sextupole family with $m_{S_{\mathrm{F,D}}}$ the sextupole strength to correct the natural chromaticity. In the case of $\phi_x^c = \pi/2$ phase advance in the horizontal plane, thus 2 families, one family has to be increased by $\Delta m_{S_\mathrm{F}}$ and the other one decreased by $\Delta m_{S_\mathrm{F}}$ in order to not change the linear chormaticity, thus $\Delta m_{S_{\mathrm{F}_1}} = -\Delta m_{S_{\mathrm{F}_2}} =: \Delta m_{S_\mathrm{F}}$. The contribution of the defocusing sextupole families $S_{\mathrm{D}_i}$ has been summarized in the term $I_x(\Delta m_{S_{\mathrm{D}_i}})$ and is expected to be small due to the small beta-function and dispersion at the location of the $S_{\mathrm{D}_i}$ sextupoles.
From Eqn. C.19, two important conclusions can be drawn:

- an optimal correction is obtained if the phase advance between the IP and the first arc sextupole is a multiple of $\frac{\pi}{2}$

$$(N_c - 1)\delta\phi_x^c + 2\phi_x^L = 0 \bmod [\pi] \,. \tag{C.20}$$

- the diffracting function $\zeta(u) = \frac{\sin(N_c u)}{\sin(u)}$ takes its maximum $N_c$ for $u = 0$, thus in the case of no phase errors. For an increasing number of cells, $N_c$, $\zeta(u)$ starts to fall steeply for $u \neq 0$, meaning that the correction scheme becomes sensitive to even small phase errors.

For the vertical plane with a phase advance of 60°, the expression for $I_y^{L,\mathrm{arc}}$ becomes a bit more complicated as the defocusing sextupoles are not orthogonal to each other:

$$\begin{aligned} I_y^{L,\mathrm{arc}} &= C_y(s)\left(\sum_{j=1}^{3}\sum_{k=0}^{N_c/3-1}\Delta m_{S_{\mathrm{D}_j}}\beta_{y,S_{\mathrm{D}}}D_{x,S_{\mathrm{D}}}e^{i2(k\phi_y^c+(j-1)\frac{\pi}{3}+\phi_y^L)}\right)+I_y(\Delta m_{S_{\mathrm{F}}}) \\ &= C_y(s)\sum_{j=1}^{3}\Delta m_{S_{\mathrm{D}_j}}\beta_{y,S_{\mathrm{D}_j}}D_{x,S_{\mathrm{D}_j}}\frac{\sin\left(\frac{N_c}{3}\delta\phi_x^c\right)}{\sin\left(\delta\phi_x^c\right)}e^{i((\frac{N_c}{3}-1)\delta\phi_y^c+2(j\frac{\pi}{3}+\phi_y^L))} \\ &\qquad +I_y(\Delta m_{S_{\mathrm{F}}})\,, \end{aligned} \tag{C.21}$$

where $C_y(s)=\frac{e^{-i2(\pi Q_y+\phi_y(s))}}{2\sin(2\pi Q_y)}$ is defined analogous to the horizontal plane and $I_y(\Delta m_{S_{\mathrm{F}}})$ summarizes the contribution of the focusing quadrupoles and is considered to be small. As the sextupoles are all placed at the same position in the cell, the twiss parameters at their position are the same, i.e. $\beta_{y,S_{\mathrm{D}_j}}=\beta_{y,S_{\mathrm{D}}}$ and $D_{x,S_{\mathrm{D}_j}}=D_{x,S_{\mathrm{D}}}$. This also implies that $\sum_{j=1}^{3}\Delta m_{S_{\mathrm{D}_j}}=0$, in order to not change the linear chromaticity.
In the case of the vertical plane, similar conclusions as for the horizontal plane can be drawn with the following differences

- an optimal correction is obtained if the phase advance between the IP and one of the defocusing arc sextupoles is a multiple of $\frac{\pi}{2}$

  $$((N_c/3-1)\delta\phi_y^c+2(j\frac{\pi}{3}+\phi_y^L))=0\,\mathrm{mod}[\pi]\,. \tag{C.22}$$

  Usually, the family with a phase advance closest to $\frac{\pi}{2}$ in respect to the IP is chosen, so that only a small rematch of the lattice is necessary.

- the number of cells $N_c$ is replaced by the number of sextupoles per family, i.e. $\frac{N_c}{3}$ in the argument of the diffracting function $\zeta(u)$, thus also in this case, the correction scheme becomes more sensitive to phase errors with an increasing number of arc cells.

# D Equilibrium Emittance with Coupling

The expression Eqn. 1.65 for the transverse emittances

$$\epsilon_i=C_q\frac{\gamma^2}{J_i}\frac{I_{5i}}{I_2},\ i=x,y \tag{D.1}$$

yields that the sum over the product of the damping partition number and emittance is constant

$$J_x\epsilon_x+J_y\epsilon_y=C_{\mathrm{q}}\gamma^2\frac{I_{5x}+I_{5y}}{I_2}=\mathrm{const}\,, \tag{D.2}$$

leading to the following relation between the emittances of the coupled and uncoupled lattice:

$$J_x\epsilon_x+J_y\epsilon_y=J_{0x}\epsilon_{0x}+J_{0y}\epsilon_{0y}\,, \tag{D.3}$$

where the index 0 denotes the parameters of the uncoupled machine.

In most storage rings dominated by synchrotron radiation, the vertical dispersion and emittance are both very small in the case of no coupling, and Eqn. D.3 simplifies to:

$$J_x\epsilon_x + J_y\epsilon_y = J_x\epsilon_{0x}\,. \tag{D.4}$$

Defining the coupling constant $\kappa$ as the ratio between horizontal and vertical emittance

$$\epsilon_y = \kappa\epsilon_x\,, \tag{D.5}$$

the horizontal and vertical emittance in the coupled case read

$$\epsilon_x = \frac{\epsilon_{0x}J_{0x}}{J_x + J_y\kappa}, \qquad \epsilon_y = \frac{\epsilon_{0x}J_{0x}\kappa}{J_x + J_y\kappa}\,. \tag{D.6}$$

Furthermore, under the assumption of no vertical dispersion in the coupled as well as uncoupled case, $I_{4y}$ vanishes and the damping partition numbers, using Robinson's criterion, are given by:

$$\begin{aligned} J_x &= 3 - J_s\,, \\ J_y &= 1\,. \end{aligned} \tag{D.7}$$

With the additional condition of $J_x = J_{0x}$, Eqn. D.6 yields

$$\epsilon_x = \frac{\epsilon_{0x}J_x}{J_x + \kappa}, \qquad \epsilon_y = \frac{\epsilon_{0x}J_x\kappa}{J_x + \kappa}\,. \tag{D.8}$$

# E Damping Decrements and Equilibrium Emittances in the Case of Coupling

In this section, a short summary of the method by Chao [21], [81] to obtain expressions for the damping decrements and equilibrium emittances is given. This summary also has the intention to define the damping decrements and equilibrium emittances as understood in this formalism and implemented in MAD-X [32].

## E.1 Damping decrements

The damping decrements can be derived by including the effect of radiation damping in the $6\times6$ transport matrices of the elements [21]. For example, an electron passing through an RF cavity will change its longitudinal momentum while keeping the transverse momentum unchanged, resulting in a reduction of the slopes $x'$ and $y'$. In the matrix formalism, this change is expressed by replacing the affected matrix elements $m_{22}$ and $m_{44}$ by

$$m_{22} = m_{44} = 1 - \frac{u}{E_0}\,, \tag{E.1}$$

where $u$ is the energy gain at the RF cavity and $E_0$ the energy of the reference particle. Similar expressions can be derived for quadrupoles, sextupoles etc. By concatenating all matrices from the initial position $s$ to $s+C$, where $C$ is the circumference of the ring, one then obtains the one-turn transfer matrix $D(s)$. The eigenvalues of $D(s)$ are then given by

$e^{-\alpha_k \pm i2\pi\nu_k}$, $k = 1, 2, 3$ where $\nu_k$ is the tune of mode $k$ and $\alpha_k$ the damping decrements. It follows that

$$e^{-2(\alpha_1+\alpha_2+\alpha_3)} = \det\left(D(s)\right), \tag{E.2}$$

which reduces to the Robinson criterion (Eqn. 1.60) for weak damping

$$\alpha_1 + \alpha_2 + \alpha_3 = \frac{2U_0}{E_0}, \tag{E.3}$$

where $U_0$ is the energy loss per turn and the horizontal, vertical and longitudinal damping decrements in Eqn. 1.60 have taken the place of the damping decrements of the three eigen-modes.

## E.2 Equilibrium emittances in the case of coupling

In an electron storage ring, the beam distribution can in general be assumed to be Gaussian and can be written in the following form

$$f(\mathbf{x}) = \frac{1}{(2\pi)^3\sqrt{\det(\Sigma)}} e^{-\frac{1}{2}\mathbf{x}^T\Sigma^{-1}\mathbf{x}}, \tag{E.4}$$

where $\Sigma$ is the envelope matrix with

$$\Sigma_{ij} = \langle (x-\bar{x})_i (x-\bar{x})_j \rangle = \int (x-\bar{x})_i (x-\bar{x})_j f(\mathbf{x}), d\mathbf{x} \tag{E.5}$$

and $x_i$ the canonical coordinates of the state vector $\mathbf{x}$.

In [21] it is shown that the envelope matrix $\Sigma(s)$, including the effect of radiation damping and diffusion due to quantum excitation, is given in terms of the eigenvectors $v_k$ of the coupled $6 \times 6$ one-turn matrix $T(s)$ without radiation, explicitly

$$\Sigma_{ij}(s) = \langle x_i x_j \rangle(s) = 2 \sum_{k=1,2,3} \langle |A_k|^2 \rangle \mathrm{Re}\left[v_{ki}(s) v_{kj}(s)\right] \tag{E.6}$$

with

$$\langle |A_k|^2 \rangle = C_L \frac{\gamma^5}{\alpha_k} \oint \frac{|v_{k5}(s)|^2}{|\rho(s)|^3}, \tag{E.7}$$

where $v_{ki}$ is the $i$th component of the vector $v_k$, $\alpha_k$ the damping decrements, $C_L = \frac{55}{48\sqrt{3}} \frac{r_e \hbar}{m_e}$ and $\rho(s)$ the bending radius.

The envelope matrix or the beam distribution respectively - not taking the effect of synchrotron radiation into account - can be now expressed in terms of the quadratic invariants $g_i$, defined by $g_i = \mathbf{x}^T G_i \mathbf{x}$ with $g_i(s) = g_i(s+C)$ for all $\mathbf{x}$ and $G_i$ being a symmetric matrix with $T^T G_i T = G_i$, explicitly [81]:

$$f(\mathbf{x}) = \frac{1}{\pi^3 \langle g_1 \rangle \langle g_2 \rangle \langle g_3 \rangle} e^{-\frac{g_1}{\langle g_1 \rangle} - \frac{g_2}{\langle g_2 \rangle} - \frac{g_3}{\langle g_3 \rangle}}, \tag{E.8}$$

where the average of $g_i$ is defined by $\langle g_i \rangle = \int d\mathbf{x}\, g_i f(\mathbf{x})$. Assuming now that the distribution remains a function of the invariants $g_i$, one obtains an evolution equation for the envelope matrix and the invariants $\langle g_i \rangle$, including the effect of synchrotron radiation. The equilibrium values of the invariants $\langle g_i \rangle_{\mathrm{eq}}$ are then defined as

$$\langle g_i \rangle(s+C) = \langle g_i \rangle(s) = \langle g_i \rangle_{\mathrm{eq}}(s). \tag{E.9}$$

Using the explicit expressions for the envelope matrix [81] ,one obtains that the equilibrium values of the invariants are independent of $s$ and given by

$$\langle g_i \rangle_{\mathrm{eq}} = \frac{\bar{d}_i}{2\chi_i}\,, \tag{E.10}$$

where $\bar{d}_i$ is the diffusion coefficient and $\chi_i$ the global damping decrements, both independent of $s$. For the exact definition of $\bar{d}_i$ and $\chi_i$ it is referred to [81]. Using the definition of the envelope matrix and that it can be expressed with the equilibrium values of $\langle g_i \rangle$, one obtains for the equilibrium emittance of the three different modes

$$\epsilon_{i,\mathrm{eq}} = \frac{1}{2}\langle g_i \rangle_{\mathrm{eq}}\,. \tag{E.11}$$

Note that this definition of the emittance is independent of $s$.

# F Hamiltonian Perturbation Theory Including Linear Coupling

This short summary of the Hamiltonian perturbation theory including linear coupling is based on [82], which is referred to for further details.
Applying a row of canonical transformation the Hamiltonian can be reduced to the linear coupling perturbation term:

$$H' = N(s)xy\,, \tag{F.1}$$

where $N(s)$ is the strength of one skew quadrupole. Using

$$z(s) = \sqrt{2J_z}\sqrt{\beta_z(s)}\cos\left(\Phi_z(s) + \phi_z\right), \quad z = x,\, y$$

where $J_z$ is the action, $\beta_z(s)$ the beta-function, $\phi_z$ the initial phase and $\Phi_z(s)$ is the periodic betatron phase, one obtains

$$H' = 2N(s)\sqrt{J_x J_y \beta_x(s)\beta_y(s)}\cos\left(\Phi_x(s) + \phi_x\right)\cos\Phi_y(s) + \phi_y)\,. \tag{F.2}$$

The equation of motions for this Hamiltonian cannot be solved exactly. In order to get an approximate solution, the Hamiltonian is split up in a periodic and a non-periodic part

$$\begin{aligned} H' &= 2N(s)\sqrt{J_x J_y \beta_x(s)\beta_y(s)}\cos\left(\Phi_x(s) + \phi_x\right)\cos\Phi_y(s) + \phi_y) \\ &= \sum_{j,k=\pm 1} \underbrace{N(s)\sqrt{\beta_x(s)\beta_y(s)}e^{ik(\Phi_x(s)+j\Phi_y(s)-(Q_x+jQ_y)\frac{2\pi s}{L})}}_{\text{periodic in s}} \cdot \\ &\qquad\qquad \frac{\sqrt{J_x J_y}}{2}e^{ik(\phi_x+j\phi_y+(Q_x+jQ_y)\frac{2\pi s}{L})}\,, \end{aligned} \tag{F.3}$$

where $Q_z$ is the betatron tune.
Substituting $s$ with the azimuthal angle $\theta = \frac{2\pi s}{L}$ and scaling the Hamiltonian with $\frac{L}{2\pi}$ to preserve the equations of motion, one can develop the periodic part of the Hamiltonian into a Fourier series

$$\frac{L}{2\pi}N(s)\sqrt{\beta_x(s)\beta_y(s)}e^{ik(\Phi_x(s)+j\Phi_y(s)-(Q_x+jQ_y)\theta)} = \sum_q \kappa_{jkq}e^{ikq\theta} \tag{F.4}$$

with

$$\kappa_{jkq} = \kappa_{jq} e^{ik\phi_{jq}} = \frac{1}{2\pi} \int_{s_0}^{s_0+L} ds\ N(s) \sqrt{\beta_x(s)\beta_y(s)} e^{ik(\Phi_x(s) + j\Phi_y(s) - (Q_x + jQ_y + q)\theta)} \,. \quad \text{(F.5)}$$

The effect of a skew quadrupole on the equations of motion is then given by $\kappa_{jkq}$ and consists of an absolute value $\kappa_{jq}$ independent of $k$ and a phase $e^{ik\phi_{jq}}$, which changes sign with $k$.
Substituting the exponential function with the cosine, one finally obtains:

$$H' = \sum_q \sum_{j=\pm 1} \kappa_{jq} \sqrt{J_x J_y} \cos\left(\phi_x + j\phi_y + (Q_x + jQ_y + q)\theta + \phi_{jq}\right). \quad \text{(F.6)}$$

Note that the above Hamiltonian is independent of $k$. Furthermore, it consists of different perturbations, which oscillate with different frequencies. Most frequencies are higher than the revolution frequency of the particles $Q_x \pm Q_y + q > 1$. Assuming that the perturbations are small, only the perturbations which sum up over several turns have an effect and the rest can be neglected, i.e. perturbations with a period of

$$Q_x \pm Q_y + q \approx 0, \quad q \in \mathbb{Z}\,, \quad \text{(F.7)}$$

where $Q_x + Q_y = q$ is the linear sum resonance ($j = 1$) and $Q_x - Q_y = q$ is the linear difference resonance ($j = -1$).
In thin-lens approximation, the Fourier coefficients $\kappa_{jkq}$ of Eqn. F.5 can be simplified, yielding for the contribution of one skew quadrupole to the sum resonance ($j = 1$)

$$\kappa_{1i} e^{i\phi_{1i}} = \underbrace{\frac{1}{2\pi} N_i \sqrt{\beta_{xi}\beta_{yi}}}_{=\kappa_{1i}} e^{i\psi_i}\,, \quad \text{(F.8)}$$

where $N_i$ is the integrated quadrupole strength and $\psi_i = \Phi_{xi} + \Phi_{yi}$, and for the difference resonance ($j = -1$)

$$\kappa_{-1i} e^{i\phi_{-1i}} = \underbrace{\frac{1}{2\pi} N_i \sqrt{\beta_{xi}\beta_{yi}}}_{=\kappa_{-1i}} e^{i\varphi_i} \quad \text{(F.9)}$$

with $\varphi_i = \Phi_{xi} - \Phi_{yi}$. The total contribution to the sum and difference resonance is then just the sum over all contributions.

# G LHeC Parameters

The beam and lattice parameters used and achieved with the optics designed in this thesis are listed in Table 3.24 and Table 3.25 and the magnet strengths and RF parameters are summarized in Table 3.26 and Table 3.27. The damping times, damping partition numbers, longitudinal parameters and optics parameters are given for the uncoupled lattice. The emittance values given are the unnormalized rms emittances $\epsilon_{\text{rms}}$ at the top energy of 60 GeV with $\epsilon_{\text{rms}} = \epsilon_{\text{normalized}}/(\beta\gamma)$.

| | |
|---|---|
| beam energy | 60 GeV |
| number of particles per bunch | $1.98 \times 10^{10}$ |
| number of bunches | 2808 |
| synchrotron radiation loss per turn | 437.2 MeV |
| synchrotron radiation power | 43.72 MW |
| damping Partition $J_x/J_y/J_s$ | 1.5/1/1.5 |
| hor./vert./long. damping time $\tau_x/\tau_y/\tau_s$ ($\kappa = 0$) | 0.016/0.024/0.016 s |
| polarization time | 61.7 min |
| hor. rms emittance ($\kappa = 0$) | 5.55 nm |
| emittance ratio $\epsilon_y = \kappa\epsilon_x$ | 0.5 |
| hor./vert. rms emittance ($\kappa = 0.5$) | 4.16/2.08 nm |
| fractional energy spread $\sigma_E/E$ ($\kappa = 0$) | 0.00116 |
| bunch length ($\kappa = 0$) | 5.72 mm |

**Table 3.24:** LHeC beam parameters.

| | |
|---|---|
| circumference | 26658.8832 m |
| momentum compaction | $0.0807 \times 10^{-3}$ |
| hor./vert. tune | 123.155/83.123 |
| hor./vert. linear chromaticity | 2.0/2.0 |
| synchr. tune | 0.069 |
| max. horiz./vert. beta (total) | 140.4/135.0 m |
| max. horiz./vert. dispersion (total) | 1.68/0.0 m |
| max. horiz./vert. beta (arc) | 82.5/103.3 m |
| max. horiz./vert. dispersion (arc) | 0.56/0.0 m |

**Table 3.25:** LHeC lattice and optics parameters. The maximum beta and dispersion values are given for the optics not including the interaction region.

| **dipoles** | |
|---|---|
| number | 3080 |
| length | 5.35 m |
| bending radius | 2622.56 m |
| magnetic field at 10-60 GeV | $0.0127 - 0.0763$ T |
| hor./vert. half aperture | 30/20 mm |
| **arc quadrupoles** | |
| number (QF/QD) | 336/336 |
| length | 1 m |
| normalized magnetic field (QF/QD) | $0.052/-0.042$ 1/m |
| magnetic field at 60 GeV (QF/QD) | $10.28/-8.4$ T/m |
| aperture radius | 30 mm |
| **individual quadrupoles** | |
| number (QF/QD) | 148/148 |
| length (QF/QD) | 1/0.7 m |
| max. normalized magnetic field (QF/QD) | $0.090/-0.086$ 1/m |
| magnetic field at 60 GeV (QF/QD) | $< 18$ T/m |
| aperture radius | 30 mm |

**Table 3.26:** LHeC magnet parameters excluding the magnets needed for the interaction region.

| | |
|---|---|
| number of cavities | 112 |
| number of 8-cavity cryo modules | 14 |
| RF voltage | 560 MV |
| RF voltage for 50 h quantum lifetime | 510 MV |
| RF frequency | 721.421 MHz |
| harmonic number | 64152 |

**Table 3.27:** LHeC RF parameters.

# H Analytical Estimate of the Linear Transverse Mismatch

Let $\alpha_1,\ \beta_1$ and $\gamma_1$ be the twiss parameters of the distribution matched to the linear lattice without space-charge. The phase space coordinates $z$ and $z'$ of a particle with the single particle emittance $\epsilon_1$ and phase $\phi$ are given by Eqn. 1.20:

$$z = \sqrt{\beta_1 \epsilon_1}\cos\phi, \quad z' = -\sqrt{\frac{\epsilon_1}{\beta_1}}\left(\sin\phi + \alpha_1\cos\phi\right) . \tag{H.1}$$

Note that a particle distribution matched to a machine (linear, neglecting e.g. direct space-charge) is given by a uniform distribution in phase $\phi$ and any distribution in $\epsilon_1$. The rms emittance of the beam is then just one half of the average of the single particle emittances.

Assuming now that $\alpha_2,\ \beta_2$ and $\gamma_2$ are the new twiss parameters. The single particle emittance of this particle is then described by the Courant-Snyder Invariant (Eqn. 1.17)

$$\gamma_2 z^2 + 2\alpha_2 z z' + \beta_2 z'^2 = \epsilon_2 . \tag{H.2}$$

Inserting Eqn. H.1 into Eqn. H.2, one obtains for the single particle emittance $\epsilon_2$ of the mismatched beam

$$\begin{aligned} \epsilon_2(\phi) \;=\; \epsilon_1 \Bigg( \left(\gamma_2\beta_1 - 2\alpha_2\alpha_1 + \frac{\beta_2}{\beta_1}\alpha_1^2\right)\cos^2\phi + \frac{\beta_2}{\beta_1}\sin^2\phi \\ + \left(\frac{\beta_2}{\beta_1}\alpha_1 - 2\alpha_2\right)\cos\phi\sin\phi \Bigg) . \end{aligned} \tag{H.3}$$

The average single particle emittance $\epsilon_2$ is then given by the average over the phase angle $\phi$, leading to

$$\epsilon_2 = \frac{1}{2\pi}\int_0^{2\pi} \epsilon_2(\phi)\ d\phi = \frac{\epsilon_1}{2}\left(\beta_1\gamma_2 - 2\alpha_2\alpha_1 + \beta_2\gamma_1\right) . \tag{H.4}$$

The rms emittance of the beam after filamentation of the mismatch is obtained after averaging over the single particle emittances

$$\epsilon_{2,\mathrm{rms}} = \epsilon_{1,\mathrm{rms}}\frac{\left(\beta_1\gamma_2 - 2\alpha_2\alpha_1 + \beta_2\gamma_1\right)}{2} , \tag{H.5}$$

and the relative blow-up is given by

$$\frac{\Delta\epsilon}{\epsilon} = \frac{\epsilon_{2,\mathrm{rms}} - \epsilon_{1,\mathrm{rms}}}{\epsilon_{1,\mathrm{rms}}} = \frac{\left(\alpha_1 - \alpha_2\right)^2 - \left(\beta_1 - \beta_2\right)\left(\gamma_1 - \gamma_2\right)}{2} . \tag{H.6}$$

At a point of symmetry with $\alpha_2 = \alpha_1 = 0$, Eqn. H.6 reduces to

$$\frac{\Delta\epsilon}{\epsilon} = \frac{(\Delta\beta)^2}{2\beta_1\beta_2} \approx \frac{1}{2}\left(\frac{\Delta\beta}{\beta_1}\right)^2 , \tag{H.7}$$

where $\Delta\beta = \beta_2 - \beta_1$. From Eqn. H.7 it is obvious that a transverse mismatch always leads to emittance growth and never to a reduction in agreement with the law of phase space conservation.

In order to apply Eqn. H.7, the change of the twiss parameters caused by the space-charge effect has to be calculated. In linear approximation and neglecting the variation of the beam size, the effect can be treated like a constant quadrupole error increasing linearly with the beam intensity $I$ (Sec. 1.7.3):

$$k_{\mathrm{SC}} = \tilde{a}\cdot I , \tag{H.8}$$

where $\tilde{a}$ depends only on the beam distribution. After Eqn. 1.79, the linear dependence of $k_{\mathrm{SC}}$ results also in a linear dependence of $\Delta\beta$ on the beam intensity $I$

$$\begin{aligned}\Delta\beta &= k_{\mathrm{SC}} \underbrace{\left(-\frac{\beta_1}{2\sin 2\pi Q_1}\int_0^C \beta(s)\cos\left(2Q_1(\pi+\phi-\phi_1)\right)ds\right)}_{\text{constant for all intensities}} \\ &\overset{(H.8)}{=} \underbrace{\tilde{a}\left(-\frac{\beta_1}{2\sin 2\pi Q_1}\int_0^C \beta(s)\cos\left(2Q_1(\pi+\phi-\phi_1)\right)ds\right)}_{=:a}\cdot I \\ &= a\cdot I\,. \end{aligned} \tag{H.9}$$

According to Eqn. H.7 this leads in turn to a quadratic dependence of the relative emittance growth on the intensity

$$\frac{\Delta\epsilon}{\epsilon_1} = \frac{(\Delta\beta)^2}{2\beta_1\beta_2} = \frac{(aI)^2}{2\beta_1(\beta_1+a\cdot I)} = \text{const.}\cdot I^2\,. \tag{H.10}$$

# Bibliography


[1] ATLAS Collaboration, "Observation of a new particle in the search for the Standard Model Higgs boson with the ATLAS detector at the LHC," *Physics Letters B*, vol. 716, no. 1, pp. 1 – 29, 2012.

[2] CMS Collaboration, "Observation of a new boson at a mass of 125 GeV with the CMS experiment at the LHC," *Physics Letters B*, vol. 716, no. 1, pp. 30 – 61, 2012.

[3] W. J. Stirling, private communication, 15.01.2012. http://www.hep.phy.cam.ac.uk/~wjs/plots/plots.html.

[4] L. Rossi, "LHC Upgrade Plans: Options and Strategy," *IPAC2011*, 2011.

[5] B. Goddard *et al.*, "Can the proton injectors meet the HL-LHC requirements after LS2?," *Proceedings of Chamonix 2011 workshop on LHC Performance*, 2012.

[6] CERN Document Server, CERN-DI-0812015, 15.01.2012. http://cds.cern.ch/record/1260465.

[7] K. Hanke *et al.*, "Study of an energy upgrade of the CERN PS Booster.," *IPAC2011*, 2011.

[8] K. Hanke *et al.*, "PS Booster Energy Upgrade, Feasibility Study, First Report," tech. rep., CERN, 2010. https://edms.cern.ch/document/1082646/3.

[9] K. Hanke *et al.*, "Feasibility Study of a Rapid Cycling Synchrotron to replace the PS Booster," tech. rep., CERN, 2011. https://edms.cern.ch/document/1154705/1.0.

[10] LHeC Study Group, "A Large Hadron Electron Collider at CERN: Report on the Physics and Design Concepts for Machine and Detector," *J. Phys. G.*, no. 39, 2012. arXiv:1206.2913.

[11] LHeC Study Group, "A Large Hadron Electron Collider at CERN.," Tech. Rep. arXiv:1211.4831. CERN-LHeC-Note-2012-004-GEN, CERN, Geneva, 2012. Contribution 1 to the European Strategy Process 2012 by the LHeC Study Group.

[12] H. Wiedemann, *Particle Accelerator Physics, 3rd edition.* Berlin: Springer, 2007.

[13] S. Y. Lee, *Accelerator Physics.* World Scientific, second edition ed., 2004.

[14] A. W. Chao and M. Tigner, eds., *Handbook of Accelerator Physics and Engineering.* World Scientific, 2006.

[15] F. Willeke and G. Ripken, "Methods of Beam Optics," tech. rep., DESY, 1988.

[16] A. W. Chao, "Coherent Instabilities of a Relativistic Bunched Beam," *SLAC-PUB-2946*, 1982.

[17] M. Sands, "The Physics of Electron Storage Rings," Tech. Rep. SLAC-PUB 121, SLAC, 1970.

[18] J. M. Jowett, "Introductory Statistical Mechanics for Electron Storage Rings," *SLAC-PUB-4033*, 1986.

[19] K. W. Robinson, "Radiation Effects in Circular Electron Accelerators," *Phys. Rev.*, vol. 111, no. 2, pp. 373–380, 1958.

[20] K. Ohmi, K. Hirata, and K. Oide, "From the Beam-Envelope Matrix to Synchrotron-Radiation Integrals," *Phys. Rev. E*, vol. 49, pp. 751–765, 1994.

[21] A. W. Chao, "Evaluation of Beam Distribution Parameters in an Electron Storage Ring," *Journal of Applied Physics*, vol. 50, no. 2, pp. 595–598, 1979.

[22] W. Fischer and W. Chou, "Beam-Beam." Beam Dynamics Newsletter, 2010.

[23] R. Alemany, X. Buffat, R. Calaga, K. Cornelis, M. Fitterer, R. Giachino, W. Herr, A. McPherson, R. Miyamoto, G. Papotti, T. Pieloni, S. Redaelli, F. Roncarolo, M. Schaumann, R. Suykerbuyk, G. Trad, and S. Paret, "Head-on beam-beam tune shifts with high brightness beams in the LHC," 2011.

[24] M. Bassetti and G. A. Erskine, "Closed expression for the electrical field of a two-dimensional Gaussian charge," Tech. Rep. CERN-ISR-TH-80-06. ISR-TH-80-06, CERN, Geneva, 1980.

[25] M. Abramowitz and I. Stegan, eds., *Handbook of Mathematical Functions.* Dover Publications, 1964.

[26] L. J. Laslett, "On Intensity Limitations Imposed by Transverse Space-Charge Effects in Circular Particle Accelerators," *BNL Report*, pp. 324 – 367, 1963.

[27] F. J. Sacherer, "RMS Envelope Equations with Space Charge.," *Nuclear Science, IEEE Transactions on*, vol. 18, no. 3, pp. 1105 –1107, 1971.

[28] K. Schindl, "Space Charge," *CERN Accelerator School*, pp. 305–320, 2006.

[29] A. W. Chao, "The Beam-Beam Instability," *AIP Conf. Proc.*, vol. 127, pp. 201–242, 1985.

[30] M. Furman, "The Hourglass reduction factor for asymmetric colliders," 1991.

[31] W. Herr, "Beam-Beam Interactions," *CERN Accelerator School*, pp. 379–410, 2006.

[32] "MAD-X User's Guide," http://cern.ch/madx/doc/madx_manual.pdf.

[33] D. T. Abell, "PTC Library User Guide," 2011.

[34] E. Forest, F. Schmidt, and E. McIntosh, "Introduction to the Polymorphic Tracking Code," *KEK Report*, no. 2002-3, 2002.

[35] A. W. Chao, *Lecture Notes on Topics in Accelerator Physics*. Stanford, CA: SLAC, 2002.

[36] O. S. Brüning, R. Cappi, R. Garoby, O. Gröbner, W. Herr, T. P. R. Linnecar, R. Ostojic, K. Potter, L. Rossi, F. Ruggiero, K. Schindl, G. R. Stevenson, L. Tavian, T. Taylor, E. Tsesmelis, E. Weisse, and F. Zimmermann, "LHC Luminosity and energy upgrade: A Feasibility Study," Tech. Rep. LHC-Project-Report-626. CERN-LHC-Project-Report-626, CERN, Geneva, 2002.

[37] R. Brinkmann and F. Willeke, "First experience with colliding electron-proton beams in HERA," in *Particle Accelerator Conference*, pp. 3742–3744 vol.5, 1993.

[38] N. Bernard, "Analytic Method to Calculate the Power Produced by Synchrotron Radiation in a Quadrupole Magnet," no. CERN-LHeC-Note-2010-002, 2010.

[39] D. Barber, H. Wienands, M. Fitterer, and H. Burkhardt, "The possibility of polarisation in the LHeC Ring-Ring scenario," *J. Phys. Conf. Ser.*, vol. 295, p. 012145, 2011.

[40] A. A. Sokolov and I. M. Ternov, "On Polarization and Spin Effects in the Theory of Synchrotron Radiation," *Soviet Physics Doklady*, vol. 8, p. 1203, 1964.

[41] U. Wienands, private communcation.

[42] Y. S. Derbenev and H. Grote, "Bending siberian snake as a spin rotator," Tech. Rep. SL-Note-95-37-AP, CERN, Geneva, 1995.

[43] U. Wienands, "Polarized $e^-$ in the LHeC." 3rd CERN-ECFA-NuPECC Workshop on the LHeC, 2010. Chavannes-de-Bogis, Switzerland.

[44] M. Benedikt, P. Collier, V. Mertens, J. Poole, and K. Schindl, *LHC Design Report*. Geneva: CERN, 2004.

[45] A. M. Hutton, M. Placidi, and T. Taylor, "The design principles of LEP version 13: low beta insertions and dispersion suppressors," Tech. Rep. CERN-LEP-Note-465. LEP-Note-465, CERN, Geneva, 1983.

[46] K. Hirata and E. Keil, "Barycentre motion of beams due to beam-beam interaction in asymmetric ring colliders," *Nuclear Instruments and Methods in Physics Research Section A: Accelerators, Spectrometers, Detectors and Associated Equipment*, vol. 292, no. 1, pp. 156 – 168, 1990.

[47] S. Myers, "Overlap Knock-Out Resonances with Colliding Bunched Beams in the CERN ISR," *IEEE Transactions on Nuclear Science*, vol. 26, no. 3, pp. 3574 –3576, 1979.

[48] S. Weisz, private communcation.

[49] J. Osborne, private communcation.

[50] H. Burkhardt, "Considerations for RR." 2nd CERN-ECFA-NuPECC Workshop on the LHeC, 2009. Divonne-les-Bains, France.

[51] Y. Muttoni, private communcation.

[52] H. Burkhardt, private communcation.

[53] J. Jowett, private communcation.

[54] B. W. Montague, "Non-linear coupling from the beam-beam force in electron-positron storage rings," *Nuclear Instruments and Methods in Physics Research*, vol. 187, no. 2-3, pp. 335 – 340, 1981.

[55] S. Fartoukh, private communcation.

[56] A. Burov, S. Nagaitsev, and Y. Derbenev, "Circular modes, beam adapters, and their applications in beam optics," *Phys. Rev. E*, vol. 66, p. 016503, 2002.

[57] J. Jowett and D. Tommasini, "LHeC Electron Ring Arc Design." 2nd CERN-ECFA-NuPECC Workshop on the LHeC, 2009. Divonne.

[58] J. Jowett, "Ions in 2012," *Chamonix Workshop 2012*, 2012.

[59] W. Kriens, "Neue Kontrollen für die Frequenzsteuerung und Synchronisation bei Hera p," *HERA-Seminar in Grömitz*, 2000.

[60] K. Hanke *et al.*, "Study of a Rapid Cycling Synchrotron to replace the CERN PS Booster," *IPAC2011*, 2011.

[61] K. Shigaki, F. Noda, K. Yamamoto, S. Machida, A. Molodozhentsev, *et al.*, "The JKJ lattice.," *AIP Conf.Proc.*, vol. 642, pp. 140–142, 2003.

[62] A. Lachaize, "RCS Design.," *PoS*, vol. Nufact08, 2008.

[63] S. Wang, "Beam Dynamics Design of CSNS/RCS," *ICFA Beam Dynamics Newsletter*, vol. 40, pp. 52–61, 2006.

[64] C. Carli, M. Benedikt, H. Damerau, R. Garoby, B. Goddard, K. Hanke, S. Hancock, and S. Gilardoni, "Alternative/Complementary Possiblities," *Proceedings of Chamonix 2011 workshop on LHC Performance*, 2011.

[65] B. W. Montague, "Fourth-Order Coupling Resonance Excited by Space-Charge Forces in a Synchrotron," *CERN-68-38*, 1968.

[66] W. Bartmann, B. Balhan, J. Borburgh, L. Ducimetière, M. Fitterer, B. Goddard, and L. Sermeus, "Injection and Extraction Considerations for a 2 GeV RCS at CERN," *IPAC2011*, 2011.

[67] C. Carli, private communcation.

[68] M. Fitterer, M. Benedikt, H. Burkhardt, C. Carli, R. Garoby, B. Goddard, K. Hanke, H. Schönauer, and A. S. Müller, "Lattice Design of a RCS as possible alternative to the PS Booster Upgrade," *IPAC2011*, 2011.

[69] E. Forest, A. Molodojentsev, A. Shishlo, and J. Holmes, "Synopsis of the PTC and ORBIT Integration," *KEK Internal 2007-4 (A)*, 2007.

[70] J. D. Galambos, J. A. Holmes, and D. K. Olsen, "ORBIT User Manual," *SNS/ORNL/AP Technical Note*, no. 011, 1999.

[71] F. Schmidt, private communcation.

[72] A. Molodozhentsev, private communcation.

[73] Space-Charge Study Group. Space-Charge Meetings. http://frs.web.cern.ch/frs/Source/space_charge/Meetings.

[74] R. Baartman, "Betatron Resonances with Space Charge," tech. rep., TRIUMF.

[75] A. Verdier, "Chromaticity," *CERN Accelerator School*, pp. 77–100, 1995.

[76] S. Fartoukh, "Second order chromaticity correction of LHC V 6.0 at collision.," Tech. Rep. LHC-Project-Report-308. CERN-LHC-Project-Report-308, CERN, Geneva, 1999.

[77] B. W. Montague, "Linear Optics For Improved Chromaticity Correction," Tech. Rep. CERN-LEP-Note-165. LEP-Note-165, CERN, Geneva, 1979.

[78] P. J. Bryant, "Planning sextupole families in a circular collider," 1989.

[79] S. Fartoukh, "Low-Beta Insertions inducing Chromatic Aberrations in Storage Rings and their Local and Global Correction," Tech. Rep. PAC'09, 2009.

[80] K. L. Brown, "A Second Order Magnetic Optical Achromat," *Nucl. Instrum. Methods*, no. SLAC-PUB-2257, 1979.

[81] B. Nash, J. Wu, and A. W. Chao, "Equilibrium beam distribution in an electron storage ring near linear synchrobetatron coupling resonances," *Phys. Rev. ST Accel. Beams*, vol. 9, p. 032801, 2006.

[82] A. Rostami, "Untersuchung zur Kopplung der Betatronschwingung bei HERA," Master's thesis, Universität Hamburg, 1997.

# Acknowledgements

Firstly, I want to thank Prof. Baumbach and Prof. Quast for giving me the possibility to write my thesis. I would like to thank Anke-Susanne Müller for her support especially in more difficult times, her encouragement and her good supervision despite the larger distance between Karlsruhe and Geneva.
I want to thank my CERN supervisors Helmut Burkhardt and Christian Carli for their guidance and many fruitful discussions throughout the PhD.
I would like to thank Max Klein and Oliver Brüning for the support of my work for the LHeC and its presentation on workshops and conferences.
I like to express my gratitude to my CERN colleagues. In particular, I would like to thank John Jowett, who guided and advised me throughout the LHeC studies, Werner Herr for his patience in answering my many questions about different topics in accelerator physics and his always excellent explanations, Bernhard Holzer for his discussions about optics, Stephane Fartoukh, from who I learned all about chromatic and beta-beating correction and many tricks concerning their practical implementation, Ricardo de Maria, who patiently answered all my questions about optics and MAD-X, Frank Schmidt for his help with PTC and MAD-X, and at last my office mates for the always good atmosphere in our office.
I would like to thank my colleague Alexander Molodozhentsev from KEK for teaching me how to use the simulation code PTC-ORBIT and the general discussion about space-charge effects.
I also like to thank all my colleagues of the THz group in Karlsruhe, especially Steffen Hillenbrand who fought his way bravely through the many pages of my thesis and didn't let one wrong index, figure capture or not introduced variable escape, and my colleague Markus Schwarz for his very useful feedback on the theory parts of this thesis.
I especially would like to thank my good friend Anne Szostek, who checked the complete thesis for any language mistakes.
I would like to thank my boyfriend Joni Hahkala for always supporting me.
Zuletzt möchte ich mich bei meinen Eltern bedanken, die mich immer unterstützt haben.